Green Energy and Technology

Takeshi Yao *Editor*

Zero-Carbon Energy Kyoto 2011

Special Edition of Jointed Symposium of Kyoto University Global COE "Energy Science in the Age of Global Warming" and Ajou University BK21

Springer

Green Energy and Technology

For further volumes:
http://www.springer.com/series/8059

Takeshi Yao
Editor

Zero-Carbon Energy Kyoto 2011

Special Edition of Jointed Symposium of Kyoto University Global COE "Energy Science in the Age of Global Warming" and Ajou University BK21

Springer

Editor
Takeshi Yao
Program Leader
Professor of the Graduate School of Energy Science
Kyoto University
Steering Committee of GCOE Unit for Energy Science Education
Yoshida-honmachi, Sakyo-ku
Kyoto 606-8501, Japan
gcoe-office@energy.kyoto-u.ac.jp

ISSN 1865-3529 e-ISSN 1865-3537
ISBN 978-4-431-54066-3 e-ISBN 978-4-431-54067-0
DOI 10.1007/978-4-431-54067-0
Springer Tokyo Berlin Heidelberg New York

Library of Congress Control Number: 2012931236

Preface

The Great East Japan Earthquake with a magnitude of 9.0 hit east Japan and brought about an unprecedented disaster on March 11, 2011. The tsunami that followed caused great damage. The Fukushima Dai'ichi Nuclear Plant lost all electric power and lapsed into an uncontrollable state. The nuclear plant accident has had a major impact on the energy strategy of Japan and the world. Approach to the energy issue is becoming more and more important.

Since 2008, four departments of Kyoto University, Japan—the Graduate School of Energy Science, the Institute of Advanced Energy, the Department of Nuclear Engineering, and the Research Reactor Institute—have joined forces, and with the participation of the Research Unit for comprehensive activities on local area survivability, they have been engaged in a program entitled "Energy Science in the Age of Global Warming—Toward a CO2 Zero-Emission Energy System" as the Global Center of Excellence (COE) Program of the Ministry of Education, Culture, Sports, Science and Technology of Japan, with the support of university faculty members. This program aims to establish an international education and research platform to foster educators, researchers, and policy makers who can develop technologies and propose policies for establishing a scenario toward a CO2 zero-emission society no longer dependent on fossil fuels by the year 2100.

The Global COE is fully in action. The Scenario Planning Group is setting out a CO2 zero-emission technology roadmap and establishing a CO2 zero-emission scenario based on analyses from the standpoints of social values and human behavior. The Advanced Research Cluster is promoting a socio-economic study of energy, a study of new technologies for renewable energies, and research for advanced nuclear energy by following the roadmap established by the Scenario Planning Group. At the GCOE Unit for Energy Science Education, the students are planning and conducting interdisciplinary group research on their own initiative, combining social and human science with natural science, and working toward CO2 zero emission. At the same time, the students are acquiring the skills to survey the whole energy system by participating in scenario planning and through interaction with researchers from other fields, and are applying the experience to their own research. The Global COE is striving to foster young researchers who will be able to

employ their skills, knowledge, and expertise in their field of study, along with a broad international perspective, to respond to the needs of society in terms of energy and the environment.

The Global COE, in order to transmit the achievements of this platform to the public, posts information on a website, publishes annual reports, quarterly newsletters, books, self-inspection and evaluation reports, hosts domestic and international symposiums and activity reports on meetings, hosts an industry–government–academia collaboration symposium and citizen lectures, and co-hosts related meetings both domestically and internationally.

The Third International Symposium of the Global COE titled "Zero-Carbon Energy, Kyoto 2011" was held jointly with the BK21 Program of Ajou University at Suwon, Korea, August 18–19, 2011, succeeding the International Symposium "Zero-Carbon Energy, Kyoto 2009" at Kyoto University Clock Tower and "Zero-Carbon Energy, Kyoto 2010" at Kyoto University Oubaku Plaza. The international cooperation made the discussions more meaningful and the information exchange more dynamic. Many important lectures and discussions by invited speakers and members of the Global COE, and interesting presentations by students of the GCOE Unit for Energy Science Education, were given. This book is a compilation of the lectures and presentations.

It is very important to promote a wide range of studies in order to cope with the complex and delicate energy and environment problems. The Global COE continues to promote the establishment of a "Low-carbon Energy science," as an interdisciplinary field integrating social science and human science with the natural sciences, for securing energy and conserving the environment, which are the most important issues for the sustainable development of human beings.

Takeshi Yao
Program Leader
Global COE "Energy Science in the Age of Global Warming
—Toward a CO_2 Zero-emission Energy System"

Contents

(ii) Contributed Papers

(iii) Session Papers

Part I
Scenario Planning and Socio-economic Energy Research

(i)
Contributed Papers

Potential of Drastic Improvement of Energy Efficiency in Japan

Seiji Ikkatai and Haruki Tsuchiya

Abstract This research has estimated the potential of drastic improvement of energy efficiency in Japan by classifying the end use services such as transport, food, heating and cooling, power, access to information and lighting. We made tables of potential improvement factors on each fields and has quantified the improvement potential in Japan by 2050. The improvement potential by using existing technology is 31.6% and the improving potential by using the future technology based on theoretical efficiency limit by referring a research result of Cullen and Allwood of Cambridge University is 74.8%.

Introduction of effective policy measures to improve energy efficiency not only for industry sector but for household and commercial sector etc. should be explored more.

Keywords Drastic improvement of energy efficiency • End use services • Existing technology • Future technology • Theoretical efficiency limits

1 Introduction

After the huge earthquake and the accident of nuclear power plant in Eastern Japan, the management of energy supply and demand has become more and more crucial issue in Japan towards the low carbon society. Drastic improvement of energy efficiency of the various sectors including industry, transportation and

S. Ikkatai (✉)
Center for the Promotion of Interdisciplinary Education and Study, Kyoto University, Yoshida-Honmachi Kyoto, Japan
e-mail: ikkatai.seiji.3u@kyoto-u.ac.jp

H. Tsuchiya
Research Institute for Systems Technology, 1-1-5 Higashi-Nihonbashi, Tokyo, Japan

T. Yao (ed.), *Zero-Carbon Energy Kyoto 2011*, Green Energy and Technology,
DOI 10.1007/978-4-431-54067-0_1,

household etc. could be an effective measure to reduce energy usage and reduce environmental pressure without deteriorating people's satisfaction on energy.

This research has estimated the potential of drastic improvement of energy efficiency in Japan by classifying the end use services such as transport, food, heating and cooling, power, access to information and lighting. We made tables of potential improvement factors on each fields and has quantified the improvement potential in Japan by 2050. The improvement potential by using the future technology has been estimated based on theoretical efficiency limit by referring a research result of Jurian Allwood of Cambridge University.

2 Improvement of Overall Energy Efficiency

2.1 Factors on Improvement of Energy Efficiency

Energy efficiency Improvement is combination of Energy device efficiency, social system efficiency and lifestyle efficiency (Fig. 1). Energy device efficiency is known to be improved more than twice with existing technologies, for example, hybrid cars. Sometimes they are called BAT (Best Available Technology). If social system efficiency and lifestyle efficiency are improved, the overall energy efficiency will be much higher.

2.2 Improvement of Energy Efficiency with Existing Technology

We made several tables by classifying the end use services such as access to information, transportation, lighting, heating and cooling, etc. in industry, household, commercial and transport sector.

For example, the improvement of energy efficiency to obtain information with existing technology is shown in Table 1. Electronic devices are more efficient for communication than paper communication. Resource efficiency will be improved by electronic technology as much information on paper is read only once. Energy efficiency will be 60 times for newspaper and 37 times for paper book when substituted by electronic devices.

Another example is "hybrid car" which has engine, electric motor and battery. The millage is 35 km/gas.l (catalogue) and 20–22 km/gas.l (real) which are twice efficient than ordinal car 10–12 km/gas.l (1,500 cc). New infrastructure is not necessary compared with hydrogen fuel cell vehicle. Now, plug-in hybrid is emerging. Electricity is supplied for it at home with larger battery added.

"Eco-drive" is an existing soft technology which is a driving method of cars can affect fuel consumption. It is a driving method with moderate acceleration and braking, keeping constant speed, using engine brake, no idling and no necessary baggage in trunk room. It saves 10–20% of fuel consumption. A construction company saved 30% of truck fuels by eco-drive in Japan (CSR report 2001).

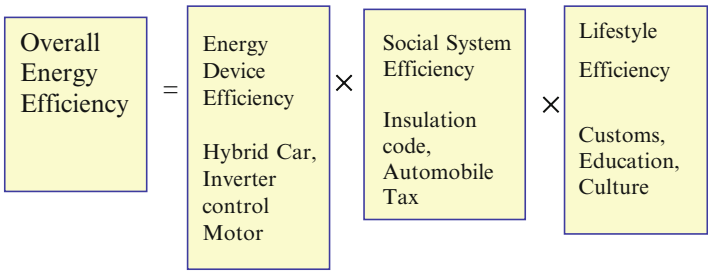

Fig. 1 Improvement of overall energy efficiency

Table 1 Energy efficiency to obtain information

Information	Substitute	Base	Energy/base (kcal)	Electronics (kcal)	Ratio	Use pattern
Book	Electronic book	1 copy	5,403	148	37	8 h to read
Magazine	Electronic Book	1 copy	3,782	55	68	3 h to read
News paper	Electronic news	1 copy	2,231	37	60	1 h for 2 person
Leaflet	Electronic news	1 day	9,950	37	269	1 h for 2 person
CD	Music download	1 copy	800	24	33	PC for 10 min
Post mail	E-mail	1 mail	269	24	11	PC for 10 min

Energy efficiency ratios are calculated for electronic devices compared with conventional methods to obtain information

Truck cargo companies are introducing eco-drive because it can save insurance cost as it affects drivers to drive carefully and to decrease accidents.

Another example is a "car-sharing" which is an easy rent-a-car system with reservation by internet and card systems. It changes people's habitat of driving and decrease car use by nearly 80% reportedly. This means that the rest of transport demand goes to public transportation. It will affect that car production. The habitat of car possession may turn to the habitat of using car.

Efficiency improvement potential factors in transport with existing technology is shown in Table 2 and the total efficiency improvement potential by using existing best available technologies in transport sector in 2050 is shown in Table 3.

2.3 Improvement of Energy Efficiency with Future Technology

Estimating improvement of energy efficiency with future technology is not an easy work because it is difficult to know when and which technology will be developed in the future. Also, it is difficult to predict people's future lifestyle and accepted social systems so on. But still it is beneficial for us to estimate the potential of energy efficiency improvement in the future because it could reduce the difficulty to reduce

Table 2 Efficiency improvement in transport sector

Means	Efficiency improvement	Ratio
Car navigation system	2.4% fuel saving reportedly	0.977
Eco drive	15% saving fuel economy	0.850
Down sizing lighter body	20% better fuel economy	0.833
Hybrid vehicle	Twice fuel economy	0.500
Plug-in-hybrid	2.37 times fuel economy	0.422
Electric vehicle	2.9 times fuel economy	0.345
Fuel cell vehicle	2.26 times fuel economy	0.444
Solar assist car	1.25 times fuel economy	0.800
Bicycle to electric bicycle	70 times efficiency improvement	0.014
Car to railways	12 times efficiency improvement	0.083
Car to bus	3 times efficiency improvement	0.333
Shinkansen to TV conference	16.7 times efficiency improvement	0.060
Aircraft to Shinkansen	12 times efficiency improvement	0.083
Aircraft to TV conference	83.3 times efficiency improvement	0.012

Table 3 Efficiency improvement in transport sector

Scenario 1	2050 efficiency improvement by BAT				
End use energy consumption				Data 2008 10,000 TOE	
	Energy	Efficiency improvement			Result
End use	10000 TOE		Reduce ratio	Ratio	10000 TOE
Transport					
Passenger	5,475			0.345	1,890
Automobile	4,542	Electric vehicle, Plug-in-hybrid, Fuel	−71%	0.286	1,299
Business use	138	Electric vehicle, Plug-in-hybrid, Fuel	−71%	0.286	39
Bus	145	Electric bus, fuel cell Bus	−10%	0.9	131
Railways	191	Efficiency improvement of power tra	−72%	0.28	53
Marine	16	Energy saving design and drive	−20%	0.8	13
Air	443	Energy saving design and drive	−20%	0.8	354
Cargo	2,945			0.731	2,152
Truck	2,502	efficient × reduce execess food + Pay	70% × 94%	0.66	1,651
Railways	191	Efficiency improvement of power tra	−10%	0.9	172
Marine	374	Energy saving design and drive	−20%	0.8	299
Air	55	Energy saving design and drive	−46%	0.54	30

Reducing potentials from present level are to 34% in passenger sector and to 73% in cargo sector around 2050. (Data 2008)

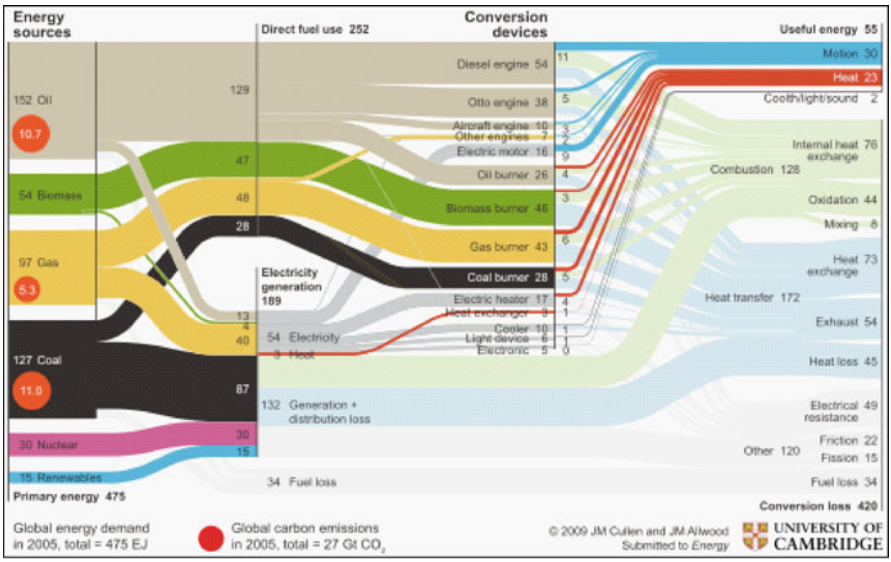

The study by Allwood and others at Cambridge University by excergy efficiency and engineering models shows only 11 per cent of global energy consumption is used effectively and the rest is wasted.

Fig. 2 Efficiency limit of global Energy flow. (Cullen and Allwood, 2010)

the greenhouse gas emission by replacing conventional energies such as fossil fuel energies and nuclear energies by renewable energies.

In this field, there is little studies, but Cullen and Allwood of Cambridge University challenged it 2010. They estimated the efficiency limit of global energy flow (Fig. 2). The point of his study is as follows.

1. Excergy model is used for energy conversion process. Electricity generation, thermal energy use from high temperature to low temperature heat etc.
2. Engineering models are used for energy end use. Heating and cooling at home, electric appliances, automobile etc.
3. Focus on ultimate recycle of material resources. Improvement of design process of steel, copper and aluminum so on
4. 3R (reduce, reuse and, recycle). Reuse is most favorable. If recycle process include melting process then the loss will increase.
5. Estimate of efficiency improvement in industrial activities. Multi stage use of thermal energy, efficient use of mechanical power through electronic devices, Efficient operation of fluid machineries etc.

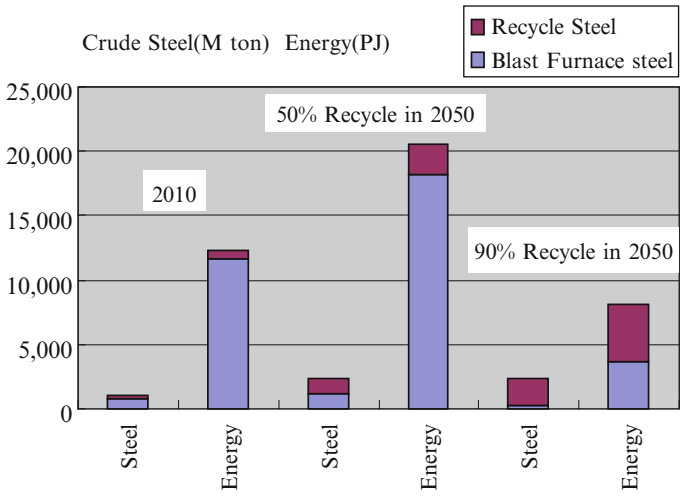

Fig. 3 Production of crude steel in 2050

Table 4 Compound (Cullen and Allwood)

	ε f(%)	ε e(%)	ε d(%)	ε c(%)	100-ε c
End use equipment	Fuel transform efficiency	Efficiency of power generation and transmission	End use device efficiency	Compound efficiency	Reducing potential (%)
Aircraft engine	93	100	27	25	75
Diesel engine	93	100	21	20	80
Other engines	92	78	25	18	82
Electric motor	93	32	56	17	83
Gasoline engine	93	100	12	12	88
Coal burner	90	100	19	17	83
Oil burner	93	100	15	14	86
Gas burner	91	100	13	12	88
Electric heater	93	32	24	7	93
Lighting	93	34	12	4	96
Air conditioner	93	33	7	2	98
Electronic device	93	32	6	2	98
ε c(%) = ε f(%) × ε e(%) × ε d(%)					

Regarding the point 3 above, for example, the case of production of steel is shown at Fig. 3. Crude steel demand in 2050 is estimated 2,400M ton. If recycle rate increases to 50%, energy demand would be depressed but still exceeds the energy consumption in 2010. If the rate increases to 90%, energy demand will decrease absolute terms.

Compound efficiency is calculated by multiplied with fuel transformation, electricity generation and transmission, and end use device efficiency (Table 4).

Limit of energy efficiency of Automobile, for example, is calculated by three factors; rolling resistance, aerodynamic drag, and acceleration resistance (Fig. 4).

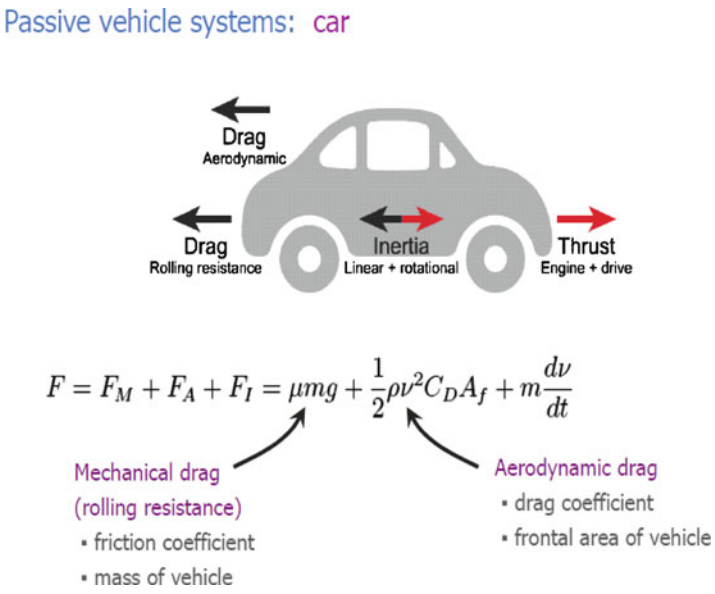

Fig. 4 Limit of energy efficiency of automobiles

Table 5 Realistic limit of energy efficiency

End use	Points of design	Saving potential
Home heating and cooling	Insulation wall, insulation glass, mass of room	100%
Hot water	Use only when necessary, heat recovery, lower temperature	80%
Appliances	Refrigerator, freezer, dish washer, cloth dryer	67%
Lighting	Task lighting	95%
Factory furnace	Loss from wall, ventilation loss, thermal mass	62%
Steam system	Loss from wall, distribution loss, thermal mass	66%
Power systems	Pump, material processing, compressed air, Fan, etc.	59%

Saving potential is estimated by engineering model of energy end use. (Cullen and Alwood, 2010)

By using engineering model, weight can be reduced to 300 kg from 1,300 kg, rolling resistance can be reduced to 0.001 from 0.015, aerodynamic drag coefficient can be reduced to 0.1 from 0.4 and front projected area can be reduced to 1.5 from 2 m^2. The total energy reducing potential is 91%.

The result is understandable, because Toyota released plug-in hybrid 1/X for the 40th Tokyo motor show in 2007. The body size of 1/X is length 3,900 × width 1,620 × height 1,410 mm, wheel base is 2,600 mm. CFRP (Carbon Fiber Reinforced Plastic) is applied. The room space is the same as hybrid car Prius. Weight is 1/3 of Prius 420 kg.

Table 6 Efficiency improvement in household and commercial sector

Scenario 2	2050 Efficiency improvement to Limit					Data 2008	
End use energy consumption						10000 TOF	
	Energy	Fuel		Electricity			Result
End use	10000TOE	10000TOE	Efficiency (%)	10000TOE	Efficiency (%)	Compound Effiency (%)	10000TOE
Household	5,265					0.224	1,181
Cooling	113	0		113	7	0.070	8
Heating	1,280	1,113	15	167	24	0.162	207
Hot water	1,553	1,376	13	177	24	0.143	221
Cooking	428	325	13	103	24	0.157	67
Power	996			996	56	0.560	558
Lighting	996			996	12	0.120	120
Commercial	4,192					0.237	994
Cooling	505	294	15	211	7	0.117	59
Heating	644	586	15	58	24	0.158	102
Hot water	622	597	13	25	24	0.134	84
Cooking	373	333	13	40	24	0.142	53
Power	1,024			1024	56	0.560	573
Lighting	1,024			1024	12	0.120	123

Realistic limit of energy efficiency is calculated by using excergy model and engineering model for end use services shown in Table 5. For example, saving potential of home heating and cooling is 100%. It means home heating and cooling can be controlled only with heat from the sun and the resident him/herself.

Table 6 shows the efficiency improvement of household and commercial sector by future technology in Japan using Cullen and Allwood's research method. Reducing potentials from present level are to 22% in household and to 24% in commercial sector around 2050.

Efficiency Improvement by future technology of transport sector and other sectors in Japan by 2050 are also calculated.

3 Conclusion

Based on the research above, we studied two scenarios of energy saving potential end use energy around 2050. Scenario 1 is applying BAT and adding compound efficiency improvement (decreasing excess food, paper alternative). Scenario 2 is calculated ultimate energy efficiency limit of end use energy referring works of excergy and engineering model by Cullen and Allwood.

Energy reducing potential at end use of scenario 1 is to 68.4% of present level, and that of scenario 2 is to 25.2% of present level

The energy consumption of household depends on lifestyles, and differs sometimes twice even for the same constituent. Lifestyle changed drastically in the last 50 years by automobiles, TV, mobile phones, internet and so on by using relatively cheap energy cost to save time. Also, industrial sector uses more and more energy to produce goods and services. In order to change these trends, there is wide range of policies such as tax, cap and trade, efficiency labeling etc. Introduction of effective policy measures to improve energy efficiency should be explored more.

References

1. Onishi T, Kobayashi H (2010) teitanso toshi korekara no machizukuri (in Japanese), Gaugei-shuppan-shya
2. Weizsaker EV, Lovins A (1997) Factor four. Earthscan Publications Ltd., London
3. Nisioka S (2008) Scenario for low carbon society in Japan (Nihon teitannsoshyakai no sinario, in Japanese), Nikkan-kogyo-shinbun-shya
4. Cullen JM, Allwood JM (2010) Theoretical efficiency limits for energy conversion process. Energy 35
5. Institute for Energy Economics (2009) Handbook of energy and economic statistics in Japan. The Energy Data and Modelling Center, Japan (Nihon Enerugi keizai kennkyujyo, enerugi keizai toukei youran, in Japanese)
6. Tsuchiya H (2003) Energy now and future (Enerugii no ima mirai, in Japanese), Iwanami

Feasibility of Natural Gas Supply from Russia to Korea

Ekaterina Zelenovskaya

Abstract In this paper author calculates the price of gas for the planned gas supply project from Russia to Korea. That price includes: the gas production cost in the prospective gas fields in Russian East regions, gas pipeline transportation cost across Russia to the Pacific coast, and further gas transportation by gas pipeline through the Korean Peninsula or transportation of gas by tankers as liquefied natural gas (LNG), to the Korean consumers. It also includes the minimum expected rates of return on capital by investor (hurdle rates).

Our calculations show that the estimated prices of Russian gas in Korea in constant 2010 US dollars during the period of the possible contract from 2017 to 2041 could be as follows: for PNG (pipeline natural gas) 12.91 $/MBtu (468 $/1,000 m^3), and for LNG 13.22 $/MBtu (479 $/1,000 m^3), which is rather competitive under the projected oil price between 18.37 and 25.79 $/MBtu or 106 and 150 $ per barrel of crude oil for the same period of time. This suggests that supplying Russian natural gas to Korea is cost effective in either PNG or LNG form.

Keywords Energy cooperation • Gas pipeline • Gas supply cost • Korea • LNG • Northeast Asia

1 Introduction

For substantial strengthening of climate policy actions and since fossil fuels will remain the dominant sources of primary energy in the next decades, natural gas, having the lowest carbon emissions content per unit of energy relative to coal and oil, will play a key role in the energy policies worldwide [1]. The demand for gas

E. Zelenovskaya
Institute of Energy Systems and Climate Change (IECC), Ajou University,
San 5, Woncheon-dong, Yeongtong-gu, Suwon 443-749, Republic of Korea
e-mail: katyshali@gmail.com

T. Yao (ed.), *Zero-Carbon Energy Kyoto 2011*, Green Energy and Technology,
DOI 10.1007/978-4-431-54067-0_2,

has consequently significantly increased, especially in the Asia Pacific Region. China and India see the most rapid rates of gas share increase in their primary energy mix. At the same time Korea, Japan, and Taiwan heavily rely on liquefied natural gas (LNG) imports for their gas supplies from Malaysia, Brunei, Indonesia, Australia and the Middle East. On the other hand, Russian Eastern Siberia (RES) and Far East (RFE) regions (which are also part of the NEA) are rich with natural gas, oil and coal and considerably closer to the NEA consumers than the other gas producers. For instance, a possible onshore pipeline route from Russian port Vladivostok to South Korean port Samchuck is about 980 km and offshore it is 690 km, respectively, while the distances between Korea and its other LNG suppliers are 4,140 km—from the closest producer—Brunei, and 13,800 km—from the farthest supplier—Qatar.

Moreover, Korea has a growing gas industry that is heavily dependent on imports and relies almost exclusively on importing gas in liquefied form. LNG imports account for nearly all of the Korean gas supply. Due to the high dependence on LNG imports from the Middle East producers (51% of the total LNG import) and unexpected disruption of gas supply from Indonesia such as the shutdown of the Arun LNG plant for several months [2], diversification of the Korean gas import sources became a very important matter for Korea, and one of the preferable sources of alternative gas supply is Russia [3].

At the same time, Russia seeks to increase its presence in Asian markets [4], but the high cost of development of Greenfield gas deposits in RES and RFE regions and its associated long-distance transportation to the Asian gas markets made the supply of Russian gas to Korea economically inefficient [3]. The economics is becoming more favourable in the last decade because of the rapid increasing in oil prices and correspondingly in the gas prices.[1] This makes gas production from the difficultly-accessible deposits in the RES and RFE regions more practical and also very attractive for sustainable development of the Russian Eastern part and for Northeast Asia as a whole.

This study developed the methodology for enabling the calculation of the minimum prices of gas supply from the RES and RFE regions to Korea. Specifically it determines the price of gas supply from the Chayanda oil and gas condensate field (OGCF) in the Republic of Sakha (RES) together with the gas from Sakhalin III gas fields offshore of Sakhalin Island (RFE), with gas transportation by pipelines across Russia to the Pacific coast (port Vladivostok) and further gas transportation from Vladivostok to South Korean consumers, by tankers as LNG, or, alternatively, by a land pipeline through the Korean Peninsula.

While there are several publications analysing the economic feasibility of Russian gas supply to Korea [5, 6], including feasibility studies conducted by companies such as UKOS (Russia), BP (UK), Kogas (Korea) jointly with the government of Sakha Republic (RES) that worked in eastern Russian gas projects,

[1] Since in all Korean long-term gas supply contracts the gas price is still linked to the oil price by the price formula.

the question of the Russian gas supply cost for Korea still remains open because of two reasons. First, because the previous works examined the different sources and therefore routes of gas supply to Korea [5] which are resulting in different level of final gas price. For example such as the gas supply from Kovykta field near Irkutsk city (RES) by 4,100 km gas pipeline to northeast China and Korea [3, 5]. Second, because the past studies were conducted under different economic assumptions of the gas supply projects, such as different levels of taxation, different field development schemes (production sharing agreements, concessions etc.), as well as for different inflation and discount rates. The previous studies also employed the assessment of the economic feasibility of the project mostly by the Net Present Value (NPV) criteria. This criterion, however, do not show to the buyer the economic merit of the project. From the gas buyer point of view, the project is feasible and desirable if the price of gas by the planning project is equal or lower than the projected gas market price. In this connection, in this study author employed the assessment of the economic feasibility of the project by slight different methodology which allows calculating the minimum acceptable price of gas at which the project could already proceed. Taking into account all differences with the previous studies mentioned above, our study on the gas supply from Cahyanda and Sakhalin III gas fields with its consequent transportation to Pacific coast and then directly to Korea is unique in the literature on Russian gas supply to Korea and important for assessing the feasibility of the Russian-Korean gas supply project under the current economic conditions.

To define the possible minimum price of Russian gas supplied to Korea: DES[2] (Samchuck[3]) we calculate the total price of gas supply which includes the gas production cost in the prospective gas fields (Chayanda and Sakhalin III), gas pipeline transportation cost across Russia to the Pacific coast, the gas transportation cost from the Pacific coast by LNG tankers and alternatively by gas pipeline through the Korean Peninsula (PNG transportation), as well as the minimum rates of return by capital in each element of gas supply chain (gas production, transportation, liquefaction).

To determine the optimal parameters (diameter and working pressure) of trunk gas pipelines the author employed computational methods of fluid dynamics. constituting thereby a bottom-up cost estimation to make pre-engineering estimates of gas production, pipeline and LNG transportation costs. This analysis is integrated with a cost–benefit and breakeven analysis of all gas supply related projects, such as production, transportation, gas liquefaction projects.

[2] Delivered Ex Ship (named port) -where goods are delivered ex ship, the passing of risk does not occur until the ship has arrived at the named port of destination and the goods made available for unloading to the buyer. The seller pays the freight and insurance costs. Costs for unloading the goods and any duties, taxes, etc.. . . are for the Buyer [15].

[3] The marine port, planning LNG terminal at the North-East cost of the Republic of Korea.

2 Planning Russian–Korean Natural Gas Supply Project: General Information

This section provides some general information about the possible Russian-Korean natural gas supply project and its background.

2.1 Russian–Korean Natural Gas Supply Project: Background

Korea's interest in the Russian gas supply dates back to the late 1980s. Since that time, the Russian Eastern Siberia and Far East regions had been considered as a potential base for gas supply to Korea. During the Soviet era and the first decade after the breakup of the Soviet union in 1991, all gas export projects to Asian markets have however failed to progress because of a mixture of political, commercial and institutional obstacles [3]. Since 2002 the situation changed fundamentally after the Russian Government started preparing the program for a unified system of gas production, transmission and distribution in Eastern Siberia and the Far East, taking into account the possibility of exports to China and other Pacific-Asia countries (Eastern gas program [7]). The Russian gas monopoly company JSC Gazprom was appointed by the Russian government as the program execution coordinator. Russian–Korean negotiations about the gas industry progressed since that time. On May 12, 2003 Gazprom and Korea's Kogas entered into a 5-year Agreement of Cooperation which was extended for another 5-year term in 2008. The agreement embraces a wide spectrum of issues including the study of possible ways to deliver Russian natural gas to Korea. In November 2010 the parties entered into the next stage of negotiations and signed a "road map" to export Russian gas to South Korea. According to the document deliveries of natural gas will start in 2017, and the volumes of import are planned to be as much as 10 billion cubic meters per year [4]. The duration of the planned long-term contract is expected to be 25 years.

2.2 Details of the Gas Supply

The natural gas to Korea from Russia may be delivered in liquefied (as LNG) or compressed (as CNG) form, by tankers or by a land pipeline (as PNG) [4]. A possible route of the pipeline is through the Korean Peninsula.

According to the Eastern Gas Program, the sources of gas supply to Korea would be the Sakhalin III gas field offshore of Sakhalin Island (RFE) and the Chayanda oil and gas condensate field (OGCF) in the Republic of Sakha (RES). According to this

program, the transportation of gas will start from the Russian fields to its Pacific coast as follows:

1. From the Sakhalin III gas fields by the recently constructed Sakhalin–Khabarovsk–Vladivostok gas transportation system (GTS)
2. From the Chayanda gas field, by a planned pipeline Yakutia-Khabarovsk with subsequent integration into the Sakhalin–Khabarovsk–Vladivostok GTS

In the Russian Pacific port Vladivostok, the gas would be pumped into the planned Trans-Korean gas pipeline, or optionally, liquefied in the planned LNG plant [8] and transported to Korea by tankers (Fig. 1). The CNG transportation which is also one of the options of international gas transportation to Korea is not included in the scope of our study due to the lack of sufficient technical and economical data on marine CNG transportation methodology and gas compression plants.

As seen from the map, the physical infrastructure of the planned gas supply system to Korea includes the following seven elements:

1. The Sakhalin III gas field
2. The Chayanda OGCF
3. The Sakhalin–Khabarovsk–Vladivostok GTS
4. The Yakutia–Khabarovsk gas pipeline
5. The liquefaction plant (optional)
6. Marine LNG transportation (optional)
7. Trans-Korean gas pipeline (optional)

A short description of each of these elements follows.

2.3 Description of the Projects

The Sakhalin III project involves the development of the Kirinskoye gas field (located 50 km offshore, at water depth around 150 m), which are the Ayashsky and East Odoptinsky blocks of Sakhalin III field. Gas reserves and resources of the Sakhalin III project are estimated at some 1.4 trillion cubic meters. The field is scheduled to become operational in 2014 [9] and the annual gas production from the field will be at the level of 28.6 billion cubic meters (bcm) [10].

The Chayanda OGCF in East Siberia in Sakha Repuplic (also known as Republic of Yakutia) is the biggest gas field in the planned Yakutsk center of gas production in Eastern Siberia.[4] The Chayandinskoye field's proved reserves consist of 1.24 trillion cubic meters of gas and 68.4 million (M) tons of oil and gas condensate [11]. Annual gas production from the field will be at the level of 31 bcm [12].

[4] According to the [7] it is planned to establish four new gas production provinces in east Siberia, namely Krasnoyarsk, Irkutsk, Sakhalin, Yakutsk gas production centers.

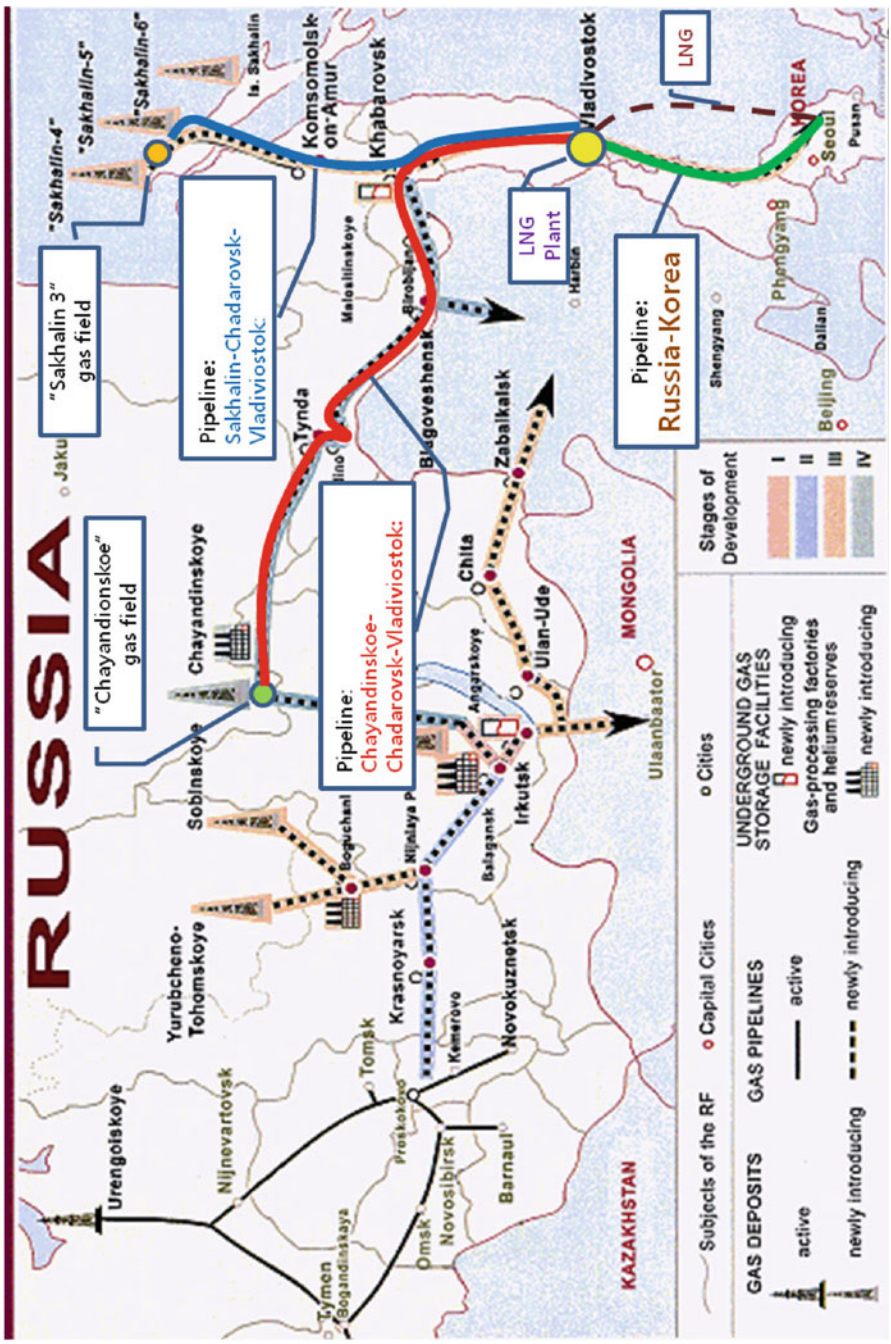

Fig. 1 The map of the possible project of gas supply from Russia to Korea

It is projected to start oil and gas production from the Chayandinskoye field in 2014 and 2016, respectively.

The Sakhalin–Khabarovsk–Vladivostok pipeline is for the transport of Sakhalin's gas to the Vladivostok port and then to the customers in the Far East countries. The total length of the Sakhalin–Khabarovsk–Vladivostok pipeline is 1,837 km. The maximal annual capacity is 31.7 bcm. The diameter of the pipeline is 1,220 mm, and the maximum rated pressure is 9.8 megapascals (MPa).

The Yakutia–Khabarovsk pipeline will start from the Chayanda OGCF in Yakutia. In Khabarovsk city, it will be connected with the Sakhalin–Khabarovsk–Vladivostok GTS. Together, the pipelines will feed a planned LNG plant that will produce LNG for export to NEA, or that will feed a Trans-Korean gas pipeline (if built). The total length of the Yakutia–Khabarovsk pipeline will be about 2,800 km and total length of pipeline from Yakytia to Pacific Ocean (port Vladivostok) is 4,383 km. The maximum annual capacity is 31.7 bcm. The diameter of the pipeline is 1,220 mm, and the maximum rated pressure is 9.8 MPa.

The LNG plant near Vladivostok will be built in the period 2015–2018, and its capacity could be 10 M tons of LNG per year. Two 5 M tons LNG trains are expected to be built. Such plans had been considered by the Board of Gazprom's Directors (as related to the development of gas processing and gas chemicals industry in eastern Russia) in February 2011.

Until our study completion time there was no technical and economic information on a planned Trans-Korean gas pipeline (Fig. 2). Consequently, the technical and economic parameters of planning this gas pipeline were determined and calculated by the author for this study. In this analysis she determined that for supplying 10 bcm of gas to Korea per year it is optimal to build the pipeline with a 1,020 mm internal diameter and operation at 5.45 MPa maximum rated pressure. The length of the pipeline from the Vladivostok port to the destination point—Korean port Samchuck, is 980 km. In the optimization analysis it was chosen to space the compressor stations 130 km apart, thus requiring eight such stations.

Correspondingly, to calculate the final gas price of Russian gas in Korea it is necessary first, to find the price of gas in each of seven elements of the gas supply chain, described above, namely the price of gas production from two fields in Russia, the price of domestic gas transmission by two pipelines, the price of consequent gas liquefaction and LNG transportation as one alternative, and of compressed gas transportation by a Trans-Korean gas pipeline as the other.

For asses the economic merit of the project, the calculated minimum acceptable price (prices—according to the different means of international transportation: LNG or PNG[5]) of Russian gas in Korea must finally be compared with the projected market price of crude oil (since currently the crude oil price serves as a reference for the LNG price in Korea) or the price of gas for the same region (NEA).

[5] Pipeline natural gas.

Fig. 2 Map of the Trans-Korean planned gas pipeline

The comparison must be made on the same energy basis and in the same units, here million British thermal units (MBtu). In this study the comparison is made under the assumption that the average barrel of crude oil has an energy content of 5.8 MBtu and the energy content of 1,000 m^3 of gas is 36.235 MBtu as recommended by International Energy Agency (IEA) for natural gas from Russia [13].

The future crude oil prices in 2010 United States dollars ($) for the period of the contract from 2017 to 2041 obtained from the projections of the IEA [1] while ignoring the effect of inflation[6] and extrapolating the price trend up to the end of the contract, are in the range from 18.37 and 25.79 $/MBtu or 107 $ to 150 $ per barrel of crude oil. This information will be used as the base for comparison of the obtained gas prices with the projected oil price. We also compared the obtained gas prices by the contract with the average gas price projection. According to the

[6] The inflation rate is taken equal to 2.5% annually.

IEA forecast on the gas prices in the different regions, the market price of gas for Asia during the same period of time is expected to be about 0.7 of the price of oil [1] in other words in the range of 12.86 and 18.05 $/MBtu.

3 Methodology

In this study the cost-plus pricing methodology for calculation of the possible minimum price of Russian gas in Korea is described.

3.1 Cost-Plus Pricing Methodology

Cost-plus pricing is a bottom-up approach in the sense that it starts by specifying production costs of gas, gas transmission costs, optionally cost of gas liquefaction and marine gas transportation, adds a profit elements in each segment[7] of the gas chain, and arrives at a cost and profit based price at the delivery point [13]. This method of pricing could help to determine the minimum price that the seller can accept, which includes the sellers' expenses for gas supply as well as the value that the sellers place for their own efforts to participate in this gas supply contract, i.e. the desired minimum rate of return on investment (hurdle rate). In other words the price which allows the project to *break even financially*. We will call this price a breakeven price (BEP) of gas and it is a key element for the calculation of the minimum price of Russian gas in Korea.

3.2 Calculation of the BEP Through the Cost–Benefit Analysis

To calculate the BEP of gas in each element of gas supply chain first it is necessary to conduct the cost–benefit analysis (CBA) of each element, precisely: CBA of gas production projects, CBAs of liquefaction and transportation projects. By CBA all benefits and costs related to the project (in money terms) then will be adjusted for the time value of money, using the discount technique, so that all flows of benefits and costs of project over time (which tend to occur at different points in time) are expressed on a common basis in terms of their "present value".

[7] The adding of the profit elements separately by the each element of the seller's gas chain or aggregately to the total cost of gas supply depends on the physical structure of the seller's company, e.g. whether its gas production and transportation segments working as a separated businesses each with each own financial accounting system or not.

The central tool of CBA and the convenient method for identification of the break-even point (and consequently, the BEP) is the Net present value (NPV) of the project cash flows.

The formula for NPV is as follow:

$$\mathrm{NPV} = \sum_{n=1}^{N} \frac{B_n - C_n}{(1+r)^n} \tag{1}$$

where:

N: Analysis period (years)

B_n: Benefit of the project in year n (M USD)

C_n: Cost of the project in year n (M USD)

R: Discount rate (the time value of cash flows)

Since the price of gas (**P**) directly influences the benefits (B_n) of the project ((2)) and the investment and operational cost are essential components of the total costs (C_n) (3), they are integral parts of the NPV (4).

$$B_n = Q_n \times P \tag{2}$$

$$C_n = I_n + O_n \tag{3}$$

$$\mathrm{NPV} = \sum_{n=1}^{N} \frac{(Q_n \times P) - (I_n + O_n)}{(1+r)^n} \tag{4}$$

where:

B_n, C_n, r, n and N: as in (1)

Q_n: Gas production/transmission/liquefaction rate in year n (bcm)

P: Unit price of gas in project in question (USD/1,000 m^3 of gas)

I_n: Investment expenditures in year n (M USD)

O_n: Operation and maintenance expenditures in year n (M USD)

The calculation of NPV is to asses the total gain/loss from the project and therefore to identify the break-even point of the project. If NPV of the planning project under the chosen discount rate is less than zero ($\mathrm{NPV} < 0$) the project will create financial losses to the investor and he would probably refuse to participate in the project; if $\mathrm{NPV} = 0$, the investor would be indifferent whether to participate or not, because he will not see any profit or loss from the project. If, however, $\mathrm{NPV} > 0$, the seller may be interested in participation because the investment creates added value for him.

The situation when $\mathrm{NPV} = 0$ is very similar to the break-even point situation by definition. When $\mathrm{NPV} = 0$ the total cost and benefit of the project are equal, i.e. there is no net loss or gain, which is a necessary but still insufficient condition for achieving the break-even point. The sufficient condition for achieving the

break-even point is NPV = 0 at a discount rate (r) equal to the minimum expected *rate of return* by investor or hurdle rate (HR)[8] [14] (5).

$$\sum_{n=1}^{N} \frac{(Q_n \times P) - (I_n + O_n)}{(1 + HR)^n} = 0 \tag{5}$$

Therefore from (5) the equation for the price (P) at a break-even point is:

$$BEP = \frac{\sum_{n=1}^{N} \frac{I_n + O_n}{(1+HR)^n}}{\sum_{n=1}^{N} \frac{Q_n}{(1+HR)^n}} \tag{6}$$

where: BEP: break-even price which is equal to the P at a break-even point.

For calculation of the minimum price of Russian gas to Korea, the BEPs of gas must be calculated for each of the seven component-projects described above, then correspondent BEPs must be added together to come up with two final prices of Russian gas, corresponding to the two alternate means of international gas transportation to Korea, namely as PNG and LNG.

3.3 Calculation of the Cost-Based Price of Russian Gas in Korea

The prices of Russian gas delivered ex-ship to Korean port Samchuck (DES_Samchuck (Korea)) consist of two essential parts. The first part is the price of Russian gas delivered to Russian Pacific coast to port Vladivostok (FCA_Vladivostok).[9] This part is the same for both final PNG and LNG prices. However, the second part of the prices varies and depends on the chosen mean of international transportation, PNG or LNG, respectively.

To find the cost-based price of Russian gas at the Russian Pacific coast in port Vladivostok (P_{FCA}), after which the two different means of international gas transportation could be applied, the BEPs of gas production and pipeline natural gas

[8] In business and engineering, the minimum acceptable rate of return, or hurdle rate is the minimum rate of return on a project a manager or company is willing to accept before starting a project, given its risk and the opportunity cost of forgoing other projects.

[9] FCA—Free Carrier (named places). The seller hands over the goods, cleared for export, into the custody of the first carrier (named by the buyer) at the named place [15].

(PNG) transportation across Russia must be summed together in the proportion shown in (7):

$$P_{FCA} = 0.4 \times (BEP_{prod}^{Ch} + BEP_{tr}^{Ch}) + 0.6 \times (BEP_{prod}^{Skh} + BEP_{tr}^{Skh})^{10} \quad (7)$$

where:

P_{FCA}: Price of gas in Russian Pacific port Vladivostok (USD/1,000 m^3 of gas)

BEP_{prod}^{Ch}: BEP of gas production in Chayanda OGCF (USD/1,000 m^3 of gas)

BEP_{tr}^{Ch}: BEP of gas transportation from Chayanda field to Vladivostok by Yakutia–Khabarovsk and then by Khabarovsk–Vladivostok gas pipelines (USD/1,000 m^3 of gas)

BEP_{prod}^{Skh}: BEP of gas production in Sakhalin III fields (USD/1,000 m^3 of gas)

BEP: BEP of gas transportation from Sakhalin III fields to Vladivostok by Sakhalin–Khabarovsk–Vladivostok GTS (USD/1,000 m^3 of gas)

The price of gas in port Vladivostok is serving as a basis for the calculation of the final price of Russian gas in Korea (DES_Samchuck).

As mentioned, in this study two options for international transportation of Russian gas to Korea (PNG and LNG) is considered, which will obviously have an influence on the level of the final prices of gas in Korea.

The formulae for final prise of Russian gas in Korea are,

$$PNG_{Kor} = \frac{(P_{FCA} + BEP_{tr}^{PNG})^{11}}{(1 - 0.3)} \quad (8)$$

$$LNG_{Kor} = P_{FCA} + BEP_{liq} + BEP_{tr}^{LNG} \quad (9)$$

where:

P_{FCA}: is as in (7)

BEP_{tr}^{PNG}: BEP of PNG transportation by Trans-Korean gas pipeline

BEP_{liq}: BEP of planning gas liquefaction project at Vladivostok

BEP_{tr}^{LNG}: BEP of marine LNG transportation to Korea

4 Data

The BEP calculation in each component project includes the following elements: investment, operational cost, related taxes and minimum rate of return expected by seller (HR). It does not include here the R&D cost, environmental impact studies

[10] Since there is no any public information on the rate of gas which will come from Chayanda and Sakhalin III fields for supplying the natural gas to Rep. of Korea, the author decided to choose the rates of gas as follows: 0.6 parts of gas from the closer field Sakhalin III and 0.4 from the Chayanda field.

[11] The export of natural gas from Russia is subject to export duty equal to 30% (or 0.3) of the money-value of the exported gas, but the duty does not apply to gas exported as LNG [16].

cost, costs of impacts on public health and environmental damage, costs of government subsidies, cost of rights of way for pipelines, transit fee, and others possible costs.

For the calculation of the BEP by each of seven planning investment component projects included in the gas supply plan, first we estimated the investment and operation costs for each project.

The estimation of the investment cost was primarily based on open media sources because most of the component projects for gas production and its transportation to the Russian Pacific coast are already in the planning stage and information on them is available to the public. However, the information on the investment cost for a Trans Korean gas pipeline is unavailable yet because the planning for it is still in an early stage. Author therefore used for this component the capital cost estimation methodology at the pre-design stage for gas pipelines that was developed in [17].

4.1 Cost Estimation for CBA of the Projects

In all component projects related to the gas supply to Korea the calculation of the operational expenses (O^{total}) include depreciation charges (D), other operational & maintenance costs (O), and in some cases the cost of fuel gas (F).

Based on the different publications and opinions of the experts working in the gas industry, the operational & maintenance cost (O) and volume of the fuel gas (F) in our study are taken as the annual percentage rate of the total investment[12] or annual throughput, respectively.

The annual cost of fuel gas (F_n) is calculated as (10)

$$F_n = BEP^{pr} \times r_f \tag{10}$$

where:

BEP^{pr}—The BEP of gas in the project, prior to the project in question[13]

r_f—Fuel gas rate taken annually as a percentage of the total annual volume of gas production/transportation/liquefaction

All investments in this study are subject to value-added tax (VAT) and income tax, whose rates in Russia at the time of this study were 18% and 20%, respectively. Gas fields, LNG plants and LNG tankers in Russia are subject to property tax whose rate is 2.2% of the value of assets minus the value-added tax. Gas production is taxed by severance tax.[14] From the January 1st, 2013, the severance tax rate will be

[12] Precisely the O is taken annually as the percentage rate of the total sum of the investment minus the Value-added tax charge from this sum of the investment.

[13] For example, if the cost of fuel gas is calculated for the Sakhalin–Khabarovsk–Vladivostok gas pipeline project, then it is equal to the BEP of gas production in the Sakhalin III gas field.

[14] Severance taxes are incurred when non-renewable natural resources are separated (or severed) from a taxing jurisdiction.

265 roubles[15] per 1,000 m^3 of gas produced [18] (or \$8.73/1,000 m^3 in year 2014). The basic calculation of the BEP of gas production will therefore be based on the rate of severance tax equal to \$8.73/1,000 m^3 (for the period from 2014). As it was already mentioned the export of natural gas from Russia is subject to export duty. For PNG it is equal to 30% of the value of the exported gas, and for LNG is 0%.

For calculation of BEP in the possible Russian–Korean gas supply contract we took the standard HRs of seller separately by up- and middle-stream segments of the gas chain. Since the gas seller in the planning contracts is the Russian monopoly gas company Gazprom, in our CBA we will use the HR of Gazprom in up- and middle-stream segments of gas chain, which is respectively 12% and 15%.[16]

Most of the input data for CBA differs from project to project of our study, but there are several common elements. The base year to which all cash flows in the projects are converted is 2010. The Final year for all projects is 2041 because the gas supply contract will probably end in that year: the duration of the gas supply contract are expected to be 25 years.

Since almost all elements of the planned project will be constructed in Russia (except the LNG tankers), the calculation of costs was firstly made in current roubles (RUB). The costs in current RUB were then converted into constant RUB, using the inflation rate indexes. The base inflation rate index used in the study is the Producer Price Index (PPI) and the Core inflation index published by The Central Bank of the Russian Federation (CBRF) [19]. The CBA had been performed in current 2010M United States Dollars. For this purpose, the values of costs in constant RUB had been transformed into the value in constant USD, by using the official exchange rate of the RUB, published by CBRF [20].

5 Results

As the result of the seven subsequent CBAs of related gas production and transportation projects the following elements of the final prices of Russian gas in Korea had been obtained. The obtained BEPs of gas production in the distinguished fields and BEPs of transportation by pipelines, which are necessary for calculation of the price of gas at the Russian Pacific coast (P_{FCA}) by (7) are given as in Table 1.

As seen from the Table 1 the cost of gas production in Chayanda and Sakhalin III varies significantly. The price of gas is higher in Sakhalin III offshore gas fields due to the much higher investment costs, which is necessary to develop a gas fields in the more severe conditions of offshore gas production that onshore. The costs of gas transportation also vary more than two-fold mostly due to the different distances between the specific fields and the Pacific coast; the total route from Chayanda field

[15] Currency of the Russian Federation (RUB).

[16] The exception is the project of LNG marine transportation, where the ROR is taken equal to 10% as in the world in average.

Table 1 BEP of Russian gas at the Russian pacific coast (P_{FCA}), USD/1,000 m^3

BEP	Chayanda field	Sakhalin III field
BEP of gas production, BEP_{prod}	79.31	144.62
BEP of gas transportation to Vladivostok, BEP_{tr}	254.08	90.73
Total: (BEP_{prod} + BEP_{tr})	333	235
P_{FCA}	275	

Table 2 BEP of international gas transportation

BEP	USD/1,000 m^3
Trans-Korean pipeline (BEP_{tr}^{PNG})	52.8
Total by LNG, which is including:	204
Liquefaction (BEP_{liq})	164
LNG transportation (BEP_{tr}^{LNG})	40

Table 3 Obtained cost-based prices of gas and its oil price equivalent

Cost-base price	USD/1,000 m^3	$/MBtu	Crude oil price parity, $/Bbl
PNG_{Kor}	468	12.91	75.03
LNG_{Kor}	479	13.22	76.88

Table 4 Comparison of the project gas prices with the price projections

Price		USD/MBtu	Percentage of the oil price
Oil price projection	130 $/bbl	22.31	100
Gas price projection	568 $/1,000 m^3	15.62	70
Project PNG	468 $/1,000 m^3	12.91	58
Project LNG	479 $/1,000 m^3	13.22	59

to Vladivostok is about 4,383 km, while the distance between Sakhalin III and Vladivostok is only about 1,890 km.

In Table 2 the BEPs of international gas transportation by pipeline (BEP_{tr}^{PNG}) and as LNG (BEP_{tr}^{LNG}), which are necessary for calculating the final prices of PNG and LNG by (8) and (9) are given.

Table 3 shows the results of calculation of the final minimum prices gas in Korea by the project in USD per 1,000 m^3 of gas and in USD per MBtu for the further comparison purpose with the projected price of oil at the same energy basis.

As seen from the Table 3 the price of LNG and PNG or Russian gas in Korea is practically the same: LNG is more expensive than PNG by less than 3%.

Finally the author compared the obtained prices with the oil and gas prices projection given by IEA for the same period of time. The comparison is showed in Table 4.

The projections of the IEA crude oil import prices in 2010 dollars by the Current Policies Scenario assume the average price of oil for the period of the contract at the level of $130/bbl and the ratio of gas prices (in the Asia Pacific Region (APR)) is forecasted to be equal to around 0.7 of crude oil price [1].

6 Conclusion

As it is follow from the comparison of the PNG and LNG price by the project, the total economic effect on the supply of PNG compared with the supply of LNG could be: $(479–468) \times 10^6 = 110$ M \$/annum. However, under the existing conditions of political instability on the Korean peninsula, which makes the gas pipeline project through North Korea extremely risky, the potential economic losses in the event of unforeseen hostile acts or overlap of gas supply could, reach billions of dollars. Therefore, this economic benefit could be obtained only under conditions of signing the additional agreements which will warranty the security of the pipeline and the absence of the military actions in the Korean peninsula.

On the positive side, however, a joint project for pipeline construction between Russia, North and South Korea can pull the conflicting parties together, to develop economic and social ties between parts of the country that have the same language and ethnicity but separated by political tensions, and thus help to finally bring peace to the Korean peninsula, for which the residents of both Koreas have been waiting more than 50 years. Cooperation in the pipeline construction through the Korean Peninsula can thus be an *important opportunity* to bring together the peoples of North and South Korea, with benefits far greater than just gas transportation.

Turning back to the assessment of the economic feasibility of the project, it is necessary to say that the following conversion of the obtained prices of gas by the energy parity basis to the price of oil (Table 3) shows that the price of PNG of 468 \$/1,000 m^3 and LNG of 479 \$/1,000 m^3 are competitive with oil price already at the level of 75–77 \$/bbl. Taking into account the level of world oil prices at the time of writing this paper (April 2011) at around 110 \$/bbl and the projected increase of oil prices in the period of the contract being up to 130 \$/bbl (Table 4), it is obvious that the possible prices of gas by this project is much lower than the current and projected world oil prices. The project PNG and LNG prices are lower than the oil price projection by 42% and 41% correspondently. Moreover, the comparison with the projected average gas prices for APR given by IEA, showed that the project also has the economic advantage. The project PNG and LNG prices are also lower than the IEA "Asian" gas price projection by 17.6% and 15.7% correspondingly.

This facts lead to the conclusion that the proposed contract for gas supplies from Russia to Korea has economically a good chance of success and could provide Korea with additional gas supply at reasonable price, as well as provide Russia with new gas consumers in the Asia-Pacific gas market. In this connection we could rather say that the gas supply project from Russia to Korea is economically feasible and could bring the additional benefits to all parties of the contract such as financial benefits, social benefits and improvement of energy security of the North–East Asian countries.

It should be noticed again, that the estimation does not include the cost of environmental impact study and assessment, environmental damage, health issue of the population, cost of rights of way for pipelines, transit fee, and others possible

costs, which could easily overlap the calculated gas prices. The calculation of the prices also is not considering the tax reduction (such as the severance tax and export fee for PNG) for the new gas export projects of Russia in the Asia-Pacific region which is already planning by Russian government [21] and could significantly reduce the price of gas. Both this facts could influence the final prices both in the positive and negative directions and what would be the final result of the negotiations between the parties and also between the Russian government and its gas monopoly Gazprom on the rate of taxes reduction could not be known with certainty. In this connection we decided to limit the scope of this paper only to the study on the minimum gas prices which could be obtained by the calculation of the direct costs and concerning the minimum rate of return on capital. The future studies will aim to calculate the possible prices concerning the different tax reduction rates, transit fee and others minor costs associated with the of gas supply project.

References

1. World Energy Outlook (WEO) (2010) International Energy Agency, Paris
2. Doh H (2001) Shutdown of Indonesian gas fields and its impact on Korean LNG supply. Korea Energy Economic Institute (KEEI) News, 16.04.2001 Available at: http://www.keei.re.kr
3. Stern J et al (2008) Natural gas in Asia. Oxford University, Oxford
4. Medvedev pursues energy deals, Foreign investment during Korea, Japan trip", by Bloomberg News, 09.11.2010, Available at: http://www.bloomberg.com/news/2010-11-09/medvedev-pursues-energy-deals-foreign-investment-during-korea-japan-trip.html
5. Lee E (2003) Comparative economic analysis on east Russia's major gas projects. Korea Energy Economics Institute, Seoul, Republic of Korea
6. Yoon B (2007) Prospects for energy cooperation between Russian Federation and the Republic of Korea in natural gas supply field. Dissertation, Gubkin University of Oil and Gas, Moscow
7. (2007) Development program for an integrated gas production, transportation and supply system in Eastern Siberia and the Far East, taking into account potential gas exports to China and other Asia-Pacific countries (The Eastern Gas Program). Russian Federation Industry and Energy Ministry, (In Russian). Available at: http://gasforum.ru/dokumenty/1350/
8. Gas will be delivered to Japan through Vladivostok. Vladivostok Times. News, 16.06.2008. Available at: http://vladivostoktimes.com//show/?id=26289&s_year=2008&s_month=6&s_day=16&f_year=2008&f_month=6&f_day= 16&p=
9. Information about the Sakhalin III gas project: http://www.gazprom.com/production/projects/deposits/sakhalin3/
10. (2007) Gazprom wants to get without competition the Chayanda fields and sectors of the Sakhalin-III (In Russian). 20.06.2007. Information and analytical center "Mineral". Available at: http://www.mineral.ru/News/27772.html
11. Information about the Chayanda gas field: http://www.gazprom.com/production/projects/deposits/chayandinskoye/
12. On implementation of the basic directions of development of oil and gas industry in the Republic of Sakha (Yakutia) until 2020 (in Russian). Presentation, Ministry of Industry of the Republic of Sakha (Yakutia). November 27, 2009, Yakutsk. Available at: http://www.sakha.gov.ru/node/45186
13. (1995) The IEA Natural Gas Security Study. IEA, Paris

14. David L, Boldrin M (2008) Against intellectual monopoly. Cambridge University Press, Cambridge
15. International Commercial terms (Incoterms) (2010) By the international chamber of commerce (ICC), Publication No. 715, 2010 edn.
16. Russian Federation Government Resolution of 23 December 2006 No. 795 On approval of export customs duties on goods, exported from the Russian Federation outside the States—parties to the Agreement on customs union (in Russian), Available at: http://base.consultant.ru/cons/cgi/online.cgi?req=doc;base=LAW;n=121320;fld=134;dst=4294967295;from=121204-909
17. Zelenovskaya E, Kosarev A (2010) The Optimal design for a gas pipeline infrastructure that minimizes the unit cost of gas transportation. NE Asia Energ Focus 2010, 7(4): 33–43
18. Russian Federal Law N 307-FZ (2010) On Amendments to Article 342 and 361 the second part of the Tax Code of the Russian Federation, dated 27 November 2010
19. Information on the main economic indicators of Russian federation: http://www.cbr.ru/eng/statistics/default.aspx
20. Information on the exchange rate of foreign currencies against the ruble: http://www.cbr.ru/eng/currency_base/daily.aspx?C_month¼01&C_year¼2011&date_req¼01.01.2011
21. Speech by Alexey Miller at the meeting devoted to the General Scheme for gas industry development until 2030 under the chairmanship of the Russian Federation Prime Minister Vladimir Putin, 2010. Available at: http://www.gazprom.com/press/miller-journal/983525/

Scenario Analysis of Low-Carbon Smart Electricity Systems in Japan in 2030

Qi Zhang, Tetsuo Tezuka, Benjamin C. Mclellan, and Keiichi N. Ishihara

Abstract The future developments of nuclear and renewable energy need to be considered together in Japan to realize a safe and clean future electricity system after the Fukushima Nuclear Accident under continuing policies of CO_2 emission reduction. On the other hand, one of the most crucial elements of future electricity systems will be the capability for "smart" controls on both supply and demand sides to perform under real-time dynamics. Therefore, the purpose of the study is to propose electricity systems in Japan in 2030 with different mix of renewable energy and nuclear power in supply side and different penetration levels of electric devices such as battery, EV (electric vehicle) and HP (heat pump) under their smart control strategies in demand side. The scenario analysis was conducted using an input–output hour-by-hour simulation model to derive supply–demand balance subject to constraints from technological, economic and environmental perspectives. The obtained excess electricity, CO_2 emissions, operation patterns of various devices, etc. in different scenarios were compared and analyzed. The results of the analyses make us understand quantitatively the technological and environmental impacts of the different mixes of renewable and nuclear energy, as well as the corresponding operation patterns of controllable devices under their smart control strategies in different scenarios.

Keywords Control strategy • Low-carbon • Nuclear • Renewable • Smart electricity system

Q. Zhang (✉) • T. Tezuka • B.C. Mclellan • K.N. Ishihara
Graduate School of Energy Science, Kyoto University, Kyoto 605-8501, Japan
e-mail: zhnagqi@energy.kyoto-u.ac.jp

T. Yao (ed.), *Zero-Carbon Energy Kyoto 2011*, Green Energy and Technology,
DOI 10.1007/978-4-431-54067-0_3,

1 Introduction

Nuclear is viewed as the backbone power source in efforts to reduce the high rate of dependence on overseas energy imports and CO_2 emission in Japan with the restrictions of minimal domestic energy resources [1, 2]. However, the Fukushima Nuclear Accident happened on March 11, 2011 led to many criticisms on nuclear power again, and renewable energy is expected to penetrate electricity systems as quickly as possible. However, we argue that, from a long-term viewpoint, apart from the safety issues of nuclear power, there are also very serious energy security problem, global warming pressure and renewable energy penetration bottlenecks from technological, systemic and economic perspectives in Japan. Energy supply in Japan is more than 95% dependent on overseas imports, and the price of energy resources is still increasing in international markets. Building new coal-fired and oil-fired power plants are not desirable choice even in an electricity shortage situation due to CO_2 emission increase. On the other hand, renewable energy—mainly including photovoltaics (PV) and wind power—the potential is limited in Japan due to physical-geographic limitations. There are still many bottlenecks for the high level penetration of renewable energy into the electricity system particularly from the systematic perspective due to the possibilities for too much excess electricity happen [3, 4]. Therefore it is crucial to consider both renewable and nuclear energy in Japan to realize future clean and safe electricity systems. The nuclear reactors mentioned here would be new generation technology that incorporates "passive" safety features intended to avoid disasters like the one in Fukushima.

However, renewable and nuclear energy pose a significant problem to traditional grid systems, which cannot cope with rapid, intermittent and uncontrollable peaks and falls in electricity demand depending on the time of day and season. Electricity production from renewable energy mainly PV and wind depends highly on weather conditions which are unstable and cannot be adequately predicted. Nuclear power as a base load generation source with high capital cost and low operation cost cannot readily alter its power output for technological and economic reasons. Therefore, load levelling and fluctuation absorption remain a problem that power suppliers are unable to overcome by themselves [5]. On the other hand, new electric devices such as battery, electric vehicle (EV) and heat pump (HP), etc. will soon be added to the electricity system in future, and their operation pattern can be controlled in real time [6–8]. The new electric devices are expected to help electricity systems to integrate more nuclear and renewable energy by absorbing excess electricity and supplying deficient electricity. For this reason, smart control strategies of the electric devices are of vital importance to integrate renewable and nuclear energy into future electricity systems.

In order to find the property mix of nuclear, renewable and thermal power in future electricity system with various new electric devices under their control strategies, this study presents scenario analysis of the Japanese electricity system with different penetration levels of power sources and electric devices in 2030

using a model which incorporates aspects of technology, economy and environment. The model is organized into an input–output framework, and is realized using an hour-by-hour computer simulation to derive a supply–demand balance under smart control strategies. Finally, the appropriate electricity mix can be selected based on the obtained performance data and operation patterns in different scenarios.

2 Methodology

2.1 Future Smart Electricity Systems

In future electricity systems, many new electric appliances and devices will be integrated on both supply and demand sides such as PV panel, battery, EV, HP, etc. Here, we define "smart" as that electric appliances and devices can be controlled in real time to absorb excess electricity and supply deficient electricity to realize a low-waste and effective electricity system with renewable energy penetration. In practice, renewable energy particularly PV and electric devices are distributed in individual locations, and many individual locations form a region/nation. In some situations, some individual locations use their own distributed electricity systems which are isolated from big grid system. However, we assume that all the electric devices in individual locations are integrated into the big grid system and the electric power company can monitor and manage all of them using smart meter and smart control device. In the proposed methodology, target future electricity systems are in region/nation level, and we assumed that smart controls are realized automatically in all individual locations in the target region/nation.

2.2 Model

Therefore, we proposed the model shown in Fig. 1. It is organized in an "Input–Output" framework and realized by hour-by-hour computer simulation to derive demand-supply balance. The "Input" includes basic physical data and predefined operation rules (control strategies). Main input data are historical traditional electricity load, solar irradiation, wind speed, fuel supply, installed capacity, CO_2 emissions factor and basic cost information, etc. A number of alternative regulation strategies emphasis on control strategies of new devices, blackout permission, generation priority of various technologies, upper limitation of excess electricity, range of capacity factor, cost, CO_2 emission constraints, etc.

New electricity devices (battery, EV, HP, etc.) and their combinations are optional, and their control strategies are also defined as optional rules.

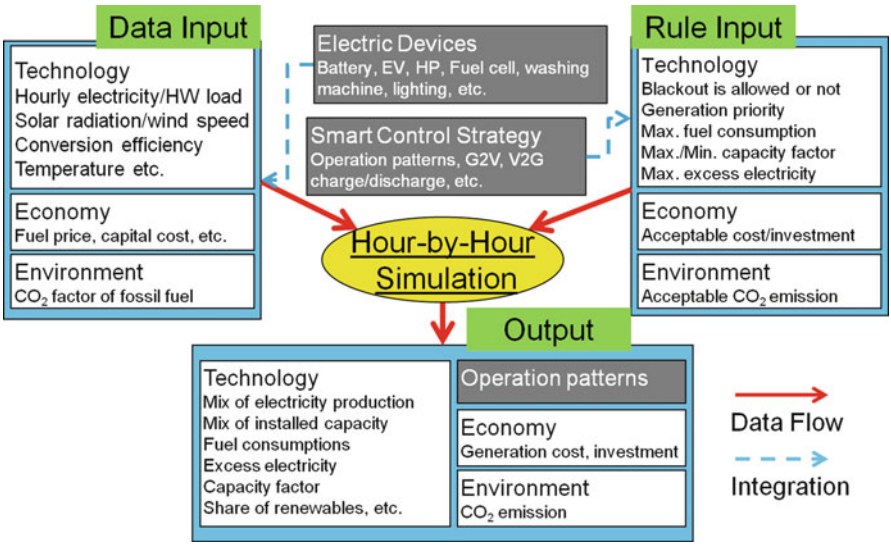

Fig. 1 Model for analyzing future smart electricity system

The "Output" includes mainly energy balances, annual electricity production, fuel consumption, total/average cost, total/average CO_2 emission, operation patterns of the new devices under their defined control strategies, etc. All the basic data is hourly, however, through statistics, daily, weekly, monthly and annul data can be obtained. Some models have been developed for analysis of the energy (electricity) mix with renewable energy penetration [9]. However, there is still not a model mainly focusing on penetration of both renewable and nuclear energy into future electricity systems with various electric devices under their smart control strategies.

The model is developed as an operable software, and the hour-by-hour simulation flow is shown in Fig. 2. Electricity generations from renewable, nuclear, thermal and hydro are considered as basic supply, when it becomes more than traditional electricity load, excess electricity will be used to drive HP and/or charge batteries. On the other hand, when basic electricity supply from renewable and nuclear energy is less than traditional load, battery is discharged to meet the deficient electricity. If no blackout happens, the system is considered as technology feasible, otherwise initial data will be changed and new iterative will start. Finally, the results are obtained through statistics on hourly data.

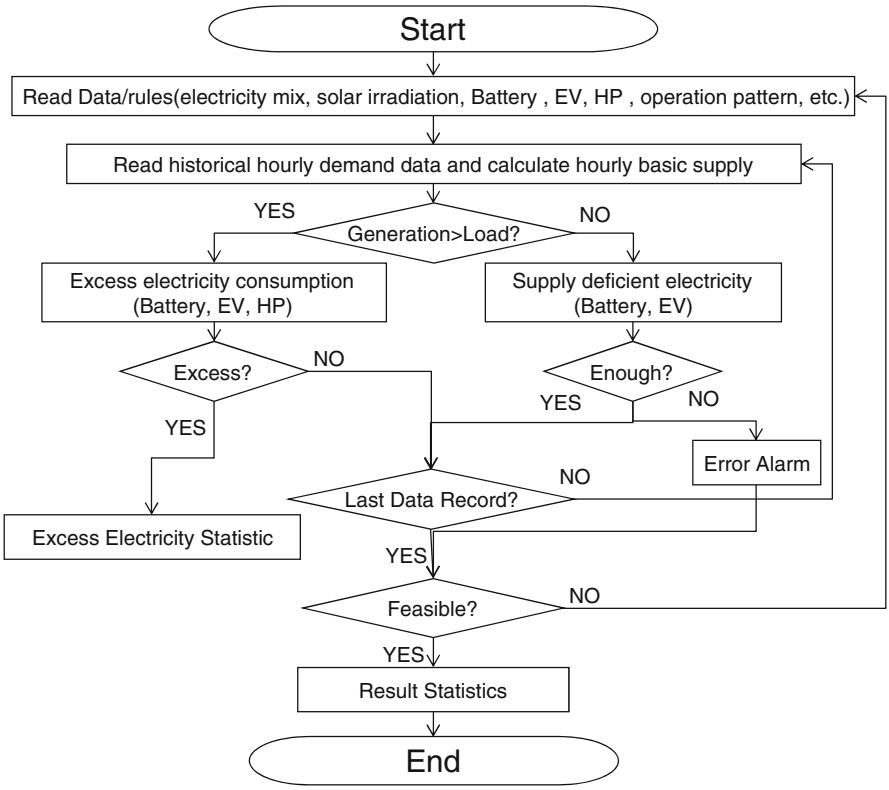

Fig. 2 Concept flow chart of hour-by-hour simulation for future smart electricity systems

3 Data

3.1 Electricity Load

The hourly distribution of traditional electricity load in 2001 is shown in Fig. 3 [10]. The electricity productions increased by about 30% from 740 TWh in 1990 to 960 TWh in 2001. However, on the demand side, energy saving is the key focus especially since the Fukushima accident [11], and possible population reduction is also predicted [12]. Therefore, we assume that demand remains at 2001 level in the demand scenario.

The electricity consumption of EV and HP is new load. There are about 120 million people, 50 million households [12], and 70 million passenger cars in Japan in 2030 [13]. A part of cars are assumed to be substituted by EV and HP is

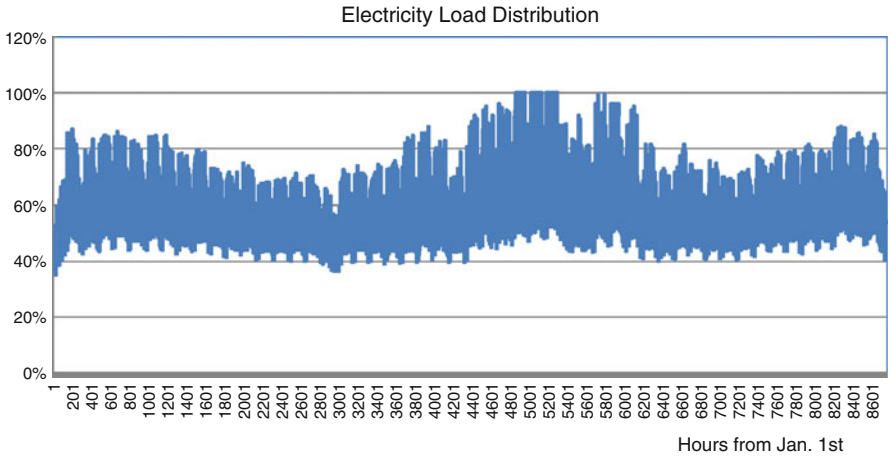

Fig. 3 Hourly electricity load distribution in Japan

installed in a part of households for hot water production. The efficiency of EV in Japan uses data from the practical EPA value-5 km/kWh in average [14], and daily travel distance is considered as 30 km per EV in their moving patterns [15]. HP is used to supply 450 l of hot water at 40°C according to revised M1 mode (hot water is 65°C) [16] to meet hot water load [17]. The hourly electricity consumption of HP for making hot water can be obtained using Coefficient of Performance (COP) calculation [18]. However, the impact on the electrical load would be different according to the patterns of EV charge and HP operation patterns.

3.2 Nuclear Power, Thermal Power and Renewable Energy

Three different nuclear power development cases in light of the Fukushima nuclear accident are proposed: (1) negative nuclear power; (2) conservative nuclear power; and (3) active pursuit of nuclear power as shown in Fig. 4. In the N1, the stopped NPPs in this earthquake will be closed permanently, all NPPs under construction and in planning will be canceled and the NPPs in operation will be closed in their early lifetime 35–40 years. On the other hand, in the N2 and N3, all NPPs under construction and in planning will be continued according to the schedule and all NPPs will operate for a long lifetime 40–50 years and very long lifetime 50–60 years, furthermore, in the S3 Fukushima Daiichi NPPs will be rebuilt before 2030.

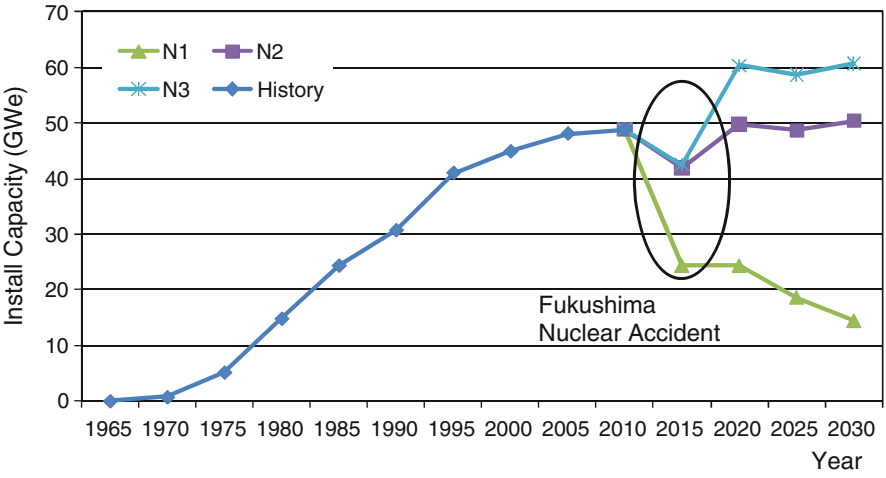

Fig. 4 Nuclear power development cases to 2030

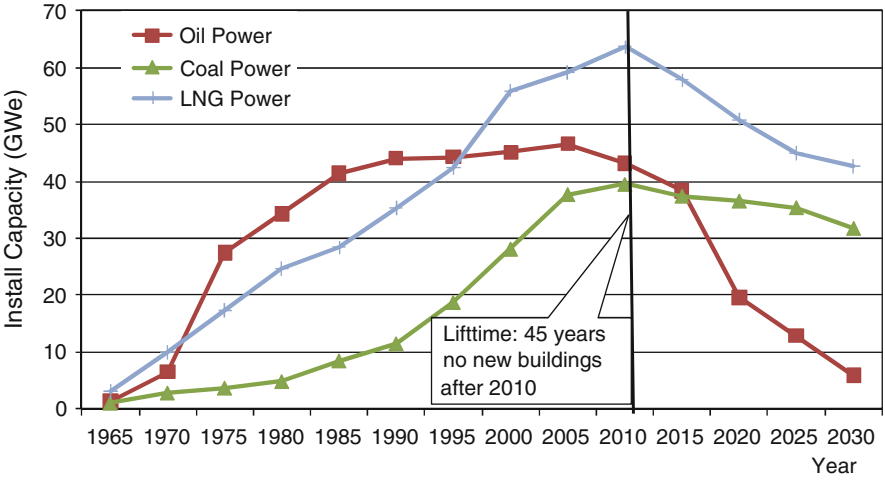

Fig. 5 Thermal power development to 2030

If all the thermal power plants (coal, LNG, oil) are stipulated to have 45 year lifetimes, and there will be no new construction of thermal plants up till 2030, the installed capacities of thermal power plants are shown in Fig. 5 based on historical installed capacity data [10]. This is the basic installed capacity for thermal power,

Table 1 Renewable energy potential in Japan

Renewables	PV	Wind	Biomass	Hydro
Potential	100 GWp	50 GWe	2 GWe	21 GWe

and in the scenario analysis, new LNG power plants can be built when necessary to provide sufficient capacity.

Japan will have to increase substantially the amount of electricity provided by renewable sources, especially "new" sources such as wind, solar, and biomass, because the country's hydroelectric potential has already been largely exploited. At present, the installed capacity of hydro power is 21 GWe [10]. We assume the value will remain constant and pumped hydropower will be replaced by batteries in this study. The potential of renewable energy in Japan is listed in Table 1 [19, 20], and the solar irradiation and wind speed historical data in 2001 same year with historical load provided by Japan Meteorological Agency (JMA) are used [21].

4 Rules

The main defined rules are shown in Table 2, which includes five aspects. Battery, LNG, oil and biomass can alter their output 100% in 1 hour to absorb fluctuations of PV and wind power. In the target electricity systems, when excess nuclear power appears, heat pumps come into operation, and the batteries are charged. On the other hand, during the demand peak of daytime or on a cloudy/rainy day, heat pumps are on standby status, and available batteries could be used to provide electricity to the grid. In case of EV is used, the processes of charging and discharging are called G2V (Grid to Vehicle) and V2G (Vehicle to Grid). There are many uncertainties in the cost information of facilities such as V2G and G2V, and distribution of battery's capital cost between EV and electricity system. Therefore, economic performance of electricity system is not considered in the study, although the model has the economy analysis function. In environment aspect, the CO_2 emission in electricity generation sector is calculated using CO_2 emission factor [22], and 1990 level is used as a indicator here. CO_2 emission reductions in transportation sector from replacing gasoline cars using EV and in residential sector from replacing gas driven hot water producer by electricity driven HP for hot water production are not accounted into electricity systems.

Table 2 Summary of main defined rules

	Defined rules
Supply–demand	1. Blackouts is not allowed 2. Only PV and wind power can become excess power 3. Excess power ratio $< 15\%$ in total 4. New building of LNG power plant is allowed
Power generation and storage	1. Generation priority: hydro, nuclear, coal, PV and Wind, Battery, LNG, biomass, oil, EV 2. Capacity factor of coal-fired power can be lowered to zero for more renewable energy penetration 3. Battery(EV): 10% (30%) $\leq$ SOC $\leq$ 95% 4. Charge speed $<$ 30%SOC/h, discharge speed $<$ 50%SOC/h
Resource availability	1. Renewable energy penetration $\leq$ physical potential 2. Fossil fuel demand $\leq$ Max. supply capability 3. Facilities and resource can be imported from overseas
Capacity factor load-following	1. Capacity factor: 75% $\leq$ nuclear $\leq$ 100%, coal $\leq$ 85% 2. Battery, LNG, oil and biomass operate in load-following mode
CO_2 emission	1. Average annual CO_2 emission per kWh $\leq$ 1990 level

5 Results

5.1 Scenario Design

As shown in Fig. 6, there are three nuclear power development cases in the supply side, and five electric device combinations in demand side.

5.2 Results

The electricity mix, excess electricity and CO_2 emission of all scenarios are shown in Figs. 7, 8 and 9 respectively. If the "N1" is selected, even renewable is developed as much as possible; Japan will have to use LNG to supply more than 30% its electricity, and thus face CO_2 emission/climate change pressure. On the other hand, in case of the "N3", much more excess electricity happens and the people in the country have to face more potential dangers of nuclear power. Furthermore, electric devices (battery, EV and HP) operated under their smart control strategies can reduce greatly excess electricity and CO_2 emission, and thus help the system to integrate more renewable and nuclear energy. However, the scenarios—especially the nuclear development policy—will ultimately be self-selected by the people, government and industry in Japan.

Supply Side (S1-S3)

Nuclear	(GWe)
N1	14.3
N2	50.4
N3	60.8

Renewable	Potential (GWp/e)
PV	100 [1]
Wind	50 [2]
Biomass	2 [1]

Other	Coal	LNG	Oil	Hydro
(Gwe)	31.8	42.6	5.8	21

×

Demand Side (D1-D5)

	Battery (GWh)	HP (Million)	EV(GWh)
D1	×	×	×
D2	500	×	×
D3	500	20	×
D4	×	×	500
D5	×	20	500

Fig. 6 Scenario design in supply and demand sides of electricity systems in Japan in 2030

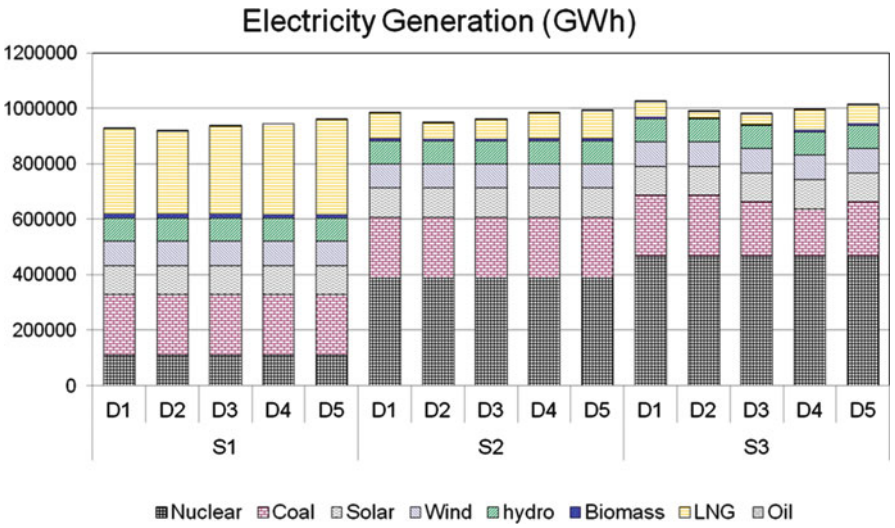

Fig. 7 Electricity mix in all scenarios

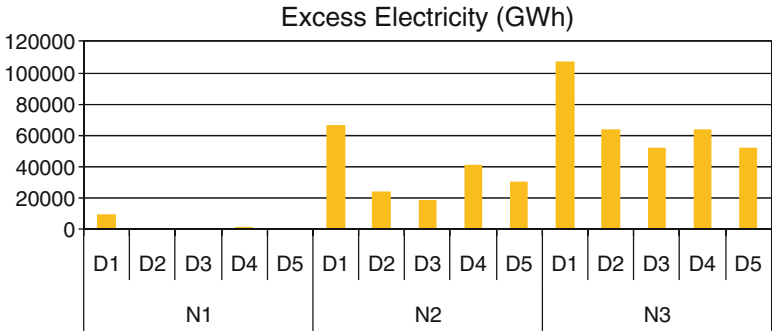

Fig. 8 Excess electricity comparison in the scenarios

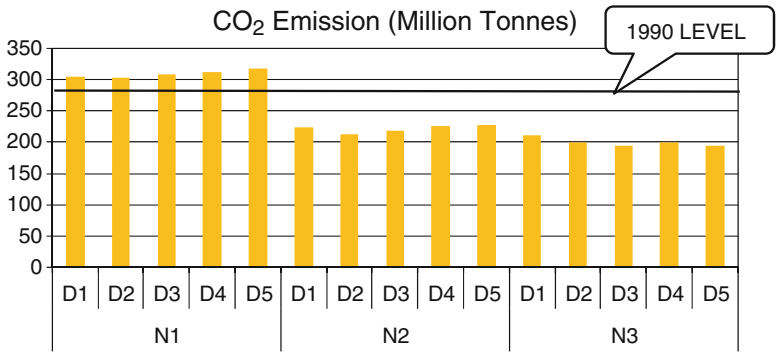

Fig. 9 CO_2 emission comparison in the scenarios

6 Conclusion

Scenario analysis was conducted on the electricity systems with electric appliances and devices operated under their smart control strategies in Japan in 2030 using an input–output hour-by-hour simulation model. Three development cases of nuclear power were proposed after the Fukushima Nuclear Accident in supply side and five electric device combinations were assumed in the demand side. The simulation results of the electricity mix, excess electricity and CO_2 emission in all scenarios were obtained based on the input data and predefined rules. The analysis results show that (1) negative nuclear policy will lead to more fossil fuel consumption and CO_2 emissions increase comparing with 1990 level; (2) however very active pursuit nuclear power policy will lead to more excess electricity; (3) excess electricity and CO_2 emissions can be reduced greatly in various scenarios with the help of electric appliances and devices (battery, EV and HP) under their smart control strategies.

Acknowledgement The authors would like to thank the GCOE program in Graduate School of Energy Science, Kyoto University and Kan Gen Kon for the great support and helpful comments.

References

1. METI (Ministry of Economy, Trade and Industry of Japan) (2010) The strategic energy plan of Japan (http://www.meti.go.jp/english/press/data/pdf/20100618_08a.pdf)
2. JAEA (Japan Atomic Energy Agency) (2009) 2100 nuclear vision (in Japanese)
3. Denholm P, Margolis MR (2007) Evaluating the limits of solar photovoltaics (PV) in traditional electric power systems. Energ Pol 35:2852–2861
4. Lund H (2006) Large-scale integration of optimal combinations of PV, wind and wave power into the electricity supply. Renew Energ 31:503–515
5. Hall PJ, Bain EJ (2008) Energy-storage technologies and electricity generation. Energ Pol 36–12:4352–4355

6. Yoda S, Ishihara K (1997) Global energy prospects in the 21st century: a battery-based society. J Power Sourc 68–1:3–7
7. Lund H, Kempton W (2008) Integration of renewable energy into the transport and electricity sectors through V2G. Energ Pol 36:3578–3587
8. Hewitt NJ (2011) Heat pumps and energy storage—The challenges of implementation. Appl Energ. doi:10.1016/j.apenergy.2010.12.028
9. Connolly D, Lund H, Mathiesen BV, Leahy M (2010) A review of computer tools for analysing the integration of renewable energy into various energy systems. Appl Energ 87:1059–1082
10. FEPC Electricity power statistic information, available at http://www.fepc.or.jp/library/data/tokei/index.html. Accessed June 2011
11. KEPCO Electricity Usage Graph, available at http://www.kepco.co.jp/setsuden/graph/index.html. Accessed July, 2011
12. National Institute of Population and Social Security Research (2008) Future population prediction in Japan (in Japanese)
13. AIRIA (Automobile Inspection & Registration Information Association) Automobile holding data in Japan, available at http://www.airia.or.jp/number/index.html. Accessed July 2011
14. US Environmental Protection Agency, Fuel Economy of Electric Vehicles, available at http://www.fueleconomy.gov/feg/evsbs.shtml. Accessed July 2011
15. JSTE (Japan Society of Traffic Engineers) (2007) Road Traffics Census OD Investigation (in Japanese)
16. IBEC (Institute for Building Environment and Energy Conservation) (2009) Energy consumption calculation
17. Imamura E, Asano H (2007) Optimal hot water supply technology sect analysis in residential house under load survey data, Socio-economic Research Center, CRIEPI, Rep. No. Y06025 (in Japanese)
18. Mita Y, Ikeya T, Miyashiro H, Kobayashi Y (2009) Development of Prototype of Battery Energy Storage System Coupled with Heat Pump Water Heater. Materials Science Research Laboratory Rep. No. Q08018 (in Japanese)
19. ME (Ministry of Environment of Japan) (2011) Study of Potential for the Introduction of Renewable Energy (in Japanese)
20. JWPA (Japan Wind Power Association) (2011) Roadmap of long-term introduction of wind power in Japan, available at http://log.jwpa.jp/content/0000289019.html
21. JMA (Japan Meteorological Agency) (2001–2005), Amedas data
22. Imamura E, Nagano K (2010) Evaluation of life cycle CO_2 emissions of power generation technologies, CRIEPI, p 34 (in Japanese)

(ii)

Session Papers

Modeling Sectoral Power Demand Using Panel Model

Zulfikar Yurnaidi, Jayeol Ku, and Suduk Kim

Abstract In this paper, a panel model is designed for the analysis of monthly electricity power demand for 35 industrial sectors using data from year 2005 to 2010 in Korea. A panel model of least square dummy variable approach is used to estimate the price elasticity of power demand for each industrial sector composed of 14 different regional data. The model specification varies among each industrial group, depending on its specification of substitution effect (gas and oil prices), lags (power demand, electricity price and production index) and the inclusion of some additional variables (number of customers and production index). The estimation results of all models give us negative price elasticity of power demand with size ranging from −0.067 (group 26, construction) to −1.109 (group 18, medical, measurement, optical, and watch instruments), which show different reaction of power demand with respect to the changes in electricity price. An experiment of price change is conducted to observe its implication to the quantity of power demand and the total revenue for KEPCO (Korea Electric Power Co.), the national power retail company in Korea. This result from industry specific analysis provides new information on power demand behavior in Korea since previous works are all based on aggregated contract type data.

Keywords Fixed effect • Industrial sector • Panel model • Power demand • Price elasticity of demand

Z. Yurnaidi • J. Ku • S. Kim (✉)
Graduate School of Energy Studies, Ajou University, Yeongtong-Gu,
Suwon 443-749, South Korea
e-mail: suduk@ajou.ac.kr

T. Yao (ed.), *Zero-Carbon Energy Kyoto 2011*, Green Energy and Technology,
DOI 10.1007/978-4-431-54067-0_4,

1 Introduction

The price elasticity of demand is defined as the measure of percentage change of demand when price changes in 1%. It is important to get the proper estimates of this to better understand the behavior of consumers in power market. In this paper we design an econometric model to analyze the monthly electricity power demand in Korea. In order to understand the characteristics of power demand for each industry, we use different specification for each industrial sector. The data set used in our analysis is monthly electricity consumption for the period of 2004–2010 provided by KEPCO (Korea Electric Power Corporation). In order to analyze this monthly demand, other exogenous variable information are gathered, including the price of electricity, gas, oil products, producer price index, industry specific production index, number of customer, and temperature (to calculate Heating Degree Days and Cooling Degree Days), omitted from various sources, such as Bank of Korea [1] and Korea Meteorological Administration (KMA) [2].

The rest of this paper is organized as follows: the second part elaborates the panel model specification which utilizes 14 regional power demand for each industrial group; the third part shows the estimation result coupled with price change experiment; the conclusion follows in the last part.

2 Model Specification

There are 14 regions that are analyzed in our model: Seoul, South Seoul, Incheon, North Gyeonggi, Gyeonggi, Gangwon, Chungbuk, Daejon-Chungnam,Jeonbuk, Gwangju-Jeonnam, Daegu-Gyeongbuk, Busan, Gyeongnam and Jeju.[1] Further, our original samples are categorized into 99 industries with their respective industrial codes. Due to the change of Korean Standard Industrial Classification (KSIC) which occurred at May 2008, however, the old and new industrial categorization cannot be matched perfectly. For our convenience of research, we decided to re-categorize our whole samples into new 35 industries, which are summarized in Table 1.

Since our data structure has time, region, and 35 industry dimension, we used panel type of model so that we can utilize the full information of data. We design a least square dummy-variable panel model for each industry with 14 regional groups [3]. The general model utilized in this study is:

[1] This information is used to identify the region-specific meteorological information out of 76 regional categories provided by KMA.

Table 1 Categorization of 35 industries

	Industry
1	Agriculture, forestry, fishing
2	Mining
3	Food and beverage manufacture
4	Cigarette manufacture
5	Textile, except clothing
6	Clothing, accessories
7	Bags and footwear
8	Wood products, except furniture
9	Pulp and paper product
10	Printing and recording media
11	Coal and petroleum products
12	Chemical, medical material
13	Rubber and plastic products
14	Non-metallic mineral product
15	Primary metal manufacture
16	Metal products, except machinery
17	Electronic, computer, and communication equipment
18	Medical, optical, watches
19	Electrical equipment
20	Other machinery
21	Car and trailer
22	Other transport equipment
23	Furniture and others
24	Electricity, gas, water supply
25	Sewage disposal and environmental restoration
26	Construction
27	Wholesale and retail
28	Hotel and restaurant
29	Publishing, broadcasting and communication information services; transportation services
30	Finance and insurance
31	Real estate and leasing; professional and technical services; business support services;
32	Public administration and educational services
33	Social services; arts, sports, and recreational services; society organizations; household self-employment
34	International and foreign agencies
35	Others, including residential and street lights

$$\hat{y}_{i,t} = \hat{\beta}_1 PE_{i,t} + \hat{\beta}_2 PG_{i,t} + \hat{\beta}_3 PO_{i,t} + \hat{\beta}_4 House_{i,t} + \hat{\beta}_5 PI_{i,t} + \hat{\beta}_6 HDD_{i,t} + \hat{\beta}_7 CDD_{i,t} + \hat{\beta}_8 CD8_{i,t} + \sum_{j=2}^{12} \hat{\beta}_{9j} D_{j,i,t} + \sum_{k=1}^{n} \hat{\beta}_{10k} y_{i,(t-k)} + \sum_{k=1}^{n} \hat{\beta}_{11k} PE_{i,(t-k)} + \sum_{k=1}^{n} \hat{\beta}_{12k} PI_{i,(t-k)} + \hat{\alpha}_i$$

where

$y_{i,t}$: Electricity consumption for regional i at time t
$PE_{i,t}$: Price of electricity (real term)
$PG_{i,t}$: Price of gas (real term)
$PO_{i,t}$: Price of oil (real term)
$House_{i,t}$: Number of household
$PI_{i,t}$: Production index
$HDD_{i,t}$: Heating Degree Days
$CDD_{i,t}$: Cooling Degree Days
$CD8_{i,t}$: 8th Industrial Code Dummy (from 200401 to 200805 = 1)
$D_{j,i,t}$: Monthly Dummy
$y_{i,(t-k)}$: Electricity consumption at time t-k (k-th lag)
$PE_{i,(t-k)}$: Price of electricity (real term) at time t-k (k-th lag)
$PI_{i,(t-k)}$: Production index at time t-k (k-th lag)
α_i: Regional fixed effect

Note that all variables above (except dummies) are subject to natural logarithmic. The model specification for each industry differs depending upon the following choices:

- Lags, which is divided into the lags of demand, the lags of electricity price, and the lags of production index. The maximum lags allowed for the purpose of simplicity are up to 3 years.
- Cross price elasticity effect. It measures the percentage change of power demand when the prices of other energy source (gas and oil product) change in 1%.
- Number of customers and production index.

3 Estimation Results

As mentioned before, the estimation processes are performed for each industry and Table 2 summarizes the complete structure of model with some of the estimated parameters.[2]

As is predicted by economic theory, we observe negative price elasticity for each industry in the study although a couple of which does not provide a statistical significance. The size elasticity ranges from −0.0669 (group 26) to −1.1093 (group 18). Meanwhile the cross price elasticity (gas and petroleum product) exhibits both positive and negative values, which explain substitute and complementary effect of the other energy prices (gas or petroleum product), respectively. For most of the industry, the sign of gas price indicates that it is a complement while the sign of oil price is mixed. For the parameter estimates of the coefficient of the number of

[2] The complete estimation results are available upon request to the author.

Table 2 Model specification and estimation results

	Number of lags								
Industries	y	P_{Elec}	PI	Gas price	Oil price	House	PI	P_{Elec}	R^2
1	1	0	0	0.1617***	−0.0357	0.5771***	*n/a*	−0.8377***	0.944
2	1	0	0	−0.1929	−0.4274***	0.3928***	0.4588***	−0.2492**	0.743
3	1	3	0	0.1001	−0.0236	0.6163***	0.3458*	−0.5194***	0.819
4	1	0	0	0.4042***	−0.0244	0.1400***	0.3049***	−0.6173***	0.889
5	1	3	0	*n/a*	*n/a*	*n/a*	0.0217	−0.1745	0.616
6	1	0	0	0.0692	0.1029	0.6203***	0.1608**	−0.4822***	0.913
7	1	0	0	0.4809***	−0.0417	0.4963***	*n/a*	−0.5712***	0.915
8	1	0	0	0.2591***	−0.0404	0.4660***	0.1050	−0.4335***	0.873
9	1	0	0	0.2218*	−0.2382***	1.1065***	0.5286***	−0.6423***	0.849
10	2	3	1	*n/a*	*n/a*	0.2629***	0.1450	−0.2548**	0.881
11	2	0	0	0.3689**	−0.2630**	0.6122***	*n/a*	−0.6940***	0.547
12	1	0	0	−0.1130	−0.3625***	0.7487***	0.7472***	−0.7649***	0.770
13	3	3	0	*n/a*	*n/a*	0.6249***	0.2101***	−0.2263*	0.851
14	1	3	3	0.2179***	0.2560***	0.7651***	0.1273	−0.3626***	0.808
15	1	0	0	*n/a*	*n/a*	0.9196***	0.5232***	−0.7567***	0.802
16	1	1	0	0.0934	−0.0708	*n/a*	0.1521	−0.3482*	0.876
17	1	0	0	−0.0872	−0.4472***	0.2104***	0.1326**	−0.8635***	0.760
18	2	0	2	0.4247***	0.2572*	*n/a*	*n/a*	−1.1093***	0.892
19	1	0	0	−0.2268*	−0.1854*	0.9593***	0.4232***	−0.4857***	0.904
20	1	0	2	*n/a*	*n/a*	0.3375***	0.4579***	−0.1354	0.902
21	1	0	0	0.0589	0.0125	0.8334***	0.2930***	−0.6195***	0.887
22	1	3	2	0.0488	−0.0310	0.7884***	0.2677	−0.5976*	0.856
23	1	3	0	0.0953	0.5448***	0.5557***	*n/a*	−0.7074***	0.850
24	3	1	3	*n/a*	*n/a*	0.9574***	0.5667*	−0.8817***	0.857
25	1	0	0	0.0957	−0.1507*	0.6912***	0.2702*	−0.7644***	0.878
26	2	0	0	*n/a*	*n/a*	*n/a*	*n/a*	−0.0669	0.940
27	1	0	0	0.1593***	0.0667**	0.8300***	0.7281***	−0.2076**	0.951
28	1	0	0	0.2447***	−0.0084	0.9037***	0.9022***	−0.2269***	0.970
29	2	0	0	−0.3463***	−0.2733***	0.3906***	*n/a*	−0.7354***	0.905
30	1	0	0	−0.0071	−0.3372***	0.3825***	0.3056***	−0.3685*	0.917
31	2	0	1	0.6671	0.9004	*n/a*	0.1047	−0.1799	0.934
32	1	3	0	0.0611	0.3423***	1.0762***	0.2463	−0.4908***	0.953
33	1	0	0	−0.0158	0.0712**	0.6352***	0.5970***	−0.5143***	0.968
34	3	0	0	−0.1319	−0.1602	0.0752***	*n/a*	−0.7798***	0.662
35	1	0	0	0.3748	0.1795	0.9126***	1.1481	−0.1974	0.987

Note: ***, **, *indicate the significance level of 1%, 5%, 10%, respectively.

household, the positive sign and the high significance is worth note here. Most of the model has R^2 above 0.8 with a few exceptions.

The most recent previous study on power demand in Korea is conducted by KEEI (2004) [4]. However, the data used for the analysis is based on the aggregated time series of contract types not on the industry specific information. Overall size of

estimates for price elasticity of demand is ranging in between +0.178 and −0.705. Patrick and Wolak reported that the day-ahead price elasticity estimates vary substantially by time-of-use, industry, and firms within industries, with sample mean averages ranging from essentially zero to 0.86 in absolute value [5] although it may not be proper to have direct comparison since the data frequency is different. In comparison with that, our estimation results have a larger range.

Figure 1 shows the actual and fitted values for the first four industries. Amidst the irregularity of load data, our model successfully fits and mimics the actual data.

For the simulation purpose, an experiment of price change is conducted. A new price system which is 105% of the actual price is assumed for this purpose. Table 3 summarizes the change in electricity demand and expected changes in revenue due to this price change (for the first group in year 2010). It can be seen from this result that increasing the price by 5% will decrease the demand and revenue by around 4% and 2.6%, respectively. This kind of price simulation can be conducted for all industries with the inclusion of the changes in other energy prices, too.

This study can be improved further by applying more detailed panel model, including random effect, or even multilevel structures type of panel model to be able to incorporate contract type, regional and industrial groups into one model.

4 Conclusion

In this paper, the monthly power demand for each industry in Korea has been modeled using fixed effect panel model, trying to fully utilize the nature of given data structure. The estimation process shows negative price elasticity of demands for all groups, which varies from −0.0669 to −1.1093. Meanwhile the cross price elasticity is various among each industry. Previous studies on the power demand in Korean market have been focused on the contract type-wise analysis since the publicly available data is announced in this format while this preliminary study is conducted based on the industry specific information. Customers change the contract types depending upon their choice of contracts while the industry-specific analysis of power demand reveals the consumer behavior of each industry.

One thing to note here is the quality of data due to the change of KSIC on May 2008. The structure breaks in industry 02 and 04 (Figure 1) clearly show such problem at that specific point of time. The result of this analysis would be greatly improved if this change in KSIC is well managed in the construction of monthly data from KEPCO.

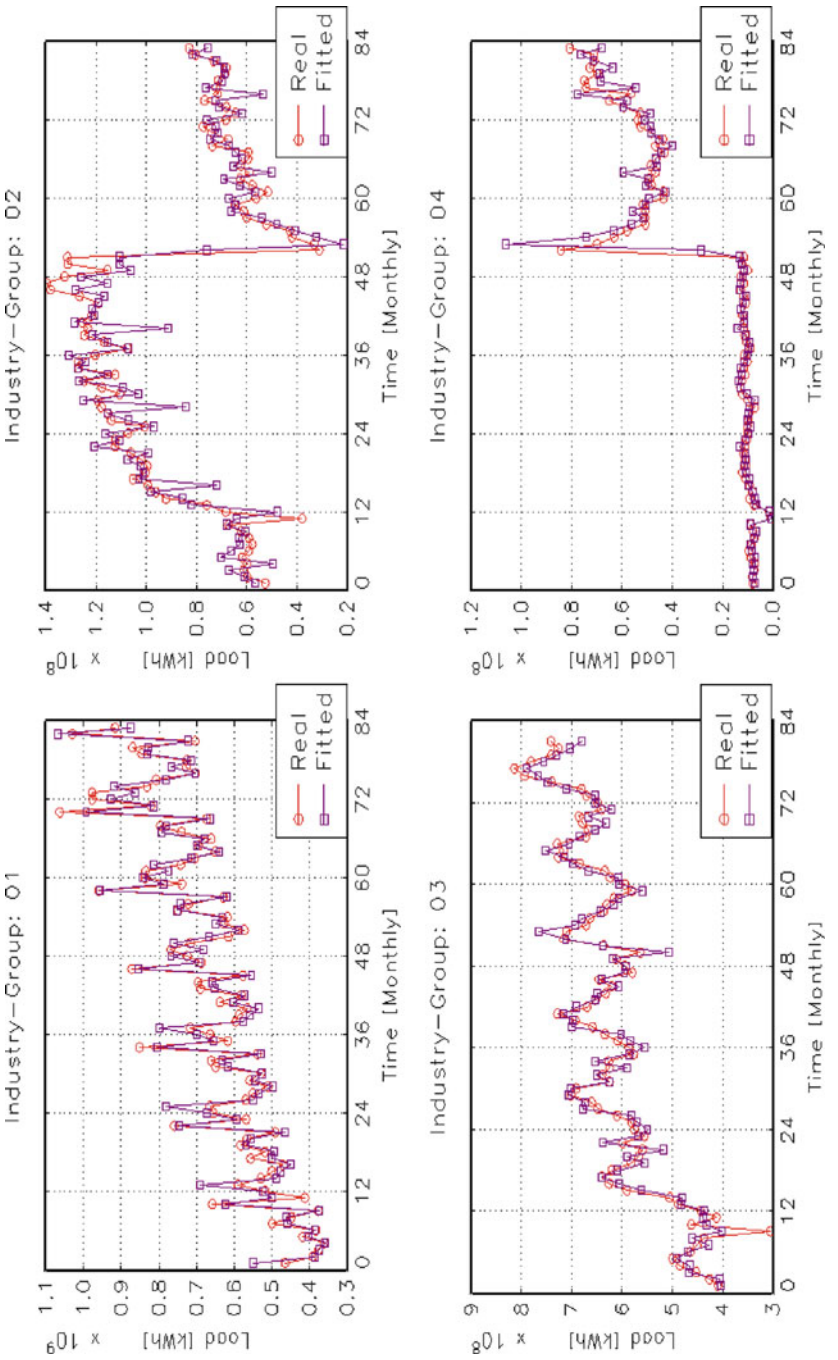

Fig. 1 Fitting result of the first four industries

Table 3 Price simulation

	Demand (GWh)			Revenue (million won)		
Month	Actual	+5%	Difference	Actual	+5%	Difference
2010 01	928.89	891.46	37.43	3236.11	3149.21	86.90
2010 02	862.17	827.43	34.74	3000.34	2919.82	80.52
2010 03	919.72	882.66	37.06	3190.54	3105.05	85.49
2010 04	780.29	748.85	31.44	2698.75	2626.54	72.21
2010 05	703.87	675.51	28.36	2408.81	2344.71	64.10
2010 06	765.20	734.36	30.83	2591.94	2523.33	68.61
2010 07	714.80	686.00	28.80	2446.21	2381.12	65.10
2010 08	830.44	796.98	33.46	2856.35	2780.14	76.21
2010 09	827.70	794.35	33.35	2850.02	2773.94	76.08
2010 10	722.20	693.10	29.10	2490.07	2423.56	66.52

References

1. Bank of Korea, Economic statistics system (http://ecos.bok.or.kr). Accessed at August 2011
2. Korea Meteorological Administration (http://web.kma.go.kr). Accessed at August 2011
3. Hsiao C (2003) Analysis of panel data, 2nd edn. Cambridge University Press, Cambridge
4. Korea Energy Economics Institute (KEEI) (2004) The estimation of power price elasticity of demand and its application, Final report
5. Patrick RH, Wolak FA (2001) Using customer demands under spot market prices for service design and analysis, EPRI Working Paper WO 2801-11

Understanding Socio-Economic Driving Factors of Indonesian Households Electricity Consumption in Two Urban Areas

Muhammad Ery Wijaya and Tetsuo Tezuka

Abstract Indonesia is one of the most diverse countries in the world in terms of its society. Therefore, there are several different characteristics in daily practices, including in consuming electricity. In order to understand the variety of socio-economic driving factors in household electricity consumption to achieve success in promoting electricity saving effort, a survey was conducted for two different areas with different cultural backgrounds: Bandung and Yogyakarta, in Java Island. The results shows that in Bandung, factors like income, duration of at home, and family size have clear positive effects on monthly electricity bills. In contrast, in Yogyakarta, duration of at home tended to negatively impact monthly electricity bills. It also suggests that socio-economic factors are potential for electricity saving effort through promoting energy saving behavior and also improving appliances efficiency.

Keywords Electricity demand • Electricity saving • Households • Indonesia

1 Introduction

Post economic crisis in 1997, and followed by political reform in 1998, the Indonesia's economic growth shows promising potential to be one of large economic player in the world. As the result, the Gross Domestic Product (GDP) per capita continues to increase over recent years. In 2001 the GDP per capita recorded to US$ 748, and in 2009 amounted US$ 2,698. The great economic growth impacted to the increasing people's welfare. Furthermore, the impact of economic growth also affected to the high growth of electricity demand from the household

M.E. Wijaya (✉) • T. Tezuka
Energy Economics Lab, Department of Socio-Environmental Energy Science,
Graduate School of Energy Science, Kyoto University, Yoshida, Kyoto 606-8501, Japan
e-mail: m.wijaya@at2.ecs.kyoto-u.ac.jp

T. Yao (ed.), *Zero-Carbon Energy Kyoto 2011*, Green Energy and Technology,
DOI 10.1007/978-4-431-54067-0_5,

sector, drastically. It has been recorded about 30.5 TWh in year 2001, and increasing almost doubled in 2009 by 55 TWh [1]. Java Island as the center of population and economic development, consumed more than 75% of total electricity demand in the country.

There are number of household energy conservation regulations have been issued by government to solve the high growth rate of electricity demand. The story of Indonesian energy conservation policy dates back to year 1982, when for the first time government issued Presidential Instruction No. 9/1982 about energy conservation. The newest regulation was Government Regulation No. 70/2009 about energy conservation; this regulation gives mandatory command on energy standard and labeling for appliances, incentive of energy conservation, and also gives authority to the local government to handle the energy conservation effort in their jurisdiction. However, results of the real application do not seem so convincing and has not been systematically analyzed. Therefore, the result is far from the expected consumption by policy makers.

In term of society, there are more than 300 distinct native ethnicities in Indonesia, which some of them operate in different regions. The variety of cultural backgrounds in Indonesia might affect to the residents' daily activity, including behavior in using electricity. Therefore, understanding the variety of driving factors in household electricity consumption is the key to achieve success in promoting electricity saving effort. This paper explores the study of socio-economic driving factors of Indonesian household electricity consumption in two different areas with different cultural backgrounds of its society, which are Bandung as the representation of Sundanese culture and Yogyakarta to reflect the Javanese culture. In addition, Sundanese and Javanese people counted as the largest electricity consumers in Indonesia. The reason to select Bandung and Yogyakarta is that the location of both cities in Java Island, the most advanced island in Indonesia, beside of its unique culture. Genjo et al. [2] and Biesiot and Noorman [3] found that household energy consumption would have a closer relationship with income and family size. Guerin et al. [4] added that duration to stay at home also contributes to the energy consumption in household. Therefore, the socio-economic factors considered in this study are income, family size, and duration to stay at home.

2 Socio-Economic Factors Being Influenced to Electricity Consumption

This research obtained the primary information by using questionnaire survey. There are 100 households investigated from each city. In Bandung, the only Sundanese families were recruited as respondents, while in Yogyakarta only Javanese families were selected. The respondents are recruited through a door-to-door solicitation procedure for surveying their home appliances, checking their monthly electricity bill, and asking their typical behavior in electricity use.

Table 1 The average appliances electricity use per household in Yogyakarta and Bandung

	Home appliances (KWh/month)				
City	Cooling	Cooking	Lighting	Entertainment	Others
Bandung	67.3	178.6	41.2	101.6	25.7
Yogyakarta	79.7	122.4	33.2	65.3	17.4

Table 2 Socio-economic characteristics of respondents in Bandung and Yogyakarta

		Number of households based on family size			
City	Income (US$/month)	1–2 persons	3–4 persons	5–6 persons	7 persons
Bandung	≤300	7	39	0	0
	301–500	3	18	5	0
	501–1,000	0	7	15	0
	>1,000	0	0	5	1
Yogyakarta	≤300	23	53	0	0
	301–500	0	8	6	1
	501–1,000	0	0	6	1
	>1,000	0	0	1	1

2.1 Monthly Electricity Consumption

The survey found that electricity consumptions per household by cooking, lighting, entertainment and information and other devices in Bandung were higher than in Yogyakarta, those lead to the higher in average monthly electricity bill. Although the possession of cooking devices in Bandung was lower than in Yogyakarta, but the frequency of use was higher. In addition, in Yogyakarta, electricity consumption in cooling devices was higher than in Bandung, this is due to the intensity of cooling devices and uses. Table 1 presents profile of electricity consumption per household in both cities. The average monthly electricity bill paid by households in Bandung and Yogyakarta are US$ 21.6 and US$ 16, respectively.

2.2 Characteristics of Respondents

From the survey, the average households' income level in Bandung was higher than in Yogyakarta. The average number of residents per household was three persons in Bandung and Yogyakarta. Family size is then compared to the income level of households from both cities in Table 2. The average daily activity of residents at home from both cities was similar, about 7.2 h per day excluding sleeping time. The duration of daily activity at home was mostly dominated by children and housewife. Meanwhile the average workers duration staying at home was 4.5 h per day during working days. At weekend days, about 76% of respondents in Bandung chose to stay at home, and 24% of respondents spent time at outside.

Table 3 Model parameters estimates for statistical analysis in Bandung and Yogyakarta

City	Variable	*t*-Value	*p*-Value
Bandung	Income	9.031	0.000
	Family size	5.033	0.000
	Duration to stay at home	3.422	0.034
Yogyakarta	Income	11.552	0.000
	Family size	4.420	0.000
	Duration to stay at home	−2.755	0.022

Table 4 Statistical estimation analysis of the multiple linear regression models

City	R^2	F	Std. error of the estimate
Bandung	0.721	182.5	7.605
Yogyakarta	0.906	306.8	4.441

In Yogyakarta, almost all respondents preferred to spend the weekend days at home, accounted for about 91%.

From the observation, it seemed that the households' lifestyle in Bandung inclined to a consumer lifestyle, even though the time spent at home was shorter, but the electricity consumption was higher than in Yogyakarta. Moreover, the habit of using too much electrical devices by highly educated people also led to the higher electricity consumption. On the contrary, households in Yogyakarta typically live in modest practical lifestyle originating by Javanese tradition. Those with a higher education had better understanding for saving electricity. Interestingly, the respondents in Yogyakarta preferred to use their time at home for meeting with their family after working hours rather than using the electrical device excessively.

2.3 Impact of Socio-Economic Factors to Electricity Consumption

The multiple linear regression analysis was employed to investigate the contribution of each socio-economic driving factor to monthly electricity bill in each city. The analysis is conducted for households in Bandung and Yogyakarta, and the multiple linear regression models are presented in (1) and (2), respectively. Explanation variables are monthly electricity bill (y), income (x_1), family size (x_2), and duration to stay at home (x_3). The models were confirmed that all factors were statistically significant predictors of monthly electricity bill (where p-value was less than 0.05). Details of the model parameter are explained in Table 3, while details of estimation analysis are presented in Table 4.

$$y = (0.021 \times x_1) + (4.066 \times x_2) + (0.205 \times x_3) - 5.579 \quad (1)$$

$$y = (0.044 \times x_1) + (2.492 \times x_2) - (0.889 \times x_3) + 3.447 \quad (2)$$

There were several differences in characteristics of electricity consumption between two cities. In Bandung, all factors gave positive effect to monthly electricity bill. Meanwhile, the different results were found in Yogyakarta, daily activity gave negative impact to monthly electricity bill. From (1) for Bandung, if the effects of all other factors are held constant, thus the monthly electricity bill per household would increase as follows: US$ 0.021 with the growth of income; US$ 4.066 per head with the rise of family size; US$ 0.205 per h with the increment of the daily duration activity at home. Slightly different on (2) for Yogyakarta, if the effects of all other factors are held constant, then it could be predicted that monthly electricity bill per household would decrease by US$ 0.889 per h with the increase of duration to stay at home. Meanwhile, by the similar assumption, if the effects of all other factors are held constant, the monthly electricity bill per household would increase as follows: US$ 0.044 with the growth of income; US$ 2.492 per head with the rise of family size.

3 Suggestions on Electricity Saving Approaches

3.1 Promoting Electricity Saving Behavior

As the model presented in Sect. 2.3, an indicator to promote importance of electricity saving behavior was shown by the significant impact of family size and duration to stay at home to the electricity consumption in the households for both cities. It guides to the conjecture that the increasing number of family member and duration to stay at home lead to the increasing of electricity consumption due to the more intensive in using home appliances and lighting. These results suggest that promoting electricity saving behavior for resident could be an important way to control electricity consumption. In addition, duration of staying at home in Yogyakarta produced a significant negative impact on electricity consumption. This was due to fact that the respondents in Yogyakarta preferred to use their time at home for meeting with their family after working hours. Therefore, this culture needs to be fostered in order to keep the electricity consumption in Yogyakarta controllable.

3.2 Improving Appliances Efficiency

From the findings, another interesting thing that related to socio-economic factors in electricity consumption is home appliances. The reasons are: the increasing income affects to the number of appliances-owned, the increasing number of resident affects to the increase of appliance user, and finally the increment

of duration to stay at home guides to the increase of using appliances. Therefore, beside of promoting electricity saving behavior, improving home appliances efficiency is also another important key to support electricity saving effort. For an example; the introduction of LED lamps might produce significant electricity saving since the most lamps widely used for lighting in Bandung and Yogyakarta households were CFLs, fluorescent lamps, and incandescent bulbs, respectively. Bandung households, on average, comprised used almost 78% of CFLs, 15% of florescent lamps, and 7% of incandescent bulbs. Meanwhile, in Yogyakarta, household lighting comprised 82% of CFLs, 12% of florescent lamps, and 6% of incandescent bulbs. The average power of CFLs and florescent lamps ranged from 8 to 40 W, while incandescent bulbs ranged from 5 to 10 W.

4 Concluding Remarks

In a diverse society with cultural backgrounds, understanding the variety of driving factors in household electricity consumption is the key to achieve success to promote electricity saving effort. The investigation of socio-economic driving factors of households' electricity consumption in two cities shows that; in Bandung, the increasing of income, family size, and duration to stay at home lead to the increasing of electricity consumption; while in Yogyakarta, the impact of duration to stay at home would reduce the electricity consumption. These results suggest that socio-economic factors are potential for triggering electricity saving effort through promoting energy saving behavior and also improving appliances efficiency.

Acknowledgement This study was funded the Kyoto University Global Center of Excellent (GCOE) Program Energy Science in the Age of Global Warming. The authors would like to acknowledge all the people who participated as respondents in this research. The first author would convey the gratitude to Ministry of Education, Culture, Sports, Science and Technology (MEXT) Japan for providing scholarships during the study.

References

1. Center for Data and Information on Energy and Mineral Resources (2010) Handbook of energy and economic statistics of indonesia 2010, Jakarta, available at http://prokum.esdm.go.id/Publikasi/Handbook%20of%20Energy%20&%20Economic%20Statistics%20of%20Indonesia%20/Handbook%202010.pdf
2. Genjo K, Tanabe S, Matsumoto S, Hasegawa K, Yoshino H (2005) Relationship between possesion of electric appliances and electricity for linghting and others in Japanese households. Energ Build 37:259–272
3. Biesiot W, Noorman KJ (1999) Energy requirements of household consumption: a case study of the Netherlands. Ecol Econ 28:367–383
4. Guerin DA, Yust BL, Coopet JG (2000) Occupant predictors of household energy behavior and consumption change as found in energy studies since 1975. Fam Consum Sci Res J 19(1):48–80

Economic Measures for Evaluating CO_2 Emission Reduction in Japan by Using the Integrated Model of Multi-sectoral Macroeconomy and Energy

Syota Higashikura, Tetsuo Tezuka, Hideaki Fujii, and Takayuki Takeshita

Abstract In recent years policy makers have been eager to develop economy-energy models that can test the effectiveness of environmental policies for realizing low-carbon economy in Japan. We have developed the Integrated Multi-sectoral Macroeconomic Energy Model that can evaluate the amount of CO_2 emission reduction effects of macroeconomic policies. This paper presents the outline of the model, and shows the results of the simulation about the use of the tax revenue and the oil price increase. About the use of carbon tax revenue the GDP decrease of the case of income tax reduction is more than that of the case of public investment. The reduction rates of production by industry sector vary from 0.09% ("Construction" sector) to 4.7% ("Iron, steel and metal" sector).

Keywords Carbon tax • Low-carbon economy • Macroeconomic energy model • Multi-sectoral model

1 Introduction

For designing the countermeasure against the global warming a variety of economic energy models have been developed and the cost and benefit of policy measures have been evaluated.

S. Higashikura (✉) • T. Tezuka
Graduate School of Energy Science, Kyoto University, Yoshida, Sakyo-ku, Kyoto 606-8501, Japan
e-mail: s.higashikura@aw3.ecs.kyoto-u.ac.jp

H. Fujii
Kyoto Sangyo University, Motoyama Kamigamo, Kita-ku, Kyoto 603-8555, Japan

T. Takeshita
Tokyo University, 7-3-1 Hongo, Bunkyo-ku, Tokyo 113-8654, Japan

T. Yao (ed.), *Zero-Carbon Energy Kyoto 2011*, Green Energy and Technology,
DOI 10.1007/978-4-431-54067-0_6,

Macroeconomic energy models analyze the relationship between the energy policy and macroeconomic index such as the relationship between carbon tax and GDP. In the real world, however, several deferent energy policies are introduced at the same time. And the effect of the policy measures should be analyzed by industry sectors for evaluating the feasibility of simulation results. For this purpose we have developed Integrated Multi-Sectoral Macroeconomic Energy model of Japan.

In this paper, the outline of the model is explained and the impact of carbon tax and oil price change on macroeconomic index, GDP.

2 Macroeconomic Energy Model

2.1 Outline of Macroeconomic Energy Model

Two econometric models, that is, the macroeconomic model and the energy model have been developed and linked with each other. The outline of the integrated model is shown in Fig. 1. Each part of the model is explained in the following sections.

TSP [1] is used to develop the model. The main role of the software is to estimate the values of the parameters included in the model equations and test the validity of the model equations from the viewpoints of the statistical significance and the acceptability of the final-test results.

2.2 Multi-sectoral Macroeconomic Model

Table 1 shows the characteristics of the multi-sectoral macroeconomic model developed in this study. The multi-sectoral macroeconomic model is composed of the behavior equations and the definitional equations (519 equations in total) whose parameters are estimated by the least squares method with the revised estimation period referring the J-MACRO model [2]. It doesn't incorporate the equation of between supply and demand of commodity but has the disequilibrium dynamic structure and data-oriented structure in the model.

2.3 Energy Model

The energy model is also an econometric model for representing the energy supply and demand in Japan. The period for parameter estimation is from 1991 till 2008 [5]. Table 2 shows the characteristics of the developed energy model.

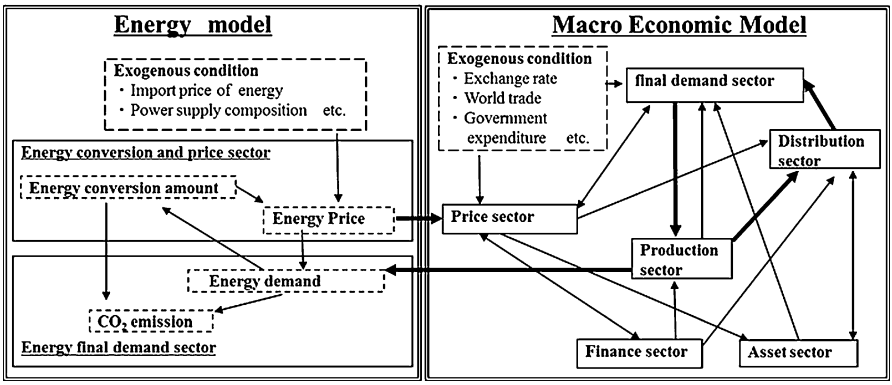

Fig. 1 Outline of integrated multi-sectoral macroeconomic energy model

Table 1 Outline of multi-sectoral macroeconometric model [3, 4]

Area	Japan
Time period	• Annual data • Estimation period: between 1997 and 2005 (9 years)
Model scale	• Number of equations: 519
Basic structure	• Disequilibrium dynamics • Markup method
Interindustry model	• Combination of commodity × commodity (SNAIO) and industry × industry (SNA) • Set out below are industry classification: (Agriculture, forestry and fisheries, Mining, Food, Textiles, Pulp, paper and wooden products, Chemical products, Petroleum refinery and coal, Ceramic, stone and clay products, Iron, steel and metal, Metal products and machinery, Miscellaneous manufacturing products, Construction, Electric power, gas supply and steam and hot water supply, Trade and communication, Service, General government, Private non-profit organizations serving household)
Consumer demand	• Macro budget consumption function (life-cycle and permanent income hypothesis)
Demand for labor	Cobb–Douglas production function

2.4 Linkage of the Two Models

By linking the Multi-Sectoral Macroeconomic model with the energy model as is shown in Fig. 1, the amounts of production of each industry (Production sector) are used in the energy consumption of each industry (Energy final demand sector), and

Table 2 Outline of energy model [6, 7]

Area	Japan
Time period	• Annual data • Estimation period: 1991–2008 (18 years)
Model scale	• Number of equations: 383
Classification of energy consumption	Industry classification: Comprehensive energy statistics-based 13 classification Transportation classification: Comprehensive energy statistics-based 9 classification Household and service classification: EDMC handbook of energy & economic statistics in Japan-based 10 classification

each energy price (Energy conversion and price sector) are used in price of products (Price sector). The energy prices give the price of products of each sector according to the information included in the model.

3 Conditions for Model Simulation

In this paper the Integrated Multi-Sectoral Macroeconomic Energy Model is simulated to evaluate the impact of the environmental policy. The Ministry of the Environment of Japan is planning to revise the taxation including carbon tax [8], and the period to be covered is from 2010 till 2020. As for the tax rate revision case the details of the change in tax rates concerning oil, natural gas and coal are shown in Table 3. The BaU case assumes that carbon tax rate is fixed with the price of 2011/9. In the model simulation seven cases are considered by combining the conditions about tax rate and oil price as is shown in Table 4.

4 Results and Discussion

4.1 Impact on GDP and CO_2 Emission

Figure 2 shows the GDP decrease ratio against Case 1(BaU) for the Cases 2–4. About the use of carbon tax revenue the GDP decrease of the case of income tax reduction is more than that of the case of public investment. And, especially, GDP decreases sharply with increase in carbon tax rate (2010–2015).

Figure 3 shows the decrease ratio of CO_2 emissions for Cases 3 and 6 against Case 1(BaU). CO_2 emissions in the BaU case in 2020 are estimated to be about 1.24 billion t-CO_2 (17% increase compared with 1990). The simulation result of Case 3 shows that continuous CO_2 emission reduction needs to increase the carbon tax rate every year.

Table 3 Scenario withincreasing carbon tax rate [8]

Year/month	Petroleum(¥/kl)	Natural gas (¥/t)	Coal (¥/t)
By 2011/9	2,040	1,080	700
From 2011/10	2,290	1,340	920
From 2013/4	2,540	1,600	1,140
From 2015/4	2,800	1,860	1,370

Table 4 Conditions of simulation

Case number	Condition of simulation	Application of fund by carbon tax
1 (BaU)	Carbon tax rate is fixed. Crude oil price is linear interpolated: $69(2009)–$121 (2020)	–
2	Carbon tax rate is raising. Crude oil price is linear interpolated: $69(2009)–$121 (2020)	Decrease in income tax (following year)
3		Increase in public investment
4		Increase in tax revenue is not used
5	Carbon tax rate is raising. Crude oil price is linear interpolated: $69(2009)–$150 (2020)	Decrease in income tax (following year)
6		Increase in public investment
7		Increase in tax revenue is not used

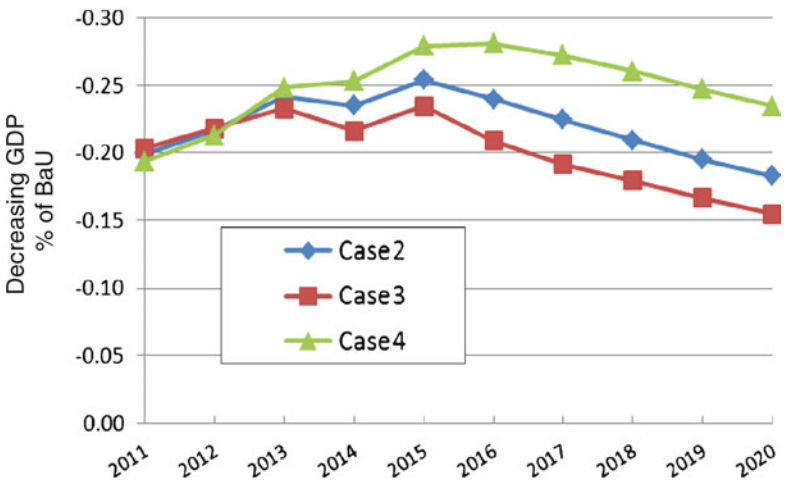

Fig. 2 Comparison result between Cases 2–4

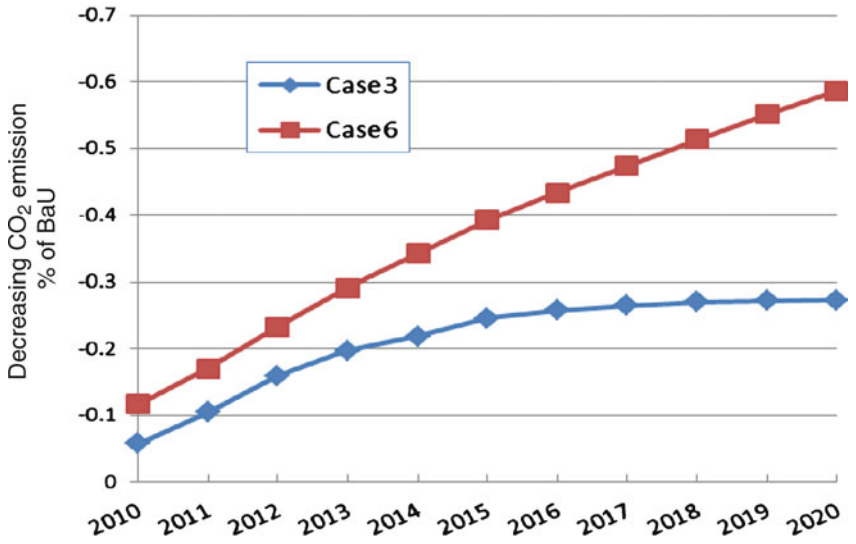

Fig. 3 Impact of oil price change

4.2 Analysis of Production by Industry Sectors

Table 5 shows the estimation results of sectoral annual productions of the years 2010, 2015 and 2020. As for the BaU case, the values of annual products of each industry is shown. On the other hand for Case 3 the decrease ratio against the BaU case is shown in the table.

As for the decrease rate of the amount of production, the increase of carbon tax will have much effects on the energy-intensive industries (Textiles, Pulp, paper and wooden products, Ceramic, stone and clay products, Iron, steel and metal). The reduction rates of production by industry sector vary from 0.09% (Construction) to 4.7% (Iron, steel and metal).

5 Conclusion

In this study, we have developed the multi-sectoral macroeconomic energy model, and analyzed the impact of the increase in the carbon tax rate and the crude oil price. Obtained results are as follows:

1. About the use of carbon tax revenue the GDP decrease of the case of income tax reduction is more than that of the case of public investment.
2. The reduction rates of production by industry sector vary from 0.09% (“Construction” sector) to 4.7% (“Iron, steel and metal” sector).

Table 5 Annual productions of industry sectors (Cases 1 and 3)

	Case	2010	2015	2020	Year
Agriculture, forestry and fisheries	1	13,686	13,811	13,895	10^9Yen
	3	−0.0159	−0.1068	−0.1025	%
Mining	1	1,349	1,313	1,297	10^9Yen
	3	0.0336	0.536	0.5879	%
Food	1	32,292	33,216	34,063	10^9Yen
	3	−0.0197	−0.1438	−0.151	%
Textiles	1	1,695	1,530	1,323	10^9Yen
	3	−0.0882	−0.5318	−0.482	%
Pulp, paper and wooden products	1	7,003	6,762	6,345	10^9Yen
	3	−0.0687	−0.427	−0.4036	%
Chemical products	1	26,742	27,868	28,911	10^9Yen
	3	−0.022	−0.1366	−0.1312	%
Petroleum refinery and coal	1	10,537	10,161	9,652	10^9Yen
	3	−0.045	−0.2166	−0.1908	%
Ceramic, stone and clay products	1	6,527	6,461	6,209	10^9Yen
	3	−0.0558	−0.8114	−0.8796	%
Iron, steel and metal	1	24,243	26,122	26,485	10^9Yen
	3	−0.1709	−4.6517	−4.6804	%
Metal products and machinery	1	18,8684	21,1386	22,2066	10^9Yen
	3	−0.0321	−0.212	−0.1352	%
Miscellaneous manufacturing products	1	30,273	29,924	28,400	10^9Yen
	3	−0.1458	−0.8811	−0.8775	%
Construction	1	60,230	56,947	52,824	10^9Yen
	3	−0.0452	−0.1799	0.0898	%
Electric power and gas supply etc.	1	24,555	25,675	26,508	10^9Yen
	3	−0.027	−0.3551	−0.3551	%
Trade and communication	1	64,046	69,108	74,138	10^9Yen
	3	−0.0234	−0.2195	−0.2005	%
Service	1	41,5308	44,3002	46,7031	10^9Yen
	3	−0.03	−0.2454	−0.2154	%
General government	1	72,008	76,781	81,536	10^9Yen
	3	−0.0007	−0.0054	−0.005	%
Private non-profit organizations	1	15,240	16,329	17,426	10^9Yen
	3	−0.0091	−0.0635	−0.0686	%

Acknowledgement The authors would like to thank the GCOE Unit for financial support to conduct this research at the Graduate School of Energy Science of Kyoto University.

References

1. Wago H, Ban K (1995) TSP ni yoru Keizai Deta no Bunseki (Empirical Analysis of Economic Data Using TSP). University of Tokyo Press, Tokyo
2. Takeshita T (2003) An analysis of the change in the government investment multiplier in the Japanese economy using several model types. J Appl Input Output Anal 9:1–34
3. Economic and Social Research Institute, Cabinet Office, Government of Japan (2010) SNA (National Accounts of Japan)
4. Economic and Social Research Institute, Cabinet Office, Government of Japan (2009) SNA interindustry table
5. Nagata Y (1995) Competition in energy model. Soc Econ Res 35:93–105
6. Agency for Natural Resources and Energy, Ministry of Economy, Trade and Industry (2011) Energy balance table. Comprehensive energy statistics
7. Institute of Energy Economics, Japan (2010) Energy resources, demand and supply, equipments. EDMC handbook of energy & economic statistics in Japan. The Energy Data and Modelling Center, Japan
8. Environmental policy, Ministry of the Environment, Government of Japan (2010) FY 2011 The result of taxation reform request by Ministry of the Environment, http://www.env.go.jp/en/policy/tax/tax-reform.html (accessed Jan 30th, 2011)

Application of Online Community for Promotion of Pro-environmental Behavior

Saizo Aoyagi, Oki Fujiwara, Hirotake Ishii, and Hiroshi Shimoda

Abstract In Japan, promotion of pro-environmental behavior (PEB) in household is one of the main challenges for energy saving. There are very few studies on the promotion of PEB dealing with the continuity. Purposes of this study are to propose a method for promotion of continuous PEB using online community, and to evaluate the effectiveness of the method. In this paper, after the overview of the conventional approach for promotion of PEB and the concept referring to the previous study, a new method to promote continuous PEB will be proposed, which is characterized by fosterage of strong community by the analogy of club activities. In order to evaluate the effectiveness of the method, experiment procedures will be introduced.

Keywords Club activities • Human relationship • Online community • Pro-environmental behavior • Social impact theory

1 Introduction

Energy problems, typified by global warming, have grown in to be serious. In this context, energy saving in household is a pressing issue in Japan. It is because both number of households and households energy consumption have increased [1], and also because of an impact of the Tohoku Earthquake with subsequent power shortage. Promotion of pro-environmental behavior (PEB) is an effective way of energy saving in residential sector and there have been many studies about factors that promote PEB of people [2] and methods of promotion of that [3].

S. Aoyagi (✉) • O. Fujiwara • H. Ishii • H. Shimoda
Graduate School of Energy Science, Kyoto University, Yoshida-Honnmachi, Kyoto 606-8501, Japan
e-mail: aoyagi@ei.energy.kyoto-u.ac.jp

T. Yao (ed.), *Zero-Carbon Energy Kyoto 2011*, Green Energy and Technology,
DOI 10.1007/978-4-431-54067-0_7,

A goal of promotion of PEB is habit formation and continuation of PEB of people. Nevertheless, there are very few studies on the promotion of PEB dealing with the continuity. In this paper, we describe our proposal about a method for promotion of continuous PEB with group communication with computer mediated communication (CMC), which solves problems described above and is characterized by fosterage of strong community utilizing analogy of club activities after the overview of the conventional approach for promotion of continuous PEB and the concept referring to the previous study.

2 Overview of Past Studies

2.1 Conventional Approaches

Recently, many information devices or services, which measure energy consumption in houses and present it to users, have been developed and applied as an approach of promotion of PEB about electricity consumption [4]. It is visualization approach, which promote spontaneous energy saving of consumers with economic thinking, and it becomes popular as a function of smart meter.

These measurement devices or services are effective in the short term. Nevertheless, Yi pointed out that these method cannot continue PEB because users grow tired of them, and Instead of that, utilization of social communication in small groups is focused as a method for promotion of continuation of PEB [5].

2.2 Group Communication as a Method for Behavior Change

Group communication is useful as a method for behavior change because a norm or conformity effect prohibit dropout of behavior change among participants through that [6]. Moreover, communication in a small group with distributed CMC is focused in this study. Distributed CMC allow participants to communicate to each other from remote places, it makes participation very easy.

However, communication has uncertainty. It is not always activated, and participants sometimes dropout of communication for various reasons. Aoyagi et al. [7] focused on communication stress as a factor of dropout from group communication. Some study said that people recently do not like conventional deep or close communication, because of social stress associated with it and stress-free is a main point of continue communication [8].

Aoyagi developed an easy communication system as a way of stress-free communication. Easy communication is a kind of group communication where participants just share a place and feel each other's presence and behaviors. It will

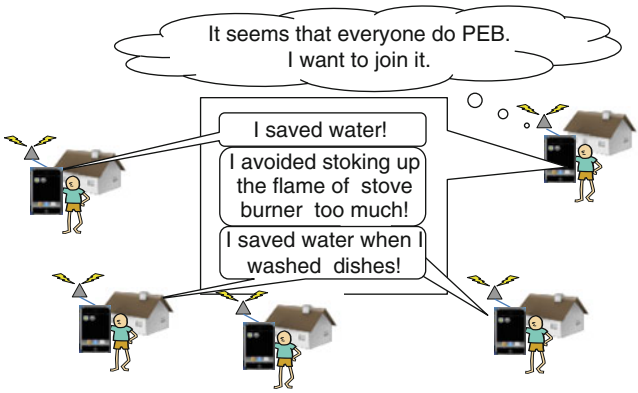

Fig. 1 A fundamental framework of group communication as behavior change

not cause these communication stresses and is sufficient to cause promotion of PEB through the conformity effect.

A fundamental framework of group communication in the study is shown in Fig. 1. Participants form a group that consists of five or more members. They carry and frequently use information devices for group communication, such as smartphone in their houses. They communicate to each other using a function of sending "PEB footprints" in the easy communication system.

This function allows users to send fixed-texts, which inform that sender did PEB, such as "I saved water!" Traces of "PEB footprints" sent by members were presented in room-designated timelines in a display of iPod touch. When members see these texts, they can know that others do PEB, and then they will intend to do PEB by socio-psychological conformity effect. In addition, this function is designed to avoid users' bothering about contents of communication, which is a type of communication-stress.

The method was evaluated through an experiment with ten participants. This result shows a limitation of this method, and suggests that this method is possibly effective for not all people. More detailed results are shown in another report [7].

3 Proposal of a Method for Promoting PEB

3.1 Framework of the Method

Taking advantage of the past studies, we focus on another kind of group communication, which foster strong social ties between participants, and is named "strong community" in contrast with easy communication. Strong community is formed in order to foster strong group norm, which requires members to do PEB. Strong group

norm is a binding power to members; and it might cause a social stress. Therefore, we have to be careful about avoiding production of social stress, and making participants be interested in this community.

The fundamental framework, which is shown in Fig. 1, is common to new method and old method. Members mutually send messages that tell they did PEB. New method includes two elements, which are utilized as promotion of strong community; (1) analogy of club activities and (2) intervention with conventional agents in appropriate timings.

3.2 *Fosterage of Strong Community with Analogy of Club Activity*

The method employs a power of social relationship in order to foster group norm of PEB. According to the theory of social impact [9], "strength" which depends on types of social relationships, such as social force or social status, promotes an effect of social influence.

In particular, analogy of club activities and in Japanese schools is introduced. In other words, this method includes role-play of members of club activities. Interfaces of an application in information devices for group communication are designed to make participants feel this group communication method as something like club activities and recognize that they are members of "eco-club" shown in Fig. 2. The reason why analogy of club activities is introduced in this method is described below; (1) Club activities have asymmetrical relationships of members (senior and junior students, *senpai* and *kouhai*). It will cause strong social influence according to the theory of social impact. (2) Club activities are easy to imagine for most people in Japan because education rate is very high in Japan. (3) An image of club activities is positive for people then participants will be able to enjoy the group communication with analogy of club activities. (4) Club activities have competitive relationship of members. It is recognized by participants as a game, and then it foster motivation of participants to join the communication.

3.3 *Intervention in the Communication in Appropriate Timings*

Group communication has an ineluctable positive feedback of participation. If communication is active, average participants want to join communication. On the other hand, if communication is inactive, they do not want to join. Consequently, active community gets more active, and inactive community gets more inactive. This phenomenon might cause sudden death of community by accident. In order to avoid latter, some conventional agents are introduced in group-members. They behave actively in group communication, such as submit messages very frequently. In addition, conventional agents are required to intervene other members' behavior in appropriate timings. For example, it is predicted that some

Fig. 2 Screenshots of each display of a system of eco-club activities

participants will drop out of group communication; agents have to encourage them intensively. Their concrete action guidelines are constructed.

4 Evaluation Experiment

An experiment with eight participants is planned in order to evaluate the effectiveness of the proposed method. In this section, procedures of the experiment are described. Participants are divided into two groups (groups 2 and 3); each of them consists of four participants. In addition, two dummy groups also join in the experiment (groups 1 and 4). Each dummy group consists of four conventional agents described in Sect. 3.3.

Actual experimental period is 6 weeks, and each group joins in and exits from the experiment in order to generate asymmetrical relationships of participants as shown in Fig. 3. At the beginning of the experimental period, group 2 and group 1 (dummy) join at the same time, group 1 (dummy) however behaves as they have been joined since 2 weeks ago and they are *Senpai* of group 2. Two weeks after, group 1 (dummy) exits from the experiment and group 3 joins as *Kohai* of group 2. Two weeks after, group 2 exits and group 4 (dummy) joins. At last, two groups exit from the experiment 2 weeks after.

Actual participants and conventional agents communicate to each other and do PEB in their home using information devises (iPod touch) and developed application software while their period of participation.

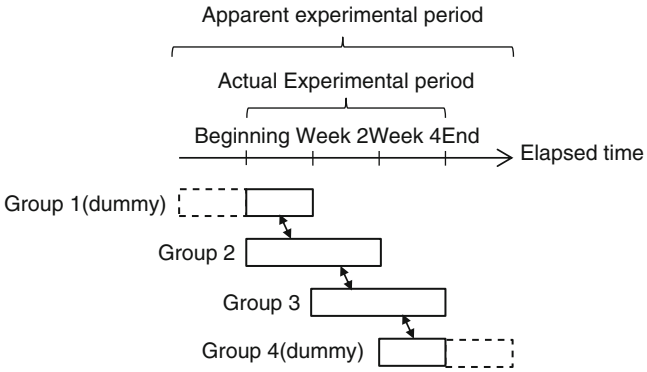

Fig. 3 The flow of the experiment

Web-based questionnaires are conducted in order to measure their frequencies of doing PEB in their home once a week. In addition, a questionnaire and an interview are conducted in order to investigate participants' impression to the system and the activity in the experiment after the experimental period finished.

5 Summary and Future Works

In this study, we overviewed the conventional approach for promotion of continuous PEB and the concept referring to the previous study, and proposed new method for promotion of PEB which is characterized by fosterage of strong community utilizing analogy of club activities. The evaluation experiment for the proposed method described in Sect. 4 is currently planned.

Acknowledgement This work was partly supported by an "Energy Science in the Age of Global Warming" of Global Center of Excellence (G-COE) program (J-051) of the Ministry of Education, Culture, Sports, Science and Technology of Japan.

References

1. METI (2010) Annual Energy Report 2010
2. Kollmus A, Agyeman J (2002) Mind the gap: why do people act environmentally and what are the barriers to pro-environmental behavior? Environ Educ Res 8(3):239–260
3. Abrahamse W, Steg L, Vlek C, Rothengatter T (2005) A review of intervention studies aimed to household energy conservation. J Environ Psychol 25:273–291
4. mDIY Kyoto (2009) WATTson (http://www.diykyoto.com/uk)
5. Tan Y (2009) Persuasive technology in motivating household energy conservation. In: Michaelles F (ed) Business aspects of the internet of things seminar of advanced topics. FS 2009, pp 52–58

6. Moscovici S, Personnaz B (1980) Studies in social influence. J Exp Soc Psychol 16:270–282
7. Aoyagi S, Okamura T, Ishii H, Shimoda H (2011) Proposal of a method for promotion of continuous pro-environmental behavior with easy communication. In: 14th international conference on human–computer interaction (HCII2011), Paper No. 6763
8. Sato I (2007) Communications of "shyness" in dance: body presentation of "I" in club. J Comm Stud 27:51–72
9. Latane B (1981) The psychology of social impact. Am Psychol 3(4):343–356

Analysis of Short Time Pauses in Office Work

Kazune Miyagi, Shou Kawano, Hirotake Ishii, and Hiroshi Shimoda

Abstract To optimize the balance between intelligent productivity and energy use in office building, we should clear the mechanism of productivity variation. For this purpose, the author had been proposed a productivity variance model. The model is two state transit model based on short time pauses. This model can explain the productivity variation in subjective experiment result. But in some cases, the explanation is insufficient. In this study, authors conducted a subjective experiment to discuss with an analysis of distribution of short pauses for improving the model. Analysis of the examination result revealed that the distribution of short time pause has two peaks. Second peak which means little longer pauses is smaller than first one. But the effect size to productivity is larger. And the shape assumed lognormal distribution. This result revealed some of mechanism of productivity variation and proposed model got more accuracy.

Keywords Modeling • Office work • Productivity • Short time pause • Task performance

1 Introduction

In office buildings, the energy consumption of lighting and air-conditioning account for big percentage [1]. Therefore many office building have been trying turning down air-conditioning and dimming a light off for saving energy. On the other hand, many studies have revealed that indoor environment condition affect intelligence productivity and workers' health. To optimize the balance between intelligent productivity and energy use, authors had been proposed productivity variance

K. Miyagi (✉) • S. Kawano • H. Ishii • H. Shimoda
Graduate School of Energy Science, Kyoto University, Yhosida-Honmachi,
Sakyo, Kyoto 606-8501, Japan
e-mail: miyagi@ei.energy.kyoto-u.ac.jp

T. Yao (ed.), *Zero-Carbon Energy Kyoto 2011*, Green Energy and Technology,
DOI 10.1007/978-4-431-54067-0_8,

model based on short time pauses [2]. But the model has some problems. The purpose of this study is improving the model by conducting experiment and analyzing the result focused on short time pauses.

2 Modeling Productivity Variance

2.1 Framework of Productivity Variance Model

Figure 1 shows a time series variance of the speed of checking slip task. It is a mental task and the time for answering one sheet should be within several second. But there were some slips taking extra time. It means office workers take short time pauses for break and the frequency of effects productivity. Based on this analysis, the authors had been proposed productivity variation model [2].

As shown in Fig. 2, the model employs a working state, a pausing state. Office worker are assumed to transit these two states with the probabilistic functions based on the variation of BF which is assumed as a brain fatigue

2.2 Problem and Improvement

By using computer simulation based on above two-state model, answering time histogram reflecting short time pauses, which was collected from a subjective experiment, is qualitatively emulated. But second peaks in some histograms as shown in Fig. 3 cannot be emulated.

Aiming to explain second peaks, the authors proposed an improved model. As shown in Fig. 4, the model employs three-state. A pausing state was divided into a short pausing and a long pausing. Short pausing is assumed "Blocking" introduced by Bills [3]. It is insensibility breaks within several seconds. Long pausing is sensibility breaks taking over several seconds. The distribution of time

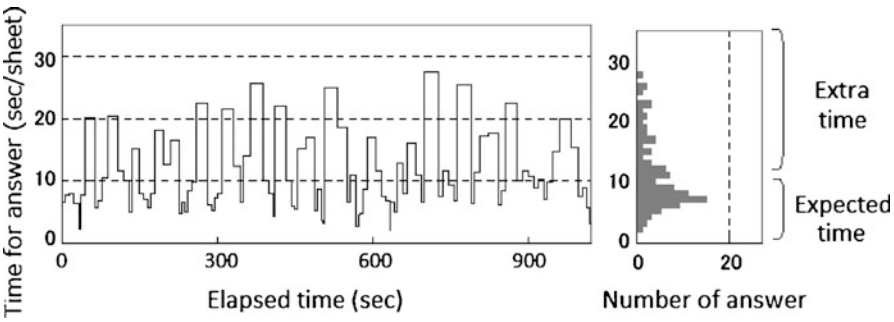

Fig. 1 Time series analysis of productivity variance

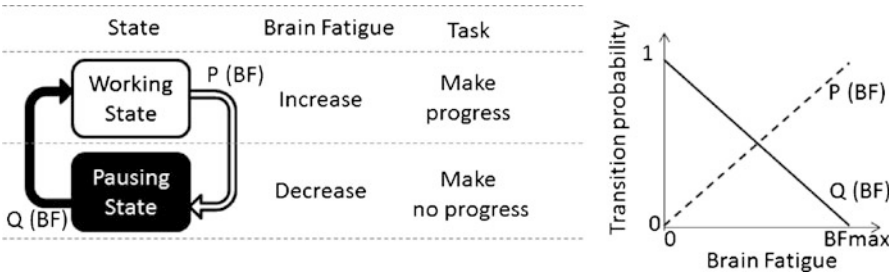

Fig. 2 Framework of the productivity variance model (two-state model)

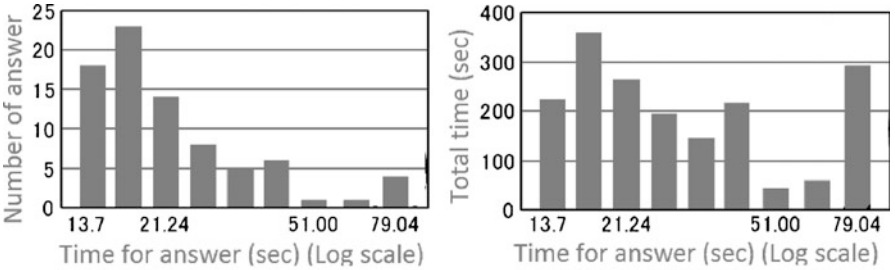

Fig. 3 Framework of the productivity variance model (previous model)

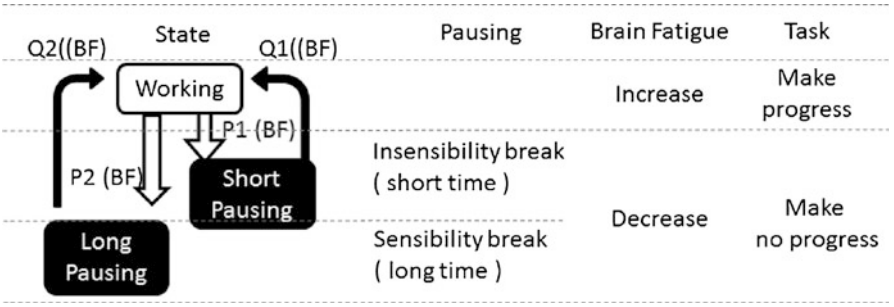

Fig. 4 Framework of the productivity variance model (three-state model)

for answer simulated with three-state model approximated by superposition of two log-normal distributions (1). The parameter μ_1 and σ_1 is the logarithm of the mode value (sec) and dispersion of first peak which reflects answering time without long pausing. The parameter μ_1 and σ_2 is that of second peak which reflects long pausing. The parameter α_1, α_2 represent the proportion of two peaks.

$$f(x) = \frac{1}{\sqrt{2\pi}\sigma_1 x} \exp\left[-\frac{(\ln(x) - \mu_1)^2}{2\sigma_1^2}\right] \times \alpha_1 + \frac{1}{\sqrt{2\pi}\sigma_2 x} \times \exp\left[-\frac{(\ln(x) - \mu_2)^2}{2\sigma_2^2}\right] \times \alpha_2 \quad (1)$$

3 Subjective Experiment

3.1 Method

This experiment was conducted to collect time series variance data of task performance in several conditions. The validity of three-state model was checked with this data by confirming that (1) fits histogram of collected data.

The experiment was conducted from November to December, 2010. Twenty-four subjects (Male: 22, Female: 2, mean age: 26.4) participated for 3 days. The flow of experiment is shown in Fig. 5. Subjects took one-figure additional task and checking slip task for 30 min. The task was settled four times in day. Luminance conditions and work-motivation condition was settled to make productivity variance. High luminance light adjusts circadian rhythm and improves productivity [4]. 2500lx condition is expected to improve productivity. HM is high motivated condition by resuming. LM is low motivated condition.

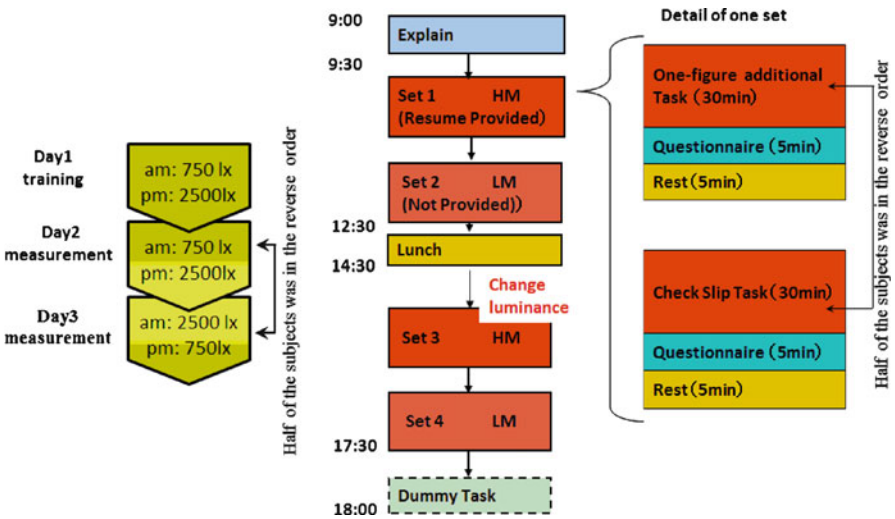

Fig. 5 Flow of the experiment

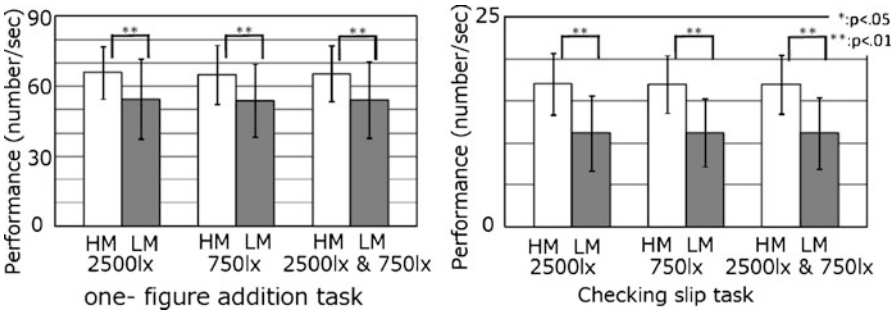

Fig. 6 Results of task performance

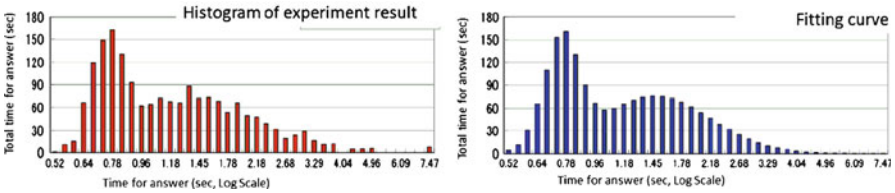

Fig. 7 Example of fitting curve (Addition task, Subject Q, LM, 2500lx, Day 3)

3.2 Result

Figure 6 shows the task performances. The average was compared with paired sample t-test. Performances in high motivated condition was higher than low motivated condition ($p < 0.001$). The luminance conditions made no difference against to expected effects. The reason of failure is thought that the experiment range was shorter for adjusting circadian rhythm.

3.3 Analysis and Discussion

The parameters of fitting curve shown in (1) were derived for each histogram data of experiment result. Parameters, which minimize the square sum of the difference between experimental histogram and fitting curve, were derived with genetic algorithm method was used. The pattern of histogram has some variations, and almost data was qualitatively well fitted. This analysis means that the three-state model have validity. Figure 7 shows an example of the derived fitting curve.

Figure 8 shows the fitting curve of checking slip task. The curve is shown in (1). The x-axis is time for answer and the y-axis is frequency. The parameters of this fitting curve were the average of each subjects' parameters. Each parameter was compared with paired sample t-test in motivation condition. As a result, μ_1 and μ_2 in

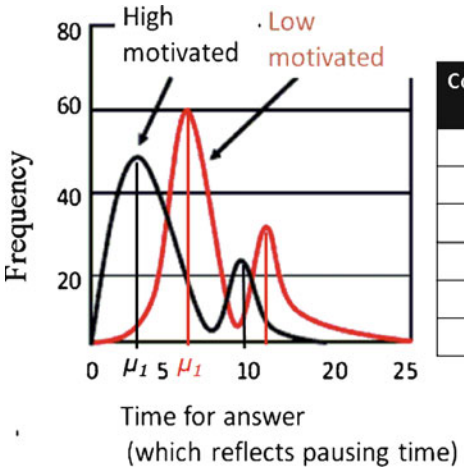

Condition	HM	LM	Significant difference
μ_1	3.24	5.74	P < 0.001
σ_1	5.82	16.69	
a_1	261.2	60.2	P < 0.001
μ_2	1.46	1.84	P < 0.001
σ_2	1.42	1.52	
a_2	38.4	58.6	P < 0.05

Fig. 8 Work motivation condition and fitting curve (checking slip task)

HM condition is shorter than them in LM condition ($p < 0.001$). It means the time range of short pausing and long pausing become shorter in HM condition. α_1 ($p < 0.01$) and α_2 ($p < 0.05$) have significant difference. It means the frequency of first peak in HM condition which reflects short pausing is larger than that of second peak which reflects long pausing. This difference is the reason why the productivity was changed with work motivation condition.

4 Conclusion

For improving productivity variance model, the authors proposed three-state transit model. By considering with an analogy with HEP, the histogram simulated from three-state model which reflects the length of short time pauses was approximated by superposition of two log-normal distributions. The authors conducted subjective experiment in which work motivation and luminance was controlled to make variance in productivity. As a result productivity was improved by high work motivated condition and the histogram data was collected. This histogram was well fitted with approximated equation. It means that the three-state model, the productivity variation was explain by transition of working, short pauses and long pauses state, can explain productivity variance. In the future, it is expected the mechanism of productivity variance is revealed more detail with this model.

Acknowledgement The authors gratefully acknowledge the support by G-COE Program.

References

1. The Agency for Natural Resources and Energy (2011) Energy white paper 2010. http://www.enecho.ineti.go.jp/topics/hakusho/2011/index.htm
2. Miyagi K et al (2011) Proposal of an office work productivity model based on short pauses in mental tasks. HCI International 2011, DVD, Paper no.LNCS 6763
3. Bills AG (1931) Blocking: a new principle of mental fatigue. Am J Psychol 43–2:230–245
4. Enomoto K et al (2008) An experimental study on improvement of office work productivity by circadian rhythm light. WMSCI 2008, Vol 6:121–126

Measures for Nuclear Power Substitution in the Electricity Supply to Kyoto City

Syota Higashikura, Muhammad Ery Wijaya, Jordi Cravioto, Kenzo Ibano, Pramila Tamunaidu, Ryota Kinjo, Im Sul Seo, Jae Hyeong Lee, Kyohei Yoshida, Emi Yamakawa, Yasuo Ose, and Jae Yong Lim

Abstract The earthquake disaster of March 2011 in the Tohoku region has led to concerns on the safety of nuclear power generation in Japan as well as all over the world. Currently, the desire to reduce the dependence on nuclear programs and the will for its substitution seems ubiquitous. The path for substitution of nuclear power, however, is far from being clear, particularly from the standpoint of high energy demand led by our current lifestyles and constraints associated to other power generation technologies. Therefore, we have initiated an evaluation on the reduction of nuclear power in the energy mix to Kyoto city from particular changes in lifestyle (working time and habits) and from the introduction of photovoltaic (PV) systems to local businesses and households. The analysis begins providing a breakdown of electricity consumption in Kyoto city from the demand side followed by estimations for the total number and average area of buildings within the city. Based on these analyses, further estimations on energy reduction from changes in lifestyle, energy production from the introduction of PV systems, and aggregated costs associated to the acquisition of these technologies is done. This study concludes with a brief discussion on the required sources for institutional and financial support to typify a carbon-free, self-reliant, safe urban centre suitable for localities with similar socio-economic profiles in the future.

S. Higashikura • M.E. Wijaya • J. Cravioto • K. Ibano • P. Tamunaidu
R. Kinjo • I.S. Seo • J.H. Lee
Graduate School of Energy Science, Kyoto University, Kyoto, Japan

K. Yoshida
Faculty of Engineering, Institute of Advanced Energy, Kyoto University, Kyoto, Japan

E. Yamakawa • Y. Ose
Graduate School of Engineering, Kyoto University, Kyoto, Japan

J.Y. Lim (✉)
Research Reactor Institute, Kyoto University, Osaka, Japan
e-mail: limjy@rri.kyoto-u.ac.jp

T. Yao (ed.), *Zero-Carbon Energy Kyoto 2011*, Green Energy and Technology,
DOI 10.1007/978-4-431-54067-0_9,

Keywords Energy mix • Kyoto city • Lifestyle change • Nuclear power • Photovoltaic

1 Introduction

The recent disaster of March 2011 in the Tohoku region has led to concerns on the safety of nuclear power generation not only in Japan but all over the world. The desire to reduce energy supply from nuclear power has so drastic calls as, in some cases, to completely stop nuclear programs. However, despite the ubiquitous will, no method for nuclear substitution seems to have a clear future. Although a limited number of countries generate electricity from nuclear energy, among them a majority has high energy demand from either "wealthy" lifestyles or booming economies hardly desirable to be reduced. This fact creates the first constraint for substitution. In addition, the fundamental role nuclear power has in most of the cases: generally used as the base load for the electricity mix represent the second constrain. On the other hand, Nuclear power has the foremost advantage, at least in the utilization stage of the life cycle, to generate electricity without CO_2 emissions; a direct constraint to fossil fuels in terms of environmental impacts. Finally, in economical terms nuclear power represents a competitive way of generation just below fossil fuels, challenging candidates as whether they can represent a viable way in terms of returns of investment and capacity for not jeopardizing costs of production. Any candidate suitable for substitution should take into account these facts. It should provide similar generation stability, comply with environmental benefits, be economically attractive and fit the structure where it is mostly used. This paper aims to provide a two-sector strategy as one candidate for nuclear power substitution in Kyoto city. The context of Kyoto city, highly dependent on tourism and education services, has made this strategy be focused on households and the commercial sector, so measures are proposed under this framework. The strategy consists of changes in the lifestyle of Kyoto households and the introduction of Solar Photovoltaic (PV) modules with batteries.

2 Method

As the first step, the characteristic of households and businesses in Kyoto city and the composition of the regional electricity supply by Kansai Electric Power (KEPCO) is presented. An emphasis is given on how much share from the total electricity supply comes from nuclear power. Following, the business reduction strategy is presented with estimations on selected actions over working habits. Next, the household strategy is detailed with estimations on how much reductions are attained from LED lights substitution and lifestyle change. Lifestyle changes in household consist of reducing the use of air conditioning, refrigerator and interior

lights, and setting the television to energy saving mode. Finally, based on the daily load by nuclear power and the generation at peak during sunny and cloudy days, the number of PV modules, batteries and their cost is estimated.

3 Results

3.1 Database

From Kyoto city's households and businesses, more than 60% of the area is taken by private houses and shops. This fact evidence how important in terms of infrastructure the commercial and residential sectors are for Kyoto city. Detailed data regarding the total number of buildings and their current use has been obtained from national statistics [1] and is summarised in Table 1. Figures for energy consumption on daily basis for households and businesses are presented in Table 2.

The composition of the regional electricity supply taken from the Kansai Electric Power Company (KEPCO) [3] is shown in Table 3. Nuclear power generation is the largest share, with over 42% from the total supply.

3.2 Commercial Sector Strategy

3.2.1 Change in Working Habits

All buildings related to commercial activities have been classified into two groups: group 1 covering shop, supermarkets, restaurants and offices, and group 2 including only factories. Actions for energy reduction are summarized in Table 4 with their respective reduction rate using data [4] from 2009. The total reduction achievement would be equivalent to 10.6% of the total energy consumption (628,350 MWh from the current 703,104 MWh).

3.3 Household Strategy

3.3.1 Introduction of LED Lights

Assuming that the luminous efficiency of one LED bulb is currently 100 lm/W, but could potentially become 150 lm/W in the near future [5], just by replacing household lights with LED lights a total reduction of 110,992 MWh and 236,957 MWh could respectively be achieved.

Table 1 Total number and area of buildings in Kyoto City, 2009 [1]

Building	Total	Area (m^2)
Houses	598,731	54,960,407
Shops	32,824	11,172,297
Factories	20,381	4,726,506
Storehouses	16,621	3,001,516
Very small buildings	48,069	2,105,338
Temples, and public facilities	14,320	9,622,190
Others	81,691	4,102,653
Total	750,248	77,963,379

Table 2 Consumption of electric energy in Kyoto city, 2009 [2]

Sector	MWh
Household	5,435,747
Commercial	703,104

Table 3 Total electric energy supply by KEPCO, 2009 [3]

Generation	GWh	%
Hydroelectric	14,020	9.1%
Thermal	42,879	27.7%
Nuclear	65,894	42.6%
New technologies	96	0.1%
Other companies	29,040	18.8%
Other companies	4,778	3.1%
From pumped-storage	−2,065	−1.3%
Total electric power	154,642	

Table 4 Working habits reduction

Measure	Shop	Supermarket	Restaurant	Office	Factory
Cut the illumination lamp by 50% in the room/outside	13	11	40	13	
Cover the outside equipment of air conditioner with blind	10	10	10	10	10
Maintain the room temperature at 28°C	4 (+2°C)	1 (+2°C)	8 (+2°C)	4 (+2°C)	6 (+2°C)
Limit the number of refrigerator. Cut the illumination lamps in each refrigerator	1	5	3		
Total	28	27	61	28	16
Average	38.5% (shop, supermarket, restaurant, office)				16%

Table 5 Lifestyle change reductions

Appliance	Energy consumption (%)	Savings	Energy savings potential
Air conditioner	24.7	0.1	2.47
Refrigerator	16.1	0.02	0.322
Illuminator	15.8	0.05	0.79
TV	9.6	0.02	0.192
Other	33.8		
Total	100	0.19	−3.8

Table 6 PV considerations

Concept	Value
Manufacturer	Mitsubishi electric
Model	PV-MDT 200 HB
Price	134,400 yen
Maximum power	200 W
Size	1657×858×46 mm

Since the current electric power consumption for household illumination in Kyoto city is about 493,903 MWh and it accounts for 9.1% of total household power, a reduction of 2% using the current efficiency and 4.4% using the future one could be achieved from the total household power consumption.

3.3.2 Lifestyle Change

Based on average measured reductions from [6], the lifestyle change impacts are summarized as follows: Savings from air conditioning set to a cooling temperature of 28 C (−10%); refrigerator set to middle cooling power (−2%); turning off lights when not used (−5%); and turning TV screen to save energy mode (−2%). Based on the breakdown of current energy consumption from related appliances shown in Table 5 [7], the total energy potential saved in the household would be −3.8%.

3.4 PV Introduction

From the total nuclear energy supply of 65,894 GWh per year to Kyoto city, a daily nuclear power supply of 6,615 MWh is obtained. Assuming that the supplied to Kyoto city is a base load between 100 and 180 MW in the hour, the patter of generation during the day is obtained.

PV modules can supply 200 W [8] at peak generation time which has been estimated to be between 11:30 am and 12:30 pm. Each module has an average area of 1.42 m^2 and an approximate cost of 134,400 yen per module. The cost of each battery for the module is approximately 25,000 yen [9]. Table 6 summarizes these considerations.

Table 7 Generation considerations

Hour	Percentage of generation
8:30–9:30	25
9:30–10:30	62.5
10:30–11:30	87.5
11:30–12:30	100
12:30–13:30	87.5
13:30–14:30	62.5
14:30–15:30	25

If we consider the pattern of generation in Table 7 and the reductions attained in the previous sections, Kyoto city would need a range of approximately 7,350,320–32,459,066 panels that would cost from 0.9 to 1.6 trillion yen, and would need batteries with an approximate cost of 0.11–0.12 trillion yen.

The cost despite being reachable remains high compared to nuclear energy use from the grid, however if the number of benefits are taken into account it may end in a favourable balance. Among the benefits identified there is a direct reduction of safety risks for those regions that generate nuclear power in the vicinity of Kyoto prefecture, an increase of energy security of Kyoto city residents by producing the own supply within their region, a potential boost for innovation by manufacturers in the renewable industry from the investments on the equipment, an expansion of jobs, experience and economical activities within the sector related to services, maintenance and provision of renewable equipments and technical and human assets if proper governmental programs are aimed to involve stakeholders such as universities, research centres or industry.

4 Conclusions

To substitute nuclear energy supply to Kyoto city, households would need to adopt the following changes in lifestyle: Savings from air conditioning set to a cooling temperature of 28°C; refrigerator set to middle cooling power; turning off lights when not used; and turning TV screen to save energy mode. Furthermore, they would have to invest 1.69–2.87 million yen/house to acquire a solar system coupled with a battery in order to increase the current 96 GWh of renewable energy to 2,410 GWh. This joint efford would mean a total increase of 7.4 million modules used in the city.

Acknowledgement The authors were grateful for the support of the Ministry of Education, Culture, Sports, Science and Technology of Japan via “Energy Science in the Age of Global Warming” of Global Center of Excellence (G-COE) program (J-051).

References

1. Kyoto City (2011) Zyutaku Tochi Tokei Cyosa (in Japanese), Statistics Kyoto city. http://www.city.kyoto.jp/sogo/toukei/Population/Housing/index.html (accessed Jul 7th, 2011)
2. Kyoto City (2011) Kokusei Cyosa (in Japanese), Statistics Kyoto city. http://www.city.kyoto.jp/sogo/toukei/Population/Census/index.html (accessed Jul 7th, 2011)
3. The Federation of Electric Power Companies (2011) Denryoku Tokei Zyoho (in Japanese). http://www.fepc.or.jp/library/data/tokei/index.html (accessed Jun 4th, 2011)
4. Tohoku Economic Federation (2011) Kaki setuden Taisaku no Gutairei (in Japanese). http://www.tokeiren.or.jp/news/pdf/1308646329-setuden-0621.pdf (accessed Aug 6th, 2011)
5. Research Institute of Environment, Agriculture and Fisheries, Osaka Prefectural Government (2004) Report on Osakafu LED Syomei Kiki Kaihatsu Suishin Keikaku Sakutei Zigyo (in Japanese). http://www.epcc.pref.osaka.jp/center/etech/led/in/report/01-18.pdf (accessed Aug 7th, 2011)
6. Kansai Electric Power (2011) Gokatei ni okeru Setsuden no Onegai (in Japanese). http://www.kepco.co.jp/home/setsuden/images/setsuden.pdf (accessed Aug 7th, 2011)
7. Iwafune, Yumiko (2001) Kurashi no nakano Enerugii (in Japanese), pp 8–9, Ohm-sya
8. Mitsubishi Electric Corporation (2011) Solar Cell Module. Accessed (in Japanese), http://www.mitsubishielectric.co.jp/service/taiyo/jutaku/product/module (accessed Aug 8th, 2011)
9. Ministry of Economy, Trade and Industry (2006) Technology Development Roadmap, http://www.meti.go.jp/english/newtopics/data/pdf/CE_RoadMap.pdf (accessed Aug 8th, 2011)

Part II
Renewable Energy Research and CO_2 Reduction Research

(i)
Invited Paper

Electrospun Metal Oxides for Energy Applications

Seeram Ramakrishna and Shengjie Peng

Abstract Nanotechnology is now providing new solutions and opportunities to ensure sustainable energy for the future. Due to their special shapes, compositions, chemical and physical properties, metal oxide nanomaterials are the focus of current research efforts in nanotechnology. One-dimentional (1D) nanostructures, such as nanofibers, nanorods, and nanotubes, have attracted significant attention, due to the interesting confinement effects and the structure-related properties. In particular, metal oxides with 1D nanostructures are considered to be promising candidates in the applications of energy conversion and storage devices, because of their high surface areas, porosities, and fast charge transport. Such 1D metal oxides can be fabricated by many techniques, including top-down synthesis and bottom-up synthesis. Among them, electrospinning is a particular simple, inexpensive technique, which allows fabrication of metal oxides and advanced functional materials on a large scale. The solar cells and lithium-ion (Li-ion) batteries based on the electrospun metal oxide nanofibers demonstrate higher photoelectric conversion efficiency, and show higher reversible capacity and electrochemical stability, respectively. This paper consists of two main sections categorized by the electrospun fabrication of metal oxides and their energy applications. After a brief description of the electrospinning process of metal oxides, we choose to focus on their major energy applications, including solar cells, Li-ion batteries, supercapacitors, and fuel cells. In addition, electrospun nanofibers used as piezoelectric and thermoelectric materials are also discussed. Finally, we conclude this review with some personal perspectives on their future research and developments.

Keywords Batteries • Electrospinning • Metal oxides • Nanofibers • Solar cells

S. Ramakrishna (✉) • S. Peng
National University of Singapore, Singapore, Singapore
e-mail: seeram@nus.edu.sg

T. Yao (ed.), *Zero-Carbon Energy Kyoto 2011*, Green Energy and Technology,
DOI 10.1007/978-4-431-54067-0_10,

1 Introduction

Energy is one of the most important global issues facing society in the Twenty-first century. Natural energy resources such as crude oil, coal, natural gas, and uranium are a vial factor for everyday life. Rapid economic growth demands more energy, which means that the rate of oil production is no longer adequate, as the reserve of fossil fuel and our ability to exploit it is not infinite. Furthermore, the processing of the fossil fuel leads to the water and environmental pollutions, which have been estimated to contribute to the global warming. In light of the rising energy demand and depleting natural energy sources, energy storage and conversion with high efficiency and cleanliness have a great effect on the sustainable development of world economics and ecology. At present, the promising clean alternative energy devices are solar cells, Li-ion batteries, supercapacitors, and fuel cells. Our primary source of clean abundant energy is the Sun. When the Sun irradiates the Earth in 1 h, the obtained energy can meet all the energy consumed on the planet in a year. Therefore, conversion of this tremendous energy into electrical power is a science and technology issue facing scientists and engineers for a long time. In addition, both primary and rechargeable batteries, which can generate clean electric energy from the stored chemical energy and convert reversely chemical energy into electric energy, are essential to the convenience and sustainability of human development in the modern mobile society. Therefore, scientists are working to control the shapes, sizes, and structures of nanomaterials because of the strong correlation between these parameters and physical/chemical properties.

Metal oxides possess a broad range of electronic, chemical, and physical properties that are often highly sensitive to changes in their chemical environment. Because of these properties, metal oxides have been widely studied, and most commercial applications are based on appropriately structured and doped oxides. In comparison with the quantum dots and wells, metal oxide nanofibers have many advantages [1]. First, as the diameter puts the radial dimension of these structures at or below the characteristic length scale of various interesting and fundamental solid state phenomena: the exciton Bohr radius, wavelength of light, phonon mean free path, critical size of magnetic domains and exciton diffusion length, many chemical and physical properties of semiconductors are significantly altered within the confines of the nanofiber surfaces. Second, their large surface-to-volume ratio allows for distinct structural and chemical behavior as well as greater chemical reactivity, which makes endow nanofibers with unique properties, and stray from those of their corresponding bulk materials. Third, the one unconstrained dimension can direct the conduction of quantum particles such as electrons, phonons, and photons. This control over various forms of energy transport recommends metal oxide nanofibers as ideal materials from which to manufacture advanced energy devices, such as dye-sensitized solar cells, hybrid solar cells, Li-ion batteries, and so on. Though nanofiberous metal oxides can be fabricated by many methods, including crystal structure governed nucleation in solution, non-metal seeded gas-phase growth, metal-promoted vapour growth, metal-assisted growth in liquids,

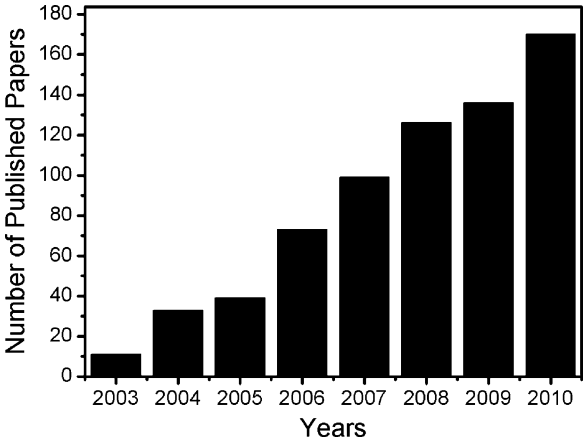

Fig. 1 The number of the papers published on the subject of the electrospun oxides

template synthesis of nanofibers/nanotubes, electrospinning and top-down approach/chemical etching, electrospinning has become more popular because of its easiness and low cost [2, 3]. Electrospinning can lead to a potential large-scale production of 1D nanofibers of micrometer to nanometer size in diameter, and especially the rapid development of electrospun oxides is reflected by the increase number of papers (Fig. 1). Therefore, the focus of this paper is mainly on electrospun metal oxides and their energy applications.

2 Principle of Electrospinning

Electrospinning is a unique approach by using a strong electric field to polymer solutions or melts and the fibers with different diameters are obtained. A schematic of the fabrication of metal oxide by combining electrospinning and annealing is shown in Fig. 2 [4]. In a typical electrospinning process of metal oxides, a syringe is filled with polymeric solution blended with respective metal ions. Then a high voltage is applied between the syringe nozzle and the voltage. When the applied electric field overcomes surface tension of the liquid, a continuous jet is ejected which upon subsequent solvent evaporation and bending produces nanofibers on a collector surface. Finally, annealing such polymeric fibers at desired temperatures would produce the nanofibrous inorganic solids, which could then be developed in various morphologies such as nanorods and nanofibers. However, the fabrication of nanofibers with fine structures requires careful consideration of many operating parameters, including selecting different polymers and tuning the electrospinning parameters such as polymer molecular weight, polymer concentration, applied voltage, and humidity. Recently, various metal oxides have been fabricated, such as TiO_2, SnO_2, Nb_2O_5, et al [5–7]. Especially, the electrospinning set up with

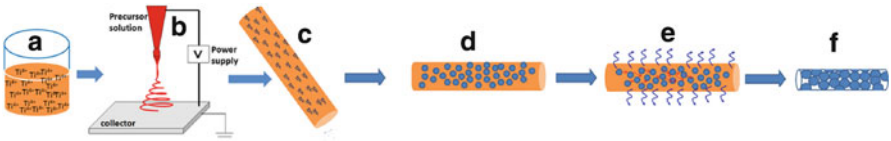

Fig. 2 Schematic illustration of the process to develop metal oxide nanofibers, TiO_2 as a typical example. precursor solution where the ions are dispersed (**a**); electrospinning apparatus and procedure (**b**); a composite fiber in which titanium ions are dispersed (**c**); heating the nanofiber at a critical temperature (**d**); crystals grow from the available monomers, grains undergo a directional mass transport with simultaneous evaporation of polymers (**e**); and ultimately forms pure inorganic nanofibers (**f**)

improvement of rotating disc or cylinder collectors or introduction of insulators can produce aligned nanofibers. Also, core-shell nanofibers can be fabricated by co-electrospinning two different polymer solutions through a spinneret comprising two coaxial capillaries.

3 Energy Applications

3.1 Solar Cells

Since invented by Grätzel in 1991, dye-sensitized solar cells (DSCs), as one of the low-cost photovoltaic devices due to the less fabrication cost and less expensive raw materials, have received a great deal of attention [8]. In general, DSCs are made up of TiO_2 photoanode, Ru-based dyes, electrolyte containing a redox couple and Pt photocathode. Figure 3 is a schematic illustration of DSCs based on TiO_2 nanoparticles and nanofibers. In DSCs, the charge transport through TiO_2 nanoparticles and the amount of dye adsorption are critical factors to the power conversion efficiency of DSCs. In conventional DSCs, TiO_2 nanoparticles can absorb a lot of dye molecules and provide photogenerated electrons. However, these electrons can also be trapped at the surface states on the TiO_2 nanoparticles, and further slow down the electron transport. The use of electrospun TiO_2 nanofibers allows the formation of a direct conduction path for the photogenerated carriers to the substrates, which ensures that the mobility of the electrons in the nanofiber-based solar cells is much higher than that of the nanoparticle-based solar cells. Also it can offer higher specific surface areas and bigger pore sizes than those of nanoparticles. By selecting the appropriate polymers, TiO_2 nanofibers with a high surface area can be fabricated by electrospinning. Kim and coworkers employed high-molecular weight polyvinyl acetate to induce phase separation, resulting in the formation of TiO_2 nanorods of size 15–30 nm within 60 nm diameter sintered nanofibers with a specific surface area of 123 $m^2\ g^{-1}$ (Fig. 4) [9]. The resultant dye loading (8.59×10^{-8} mol mg^{-1}) was 2.5 times greater than that from TiO_2 nanoparticles

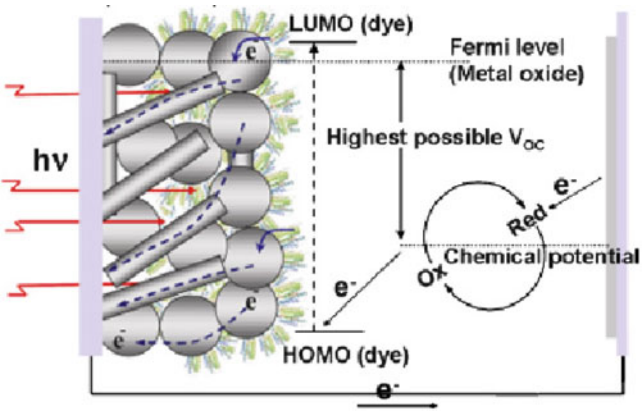

Fig. 3 Schematic of a dye-sensitized solar cell based on TiO_2 nanoparticles and nanofibers

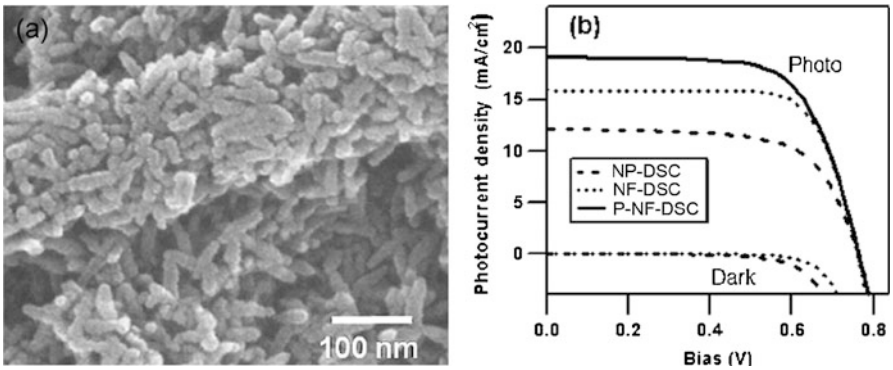

Fig. 4 SEM image (**a**) of electrospun TiO_2 nanofibers, and photocurrent density-voltage curves (**b**) of nanoparticle-DSC, nanofiber-DSC, and nanoparticle-nanofiber-DSC under simulated AM 1.5G light

(3.44×10^{-8} mol mg^{-1}) and yielded efficiency of 9% similar to the highest efficiency of the TiO_2 nanoparticle-based solar cells. Recently, our group has reported uniformly distributed rice grain-shaped TiO_2 mesostructures by electrospinning. Due to a high surface area (60 m^2 g^{-1}), single crystalline nature of the particles, and particularly low rutile nucleation temperature in the anatase matrix, preliminary results showed that the photoelectrodes fabricated by direct electrospinning TiO_2 rice grains onto fluorine-doped tin oxide (FTO) plates showed good photovoltaic parameters [5]. It is known that the capability of the photoanode to harvest light would be increased and hence the efficiency, by using an additional scattering layer. However, normal scattering layer made of large particles will unavoidably decrease the total surface area of the electrode, which in turn will decrease the dye-loading. The rice grain-shaped TiO_2 can also be used as a scattering layer, which were directly electrospun on a layer of screen-printing TiO_2

nanoparticle film. The advantages of using rice grain-shaped nanostructures as a scattering layer in DSCs not only enhanced the light scattering but also shorten the electron transport pathways and enhanced suppression of the recombination with the reduced grain boundaries, which further showed a 15.7% increase in the overall efficiency compared to the DSCs based on the electrospun nanofibers as the scattering layer [10]. In addition to randomly oriented nanofibers, TiO_2 nanofibers can be fabricated in an aligned orientation. By using the rotating disc, aligned nanofiberous TiO_2 with a thickness of 25 mm and area of 60 cm $\times$ 2 cm were electrospun onto the FTO substrate, which were first demonstrated an efficiency of 2.87% [11]. This approach could be a better alternative to the currently available methods like hydrothermal synthesis and template assisted fabrication as the diameter, height of the wires, and spacing between the wires can be effectively controlled by this method.

Hybrid materials such as inorganic-polymer composites or encapsulated functional materials have shown promise in achieving the higher performance of energy and electronic devices. Using electrospun mesoporous TiO_2 nanofibers with a high surface area of 112 $m^2\ g^{-1}$ as the photoelectrode, solid-state dye-sensitized solar cells (SDSCs) have been fabricated employing D131 as the sensitizer and P3HT as the hole transporting material to yield an energy conversion efficiency of 1.82% (Fig. 5) [12]. Compared to regular nanofiber-based devices fabricated under the same condition, incident photon-to-current conversion efficiency (IPCE) and dye-desorption test demonstrated that the increase in current density was mainly due to the greatly improved dye adsorption for mesoporous nanofibers as compared to that for regular nanofibers. Considering the simple and cost-effective features of electrospinning technique, the mesoporous TiO_2 nanofibers synthesized in this work are promising to serve as the photoelectrodes for low-cost SDSCs.

Quantum dot-based solar cells have drawn a lot of attention during past few years because of the possibility of boosting the energy conversion efficiency beyond the traditional Shockley and Queisser limit of 32% for Si-based solar cells. Nanofibers have been found to be effective in developing quantum dot-sensitized solar devices as they can facilitate unidirectional electrical transport. Kang's group described the first attempt to employ CdS and CdSe quantum dots as sensitizers onto electrospun TiO_2 nanofibrous (diameter ~80–100 nm) electrodes [13]. By coupling (CdS:CdSe) two quantum dots as the sensitizer, the obtained solar cell demonstrated 2.69% efficiency, indicating the versatility of fibrous electrodes in quantum dot-sensitized solar cell applications.

3.2 Li-Ion Batteries

Li-ion batteries become one of the most promising power storage devices with high energy density and high discharge voltage for electric vehicles and power tools. The most popular anode material in commercially available Li-ion batteries is carbon. Recently, metal oxides have showed high theoretical capacity and stable

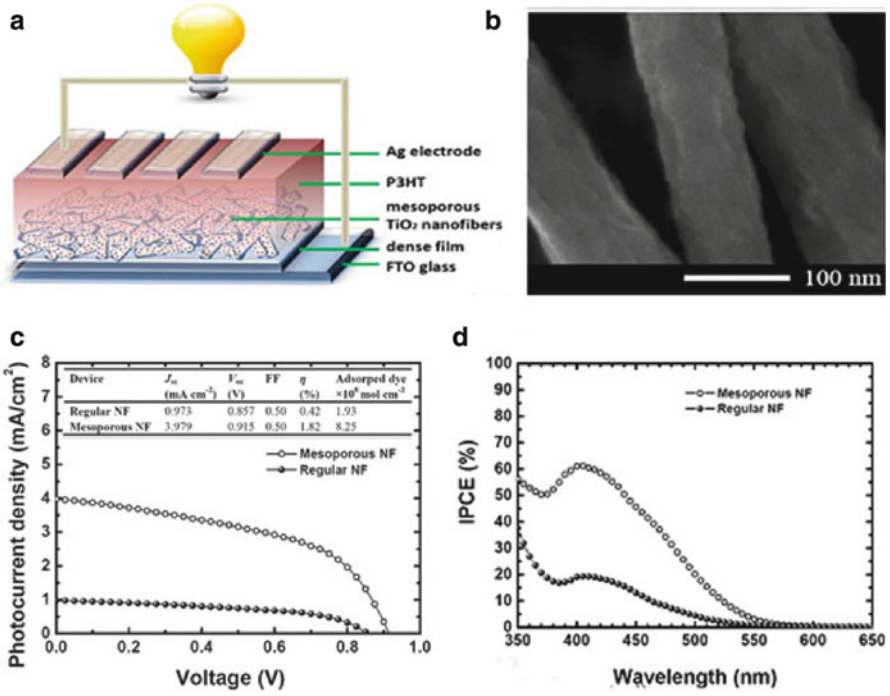

Fig. 5 The configuration (**a**) of a typical device employing mesoporous TiO_2 nanofibers as the photoelectrode, D131 as the sensitizer and P3HT as the hole transporting material, SEM image of electrospun TiO_2 (**b**), typical photocurrent density-voltage curves (**c**) and IPCE spectra (**d**) of SDSCs based on mesoporous and regular nanofiber photoelectrodes

cycling performance. Mai's group reported ultralong hierarchical vanadium oxide nanofibers with diameter of 100–200 nm and length up to several millimeters by employing electrospinning combined with annealing and their electrochemical performance (Fig. 6) [14]. The initial and 50th discharge capacities of the ultralong hierarchical vanadium oxide nanowire cathodes were up to 390 and 201 mAh g^{-1} when the Li-ion battery cycled between 1.75 and 4.0 V. Compared with self-aggregated short nanorods synthesized by a hydrothermal method, the ultralong hierarchical vanadium oxide nanofibers exhibited much higher capacity. This was due to the fact that self-aggregation of the unique nanorod-in-nanowire structures has been greatly reduced because of the attachment of nanorods in the ultralong nanofibers, which could keep the effective contact areas of active materials, conductive additives, and electrolyte large and fully realize the advantage f nanomaterial-based cathodes. This demonstrated that ultralong hierarchical vanadium oxide nanowire was one of the most favorable nanostructures as cathodes for improving cycling performance of lithium ion batteries. Our group has electrospun TiO_2 and Nb_2O_5 nanofibers and investigated their applications in Li-ion batteries [15]. Electrochemical cycling results revealed that the TiO_2 nanofibers had lower

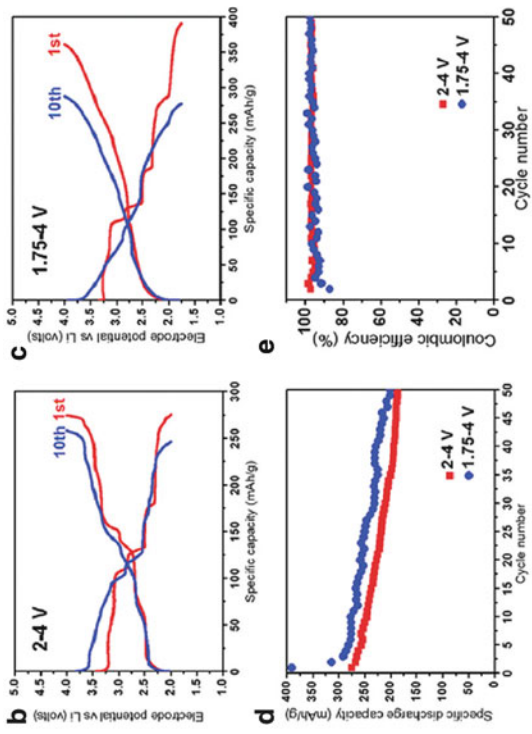

Fig. 6 Schematic illustration (**a**) of formation of the ultralong hierarchical vanadium oxide nanofibers during annealing; charge/discharge curves of hierarchical vanadium oxide nanofibers at voltages of 2–4 and 1.75–4 V, respectively (**b**, **c**); capacity vs cycle number, and Coulombic efficiency vs cycle number of the ultralong hierarchical vanadium oxide nanofibers (**d**, **e**)

capacity fading compared to that of the nanoparticles. The capacity fading for 2–50 cycles was 23% for nanofibers, which was nearly one-third of that of corresponding nanoparticles (63%). It was found that monoclinic Nb_2O_5 adopted a distorted nugget structure after calcination treatment, which exhibited the highest capacity and better capacity retention compared to the other phases. And it could be a choice of the cathode material for 2 V due to the commercial viability of the electrospinning process and characteristics of the batteries developed herewith.

3.3 Supercapacitors

Supercapacitors or electrochemical double layer capacitors, which store energy electrostatically by reversible adsorption of ions in an electrolyte onto electrodes, have gained considerable attention as an energy storage device due to their high energy density compared to the common electrolytic capacitors. The capacitance, as a key parameter of supercapacitors, depends on the surface area accessible to electrolyte ions, i.e., the pore size and porosity. For a material to be useful as a pseudocapacitor, it should have several oxidation states, high electrical conductivity, and electrochemical stability. Currently, commercial supercapacitors use porous carbon as electrodes, and porous carbon materials have been intensively studied. Also, RuO_2 is an attractive material for use in supercapacitor electrodes. As Ru is expensive, depositing thin film RuO_2 on supporting materials is an effective way to lower cost. Kim's group reported that the electrospun TiO_2 substrate was electrodeposited by aqueous ruthenium chloride solution [16]. Heat treatment of the TiO_2 substrate enhanced the electrical conductivity, hence substantially improved the response time of the RuO_2 electrode. The RuO_2 electrode deposited on heat-treated TiO_2 maintained a high capacitance, with only a 33% decrease at a fast scan rate of 1,000 mV s^{-1} with respect to the value at 10 mV s^{-1}. Further, the use of the heat-treated TiO_2 enhanced the capacitance and the charge–discharge rate by a factor of more than 20 over that of the pristine TiO_2. These results demonstrated the remarkable supercapacitor performance of RuO_2 electrodes deposited on the heat-treated TiO_2 at very fast scan rates and high current densities.

3.4 Fuel Cells

Fuel cells are devices where electrochemical oxidation of hydrogen or hydrogen-rich fuel is converted in the presence of a metal catalyst into electric current. Among different kinds of fuel cells, the direct methanol fuel cells (DMFCs) have been widely studied because they possess optional high energy density and can be operated at room temperature. In DMFCs, supporting materials are necessary to load Pt catalyst or its alloy. To achieve the uniform Pt dispersion, porous nanomaterials with larger surface areas are used as electrode materials. Through

the electrospinning technique, many continuous and porous nanofibers have been fabricated and used as good candidates for catalyst supports. Xia's group dispersed Pt nanoparticles on electrospun anatase TiO_2 nanofibers. They then studied the effects of both the coverage and morphology of the Pt nanostructures on the methanol oxidation reaction [17]. It was found that the nanofibers with a submonolayer of Pt nanoparticles displayed improved catalytic durability over commercial Pt/C as determined by chronoamperometry owing to a synergistic effect of the underlying anatase surface and the Pt nanostructures with well-defined facets.

3.5 Piezoelectric and Thermoelectric Devices

Piezoelectricity is the ability of some materials to convert electrical energy to mechanical and vice versa. Electrospun nanofibers can offer excellent flexibility and improved strength, so they are expected to be utilized in a wide variety of applications. The most common used material is lead zirconate titanate ($PbZr_{1-x}Ti_xO_3$, PZT). Kim's group electrospun PZT nanofibers and controlled the diameter ranging from 52 to 150 nm by varying the concentration of the polymer in the precursor [18]. The elastic modulus of an individual electrospun PZT nanofiber was 42.99 GPa, which was smaller than that of a thin-film PZT, due to the smaller grain size and fiber diameter. In addition, we reported a giant reversible piezoelectric strain of 4.2% achieved with single-crystalline $PbZr_{0.2}Ti_{0.8}O_3$ nanofibers of 70 nm in diameter, which was nearly 300% greater than the nominal values reported for ceramic perovskite single crystals [19].

Similar to piezoelectric materials, thermoelectric materials convert a potentially ambient source of energy to electricity. Electrospinning has played a role in developing new thermoelectric materials. Bulk calcium cobalt oxide ($Ca_3Co_4O_9$) is regarded as a competitive thermoelectric material due to the structural complexities associated with a layered structure. Li's group developed a novel technique for the process of nanocrystalline $Ca_3Co_4O_9$ ceramics [20]. Compared with La-doped $Ca_3Co_4O_9$ ceramics synthesized with solid state reaction and spark plasma sintering recently reported, these nanofiber-sintered $Ca_3Co_4O_9$ ceramics without doping substantially reduced thermal conductivity, resulting in 55% enhancement in the thermoelectric figure of merit ZT that was estimated to be around 0.40 at 975 K.

4 Conclusions

Electrospun metal oxides thus form very attractive materials in the field of clean energy such as solar cells, Li-ion batteries, supercapacitors, and fuel cells, due to their high surface area to volume. Current progress reveals that electrospinning

technology will likely play an important role in the development of new clean energy technologies. However, there are technical and theoretical issues. Though electrospinning has become an essential technique for generating 1D nanostructures, the research exploration is still young, but promising, in energy applications. One of the drawbacks of electrospinning is that, it has been difficult to obtain uniform nanofibers with diameters below 50 nm using electrospinning. Another drawback is the relatively low production rate. For future research, it requires electrospinning research communities around the world to study of the theoretical modeling of the electrospinning process, which can help to control uniform nanofibers with diameters below 50 nm. Then the roles of the nanofibers in the energy devices need dedicated and interdisciplinary research to ensure the wide energy application of electrospun metal oxides.

Acknowledgments This work was supported by Singapore NRF-CRP grant on "Nanonets for harnessing solar energy and storage".

References

1. Dong ZX, Kennedy SJ, Wu YQ (2011) Electrospinning materials for energy-related applications and devices. J Power Sourc 196:4886–4904
2. Barth S, Hernandez-Ramirez F, Holmes JD, Romano-Rodriguez A (2010) Synthesis and applications of one-dimensional semiconductors. Prog Mater Sci 55:563–627
3. Huang ZM, Zhang YZ, Kotaki M, Ramakrishna S (2003) A review on polymer nanofibers by electrospinning and their applications in nanocomposites. Compos Sci Technol 63:2223–2253
4. Thavasi V, Singh G, Ramakrishna S (2008) Electrospun nanofibers in energy and environmental applications. Energ Environ Sci 1:205–221
5. Nair AS, Yang SY, Zhu PN, Ramakrishna S (2010) Rice grain-shaped TiO_2 mesostructures by electrospinning for dye-sensitized solar cells. Chem Commun 46:7421–7423
6. Wu JJ, Chen YR, Liao WP, Wu CT, Chen CY (2010) Construction of nanocrystalline film on nanowire array via swelling electrospun polyvinylpyrrolidone-hosted nanofibers for use in dye-sensitized solar cells. ACS Nano 4:5679–5684
7. Viet AL, Jose R, Reddy MV, Chowdari BVR, Ramakrishna S (2010) Nb_2O_5 photoelectrodes for dye-sensitized solar cells: choice of the polymorph. J Phys Chem C 114:21795–21800
8. O'Regan B, Grätzel M (1991) A low-cost, high-efficiency solar cell based on dye-sensitized colloidal TiO_2 films. Nature 353:737–740
9. Lee BH, Song MY, Jang SY, Jo SM, Kwak SY, Kim DY (2009) Charge Transport characteristics of high efficiency dye-sensitized solar cells based on electrospun TiO_2 nanorod photoelectrodes. J Phys Chem C 113:21453–21457
10. Zhu PN, Nair AS, Yang SY, Peng SJ, Ramakrishna S (2011) Which is a superior scattering layer material for dye-sensitized solar cells, electrospun rice grain- or nanofiber-shaped TiO_2? J Mater Chem. 21:12210–12212
11. Krishnamoorthy T, Thavasi V, Mhaisalkar SG, Ramakrishna S (2011) A first report on the fabrication of vertically aligned anatase TiO_2 nanofibers by electrospinning: preferred architecture for nanostructured solar cells. Energ Environ Sci. 4:2807–2812
12. Zhang W, Zhu R, Ke L, Liu XZ, Liu B, Ramakrishna S (2010) Anatas mesoporous TiO_2 nanofibers with high surface area for solid-state dye-sensitized sola cells. Small 6:2176–2182

13. Sudhagar P, Jung JH, Park S, Lee YG, Sathyamoorthy R, Kang YS, Ahn H (2009) The performance of coupled (CdS:CdSe) quantum dot-sensitized TiO_2 nanofibrous solar cells. Electrochem Commun 11:2220–2224
14. Mai LQ, Xu L, Han CH, Xu X, Luo YZ, Zhao SY, Zhao YL (2010) Electrospun ultralong hierarchical vanadium oxide nanofibers with high performance for lithium ion batteries. Nano Lett 10:4750–4755
15. Reddy MV, Jose R, Teng TH, Chowdari BVR, Ramakrishna S (2010) Preparation and electrochemical studies of electrospun TiO_2 nanofibers and molten salt method nanoparticles. Electrochim Acta 55:3109–3117
16. Ahn YR, Park CR, Jo SM, Kim DY (2007) Enhanced charge–discharge characteristics of RuO_2 supercapacitors on heat-treated TiO_2 nanorods. Appl Phys Lett 90:122106-1–122106-3
17. Formo E, Peng ZM, Lee E, Lu XM, Yang H, Xia YN (2008) Direct oxidation of methanol on Pt nanostructures supported on electrospun nanofibers of anatase. J Phys Chem C 112:9970–9975
18. Xu SY, Shi Y, Kim SG (2006) Fabrication and mechanical property of nano piezoelectric fibres. Nanotechnology 17:4497–4501
19. Zhou ZH, Gao XS, Wang J, Fujihara K, Ramakrishna S, Nagarajan V (2007) Giant strain in $PbZr_{0.2}Ti_{0.8}O_3$ nanofibers. Appl Phys Lett 90:052902-1–052902-3
20. Yin TF, Liu DW, Ou Y, Ma FY, Xie SH, Li JF, Li JY (2010) Nanocrystalline thermoelectric $Ca_3Co_4O_9$ ceramics by sol gel based electrospinning and spark plasma sintering. J Phys Chem C 114:10061–10065

(ii)

Contributed Papers

Microwave Material Processing for Distributed Energy System

Taro Sonobe, Kan Hachiya, Tomohiko Mitani, Naoki Shinohara, and Hideaki Ohgaki

Abstract Microwave material processing is attracting interest as a green technology for conserving energy and improving efficiency in conventional industrial processes for mitigating CO_2 emissions. Because of various advantages over conventional methods, such as rapid and selective heating, as well its ability to provide internal heating of substances, microwave heating can reduce the time and lower the temperature necessary for material processing. Recently, we have proposed the material refinery and processing through microwave heating techniques. Microwave is one of the direct forms to transfer the electric energy into the substance to activate the chemical reaction and generate a heat without any heating media. In addition, microwave processing is rather specialized in short time process (hour) and small scale and distributed (m^3). Therefore, it is expected to achieve a good combination with the distributed renewable energy power generation, such solar cell, wind energy, and small hydro systems, for right material for right land.

Keywords Efficiency • Microwave processing • Microwave solid state physics

1 Introduction

Microwave material processing is attracting interest as a green technology for conserving energy and improving efficiency in conventional industrial processes for mitigating CO_2 emissions. Because of various advantages over conventional

T. Sonobe (✉) • K. Hachiya
Graduate School of Energy Science, Kyoto University, Gokasho, Uji, Kyoto 611-0011, Japan
e-mail: t.sonobe@iae. Kyoto-u.ac.jp

T. Mitani • N. Shinohara
Research Institute for Sustainable Humanosphere, Kyoto University, Kyoto, Japan

H. Ohgaki
Institute of Advanced Energy, Kyoto University, Kyoto, Japan

T. Yao (ed.), *Zero-Carbon Energy Kyoto 2011*, Green Energy and Technology,
DOI 10.1007/978-4-431-54067-0_11,

methods, such as rapid and selective heating, as well its ability to provide internal heating of substances, microwave heating can reduce the time and lower the temperature necessary for material processing. Recently, several approaches have been studied for microwave material processing such as the sintering of ceramics, metal powder, and the metal production. Furthermore, thermal non-equilibrium state during microwave processing has been often reported such as enhancement of chemical reactions as well as rapid phase mixing at grain boundary of iron.

To date, several approaches have been studied for microwave material processing such as the sintering of ceramics [1–3], metal powders [4–6]. In 1999, Roy et al. reported that metal powders could also be heated and sintered by microwave irradiation, while bulk metallic samples reflect microwave [6]. Buchelnikov et al. have shown experimental results and a theoretical explanation of heating mechanisms for metal powders, whose eddy current loss (in alternating *H*-field) and magnetic reversal loss (in alternating *E*-field) generate heat during microwave irradiation on metallic powders [7].

Furthermore, a novel potential of microwave heating has also been addressed in metal production [8, 9]. Sato et al. have reported that highly pure pig irons are obtained in a 2.45 GHz multimode microwave reactor from powdered iron ores with carbon as the reducing agent in nitrogen atmosphere [8]. This process also enables the marked reduction in carbon consumption during reduction reactions, since carbon powders are mainly used not as a heat source for conventional furnaces, but as a reducing agent only. The required heat for reaction can be supplied by microwave heating, which suppresses CO_2 emission in iron manufacture [8, 9]. Microwave processing is rather specialized in short time process (hour) and small scale and distributed (m^3).

This study aims at exploring the potential of microwave process for highly energy-efficient and unique material processing, as well as developing the new spectroscopic approach for elucidating the mechanism of interaction between microwave and metal oxides.

2 Microwave Material Processing

Microwave heating techniques have been widely applied for various field of science, such as foods, organic chemistry and its synthesis process, inorganic, wood science, plasma science as well as medical science, over conventional domestic purpose. In particular, several unique behaviors of microwave process in material science have been reported such as non-thermal equilibrium reaction. Furthermore, microwave is the direct form to transfer the electric energy into the substance coherently to activate the chemical reaction and generate a heat without any heating media. Figure 1 shows an overview of the application of microwave heating.

Figure 2 shows the schematic diagram of strategic material processing through three kinds of energy transferring ways, such as thermo-chemical process, photonic

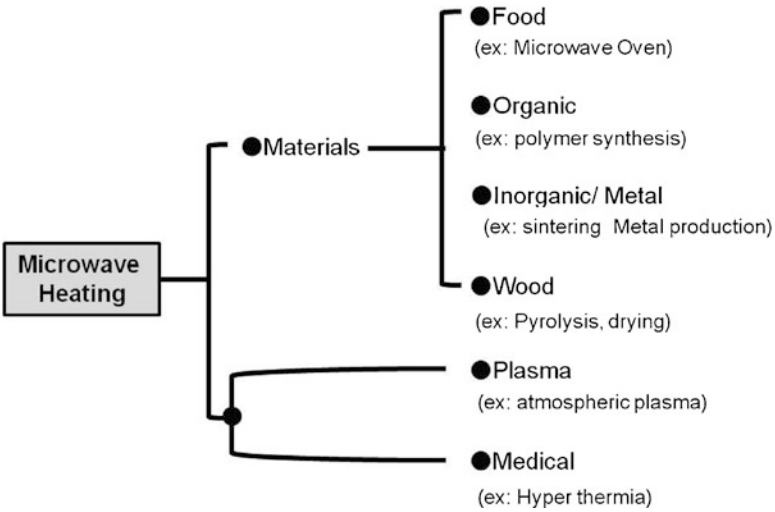

Fig. 1 Overview of the application of microwave heating process

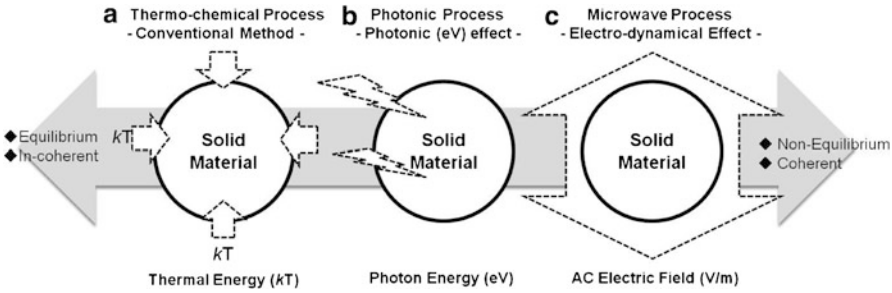

Fig. 2 Strategic material processing; (**a**) thermo-chemical process, (**b**) photonic process, and (**c**) microwave process

process, and microwave process. By using the unique properties of microwave over other methods, it is able to achieve the new chemical reaction and production of novel materials through microwave direct plasma process [10, 11].

In addition, microwave processing is rather specialized in short time process (hour) and small scale and distributed (m^3). Therefore, it is expected to achieve a good combination with the distributed renewable energy power generation, such solar cell, wind energy, and small hydro systems, for right material for right land. Furthermore, it is also expected to supply the new processing of space resource utilization, not only atmosphere but also in the space environment.

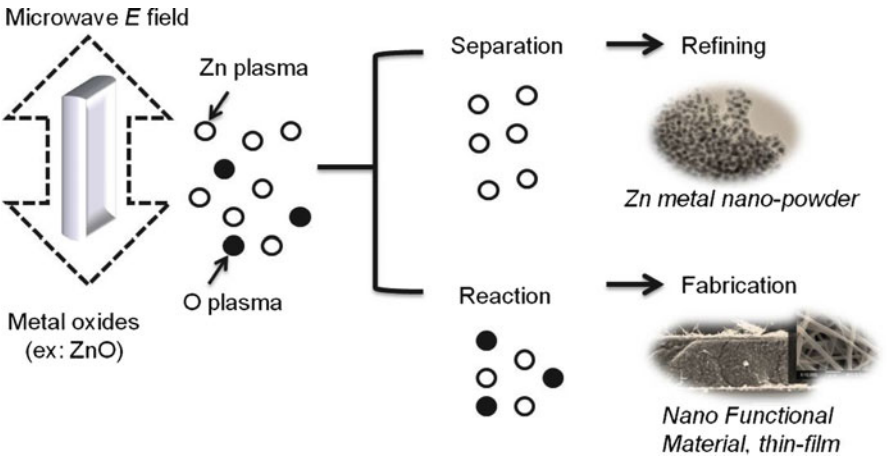

Fig. 3 Material processing through microwave direct plasma method [11]

2.1 Microwave Direct Plasma Method

It was reported in our previous study that the sintered TiO_2 and ZnO pellets show a marked absorption of microwave at the maximum position of the electric field under vacuum while glowing and emitting some types of plasma such as atomic oxygen and zinc atomic plasma [11]. As a consequence, one part of the zinc plasma was reoxidized by the atomic oxygen plasma after emission in the microwave electric field, while the other was deposited to form zinc and zinc oxide films outside the microwave electric field in the tube reactor.

By using the unique reaction upon microwave irradiation, we have proposed the microwave direct plasma method for a new material processing. Figure 3 shows the conceptual proposal of microwave material process using a microwave direct plasma method from metal oxides [10, 11].

This process can produce some nano-shaped zinc metal material as well as thin-films directly from ceramics. Figure 4 shows the conceptual system for ZnO thin-film processing from ZnO ceramics through microwave direct plasma method. This process is able to convert the low quality of ZnO ceramics to the functional properties of ZnO thin-films with simple set of apparatus.

2.2 New Approach to Elucidate the Microwave Interaction

A thermal nonequilibrium state during microwave processing has been often reported such as an enhancement of chemical reactions as well as rapid phase mixing at the grain boundaries of iron. Upon microwave irradiation on the metal oxides, many “local hot cores” on the order of 100 μm are formed inhomogeneously

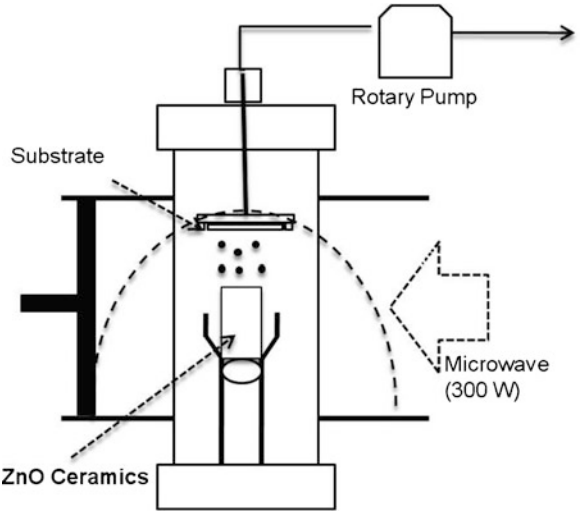

Fig. 4 Conceptual figure for thin-film processing from ZnO ceramics by microwave material processing

with huge temperature gradients at temperature of up to 400°C [6]. A strong visible-light emission over a sample surface under a microwave *E*-field, whose spectra shows a marked discrepancy in intensity with black body emission profiles, is also observed. These behaviors indicate the distinctive mechanism of energy transfer to material probably occurs over thermal heating during the microwave irradiation.

For elucidating the interaction between microwave and metal oxides, the change in crystal structure and molecule vibration are normally monitored by X-ray Diffraction (XRD), Visible–Infrared absorbance, Raman Spectra during temperature increasing upon microwave irradiation. On the other hand, we have proposed the spectroscopic method to monitor the change in electronic structure by use of photoluminescence method while suppressing the increase of temperature by microwave heating. Figure 5 shows the conceptual diagram of conventional method and new method. The new method aims at tracing a change in electronic structure of metal oxides by microwave irradiation while suppressing the increase of temperature, which probably contributes to explaining the discrepancy between thermal-effect and microwave-effects on metal oxides.

3 Conclusion

This study aims at exploring the potential of microwave process for highly energy-efficient and unique material processing, as well as developing the new spectroscopic approach for elucidating the mechanism of interaction between microwave and metal oxides.

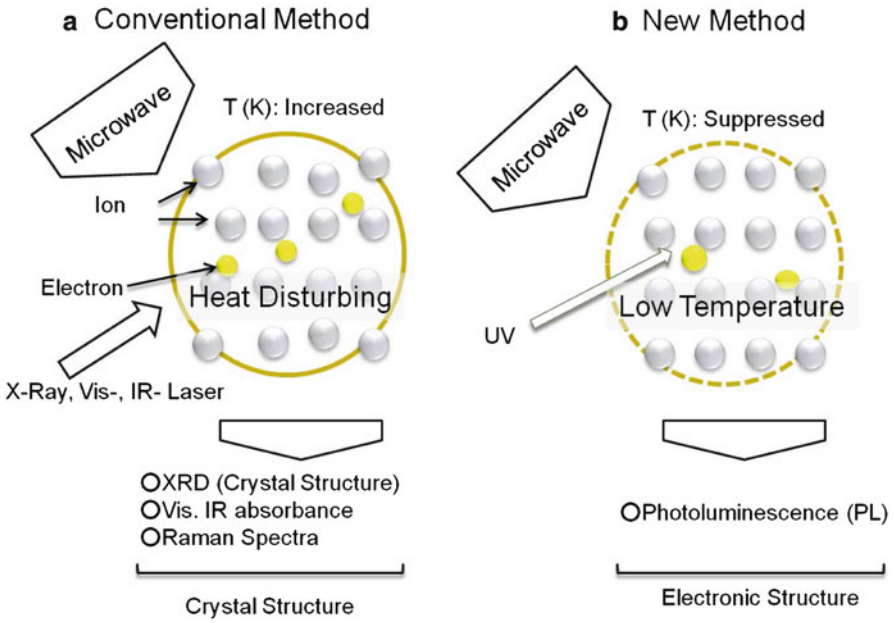

Fig. 5 New spectroscopic approach for elucidating the mechanism of interaction between microwave and metal oxides

Microwave direct plasma method is proposed to convert the low quality of ZnO ceramics to the functional properties of ZnO thin-films with simple set of apparatus. Furthermore, the spectroscopic method to monitor the change in electronic structure by use of photoluminescence method while suppressing the increase of temperature by microwave heating is also proposed to elucidate the interaction between microwave and metal oxides. Our comprehensive approach which consists of fundamental and applied scope can be expected to explore larger potential of microwave material processing.

Acknowledgement The work was partly supported by the Kansai Research Foundation for technology promotion (2011 Young Researcher Promotion Grant), the Murata Science Foundation (2011), and "Energy Science in the Age of Global Warming" of Global Center of Excellence Program (J-051) of the Ministry of Education, Culture, Sports, Science and Technology of Japan.

References

1. Park KS, Son JT, Chung HT, Kim SJ, Lee CH, Kim HG (2003) Electrochem Commun 5:839
2. Susaki M (2005) Jpn J Appl Phys 44:866
3. Jida S, Suemasu T (1999) J Appl Phys 86:2089

4. Vaidhyanathan B, Agrawal DK, Roy R (2000) J Mater Res 15:974
5. Ma J, Diehl JF, Johnson EJ, Martin KR, Miskovsky NM, Smith CT, Weisel GJ, Weiss BL, Zimmerman DT (2007) J Appl Phys 101:074906
6. Roy R, Agrawal D, Cheng J, Gedevanishvili S (1999) Nature 399:668
7. Buchelnikov VD, Louzquine-Luzgi DV, Xie G, Li S, Yoshikawa N, Sato M, Anzulevich AP, Bychkov IV, Inoue A (2008) J Appl Phys 104:113505
8. Sato M, Matsubara A, Takayama S, Sudo S, Motojima O, Nagata K, Ishizaki K, Hayashi T, Agrawal D, Roy R (2006) Proceedings of the 5th Sohn international symposium on advanced processing of metals and materials, San Diago, USA p 157
9. Ishizaki K, Nagata K (2008) Proceedings of the global congress microwave energy applications, Otsu, Japan p 453
10. Sonobe T, Mitani T, Hachiya K, Shnihara N, Yoshikawa S (2009) Jpn J Appl Phys 48:116003
11. Sonobe T, Hachiya K, Mitani T, Shnihara N, Ohgaki H (2010) Jpn J Appl Phys 49:08021

(iii)
Session Papers

On-Site Sugar Analysis and Pre-treatment of Nipa Saps

Pramila Tamunaidu and Shiro Saka

Abstract Fresh nipa sap is rich in sucrose and its physicochemical properties changes rapidly after collection and during storage. The current study was initiated to establish an on-site sugar analysis for determining chemical composition of fresh nipa saps and pre-treatment method to store nipa saps for subsequent bioethanol production. Therefore, brix measurement and subsequent heat-treatment on-site was considered in this study. For the on-site determination of the sugar content in the saps, a linear correlation was developed between brix and laboratory measurements, resulting in the total brix (wt%) value measured by handy refractometer, equivalent to 0.96 of the total sugars (wt%) determined by HPLC. Furthermore, to maintain most nipa sap sugar yield, heat-treatment at 100°C for 10 min with refluxing was found to be most acceptable as a pre-treatment of the fresh nipa saps.

Keywords Brix measurement • Heat-treatment • Nipa sap • Physicochemical properties

1 Introduction

Nipa sap is nutritious and rich in sucrose content. As sucrose is an unstable material, sucrose in the nipa sap easily hydrolyzes after harvesting and during storage into a 1:1 mixture of glucose and fructose. This may be due to the presence of acid and alkaline invertase in the sap.

Thus, preservatives, controlled atmosphere storage and heating have been studied as few approaches to maintain the fresh sap quality. However, considerable difficulty was experienced in preserving nipa sap samples for any length of time

P. Tamunaidu • S. Saka (✉)
Graduate School of Energy Science, Kyoto University, Sakyo-ku, Kyoto 606-8501, Japan
e-mail: saka@energy.kyoto-u.ac.jp

T. Yao (ed.), *Zero-Carbon Energy Kyoto 2011*, Green Energy and Technology,
DOI 10.1007/978-4-431-54067-0_12,

before analysis as reported by Gibbs [1]. The author suggested various chemical preservatives, such as mercuric chloride, formaldehyde, chloroform, toluene, ethanol and calcium hydroxide, useful to preserve these saps. However, considerable change was still observed for all preserved saps once there was an access to air. Samarajeewa et al. reported that addition of sodium metabisulphite to coconut saps suppressed non-ethanol producing microorganisms [2]. Additionally, Ajayi et al. described the importance of combined pre-treatment of filtration, preservation with sodium metabisulphite and pasteurization at 70°C for 60 min, maintained the nutritional value of oil and raphia palm saps [3].

Based on our preliminary studies, direct heat-treatment and immediate freezing below 0°C in dry ice, prolonged the sucrose stability [4]. Even though dry ice gave satisfactory results in preserving nipa saps, it is not easily available in sampling areas. Therefore heat-treatment was studied further to establish proper pre-treatment parameters based on pre-treatment time and temperature. Furthermore, since nipa saps hydrolyze almost immediately after collection, the total sugars determination in fresh sap on-site is essential. Hence, an on-site sugar analysis by brix measurement using a portable refractometer was established in this study as a quick and simple analytical on-site method.

2 Experimental

2.1 Collection and Characterization of Nipa Sap

The nipa saps used in this study were collected from Kampung Kelulut, Terengganu, Malaysia. Relative density and pH were determined through hydrometry and pH meter B-212 (Horiba Inst., Japan), respectively. Individual sugars and ethanol were quantified by high performance liquid chromatography (HPLC) LC-10A (Shimadzu, Japan) with Shodex Sugar KS-801(Showa Denko, Japan) column and water as the eluent. For organic acids determination, HPLC coupled with Aminex fermentation monitoring column (Bio-rad, USA) was used with 1 mM H_2SO_4 as the eluent. For inorganic content determination, a small volume of the sap was incinerated at 600°C for 2 h.

2.2 Brix Measurement of Nipa Sap

The HI 96801 Digital Refractometer (Hanna Inst., USA) was used to measure the % Brix of the nipa sap, which was calibrated for quantitative assay with HPLC measurement for standard sugars. The refractometer comes with Automatic Temperature Compensation (ATC) where reading is independent of changes in an ambient temperature.

2.3 Heat-Treatment Conditions of Nipa Sap

Nipa saps were heated at different temperatures ranging from 50°C to 100°C. The treatment time was fixed at 10 min as this is the minimum limit for high level disinfection [5]. Later, it was kept in full, tightly stoppered bottle and then maintained at 28°C. The samples were then kept for 6 days to observe the changes in sucrose and total sugar contents for all the nipa saps.

3 Results and Discussion

3.1 Physicochemical Properties of Fresh and 1 Day Old Saps

Physicochemical properties of fresh and 1 day old nipa saps are shown in Table 1. A clear fresh nipa sap turned milky after 1 day with the formation of white precipitates. For the pH measured, it shifted into an acidic condition from pH 6.9 to 5.9, with the increase in the organic acid contents. The density also slightly increased. In relation to this, sucrose content decreased from 10.2 to 7.0 wt% in saps with proportional increase in glucose and fructose contents 1 day afterwards. Natural fermentation started occurring with the initial increase in lactic acid, followed by ethanol and finally acetic acid, as also observed in natural fermentation of coconut sap [6]. Due to the rapid changes in nipa saps, an on-site sugar analysis technique and pre-treatment method need to be established to measure and store original quality of nipa saps prior to laboratory analysis. Inorganic contents, however, remained the same at 0.5 wt%.

3.2 Calibration of Brix Measurement for Quantitative Assay of Nipa Sap

Brix values are widely used for approximation of sugar contents in sugar-rich samples. It is essential to know the sugar content of the fresh nipa sap. However, its determination by analytical instrument is not feasible in the habitation sites. Therefore, in this study, the correlation between the brix measurements and total sugars as determined by HPLC analysis was established as shown in Fig. 1. The solid line is based on the best possible linear regression for the measured brix values of nipa saps against the total sugars determined by HPLC analysis. For this linear correlation, the actual total sugar content as analyzed by HPLC was 0.96 of the measured brix value in wt% with the coefficient correlation R being 0.9754. With this high correlation, brix measurements can be valid to determine the total sugar content in nipa saps on-site.

Table 1 Physicochemical properties of fresh and 1 day old nipa saps

Parameter	Value/observation	
	Fresh	1 day old
Color	Clear	Milky
pH	6.9	5.9
Relative density	1.03	1.07
Total chemical composition	15.0	15.0
Sucrose	10.2	7.0
Glucose	2.3	4.1
Fructose	1.5	2.4
Ethanol	0.1	0.3
Acetic acid	0.1	0.3
Lactic acid	0.3	0.4
Inorganics	0.5	0.5

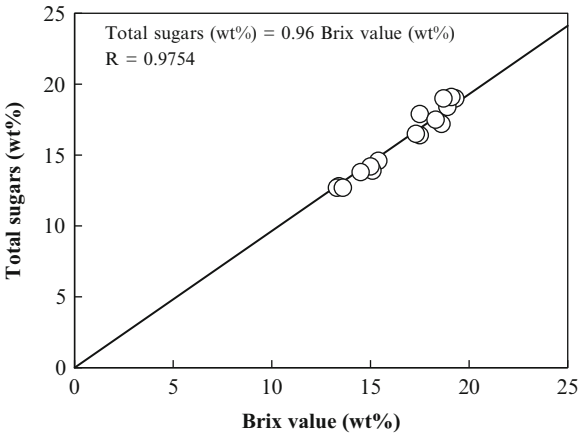

Fig. 1 Linear correlation between on-site measured brix value and actual total sugar content of the nipa saps as determined by HPLC analysis

3.3 Effect of Heat-Treatment on Nipa Saps

Figure 2 shows the obtained changes of nipa sap as heated by various temperatures from 50°C to 100°C for 10 min and kept at 28°C for 6 days. It is apparent that low temperatures from 50°C to 70°C did not assist in preserving the sucrose content. In fact, it made the sucrose in the sap to hydrolyze even faster. These temperatures could have destroyed only the microbes, however, the enzymes available could have contributed to further rapid hydrolysis. Conversely, extremely high temperatures of 90°C and 100°C may have sterilized the sap, partly or fully destroying free microbes and enzymes available in the nipa saps. For these samples, sucrose content could be preserved for the first 2–4 days. However, an important observation was that the conversion to ethanol and organic acids were only in trace amounts after the heat-treatment. In terms of total sugar content, which is the total

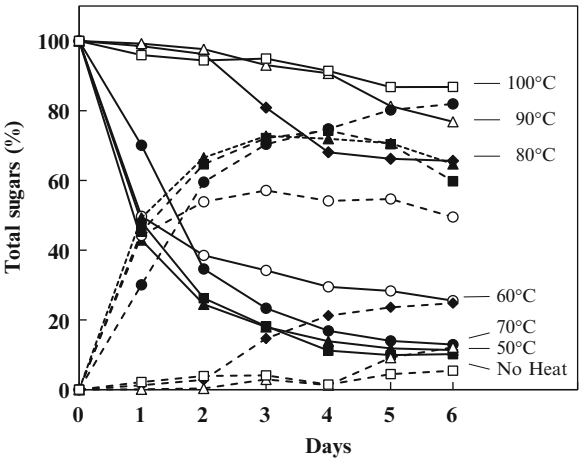

Fig. 2 Changes in total sucrose (*solid line*) and total glucose and fructose (*dashed line*) in nipa saps as heated by various temperatures from 50°C to 100°C for 10 min and kept at 28°C for 6 days

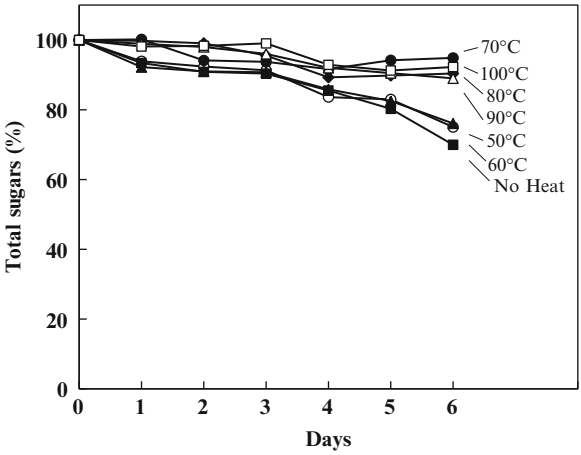

Fig. 3 Changes in total sugars in nipa saps as heated by various temperatures from 50°C to 100°C for 10 min and kept at 28°C for 6 days

of sucrose, glucose and fructose, the initial and final total after the treatment were above 60%. The change in total sugars is shown in Fig. 3. The saps treated at 70–100°C were higher in total sugars compared to saps treated at 50°C and 60°C. However, after 3 days the total sugars started to decrease for all heat-treated saps from 50°C to 100°C, as observed in the sap with no heat-treatment.

4 Conclusions

Fresh nipa saps easily hydrolyze after collection from sucrose to glucose and fructose, and further ferments to organic acids and ethanol. Therefore, on-site sugar analysis of nipa saps with brix refractometer and pre-treatment with heat was effectively established. With high correlation achieved between brix measurements and total sugars as determined by HPLC analysis, brix measurements can be valid to determine the total sugar content in nipa saps on-site. Furthermore, to maintain the total sugar content in saps to almost 100% with high sucrose, the treatment of 100°C for 10 min with refluxing is the most acceptable. By refluxing, water in the form of vapor will not be lost and the sugar content remains the same as collected.

Acknowledgements We would like to thank Dr Naohiro Matsui and Dr Yasuyuki Okimori from The General Environmental Technos Co. Ltd, Osaka, as well as Dr. Hitoshi Miyasaka and Mr. Keiyo Morimune from Environmental Research Center, Kansai Electric Power Co. Inc, Kyoto, for their generous contribution towards this research. We would also like to thank Yayasan Pembangunan Usahawan Terengganu and the people of Kampung Kelulut, Terengganu, Malaysia for providing nipa sap samples for this research work. This work was partly supported by an "Energy Science in the Age of Global Warming" of Global Center of Excellence (G-COE) program (J-051) of the Ministry of Education, Culture, Sports, Science and Technology of Japan.

References

1. Gibbs H (1911) The alcohol industry of the Philippine islands. I. A study of some palms of commercial importance with special reference to the saps and their uses. Philipp J Sci Sect A 6:99–206
2. Samarajeewa U, Mathes D, Wijeratne M, Warnakula T (1985) Effect of sodium metabisulphite on ethanol production in coconut inflorescence sap. Food Microbiol 2:11–17
3. Ajayi OA, Fakiya EO, Oladapo GO (1988) Industrial processing of palm juice and riboflavin loss. Food Chem 34:89–94
4. Tamunaidu P (2011) Potential evaluation of nipa palm (*Nypa fruticans*) for bioethanol production. Doctoral Thesis, Kyoto University, Kyoto, Japan
5. Stevens S, Cox I (1996) Sterilization and disinfection. J Comm Eye Health 9:36–42
6. Atputharajah JD, Widanapathirana S, Samarajeewa U (1986) Microbiology and biochemistry of natural fermentation of coconut palm sap. Food Microbiol 3:273–280

Conversion of Glycerol as By-Product from Biodiesel Production to Value-Added Glycerol Carbonate

Zul Ilham and Shiro Saka

Abstract Current environmental issues, fluctuating fossil fuel price and energy security have led to an increase in worldwide biodiesel production, thus, creating a large surplus of glycerol formed as a by-product during the transesterification reaction. In this study, the conversion of glycerol from three different biodiesel production technologies (two-step supercritical dimethyl carbonate, supercritical methanol and alkali-catalyzed method) to glycerol carbonate by supercritical dimethyl carbonate was investigated. It was found that after treatment at 300°C/20 MPa/20 min in supercritical dimethyl carbonate, the yield of glycerol carbonate could reach 98 wt% of the theoretical maximum when pure glycerol from two-step supercritical dimethyl carbonate or supercritical methanol were used. However, glycerol from alkali-catalyzed method which contains impurities such as sodium salts and water led to the decomposition of glycerol carbonate to glycidol. In addition, the results presented in this study showed the importance to monitor the reaction pressure in supercritical dimethyl carbonate to prevent decomposition and to ensure satisfying yield of glycerol carbonate. The non-catalytic supercritical dimethyl carbonate is, therefore, a potential method to convert glycerol to value-added product, glycerol carbonate.

Keywords Biodiesel • Dimethyl carbonate • Fatty acid methyl esters • Glycerol carbonate • Supercritical method

Z. Ilham • S. Saka (✉)
Graduate School of Energy Science, Kyoto University, Kyoto 606-8501, Japan
e-mail: saka@energy.kyoto-u.ac.jp

T. Yao (ed.), *Zero-Carbon Energy Kyoto 2011*, Green Energy and Technology,
DOI 10.1007/978-4-431-54067-0_13, © Springer 2012

1 Introduction

The growing biodiesel production in recent years has generated a surplus of glycerol as a by-product. Without new applications, the overproduction will create a glut in glycerol market. Therefore, biodiesel production methods which are related to the manufacturing of high value-added chemicals are desired and needed.

In line with this, one-step and two-step supercritical dimethyl carbonate methods [1–3] have been established as new methods for biodiesel production without producing glycerol. From these processes, glycerol carbonate could be obtained instead of glycerol. In this study, the route for glycerol carbonate formation has been further elucidated to discuss the optimized reaction condition, utilization of glycerol from other production methods and the decomposition of glycerol carbonate to glycidol.

2 Experimental

Various authentic compounds for standards and chemicals were obtained from Nacalai Tesque Inc., Japan, all of which are of highest purity available.

Glycerol from the two-step supercritical dimethyl carbonate method (hereinafter described as glycerol from the two-step method), glycerol from supercritical methanol method and unpurified glycerol from alkali-catalyzed method (hereinafter described as alkali-catalyzed method glycerol) were prepared and used in this study. Its properties are presented in Table 1. Those were, then, treated in the batch-type supercritical biomass conversion system [4] to have a reaction at supercritical conditions with dimethyl carbonate (Tc:274.9°C/Pc:4.63 MPa) in a molar ratio of 1:10. All the experiments and analysis were conducted in compliance with the procedures described in our previous papers [1–5] and the reaction temperature and pressure were monitored by thermocouple and pressure gauge, respectively.

Products were analyzed by High Performance Liquid Chromatography (HPLC) (Column: Ultrahydrogel 120, oven temperature: 40°C, flow: 1 mL/min, mobile phase: water, detector: RID 10A). Water content was detected by Karl-Fischer method and sodium salts was determined by titration [2].

Table 1 Properties of glycerol from various biodiesel production technologies

Method	Glycerol purity (wt%)	Water (wt%)	Sodium salts (wt%)
Alkali-catalyzed	70	10	20
Supercritical methanol	>99	n.d.	n.d.
Supercritical dimethyl carbonate	>98	~2	n.d.

n.d. not detected

3 Results and Discussion

3.1 Optimization of Glycerol Carbonate Formation in Supercritical Dimethyl Carbonate

Figure 1 shows the yield of glycerol carbonate from the two-step method as treated in supercritical dimethyl carbonate at 300°C with different reaction pressures. It could be seen from the graph that the trend shows higher formation of glycerol carbonate at higher reaction pressure. This is in agreement with our previous finding of supercritical fluid behavior where higher reaction pressure always leads to higher yield [5].

When the reaction condition was maintained at 300°C/20 MPa, the highest yield of glycerol carbonate based on the theoretical value at 98 wt% could be achieved after 20 min reaction. However, when treated at 300°C/5 MPa and 300°C/10 MPa, yield of glycerol carbonate are low, indicating possible decomposition of glycerol carbonate under low reaction pressures.

The reaction scheme for the conversion could be expected to proceed in a non-catalytic manner as depicted in Fig. 2. Glycerol undergoes esterification with dimethyl carbonate, leading to the formation of thermodynamically stable five-member cyclic glycerol carbonate. Methanol, formed from this reaction, was removed by evaporation. The scheme is in agreement with several previous studies describing a similar method in a catalytic manner [6, 7].

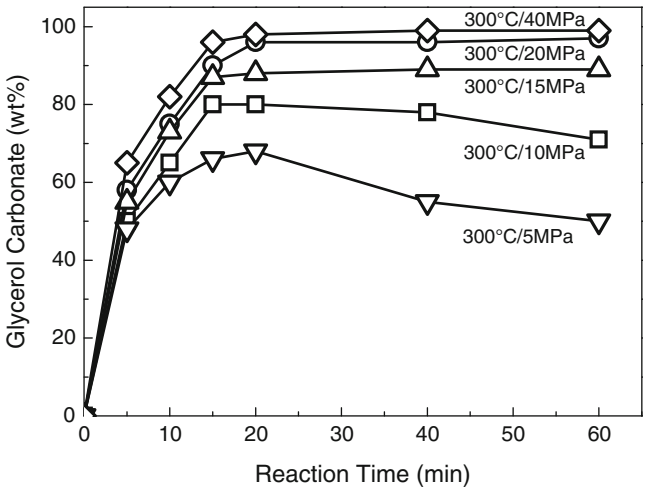

Fig. 1 Yield of glycerol carbonate as glycerol from the two-step method was treated in supercritical dimethyl carbonate at 300°C with different reaction pressure

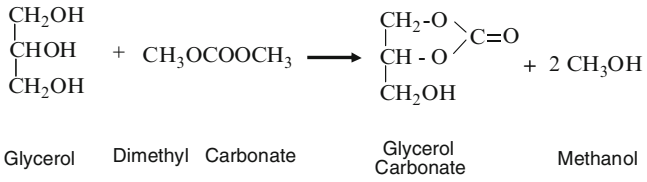

Fig. 2 Reaction scheme for glycerol carbonate formation in supercritical dimethyl carbonate

3.2 Yield of Glycerol Carbonate from Glycerol Produced by Different Production Technologies

Based on the optimized condition presented beforehand, glycerol from other biodiesel production methods (glycerol from supercritical methanol and alkali-catalyzed method glycerol [4]) were also treated in supercritical dimethyl carbonate at 300°C/20 MPa to check for the possible conversion of glycerol to glycerol carbonate. Comparison of the yield is presented in Fig. 3. Pure glycerol produced by supercritical methods (two-step supercritical dimethyl carbonate method and supercritical methanol method) showed higher conversion to glycerol carbonate while alkali-catalyzed method glycerol showed significantly lower yield. This is possibly contributed by the amount of impurities available in the alkali-catalyzed method glycerol as shown in Table 1.

3.3 Decomposition of Glycerol Carbonate to Glycidol

To confirm the effect of impurities in alkali-catalyzed method glycerol in reducing the yield of glycerol carbonate, a thorough analysis on the HPLC chromatogram of products obtained from alkali-catalyzed method glycerol was done. Interestingly, as shown in Fig. 4, the chromatogram showed an additional peak at 8.55 min, apart from only glycerol carbonate peak at 16.31 min found in products obtained from pure glycerol produced by supercritical methods (two-step supercritical dimethyl carbonate method and supercritical methanol method). When analyzed and compared with several authentic compounds, this was determined to be glycidol.

Based on these findings, decomposition was expected to occur in the presence of water and sodium salts (impurities in alkali-catalyzed glycerol) to partly decompose glycerol carbonate into glycidol. The proposed scheme for this decomposition pathway is presented in Fig. 5. As discussed beforehand (Fig. 1), low reaction pressures in supercritical condition may also lead to the decomposition, following similar pathway as described.

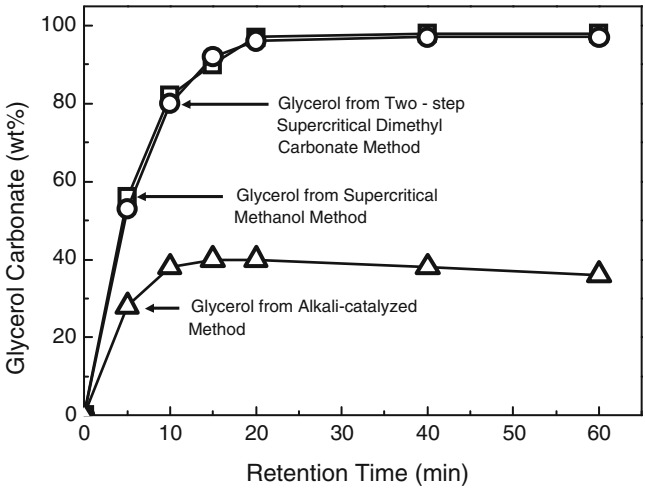

Fig. 3 Yield of glycerol carbonate from glycerol obtained by different production technologies

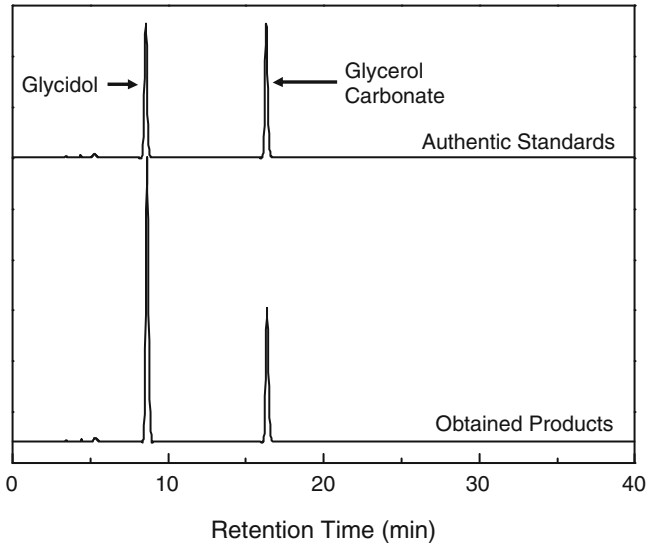

Fig. 4 HPLC chromatograms of obtained products after glycerol from alkali-catalyzed method treated in supercritical dimethyl carbonate at 300°C/20 MPa/20 min. Standards of glycerol carbonate and glycidol are shown as authentic compounds

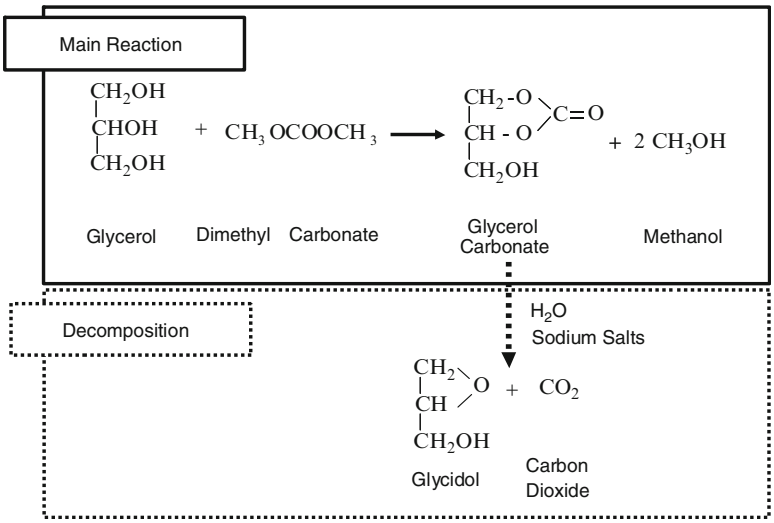

Fig. 5 Reaction scheme for decomposition pathway of glycerol carbonate to form glycidol when glycerol with impurities treated in supercritical dimethyl carbonate

3.4 Glycerol Carbonate and Glycidol from Non-catalytic Supercritical Dimethyl Carbonate

Based on the results presented beforehand, it was found that the supercritical dimethyl carbonate could esterified glycerol to glycerol carbonate in high yield without any catalyst applied and could also form glycidol when decomposed. Glycerol carbonate is a stable, colorless liquid currently used industrially as solvent and surfactant [7] while glycidol, is important in the production of epoxy resins and polyurethanes. Its high functionality, together with the versatile and well-investigated reactivity of its hydroxyl functions could supply as a basis for a variety of derivatives [8].

4 Conclusions

The results presented in this study showed that glycerol could be converted to value-added glycerol carbonate in supercritical dimethyl carbonate (300°C/20 MPa/20 min) without any catalyst applied to have 98 wt% yield. In addition, when glycerol with impurities such as water and sodium salts was used, glycerol carbonate would decompose to glycidol via the decomposition pathway. The reaction pressure must also be observed in supercritical dimethyl carbonate

process as low reaction pressure could also lead to the decomposition. The formation of value-added chemicals, glycerol carbonate as well as the formation of glycidol from the non-catalytic supercritical dimethyl carbonate method showed the potential of this method to be an alternative way to reduce glycerol glut from biodiesel production.

Acknowledgement This study is partly funded by Japan Science and Technology Agency (JST) and Global-COE Program "Energy Science in the Age of Global Warming", Kyoto University, supported by Ministry of Education, Culture, Sports, Science and Technology-Japan, for all of which the authors highly acknowledge.

References

1. Ilham Z, Saka S (2009) Dimethyl carbonate as potential reactant in non-catalytic biodiesel production by supercritical method. Bioresour Technol 100:1793–1796
2. Ilham Z, Saka S (2010) Two-step supercritical dimethyl carbonate method for biodiesel production from Jatropha curcas oil. Bioresour Technol 101:2735–2740
3. Ilham Z, Saka S (2011) Production of biodiesel with glycerol carbonate by non-catalytic supercritical dimethyl carbonate. Lipid Tech 23:10–13
4. Kusdiana D, Saka S (2004) Effects of water on biodiesel fuel production by supercritical methanol treatment. Bioresour Technol 91:289–295
5. Warabi Y, Kusdiana D, Saka S (2004) Biodiesel fuel from vegetable oil by various supercritical alcohols. Appl Biochem Biotech 113–116:793–801
6. Ochoa-Gomez JR, Gomez-Jimenez-Aberasturi O, Maestro-Madurga B, Pesquera-Rodriguez A, Ramirez-Lopez C, Lorenzo-Ibaretta L, Torrecilla-Soria J, Villaran-Velasco MC (2009) Synthesis of glycerol carbonate from glycerol and dimethyl carbonate transesterification: catalyst screening and reaction optimization. Appl Catal Gen 366:315–324
7. Herseczki Z, Varga T, Marton G (2009) Synthesis of glycerol carbonate from glycerol, a by-product of biodiesel production. Int J Chem React Eng 7:1–14
8. Pagliaro M, Ciriminna R, Kimura H, Rossi M, DellaPina C (2007) From glycerol to value-added products. Angew Chem Int Ed Engl 46:4434–4440

Holocellulose Determination in Biomass

Harifara Rabemanolontsoa and Shiro Saka

Abstract For determination of holocellulose, the residual yield and its chemical composition during delignification by acidified sodium chlorite have been studied for bamboo (*Phyllostachys heterocycla*) and Sargassum (*Sargassum horneri*). It was then found that along with the extended number of chlorination, the residue became yellowish, and then whitish. Accordingly, the holocellulose yield was reduced. Thus, in order not to lose any part of the holocellulose, the number of chlorination was found to be minimized so as for the residue to remain yellowish. Subsequently, lignin and ash corrections were made on the yellowish residue to determine the accurate holocellulose content. Such a modified procedure for the holocellulose determination was proposed in this study.

Keywords Ash correction • Carbohydrate • Lignin correction • Lignocellulosics • Sodium chlorite

1 Introduction

Sustainable and economic growth requires replacement of the massive use of fossil resources to renewable ones such as biomass for production of fuels, chemicals and materials. For those applications, one of the most interesting components of biomass is carbohydrate which is composed of cellulose and hemicellulose, and their sum is called holocellulose. By definition, holocellulose is composed of the total polysaccharide fraction of extractives-free biomass and it is the starting-point of most work in carbohydrate study of biomass. Its accurate determination is therefore very important.

H. Rabemanolontsoa • S. Saka (✉)
Graduate School of Energy Science, Kyoto University,
Yoshida-Honmachi, Sakyo-ku, Kyoto 606-8501, Japan
e-mail: saka@energy.kyoto-u.ac.jp

T. Yao (ed.), *Zero-Carbon Energy Kyoto 2011*, Green Energy and Technology,
DOI 10.1007/978-4-431-54067-0_14,

Holocellulose assays were proposed by Van Beckum and Ritter [1] as the chlorine–ethanolamine procedure, by Wise et al. [2] as the chlorite method, and by Poljak [3] as the peracetic acid method but the Wise chlorite technique has been the most widely used. It consists of performing successive treatments of acid chlorination to the sample in order to remove lignin. Improvements of the Wise method were suggested [4] and the number of chlorination for hardwoods and softwoods were settled to be respectively three and four times [5]. As chlorite method was initially dedicated for wood species, the question arises on the extent of chlorination to be applied on other non-woody biomass species.

Therefore, in this work, the chemical composition of the residual yield has been studied during delignification by acidified chlorite for bamboo (*Phyllostachys heterocycla*) as well as Sargassum (*Sargassum horneri*) and a revised new method on holocellulose determination in various biomass species was, thus, proposed.

2 Materials and Methods

Bamboo (*Phyllostachys heterocycla*) and Sargassum (*Sargassum horneri*) as respective representatives of monocotyledonous angiosperms and algae were used in this study. Sargassum, collected from the western Wakasa bay in the Japan Sea was washed with fresh water and then freeze-dried, while bamboo collected from Kyoto, Japan was air-dried.

The samples were ground with Wiley mill (1029-C, Yoshida Seisakusho Co., Ltd.), and sieved to retain particles of 150–500 μm (35–100 mesh) and then Soxhlet-extracted with acetone until the solvent was clear of any color. On the extractives-free samples, holocellulose was quantified with sodium chlorite treatment according to the procedure of Wise et al. [2] as adapted by Timell [6] with slight modifications. In brief, 150 ml of 0.2 M acetic acid buffer was poured on 2.5 g of extractives-free sample. Then, 1 g of sodium chlorite was added, followed by 0.2 ml of glacial acetic acid and the sample was put in a water bath for 1 h at 70–80°C. Sodium chlorite with acetic acid was further repeated for successive cycles of chlorination. After the necessary number of chlorination, the solution was filtered, washed with 500 ml of cold water followed by 50 ml of acetone and the holocellulose content as the remaining residue was determined gravimetrically.

Lignin in holocellulose as the sum of Klason and acid-soluble lignin was determined according to a modified Klason method [7], while ash content was quantified as the sample residue after ignition at 600°C for 4 h. Protein was also measured according to the Kjeldahl nitrogen method by using a nitrogen factor of 6.25 [8].

3 Results and Discussion

3.1 Aspects of Chlorite-Delignified Residues

Figure 1 shows examples of chlorite-delignified residues after different degrees of chlorination. For bamboo, the sample had a pronounced yellow color after the first treatment of chlorination. However, as chlorination has been repeated, it became less yellowish and the residue finally became whitish after nine times of chlorination with yield of 55.2 wt%.

As for Sargassum, the first chlorination generated a yellow-greenish residue, while second chlorination produced yellowish residue, and additional treatments of chlorination resulted in whitish, and finally clear white residue after seven times of chlorination, as observed in Fig. 1. It is, therefore, understandable that pure white residues could only be recovered after nine times of chlorination for bamboo and seven times for Sargassum.

For holocellulose determination, some authors recommended to repeat chlorination until the sample turns whitish [9, 10]. However, it was widely demonstrated that lignin removal during chlorite delignification might also engender some loss of the polysaccharide portion [11]. Therefore, in order to define an accurate holocellulose determination, the pattern of the biomass components removal during chlorite treatment must be studied.

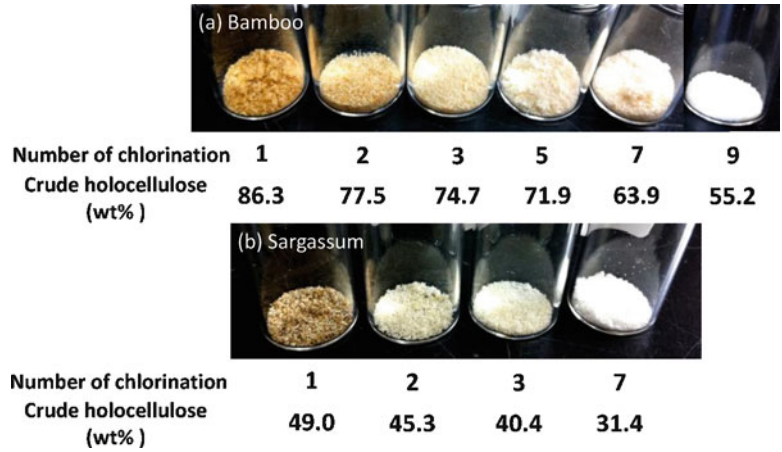

Fig. 1 Delignified residues of (**a**) bamboo and (**b**) Sargassum after different degrees of chlorination

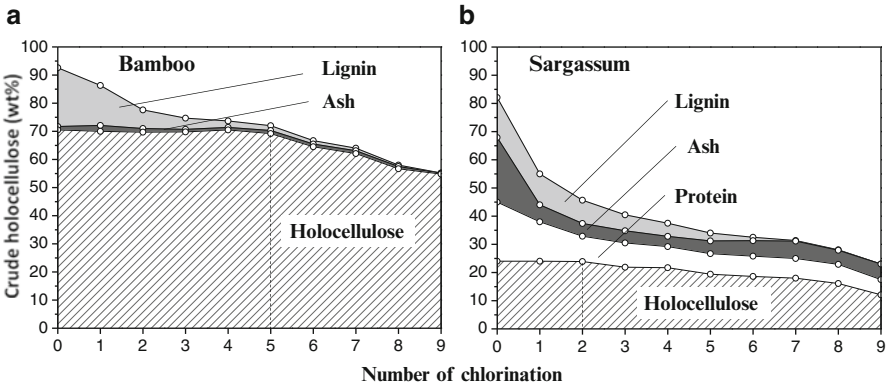

Fig. 2 Yield change of the cell wall components in (**a**) bamboo and (**b**) Sargassum during chlorite delignification

3.2 Yield Change of Cell Wall Components During Chlorite Delignification

The chemical composition of the residues from bamboo and Sargassum during the course of chlorite delignification is shown in Fig. 2. The values corresponding to zero chlorination represent the chemical composition of the untreated samples. The residue from chlorite delignification, also called crude holocellulose, is expressed in wt% of the original oven-dried sample. The holocellulose yield was calculated by subtracting the lignin, ash and protein in the residue from the total crude holocellulose. However, as bamboo had negligible protein, protein was not studied in its crude holocellulose.

In Fig. 2, the crude holocellulose decreased in its yield, while the number of chlorination was augmented. However, it is apparent that chlorite treatment on bamboo dissolved lignin selectively only for the first five times of chlorination, and on further treatments, the holocellulose decreased noticeably in its yield, confirming that extended chlorination removes carbohydrate as well in bamboo, as already reported in wood [11]. On the contrary, inorganics as ash remain in the crude holocellulose.

As it is apparent from Fig. 2, the trends on the components recovery in Sargassum are quite different from the ones in bamboo. In Sargassum, crude holocellulose retained a considerable amount of protein, ash as well as lignin, and ash content is getting even higher as chlorination was extended, supporting the fact previously demonstrated [12] as the chlorite treatment contaminates the samples with inorganics. In addition, carbohydrate loss in Sargassum is noticed to some extent after two times of chlorination, and become drastic after seven times of chlorinations when most of the lignin was dissolved.

To prevent such carbohydrate loss from the samples, chlorite treatment of bamboo and Sargassum was, therefore, respectively minimized to five and two times of

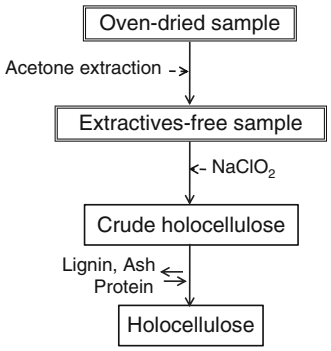

Fig. 3 Revised new procedure for holocellulose determination

chlorination. Furthermore, lignin and ash were all independently determined on the residue. Additionally, protein correction was done on crude holocellulose from Sargassum. As a result, as reported previously [12], the holocellulose content was determined to be 70.5 wt% in bamboo and 23.9 wt% in Sargassum.

3.3 Holocellulose Determination in Biomass

For an adequate determination of holocellulose, chlorination should be enough to remove lignin but not excessive to avoid a loss of carbohydrates. Therefore, the degree of chlorination should be minimized so as for the sample to be still yellowish. However, such yellowish residue possibly contains lignin and ash etc., such corrections should be done on the residue. In addition, for samples with high protein content, protein correction has to be done also. Such method is illustrated in Fig. 3, representing the revised new procedure for holocellulose determination.

4 Concluding Remarks

The results of this study showed that along with the chlorite delignification, parts of the carbohydrates were lost, while inorganics and protein still remained in the residues. Therefore, for biomass characterization, the treatment should be minimized so as for the sample to be still yellowish. Ash and lignin corrections as well as protein correction if necessary should subsequently be performed on the yellowish residue to obtain reliable results.

Acknowledgement This work was accomplished under financial support from Kyoto University Global COE Energy Science Program. The authors wish to thank the Kyoto prefectural marine research center for kindly providing the Sargassum sample.

References

1. Van Beckum WG, Ritter GJ (1937) Rapid methods for the determination of holocellulose and cross and bevan cellulose in wood. Pap Trade J 104(19):49–50
2. Wise LE, Murphy M, D'Addieco AA (1946) Chlorite holocellulose, its fractionation and bearing on summative wood analysis and on studies on the hemicelluloses. Pap Trade J 122 (2):35–43
3. Poljak A (1948) Holzaufschluss mit peressigsaure. Angew Chem 60(2):45–46
4. Timell TE (1964) Wood hemicelluloses: part 1. Adv Carbohydr Chem 19:247–302
5. Kurada K (2000) Mokuzai Bunseki. In: Yoshida H (ed) Mokushitsu kagaku jikken manual. Buneido shuppan, Tokyo, pp 87–98
6. Timell TE (1961) Isolation of galactoglucomannans from the wood of gymnosperms. Tappi 44:88–96
7. Yoshihara K, Kobayashi T, Fujii T, Akamatsu I (1984) A novel modification of klason lignin quantitative method. Jpn Tappi 38:466–475
8. Thiex NJ, Manson H, Anderson S, Persson JA (2002) Determination of crude protein in animal feed, forage, grain, and oilseeds by using block digestion with a copper catalyst and steam distillation into boric acid: collaborative study. J AOAC Int 85(2):309–317
9. Carson JF, Maclay WD (1948) Esters of lima bean pod and corn cob hemicelluloses. J Am Chem Soc 70(1):293–295
10. Samuel R, Pu Y, Foston M, Ragauskas AJ (2010) Solid-state NMR characterization of switchgrass cellulose after dilute acid pretreatment. Biofuels 1(1):85–90
11. Ahlgren PA, Goring DAI (1971) Removal of wood components during chlorite delignification of black spruce. Can J Chem 49(8):1272–1275
12. Rabemanolontsoa H, Ayada S, Saka S (2010) Method applicable to analyze various biomass species in their chemical composition. In: The 60th annual meeting of Japan Wood Research Society, Miyazaki, Japan

Hydrolysis Behavior of Various Crystalline Celluloses from Cotton Linter as Treated by One-Step Semi-flow Hot-Compressed Water

Rosnah Abdullah and Shiro Saka

Abstract This is a preliminary investigation on the hydrolysis behavior of cotton linter (*Gosspium hirstum L.*) in different crystalline forms. Celluloses I, II, III_I and IV_I were therefore prepared from cotton linter and treated by one-step semi-flow hot-compressed water (HCW) at 270°C/10 MPa/15 min. As a result, it was found that celluloses I, II, III_I and IV_I were decomposed and liquefied in HCW in respective yields of 66.0, 90.4, 74.6 and 94.4 wt%. The hydrolyzed products recovered mainly consisted of various cello-saccharides such as glucose and cello-oligosaccharides. In addition, some dehydrated and fragmented compounds as well as organic acids were produced. The highest yields of these decomposed products were realized in the hydrolysis of these various celluloses, and the hydrolysis resistance dependable on its crystalline form was found to be in the following order: cellulose I > cellulose III_I > cellulose II > cellulose IV_I. This line of evidence can clearly reveal the effect of different crystalline structures of cellulose on its hydrolysis behavior.

Keywords Cellulose • Cotton linter • Crystalline structure • Hydrolysis • Hot-compressed water

1 Introduction

Cellulose is a crystalline polysaccharide composed of linear chain of (1 → 4) β-D-glycopyranosyl units. It is one of the most abundant polymer resources available on renewable basis and has high potential to be exploited to meet future energy needs.

R. Abdullah • S. Saka (✉)
Graduate School of Energy Science, Kyoto University,
Yoshida-Honmachi, Sakyo-ku, Kyoto 606-8501, Japan
e-mail: saka@energy.kyoto-u.ac.jp

T. Yao (ed.), *Zero-Carbon Energy Kyoto 2011*, Green Energy and Technology,
DOI 10.1007/978-4-431-54067-0_15,

Cellulose has four polymorphs, cellulose I, II, III and IV, which are distinguishable by X-ray diffractometry. Celluloses I is the crystalline form of native cellulose. Cellulose II is generally formed in regenerated cellulose or mercerized cellulose. Cellulose III can be prepared from cellulose I or II by treatment with liquid ammonia or organic amines followed by removal of the chemicals and termed as cellulose III_I and cellulose III_{II}, respectively. Whereas, cellulose IV can be obtained by thermal treatment with glycerol either from cellulose III_I or cellulose III_{II} to get cellulose IV_I and cellulose $IV_{II,}$ respectively.

Hot-compressed water (HCW) treatment is seen as an environmentally clean and a non-catalytic process, which is one of the available methods used to hydrolyze cellulose to produce various valuable products. Cotton linter which has almost 100% cellulose content became a better candidate to the study of its hydrolysis. Therefore, in this study, various crystalline celluloses prepared from cotton linter were treated by one-step semi-flow HCW treatment at 270°C/10 MPa/15 min in order to investigate their hydrolysis behavior.

2 Experimental

2.1 Sample Preparations

Cotton linter (*Gosspium hirstum L.*) was used as the starting material, which is already in the form of cellulose I. Mercerized cellulose in the form of cellulose II was prepared by soaking cellulose I in 20% of aqueous NaOH solution for 24 h at room temperature, followed by washing thoroughly with water and freeze-drying [1]. Crystalline cellulose III_I was prepared from cellulose I by soaking in 100% ethylenediamine for 24 h at room temperature, then washed with dry methanol and air-dried. Whereas for the preparation of cellulose IV_I, cellulose III_I was first soaked in glycerol for 3 days at room temperature and this sample was heated in the vessel at 260°C/0.5 MPa for 30 min [2]. After cooling to room temperature, the product was washed with water and acetone successively and dried in vacuum.

2.2 Hot-Compressed Water (HCW) Treatment and Analyses

These samples of various celluloses were then treated individually in one-step semi-flow HCW at 270°C/10 MPa/15 min. Each of these samples yielded water-soluble portion and insoluble residue.

X-ray diffraction patterns of all the four crystalline celluloses prepared as well as the residues were recorded by an X-ray diffractometer RINT 2200 V, Rigaku Denki. Their crystallinities (%) were then estimated according to method by Segal [3]. As for the chemical composition analysis and the characterization of

the water-soluble portion, high performance liquid chromatography (HPLC), ion chromatograph (IC) and capillary electrophoresis (CE) were used [4].

3 Results and Discussion

3.1 X-Ray Diffractograms of Various Celluloses

Figure 1 illustrates the x-ray diffraction patterns for polymorphs of cotton linter in crystalline celluloses I, II, III_I and IV_I after the conversion processes. These patterns represent a simple method of characterizing crystalline cellulose polymorphs, and it is apparent that these crystalline structures are as intended.

The chemical composition for crystalline celluloses I, II, III_I and IV_I after the conversion processes, was found to be 99.9 wt% in glucose with 0.1 wt% of xylose.

3.2 Crystallinity Changes of Various Celluloses as Treated by HCW

Evaluation of the crystallinity before and after one-step semi-flow HCW treatment is necessary to compare the effect of the treatment on the crystalline structures. The crystallinity of each cellulose was estimated by the following equation:

$$\text{Crystallinity} = \left(\frac{I_{\max} - I_{\min}}{I_{\max}}\right) \times 100$$

where,

I_{max} = maximum peak at 002 lattice diffraction

I_{min} = minimum intensity as background at $2\theta = 30^\circ$

The maximum peak at 002 lattice diffraction occurred at 2θ of 22.8°, 21.9°, 20.9° and 22.6° was used for determining the crystallinity of celluloses I, II, III_I and IV_I, respectively, while the minimum intensity as background was fixed at $2\theta = 30^\circ$. By this way, the degree of crystallinity for various celluloses could be compared relatively.

Figures 2a–d show how the X-ray diffraction patterns transform after the treatment. In general, the crystallinity of the celluloses increases after one-step semi-flow HCW treatment with the exception of cellulose IV_I, whose crystallinity decreases. The crystallinity (%) of celluloses I, II, III_I and IV_I before the treatment was 88.9%, 73.5%, 83.2% and 84.7%, while after the treatment, their crystallinity (%) resulted in 91.7%, 84.3%, 94.0% and 78.6%, respectively.

The increase in crystallinity is due to the removal of the less crystalline portion of cellulose towards hydrolysis and/or annealing effect on the crystalline structure. As demonstrated by Yamamoto and Horii, annealing effect could take place in

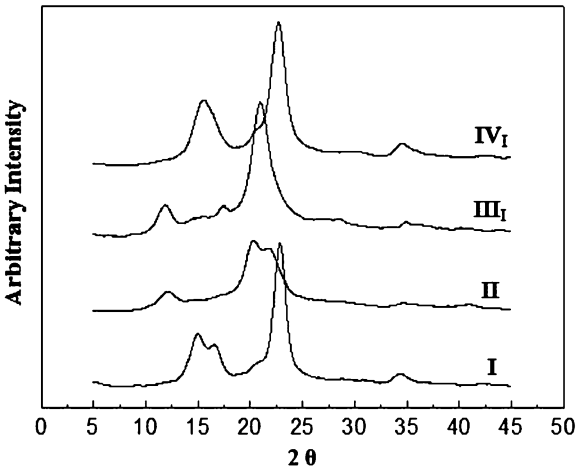

Fig. 1 X-ray diffraction patterns in crystalline cellulose I, II, III_I and IV_I forms after the conversion processes

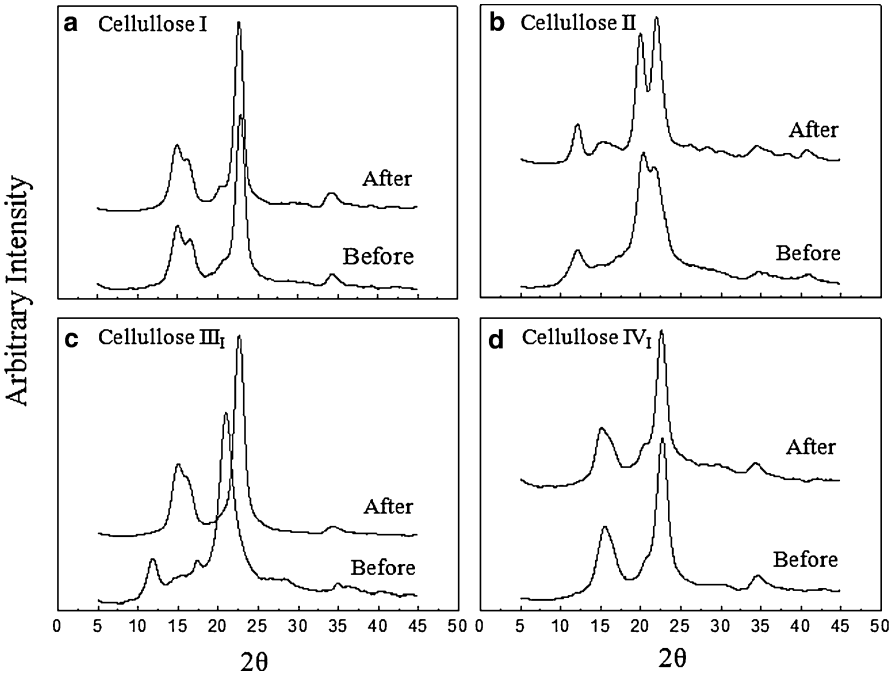

Fig. 2 (**a**)–(**d**) X-ray diffraction patterns of crystalline celluloses I, II, III_I and IV_I before and after the one-step semi-flow HCW treatment at 270°C/10 MPa/15 min

Table 1 Summarized yields of products from crystalline celluloses I, II, III_I and IV_I as treated by one-step semi-flow HCW at 270°C/10 MPa/15 min

	Yield (wt%)					
	Water-soluble portion					Non-solube portion
Cellulose	Cello-saccharides	Dehydrated compounds	Fragmented compounds	Organic acids	Unknown	Residue
I	40.6	6.7	1.7	4.0	13.0	34.0
II	59.5	10.7	3.6	3.7	12.9	9.6
III_I	40.0	5.5	1.8	3.2	24.2	25.4
IV_I	53.8	8.7	3.7	3.4	24.9	5.6

temperature between 220°C and 280°C [5]. A repetitive heating did not result in a significant increase in crystallinity of cellulose which could be the reason why the crystallinity of cellulose IV_I decreases after the HCW treatment [6]. On the other hand, Fig. 2c shows cellulose III_I transformed back to cellulose I, after the treatment, which is in agreement with study done by Isogai [7].

3.3 Characterization of the Water-Soluble Portion

The summary of the yields of products in wt% of polymorphs of cotton linter as treated by one-step semi-flow HCW at 270°C/10 MPa/15 min is shown in Table 1. The water-soluble portion for celluloses I, II, III_I and IV_I contains 40.6, 59.5, 40.0 and 53.8 wt% of hydrolyzed compounds in cello-saccharides form, respectively. Cello-saccharides mainly consisted of glucose and cello-oligosaccharides. At the same time, the decomposed compounds (dehydrated and fragmented compounds, as well as organic acids) were detected in lower values. Apart from these, 13.0, 12.9, 24.2 and 24.9 wt% of unidentified products in the water-soluble portion were respectively, considered as unknown. The residue was measured to be 34.0, 9.6, 25.4 and 5.6 wt% respectively.

4 Concluding Remarks

The hydrolysis behavior of the cotton linter in the different forms of crystalline celluloses I, II, III_I and IV_I were studied by one-step semi-flow HCW treatment at 270°C/10 MPa/15 min. As a result, under this treatment condition, various cello-saccharides such as glucose and cello-oligosaccharides were mainly recovered as the hydrolyzed products. Some dehydrated and fragmented compounds as well as organic acids were also produced. From these yields, it can be concluded that the hydrolysis resistance is dependent on their crystalline forms and can be summarized

in the following order: cellulose I > cellulose III_I > cellulose II > cellulose IV_I. Such a finding confirms the effect of different crystalline structures of cellulose on its hydrolysis behavior under HCW treatment. This is essential and useful knowledge, in sequence to further optimize the reaction condition for more recovery of hydrolyzed products from cellulose.

Acknowledgement The authors are grateful for the financial support provided under the GCOE program, Kyoto University.

References

1. Isogai A, Atalla RH (1998) Dissolution of cellulose in aqueous NaOH solutions. Cellulose 5:309–319
2. Isogai A, Usuda M, Kato T, Uryu T, Atalla RH (1989) Solid-state CP/MAS ^{13}C NMR study of cellulose polymorphs. Macromolecules 22:3168–3172
3. Segal L, Creely JJ, Martin AE Jr, Conrad C (1959) An empirical method for estimating the degree of crystallinity of native cellulose using the X-ray diffractometer. Text Res J 29:786–793
4. Lu X, Yamauchi K, Phaiboonsilpa N, Saka S (2009) Two-step hydrolysis of Japanese beech as treated by semi-flow hot-compressed water. J Wood Sci 56(4):331–338
5. Yamamoto H, Horii F (1993) CP/MAS ^{13}C NMR analysis of the crystal transformation induced for Valonia cellulose by annealing at high temperatures. Macromolecules 22:1313–1317
6. Weimer PJ, Hackney JM, French AD (1995) Effects of chemical treatments and heating on the crystallinity of celluloses and their implications for evaluating the effect of crystallinity on cellulose biodegradation. Biotechnol Bioeng 48:169–178
7. Isogai A (1994) Allomorphs of cellulose and other polysaccharides. In: Gilbert RD (ed) Celullosic polymers. Hanser, Munich, pp 1–24

Factors Affecting Biodiesel Yield in Interesterification of Rapeseed Oil by Supercritical Methyl Acetate

Fadjar Goembira and Shiro Saka

Abstract To prevent glycerol as a by-product in biodiesel production, a non-catalytic supercritical methyl acetate method has been developed earlier in our laboratory. In this study, therefore, some factors affecting the yield of products from this process were evaluated. It was, consequently, found out that reaction temperature, reaction pressure, molar ratio of methyl acetate to oil, and reaction time were important factors to be considered for product yield in biodiesel production by interesterification.

Keywords Affecting factors • Biodiesel • Interesterification • Product yield • Supercritical methyl acetate

1 Introduction

A significant increase in worldwide biodiesel use has led to a growing concern over crude glycerol formation as a by-product that is inevitable in conventional biodiesel production methods. The oversupply of crude glycerol has significantly reduced its market price [1].

A new biodiesel production process by supercritical methyl acetate method called "Saka-Isayama Process" was then developed to prevent crude glycerol by-production [2]. The process successfully exhibited the formation of fatty acid methyl esters (FAME) and triacetin as the by-product, instead of glycerol. Moreover, both products, as a mixture, have been proven not to deteriorate biodiesel fuel properties, thus to be used as biodiesel [3].

However, compared to other processes developed by the same research group, i.e., supercritical methanol [4] and supercritical dimethyl carbonate [5], equivalent

F. Goembira • S. Saka (✉)
Graduate School of Energy Science, Kyoto University, Kyoto, Japan
e-mail: saka@energy.kyoto-u.ac.jp

T. Yao (ed.), *Zero-Carbon Energy Kyoto 2011*, Green Energy and Technology,
DOI 10.1007/978-4-431-54067-0_16,

yield by supercritical methyl acetate was achieved after relatively longer reaction time. This study was, therefore, conducted to find out factors that optimize the yield of products in biodiesel production by supercritical methyl acetate method.

2 Experimental

Rapeseed oil as triglyceride and high purity methyl acetate (>99%) from Nacalai Tesque Inc. were used in this study. Furthermore, analytical grade FAME and triacetin as standard compounds were obtained from the same supplier.

A flow-type reaction system that could control reaction pressure was used, comprised of pumps, pre-heaters, supercritical reaction tube and a cooling system. The reaction tube, immersed in a molten salt bath, was made of Hastelloy C-276 alloy with 80 m length and 1.2 mm inside diameter that could stand reaction temperature and pressure up to 500°C and 50 MPa, respectively. Under such a reaction condition, supercritical condition of methyl acetate (Tc = 234°C; Pc = 4.69 MPa) can be readily achieved.

For sample analysis, the obtained product was evaporated to remove unspent solvent of methyl acetate. Furthermore, product identification and quantification were done by using a high performance liquid chromatography (HPLC) with the following setting; column: Cadenza CD-C18, mobile phase: methanol, detector: refractive index detector (RID), oven temperature: 40°C, sample injection: 10 μL. Quantification of product was done by comparing peak areas of products and standard compounds. Theoretically, maximum 100 wt% FAME and 25 wt% triacetin, totally 125 wt% in yield, could be obtained from interesterification of triglyceride by methyl acetate.

3 Results and Discussion

3.1 Effect of Reaction Time on Biodiesel Yield

Figure 1 shows the effect of reaction time up to 60 min on product yield as treated in supercritical methyl acetate at the reaction condition of 350°C with a molar ratio of 42:1 in methyl acetate to oil. We clearly see that both FAME and triacetin were formed after 15 min of reaction time. The highest yield was achieved at 45 min but longer reaction time did not further increase, but decreased the yield. This is most likely due to thermal decomposition that occurred particularly at FAME compounds, which is in line with what was reported by Imahara et al. [6] for supercritical methanol.

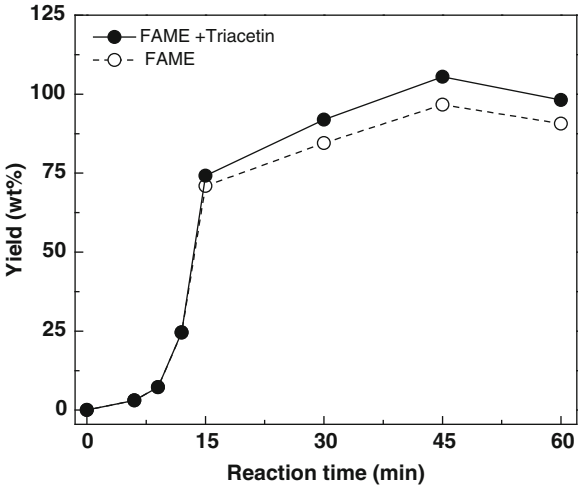

Fig. 1 Effect of reaction time on product yield from rapeseed oil as treated in supercritical methyl acetate at 350°C/20 MPa/0–60 min at a molar ratio of 42:1 in methyl acetate to oil

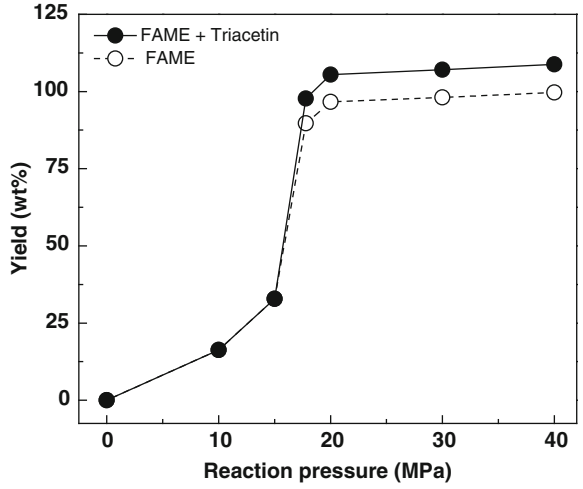

Fig. 2 Effect of reaction pressure on product yield from rapeseed oil as treated in supercritical methyl acetate at 350°C/0.1–40 MPa/45 min at a molar ratio of 42:1 in methyl acetate to oil

3.2 Effect of Reaction Pressure on Biodiesel Yield

Effect of reaction pressure up to 40 MPa on product yield is presented in Fig. 2 as treated in supercritical methyl acetate at 350°C/45 min with the same molar ratio of 42:1. As we can see from the figure, product yield was significantly increased when the reaction pressure was raised from 15 to 18 MPa. At reaction pressures lower than 18 MPa, no product yields higher than 50 wt% were achieved. The higher yields at the higher reaction pressures could be due to the higher density achieved by the reaction system that increased the possible contact between the triglyceride and the solvent molecules of methyl acetate.

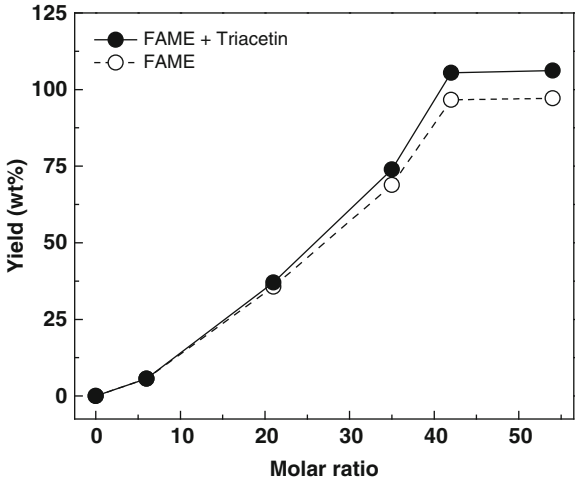

Fig. 3 Effect of molar ratio of methyl acetate to oil on product yield from rapeseed oil as treated in supercritical methyl acetate at 350°C/ 20 MPa/45 min

Furthermore, a slight increase in the reaction pressure from 18 to 20 MPa has improved the total product yield of FAME and triacetin to 105 wt%, which was higher than the maximum biodiesel yield in conventional method, i.e., 100 wt%. However, further raise in the reaction pressure did not significantly increase the yield. As we can see from the figure, 107 and 108 wt% of total yields were attained at reaction pressures of 30 and 40 MPa, respectively. This finding indicates that at higher reaction pressures than 20 MPa, the reaction rates did not increase the yield significantly. Instead, the higher reaction pressure can reduce the thermal decomposition by "cage effect" of the solvent [7].

3.3 Effect of Molar Ratio of Solvent to Oil on Biodiesel Yield

Stoichiometrically, in biodiesel production by supercritical methyl acetate method, one mole of triglyceride reacts with three moles of methyl acetate to produce three moles of FAME and one mole of triacetin through interesterification reaction. However, in order to proceed the reaction towards the product side, more amount of solvent must be utilized.

Figure 3 shows the effect of different molar ratios of the solvent to oil on the product yield. We can see from the figure that the higher molar ratio of methyl acetate to oil resulted in the higher product yields. However, significant yield increase was only observed when the molar ratio was raised from 21 to 42, whereas further increased to 54 in molar ratio did not result in a significant increase. In conclusion, therefore, the optimized molar ratio is a vicinity of 42 in the molar ratio of the solvent to the oil as observed in supercritical methanol system [4].

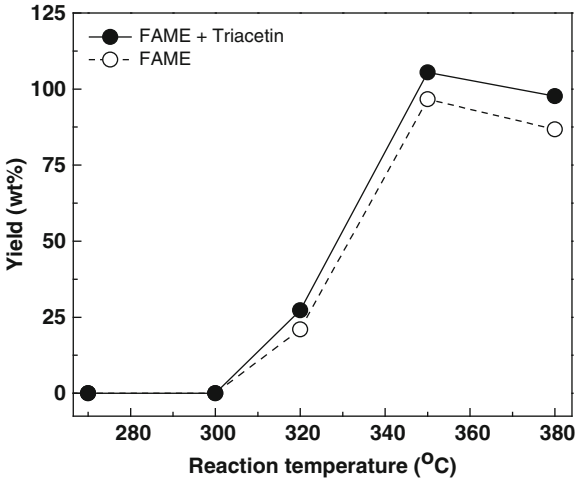

Fig. 4 Effect of reaction temperature on product yield from rapeseed oil as treated in supercritical methyl acetate at 270–380°C/20 MPa/45 min at a molar ratio of 42:1 in methyl acetate to oil

3.4 Effect of Reaction Temperature on Biodiesel Yield

In order to know the effect of reaction temperature on the product yield, a study employing various reaction temperatures was done under the condition at 20 MPa/45 min with the molar ratio of 42:1. The obtained result is presented in Fig. 4. From this figure, we could observe a significant reduction of yields at reaction temperatures lower than 350°C. Additionally, although not so significant, a yield decrease was noticed when 380°C was used as the reaction temperature, under the same reaction condition. Lower product yields at relatively lower reaction temperature were caused by lower reactivity of supercritical methyl acetate towards triglyceride, whilst the lower yield at higher temperature than 350°C was most likely due to thermal decomposition of the products.

4 Conclusions

This study has successfully exhibited some factors that influenced biodiesel yields as rapeseed oil was treated in supercritical methyl acetate. The affecting factors were reaction temperature, reaction pressure, molar ratio of methyl acetate to oil, and reaction time. Those factors contributed to a certain extent to the yields. At reaction condition of 350°C/20 MPa at a molar ratio of 42:1 in methyl acetate to oil, longer reaction time resulted in higher yields, with the maximum one at 45 min, but reducing up to 60 min. As for the reaction pressure, under the same condition for 45 min, yields were increased when it was raised. However, only slight yield increase was achieved above 20 MPa. With regard to the molar ratio, the highest yield resulted in 42. Lastly, reaction temperature up to 350°C resulted in

higher product yields. Nevertheless, further temperature increase to 380°C resulted in the lesser product yield, due perhaps to the thermal decomposition. Based on these lines of evidence, we have to be very cautious in determining optimal condition of biodiesel production process, particularly when we employed supercritical treatment. Perhaps, the most optimized condition for interesterification by supercritical methyl acetate would be in 350°C/20 MPa/42:1 molar ratio/45 min. Yet, some decomposition of products could not be entirely avoided. Thus, more precise evaluation on the reaction condition must be explored. In some cases, the higher values of the affecting factors did not necessarily contribute to the higher product yields. Failing to apply the right values could result in lower product yield or inefficient use of reactants and energy in biodiesel production by supercritical methyl acetate method.

Acknowledgement This study was completed under financial support from the Global-COE Program "Energy Science in the Age of Global Warming", Kyoto University, for all of which the authors highly acknowledge.

References

1. Bonet J, Costa J, Sire R, Reneaume J-M, Pleşu AE, Pleşu V, Bozga G (2009) Revalorization of glycerol: Comestible oil from biodiesel synthesis. Food Bioprod Proc 87:171–178
2. Saka S Manufacturing method for fatty acid methyl esters. Japan Patent no. 4378534 (application: 19 Dec 2005; granted: 2 Oct 2009)
3. Saka S, Isayama Y (2009) A new process for catalyst-free production of biodiesel using supercritical methyl acetate. Fuel 88:1307–1313
4. Saka S, Kusdiana D (2001) Biodiesel fuel from rapeseed oil as prepared in supercritical methanol. Fuel 80:225–231
5. Ilham Z, Saka S (2009) Dimethyl carbonate as potential reactant in non-catalytic biodiesel production by supercritical method. Bioresour Technol 100:1793–1796
6. Imahara H, Minami E, Hari S, Saka S (2008) Thermal stability of biodiesel in supercritical methanol. Fuel 87:1–6
7. Turro NJ (2005) Molecular structure as a blueprint for supramolecular structure chemistry in confined spaces. PNAS 2(31):10766–10770

Effects of Various Solvent on Precipitation of Phenolated Products from Japanese Beech as Treated by Subcritical Phenol

Gaurav Mishra and Shiro Saka

Abstract Liquefaction of Japanese beech (*Fagus crenata*) in subcritical phenol was investigated using a batch-type reaction vessel, and the treated sample was fractionated into phenol-soluble portion and phenol-insoluble residues. It was then, found that at 270°C/1.8 MPa/3 min, the lignin was almost decomposed and liquefied as phenol-soluble portion, whereas almost all of the cellulose and a majority of hemicelluloses remained in the phenol-insoluble residue. For the phenol-soluble portion, it was further treated with various solvents in order to precipitate the liquefied products. Based on the solubility parameters of solvents, the diethyl ether was emerged as the best solvent with the highest yield of precipitates, and precipitates were found to be mainly lignin phenolated. The obtained phenolated lignin would have a high potential for its various applications.

Keywords Japanese beech • Lignin • Solubility parameter • Subcritical phenol

1 Introduction

In recent years, considerable efforts have been made to utilize the wood as the new source of raw materials for chemicals and resins [1]. Due to the lack of plasticity of wood, it cannot be used directly by melting, dissolving or softening sufficiently in moldings etc. [2]. To meet the demand and to replace the plastics with biomaterials, effective ways of utilizing wood have been investigated over the years. Liquefaction of wood using supercritical fluid technology is one of the potential technologies, which is used to convert wood to liquefied substances and other valuable chemicals [3].

G. Mishra • S. Saka (✉)
Graduate School of Energy Science, Kyoto University, Yoshida-Honmachi, Sakyo-ku, Kyoto 606-8501, Japan
e-mail: saka@energy.kyoto-u.ac.jp

T. Yao (ed.), *Zero-Carbon Energy Kyoto 2011*, Green Energy and Technology,
DOI 10.1007/978-4-431-54067-0_17,

Through liquefaction, all major cell wall components of wood such as cellulose, hemicellulose and lignin are converted to low-molecular compounds. Lignin, in particular, by its conversion to many phenolic compounds can be used in various useful potential lignin-based applications such as preparation of resins, adhesives etc. [4]. Therefore, in this study, a non-catalytic liquefaction of Japanese beech was investigated in subcritical phenol mainly for lignin solubilization and its precipitation using different solvents based on their respective solubility parameters.

2 Experimental

The wood flour of Japanese beech (*Fagus crenata*) extracted with acetone by Soxhlet apparatus was passed through the mesh of 280-μm in size to prepare the extractive-free wood flour. As described in Fig. 1, approximately 150 mg of the oven-dried wood flour and 4.9 ml of phenol were fed into a 5-ml reaction vessel made of Inconel-625. It was then subjected to subcritical phenol treatment at 270°C/1.8 MPa for 3 min by immersing it into molten salt bath preheated at a 270°C. After the treatment, the reaction vessel was dipped in water bath to stop the reaction. The resulted reaction mixture was then filtered with 0.2-μm membrane, and phenol-soluble portion was separated from phenol-insoluble residue. The phenol-insoluble residue was then studied for its chemical composition according to the literature [5, 6].

To study the reactivity of the major cell wall components, avicel (Avicel PH-101) as cellulose xylan as hemicellulose (Sigma-Aldrich Inc, Japan) and milled wood lignin (MWL) from Japanese beech were treated in a similar manner to liquefy to have the phenol-soluble portion and phenol-insoluble residue.

The non-reacted, free phenol in phenol-soluble portion was removed using Kugelrohr bulb-to-bulb distillation unit under vacuum at 85°C. The phenolated portion after distillation was thus washed with methanol to remove any trapped free phenol in it, if any. The amount of the total phenol added in the phenolated products was thus calculated as shown in Table 1.

The precipitation of liquefied products in phenol-soluble portion was tried with an excessive amount of solvents with different solubility parameters in the volumetric ratio of 1:9. The mixture was then stirred vigorously and kept for overnight settling. The resulted one was then filtered with 0.2-μm membrane to separate the precipitates.

3 Results and Discussion

3.1 Liquefaction and Phenolation of Wood Cell Wall Components

Japanese beech was treated at subcritical condition of phenol at 270°C/1.8 MPa for 3–30 min and the chemical compositions of their respective phenol-insoluble residues were studied as in Fig. 2 [7]. From this figure, the phenol-soluble portion can be seen as the area above the lignin.

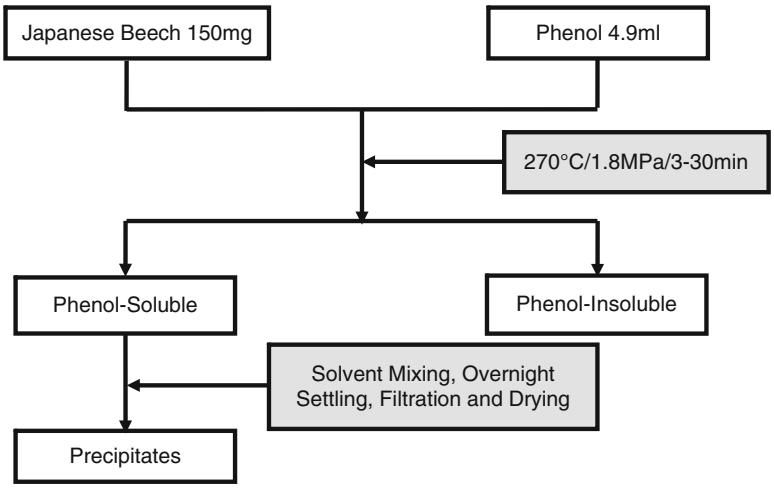

Fig. 1 Fractionation scheme of Japanese beech followed by precipitation of phenol-soluble portion obtained by the subcritical phenol treatment

Table 1 Phenol-soluble and phenol-insoluble residue and the reactivity of the major cell wall components as these components were treated with subcritical phenol at 270°C/1.8 MPa/3 min

Sample	Phenol-soluble portion wt%	Phenol-insoluble residue wt%	Total phenol added wt%	Phenol/Unit
Cellulose	18.8	81.2	1.6	0.2
Xylan	96.0	4.0	41.7	0.7
MWL	92.3	7.7	126.7	2.2
Whole wood	42.3	57.7	98.2	-

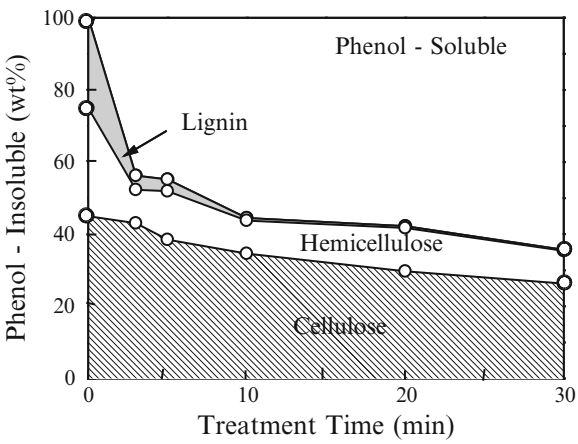

Fig. 2 Changes in phenol-insoluble residue of Japanese beech as treated by subcritical phenol at 270°C/1.8 MPa

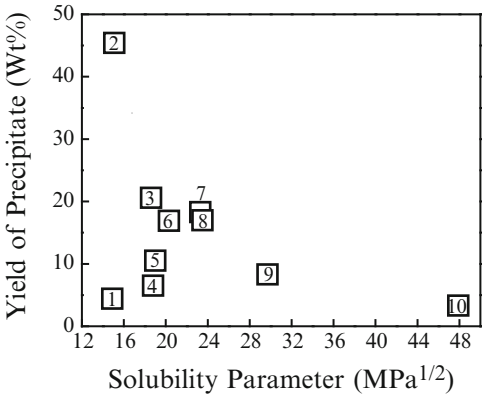

Fig. 3 Change of the yield of precipitates on the whole wood basis in various solvents with solubility parameter obtained at 270°C/1.8 MPa treatment for 3 min

At 3 min treatment, it can be seen that most of the original lignin was decomposed and liquefied into the phenol-soluble portion. On the other hand, almost all of cellulose remained to be in residue and some of hemicellulose was liquefied. Therefore, a majority of the phenol-soluble portion as treated for 3 min must be phenolated lignin with some hemicellulose.

In order to ensure the amount of phenolation over the liquefied products from Japanese beech, experiments were carried out at 3 min with cellulose, xylan, and MWL under the same treatment conditions and compared. It was found that the liquefied products were phenolated as shown by phenol added and phenol/unit in Table 1. It is clear from this that the phenolation of lignin is three times compared with that of xylan. The phenol-soluble portion consists of 2.7, 44.8 and 52.6 wt%, respectively, of cellulose, hemicellulose (xylan) and lignin liquefied, at 3 min treatment. Based on these, the total phenol added for the whole wood as treated at 270°C/1.8 MPa/3 min was evaluated to be 85.3 wt% (= 1.6 × 0.027 + 41.7 × 0.448 + 126.7 × 0.526). The value of 85.3 wt% obtained from these individual cell wall components is not to be different from, but rather in agreement with 98.2 wt% for the whole wood directly treated. Consequently, the observed different reactivity of the major cell wall components as described by Phenol/unit must be valid. The difference in the experimental and evaluated amount of phenol added could be attributed to the complex structure of wood and the way cell wall components are bound to each other.

3.2 Behavior of Liquefied Products as Mixed with Various Solvents

Japanese beech as treated at 270°C/1.8 MPa for 3 min was found out that, although hemicellulose was also liquefied, lignin was almost selectively phenolated and liquefied. The phenol-soluble portion was then treated with various solvents with different solubility parameters. Figure 3 shows the change in weight percent of the

Table 2 Precipitate and its chemical composition of the phenol-soluble portion as mixed by various solvents with different solubility parameters

No	Solvent	Solubility parameter $(MPa)^{1/2}$	Precipitate (wt%) P	Chemical composition of precipitate (wt%)	
				H	L
1	Hexane	14.1	4.4	1.1	3.3
2	Diethyl ether	15.1	45.4	11.4	34.0
3	Tetrahydrofuran	18.6	20.6	5.2	15.4
4	Benzene	18.8	6.5	1.6	4.9
5	Chloroform	19.0	10.5	2.6	7.9
6	Acetone	20.3	16.9	4.2	12.7
7	1-Butanol	23.3	18.3	4.6	13.7
8	2-Propanol	23.5	17.0	4.3	12.7
9	Methanol	29.7	8.3	2.1	6.2
10	Water	47.9	3.3	0.8	2.5

P: Precipitate; H: Hemicelluloses; L: Lignin

precipitates in different solubility parameters of the solvents. The numbers in Fig. 3 correspond to the solvents in Table 2. Diethyl ether (No. 2) has emerged out as the solvent providing the highest yield of 45.4% as compared to others.

3.3 Fractionation of Precipitates

The precipitates in a mixture of phenol-soluble portion and solvent were filtered and separated. In order to justify that the precipitates can possibly be phenolated lignin with some of hemicellulose, the experiments were carried out to find the amount of phenol reacted with lignin and hemicellulose in phenol-soluble portion, as described earlier. As a result, the precipitates contained mainly lignin and some phenol, possibly as phenolated lignin with small amounts of hemicelluloses. It is clear from Table 2 that diethyl ether has shown the highest yield of precipitates among all and the highest percentage of lignin content in the precipitate. It is expected that due to the phenolysis reaction, phenol reacted with lignin and liquefied. Hemicellulose was also phenolated to some extent, as it was found from Table 1, that the lignin and hemicelluloses were phenolated in the ratio of 3:1. Based on this finding, phenolated products for hemicellulose (H) and lignin (L) were estimated as in Table 2.

4 Conclusions

The liquefaction of Japanese beech in subcritical phenol at 270°C/1.8 MPa/3 min, suggested that its condition would be appropriate particularly for lignin liquefaction. The diethyl ether was emerged as the best solvent for precipitating the liquefied products, with its highest yield. The fractionation of precipitates suggests that it contains mainly lignin and small portions of hemicelluloses along with phenol, possibly as phenolated lignin. Therefore, these lines of evidence stipulate that selective liquefaction of lignin and its precipitation as phenolated lignin would have a high potential for various applications.

Acknowledgement The authors are grateful for the financial support provided under the Kyoto University Global COE program.

References

1. Kobayashi M, Tukamoto K, Tomita B (2000) Application of liquefied wood to a new resin system-synthesis and properties of liquefied wood/epoxy resins. Holzforchung 54:93–97
2. Shiraishi N (1993) Plasticization of wood and its application. In: Shiraishi N, Kajita H, Norimoto M (eds) Recent research on wood and wood-based materials. Elsevier Applied Science, London, pp 155–156
3. McKendry P (2002) Energy production from biomass (part 2): conversion technologies. Bioresour Technol 83:47–54
4. Alma MH, Maldas D, Shiraishi N (1998) Liquefaction of several biomass wastes into phenol in presence of various alkalis and metallic salts as catalysts. J Polym Eng 18:161–177
5. Dence CW (1992) The determination of lignin. In: Lin SY, Dence CW (eds) Methods in lignin chemistry. Springer, Berlin, pp 33–63
6. Wörmeyer K, Ingram T, Saake B, Brunner G, Smirnova I (2011) Comparison of different pretreatment methods for lignocellulosic materials. Part II: influence of pretreatment on the properties of rye straw lignin. Bioresour Technol 102:4157–4164
7. Mishra G, Saka S (2010) Liquefaction behaviors of Japanese beech as treated in subcritical phenol. In: Yao T (ed) Zero-carbon energy Kyoto 2010, Green Energy and Technology. Springer, Heidelberg, pp 147–152

Crystal Structure Analysis of γ-Fe_2O_3 in the Process of Chemical Li Insertion

Seungwon Park, Tamito Matsui, and Takeshi Yao

Abstract γ-Fe_2O_3 has a spinel structure containing cation vacancies and is expected to function as cathode material in the secondary Li-ion batteries for lithium insertion/extraction. Lithium was chemically inserted into γ-Fe_2O_3 using 0.5 M solution of n-butyl lithium hexane and the crystal structure in the process of lithium insertion was examined by means of X-ray diffraction measurement and the Rietveld analysis. It was found that the sample was mixture of two phase both belonging to the space group of *Fd3m*, one is lithium rich and another is lithium lean. It is considered that the chemical lithium insertion take two phase process, i.e. inserted lithium forms a Li-rich phase in which the Li amount is constant, and the overall Li concentration is controlled by the mol fraction change in Li-rich phase and Li-lean phase.

Keywords Chemical Li insertion • Secondary Li-ion batteries • Spinel structure • The Rietveld method • γ-Fe_2O_3

1 Introduction

Secondary Li-ion batteries (LIBs) are the most advanced energy storage system and have attracted much attention as key technologies for power leveling on renewable energy utilization and electric vehicle. As for electrode in LIBs, iron-based materials are the promising in terms of resource abundance, inexpensive and low environmental impact.

γ-Fe_2O_3 has a spinel structure including partially vacant 16*d* site and empty 8*b* and 16*c* sites, and is expected to function as an electrode material based on

S. Park • T. Matsui • T. Yao (✉)
Department of Fundamental Energy Science, Graduate School of Energy Science, Kyoto University, Yoshida-Honmachi, Sakyo-ku, Kyoto 606-8501, Japan
e-mail: yao@energy.kyoto-u.ac.jp

T. Yao (ed.), *Zero-Carbon Energy Kyoto 2011*, Green Energy and Technology,
DOI 10.1007/978-4-431-54067-0_18,

lithium insertion/extraction. Previously, Hibino et al. reported that the γ-Fe_2O_3/carbon composite prepared by the aqueous solution method showed high coulombic efficiency and rapid discharge–charge characteristics as cathode material [1]. Also, we examined the crystal structure changes of electrochemically lithium inserted γ-Fe_2O_3 at a various lithium insertion amount using the X-ray Rietveld analysis. It is revealed that iron moved from 8*a* site to 16*c* site in the process of lithium insertion, and then it is suggested that lithium is inserted at 8*a* site and iron is pushed out from 8*a* site to move into 16*c* site [2, 3].

Previously, Bonnet et al. [4] and Pernet et al. [5, 6] analyzed the crystal structure change of γ-Fe_2O_3 in terms of chemical lithium insertion using n-butyl lithium hexane solution. They reported that iron moved from tetrahedral sites to octahedral sites by the lithium insertion accompanying a spinel to rock salt transition. The detailed crystal structure analysis in the process of lithium insertion is thought to be important. In this study, we inserted lithium into γ-Fe_2O_3 at low Li concentration of n-butyl lithium hexane solution and investigate the lithium insertion mechanism by means of X-ray diffraction (XRD) measurement and the Rietveld analysis. Based on the experimental results, we discussed the crystal structure variations of γ-Fe_2O_3 in the process of lithium insertion.

2 Experimental

2.1 Chemical Lithium Insertion

Commercial γ-Fe_2O_3 powder (Soekawa chemical Co. Ltd., Japan, Particle size: ca. 1 μm, Purity: 99% min.) was used for this study. The chemical Li insertion was carried out by stirring the γ-Fe_2O_3 with 0.5 M solution of n-butyl lithium hexane. The reaction was carried out under argon gas atmosphere for 3 days. After the reaction, the products were thoroughly washed with the hexane to remove the excess n-butyl lithium and then the sample was obtained. The lithium content x in terms of $Li_XFe_2O_3$ was determined by inductively coupled plasma atomic emission spectroscopy (ICP: ICPS-7500, Shimadzu, Japan).

2.2 X-Ray Diffraction

We set the sample in a sealed holder (2391A201, Rigaku Corp., Ltd.) filled with argon gas. The sealed holder was set to the diffractometer for XRD measurement (UltimaIV, Rigaku Corp., Ltd.), and XRD patterns were measured from 25° to 135° in 2θ at a rate of 2° per min with 0.04° step width by using CuKα radiation. The tube voltage and current were set to 40 kV and 40 mA, respectively. We summed continuous ten patterns to make noise decrease and the Rietveld analysis precise.

2.3 The Rietveld Analysis

The obtained XRD pattern was analyzed by the Rietveld method using RIEVEC program coded by T. Yao [2, 3, 7, 8]. The crystal structure was represented by space group *Fd3m*, and the occupancies of iron at 8*a*, 8*b*, 16*c* and 16*d* sites were calculated. It was assumed that the atomicity of iron was constant equal to two per formula unit, and that contribution of lithium can be ignored. The lattice parameter was also refined by the Rietveld method.

3 Results and Discussion

As a result of ICP measurement, the Li content x in terms of $Li_XFe_2O_3$ reacted with 0.5 M solution of n-butyl lithium hexane for 3 days was 0.843.

In the XRD pattern, splitting of the peaks was observed. For example, in Fig. 1, splitting peak of 440 is shown. This splitting could not be explained by $K\alpha_1$, $K\alpha_2$ splitting because the peak separation did not coincide with the energy difference between $K\alpha_1$ and $K\alpha_2$ and because the intensity ratios of the splitting peaks were not constant peak by peak, but explained by the coexistence of two phase belonging to the same space group.

Figure 2 shows the fitting result of the Rietveld analysis. XRD profile of the sample was well-fitted with the pattern obtained by the Rietveld calculation. The reliability of the Rietveld calculation is given in the Fig. 1. The values of

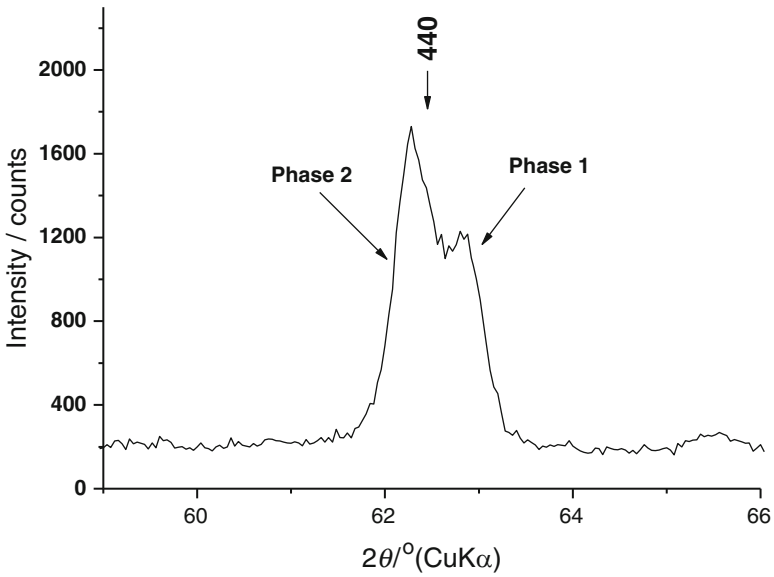

Fig. 1 Peak splitting of 440 reflection

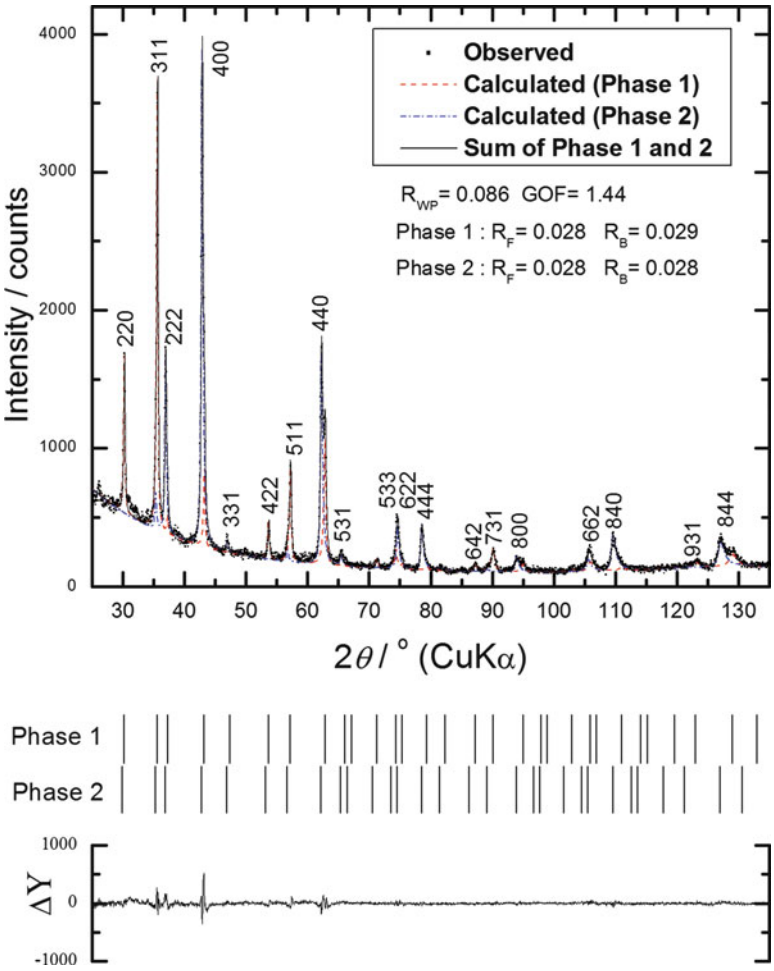

Fig. 2 A detailed drawing of the Rietveld result of the sample containing both phase 1 and phase 2 reacted with 0.5 M solution of n-butyl lithium hexane solution for 3 days. The observed pattern is shown by *dots*, and the calculated patterns for phase 1, phase 2 and the sum are shown by *red, blue and black lines*, respectively. The *vertical marks in the middle part* show positions calculated for Bragg reflection. The *trace in the bottom part* (ΔY) is a plot of the difference: observed minus calculated

R_{WP} (R-weighted pattern), R_F (R-structure factor) and R_B (R-Bragg factor) gave sufficiently small values and the GOF, goodness of fit, was close to one [9]. The Rietveld result confirmed that the sample was mixture of two phase both belonging to the space group of *Fd3m*. Only single phase refinement could not fit all of the diffraction peaks.

Table 1 The Rietveld analysis results

		Lattice parameter (Å)	Iron occupancy			
			8*a*	8*b*	16*c*	16*d*
$Li_{0.843}Fe_2O_3$	Phase 1 (Li-lean)	8.36686(10)	0.993(10)	0.000(4)	0.000(5)	0.837(5)
	Phase 2 (Li-rich)	8.44195(9)	0.000(9)	0.028(9)	0.461(7)	0.858(7)
γ-Fe_2O_3 before Li insertion[a]		8.34823(9)	1.000(3)	0.000(3)	0.008(2)	0.825(2)

[a]We also analyzed the γ-Fe_2O_3 before lithium insertion by the Rietveld method

Table 1 shows the Rietveld analysis results. In terms of phase 2, both lattice parameter and iron occupancies at each site are very near to those given by Bonnet et al. [4] and Pernet et al. [5, 6]. Phase 2 is thought to be the same phase given by them which is rich in lithium. Compared to γ-Fe_2O_3 before lithium insertion, the lattice parameter of phase 2 is far larger, the iron occupancy of 8*a* site decreased and that of 16*c* site increased by lithium insertion, and the iron occupancy at 8*b* site and 16*d* site did not changed significantly. It is indicated that iron moved from 8*a* site to 16*c* site, and then it is suggested that lithium is inserted at 8*a* site and iron is pushed out from 8*a* site to move 16*c* site. This phenomenon is very similar to that presented for electrochemical lithium insertion [2, 3]. On the other hands, in terms of phase 1, both lattice parameter and iron occupancies at each site are very similar to γ-Fe_2O_3 before lithium insertion. It is considered that phase 1 is lean in lithium.

We obtained the relative mol fraction of two phases in the sample by the Rietveld analysis. Generally, the relative mol fraction of phase p in a mixture of n phases was calculated by the following equation [10].

$$M_p = S_p(ZV)_p / \sum_{i=1}^{n} S_i(ZV)_i \tag{1}$$

where M_P, $S, Z, and\ V$ are the relative mol fraction of phase p in a mixture of n phases, the Rietveld scale factor, the number of formula units per unit cell and the unit cell volume (in $Å^3$), respectively. S can be refined by the Rietveld calculation, γ-Fe_2O_3 has eight formula units per unit cell and unit cell volume can be obtained by lattice parameter. The relative mol fraction of phase 1 and phase 2 was obtained as 37.6% and 65.4%, respectively. It is considered that the chemical lithium insertion take two phase process, i.e. inserted lithium forms a Li-rich phase (Phase 2) in which the Li amount is constant, and the overall Li concentration is controlled by the mol fraction change of phase 1 and phase 2. It is considered that the amount of phase 2 increase and phase 1 decrease with the increase of lithium insertion.

4 Conclusion

Lithium was chemically inserted into γ-Fe_2O_3 using 0.5 M solution of n-butyl lithium hexane solution. We analyzed the crystal structure in the process of lithium insertion by using the XRD measurement and the Rietveld method. It was found that the sample was mixture of two phase belonging to the space group of *Fd3m*, one is lithium rich and another is lithium lean. It is considered that the chemical lithium insertion take two phase process, i.e. inserted lithium forms a Li-rich phase in which the Li amount is constant, and the overall Li concentration is controlled by the mol fraction change in Li-rich phase and Li-lean phase.

Acknowledgement This work was partly supported by a "Energy Science in the Age of Global Warming" of Global Center of Excellence (G-COE) program (J-051) of the Ministry of Education, Culture, Sports, Science and Technology of Japan.

References

1. Hibino M, Terashima J, Yao T (2007) Reversible and rapid discharge–charge performance of γ-Fe_2O_3 prepared by aqueous solution method as the cathode for lithium-ion battery. J Electrochem Soc 154:A1107–A1111
2. Yamauchi S, Hibino M, Yao T (2011) Structure change analysis in γ-Fe_2O_3/carbon composite in the process of electrochemical lithium insertion. Solid State Ionics 191:45–48
3. Park S, Oda M, Yao T (2011) Relaxation Structure Analysis of Li Inserted γ-Fe_2O_3. Solid State Ionics 203:29–32
4. Bonnet B, Strobel P, Pernet M, Gondrand M, Gros Y, Mouget C, Chabre Y (1992) Structural aspects of lithium insertion into γ-Fe_2O_3. Mater Sci Forum 91–93:345–350
5. Pernet M, Strobel P, Bonnet B, Bordet P, Chabre Y (1993) Structural and electrochemical study of lithium insertion into γ-Fe_2O_3. Solid State Ionics 66:259–265
6. Pernet M, Strobel P (1995) Lithium insertion into iron spinels. Defect Diffusion Forum 127–128:73–92
7. Yao T, Ito T, Kokubo T (1995) Effect of Mn valence on crystal structure of La-Mn-O perovskite oxides. J Mater Res 10:1079–1082
8. Yao T, Ozawa N, Aikawa T, Yoshinaga S (2004) Analysis of layered structures of lithium–graphite intercalation compounds by one-dimensional Rietveld method. Solid State Ionics 175:199–202
9. Young RA (1995) In: Young RA (ed) The Rietveld method. Oxford University Press, Oxford, pp 21–24
10. Hill RJ (1995) In: Young RA (ed) The Rietveld method. Oxford University Press, Oxford, pp 95–96

Relaxation Phase Analysis of $LiMn_2O_4$ Cathode for Secondary Li Ion Battery

Im Sul Seo, Seungwon Park, and Takeshi Yao

Abstract Li-Mn-O system is expected to perform as a favorable electrode material for lithium ion battery due to its low cost, low toxicity and high electric capacity. We firstly extracted all amount of Li electrochemically and inserted Li till $x = 0.1$ at a rate of 1C in terms of $Li_xMn_2O_4$ electrochemically then stopped the insertion. We measured X-ray diffraction as a function of elapsed time after termination of Li insertion process and investigated phase change of $LiMn_2O_4$ material after termination of Li insertion process. From the asymmetric Lorentz peak fitting result of the XRD pattern, it was found that the two phases, Li-rich phase and Li-lean phase, coexist. It is found that the lattice constants of both phases were almost constant and that the amount of Li-lean phase decreased and Li-rich phase increased with the elapsed time.

Keywords Asymmetric Lorentz peak fitting • Li insertion • Phase change • XRD

1 Introduction

Various kinds of transition metal oxides have been investigated as an electrode material for secondary lithium ion battery. And as an example, $LiCoO_2$ has already been utilized in a practical rechargeable lithium battery. Recently among the various cathode materials, lithium manganese oxide with the spinel-type structure has expected to perform as a favorable electrode material because of its cost effectiveness, low toxicity and relatively high energy density.

It has been known that the electrochemical reactions during the charge/discharge process of secondary lithium ion battery have a considerable effect on the crystal structure of electrode material. As a previous study, Kanamura et al. reported on

I.S. Seo • S. Park • T. Yao (✉)
Graduate School of Energy Science, Kyoto University, Sakyo-ku, Kyoto 606-8501, Japan
e-mail: yao@energy.kyoto-u.ac.jp

T. Yao (ed.), *Zero-Carbon Energy Kyoto 2011*, Green Energy and Technology,
DOI 10.1007/978-4-431-54067-0_19,

crystal phase change of the $Li_xMn_2O_4$ in the process of Li extraction [1]. They found that $Li_xMn_2O_4$ is a single spinel type crystal (phase I) at $1 > x > 0.5$, then decompose to two spinel crystal (phase I and phase II) at $0.5 > x > 0.15$ and then move to another spinel crystal at $0.15 > x$ (phase II). Recently Yao et al. found that γ-Fe_2O_3, which is also one of promising electrode material, has changed its crystal structure after termination of Li insertion process by using the Rietveld crystal structure analysis [2–7]. In this regard, we investigated the phase change with time of $LiMn_2O_4$ cathode after termination of Li insertion process.

2 Experiment

$LiMn_2O_4$ was synthesized by solid-state reaction. In this study, Li_2CO_3 and MnO_2 were used as the starting materials for $LiMn_2O_4$. After we weighed Li_2CO_3 and MnO_2 in a mole ratio of 1:4, milled by electric mortar for 5 h, then calcinated at 823 K for 12 h in air. And the powder was pressed to a disk by 9.8 MPa, sintered at 1,073 K for 4 h. The crystal structure of the product was measured by X-ray diffraction (XRD) using Cu-Kα radiation, to confirm the formation of a well characterized $LiMn_2O_4$.

Electrochemical extraction and insertion of lithium from $LiMn_2O_4$ was performed by using an Ar-sealed three electrode glass cell. The working electrode was formed by mixing $LiMn_2O_4$, acetylene black (AB) and polytetrafluoro ethylene (PTFE) at a weight ratio of 0.8:0.15:0.05. The working electrode samples were crimped to a nickel mesh as the current collector. Ethylene carbonate (EC)/dimethoxyethane (DME) (1:1 volume ratio) containing 1.0 mol dm^{-3} $LiClO_4$ was used as the electrolyte solution. Lithium metal foil was used as the counter electrode and reference electrode. We firstly extracted all amount of lithium from $LiMn_2O_4$ electrochemically and took a rest for 20 min, then inserted lithium to $x = 0.1$ in terms of $Li_xMn_2O_4$ electrochemically at a rate of 1C.

In order to investigate the crystal phase change, XRD was measured as a function of elapsed time using a Model Ultima powder X-ray diffractometer (Rigaku Co., Tokyo, Japan; Cu-Kα radiation). The tube voltage and current was adjusted to 40 kV and 40 mA. The scanning technique with sampling steps of $2\theta = 0.01^\circ$ and scanning speed of 0.2° min^{-1} were used over the range $35^\circ \leq 2\theta \leq 40^\circ$. The XRD pattern was fitted by asymmetric Lorentz function and both the peak position and the peak area were obtained precisely.

3 Result and Discussion

Figure 1 shows the XRD pattern of $Li_{0.1}Mn_2O_4$ in the 2θ range from 35° to 40° (Cu-Kα). It is confirmed that two peaks coexist. We obtained the peak positions precisely by asymmetric Lorentz function fitting, as 36.98° and 36.61° in 2θ, 0.8056

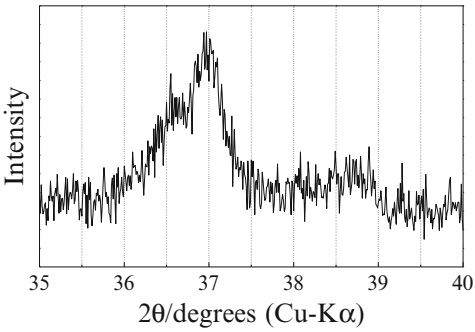

Fig. 1 XRD pattern of $Li_{0.1}Mn_2O_4$ by the electrochemical lithium insertion after lithium extraction from $LiMn_2O_4$

and 0.8134 nm in lattice constant, respectively. These lattice constants are well coincident with that of phase II (Li-lean phase) and phase I (Li-rich phase) reported by Kanamura et al. [1], respectively. From this reason, it is confirmed that $Li_{0.1}Mn_2O_4$ sample is a mixture of phase I and phase II. Maybe at Li insertion process, two phase region is different from that at extraction process. We investigated crystal phase change with time by using asymmetric Lorentz function fitting.

Figure 2 shows the observed and fitted XRD patterns of $Li_{0.1}Mn_2O_4$ for 1, 14 and 25 h of elapsed time, respectively. The observed pattern agreed well with the fitted pattern obtained from the asymmetric Lorentz function; such good agreement between the observed and fitted patterns was also obtained at every XRD pattern.

Figure 3 shows the lattice constant change of two phases in $Li_{0.1}Mn_2O_4$ with time after termination of Li insertion process. Both the lattice constant of phase I and that of phase II were almost constant. Figure 4 shows the change in the ratio of integrated intensity of the two phases. It is indicated that the amount of phase II decreased and that of phase I increased with the elapsed time. It is considered that phase II has more defects than phase I because of its lithium deficiency, so that phase II is kinetically favorable for Li to diffuse during lithium insertion. Therefore, phase II was preferably produced at the lithium insertion process. On the other hand, phase I is thermodynamically more stable than phase II because of its more stoichiometric composition. Therefore phase II decreased and phase I increased with elapsed time after termination of Li insertion process in $Li_{0.1}Mn_2O_4$.

4 Conclusion

We investigated the phase change with time of $LiMn_2O_4$ cathode after termination of Li insertion process. We firstly extracted all amount of lithium from $LiMn_2O_4$ electrochemically and took a rest for 20 min, then inserted lithium to $x = 0.1$ in terms of $Li_xMn_2O_4$ electrochemically at a rate of 1C. In order to investigate the crystal phase change, XRD was measured as a function of elapsed time.

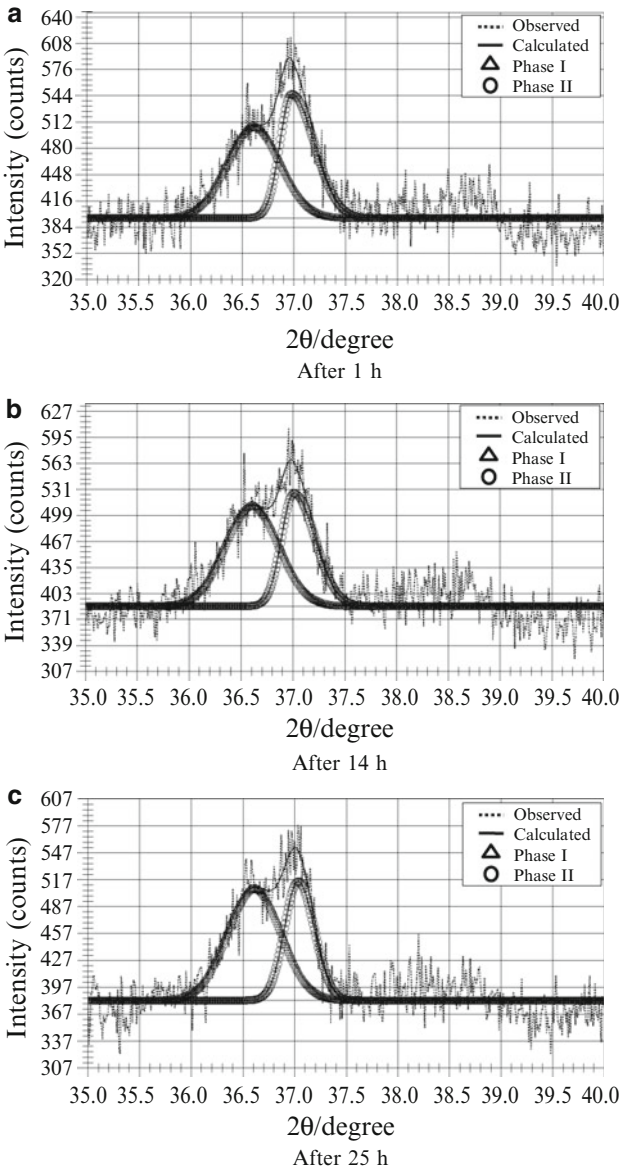

Fig. 2 The asymmetric Lorentz peak fitting to XRD patterns at (**a**) 1, (**b**) 14 and (**c**) 25 h elapsed time after termination of Li insertion process

Two phases, Li-rich phase with lattice constant 0.8136 nm and Li-lean phase with lattice constant 0.8042 nm, coexist in $Li_{0.1}Mn_2O_4$. Both two lattice constants were almost constant with the elapsed time. The Li-lean phase decreased and the Li-rich phase increased with elapsed time. It is considered that Li-lean phase has

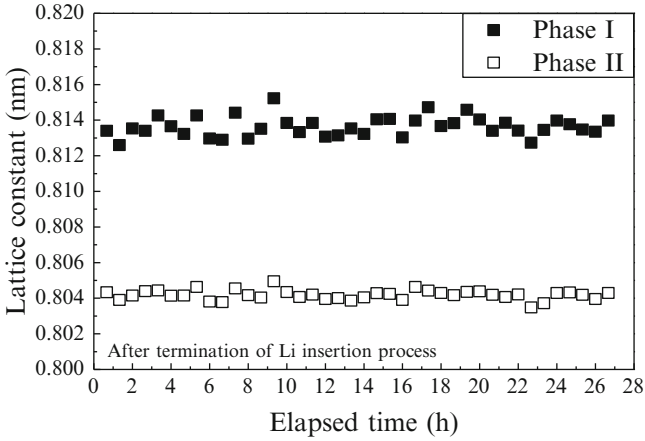

Fig. 3 Lattice constant change of two phases in $Li_{0.1}Mn_2O_4$ after termination of Li insertion process

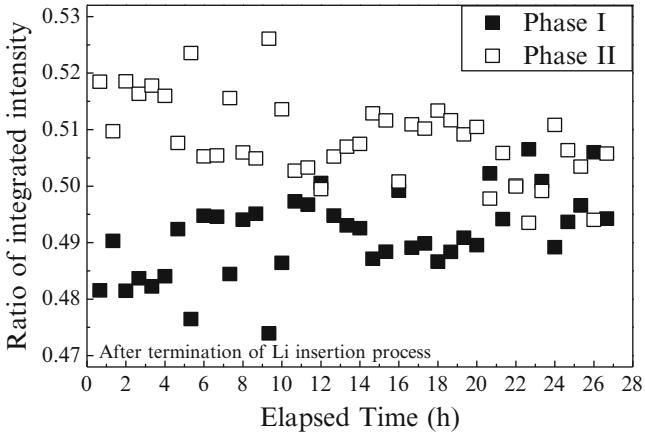

Fig. 4 Ratio of integrated intensity of two phases in $Li_{0.1}Mn_2O_4$ after termination of Li insertion process

more defects than Li-rich phase because of its Li deficiency, and that Li-lean phase is kinetically favorable for Li to diffuse. Therefore, Li-lean phase was preferably produced at the Li insertion process. On the other hand, Li-rich phase is thermodynamically more stable than Li-lean phase because of its more stoichiometric composition, therefore Li-lean phase decreased and Li-rich phase increased after termination of Li insertion process.

Acknowledgement This work was partly supported by a "Energy Science in the Age of Global Warming" of Global Center of Excellence (G-COE) program (J-051) of the Ministry of Education, Culture, Sports, Science and Technology of Japan.

References

1. Kanamura K, Naito H, Yao T, Takehara Z (1996) Structure change of the $LiMn_2O_4$ spinel structure induced by extraction of lithium. J Mater Chem 6(1):33–36
2. Yamauchi S, Hibino M, Yao T (2011) Structure change analysis in γ-Fe_2O_3/carbon composite in the process of electrochemical lithium insertion. Solid State Ionics 191:45–48
3. Park S, Oda M, Yabutsuka T, Yao T (2011) Crystal structure analysis with time for γ-Fe_2O_3 lithium inserted at various rates. Electrochem. Soc., 219th ECS Meeting, Montreal, QC, Canada, 2th May CD Abst. 042
4. Park S, Oda M, Yabutsuka T, Hibino M, Yao T (2010) Crystal structure analysis with time for lithium inserted γ-Fe_2O_3 with various insertion rate. International Conference "Innovations for Renewable Energy", Hanoi, Vietnam, 21st September pp 203–204
5. Oda M, Park S, Yabutsuka T, Hibino M, Yao T (2010) Crystal structure change analysis with time for Li inserted γ-Fe_2O_3. Electrochem. Soc., 218th ECS Meeting, Las Vegas, Nevada, 11th October CD Abst. 049
6. Park S, Oda M, Yabutsuka T, Hibino M, Yao T (2010) Crystal structure change analysis with time for lithium inserted γ-Fe_2O_3. The 51th battery symposium, Nagoya, Japan, 9th November p 172
7. Park S, Oda M, Yao T (2011) Relaxation structure analysis of Li inserted γ-Fe_2O_3. Solid State Ionics 203:29–32

Synthesis of Sodium Cerium Sulfate ($NaCe(SO_4)_2 \cdot H_2O$) from Cerium Oxide in Sulfuric Acid Solutions

Namil Um and Tetsuji Hirato

Abstract The synthesis of sodium cerium oxide ($NaCe(SO_4)_2 \cdot H_2O$) from cerium oxide (CeO_2) in sulfuric acid solutions with addition of Na_2SO_4 was examined at elevated temperatures using a batch-type glass reactor under atmospheric pressure. Na_2SO_4 concentration, sulfuric acid concentration and reaction temperature were chosen for the factors, and the effect of three factors on conversion of CeO_2 into $NaCe(SO_4)_2 \cdot H_2O$ in sulfuric acid solutions was investigated. The conversion includes two chemical reactions; CeO_2 dissolution and $NaCe(SO_4)_2 \cdot H_2O$ precipitation. It was found that the increase of Na_2SO_4 concentrations and sulfuric acid decreased the conversion rate, whereas the conversion rate increased with increasing reaction temperature.

Keywords Cerium oxide • Convert • Sodium cerium sulfate • Sulfuric acid • Synthesis

1 Introduction

Since cerium oxide is widely used as a polishing powder for glass, semiconductor and ceramic, the large amounts of polishing powder wastes (PPWs) containing cerium oxide have been generated [1, 2]. Unfortunately most of PPWs have been buried in landfill because it is not easy to be treated chemically or physically. Recently the demand of rare earth metals has been increased in the world, therefore, many researchers are beginning to take interest in recovery of cerium oxide from PPWs. One of the treatment processes proposed for cerium oxide recovery from PPWs is a hydrometallurgical one including the acid leaching of PPWs in sulfuric

N. Um • T. Hirato (✉)
Department of Energy Science and Technology, Kyoto University,
Yoshida-Honmachi, Sakyo-ku, Kyoto 611-0011, Japan
e-mail: hiratou@energy.kyoto-u.ac.jp

T. Yao (ed.), *Zero-Carbon Energy Kyoto 2011*, Green Energy and Technology,
DOI 10.1007/978-4-431-54067-0_20,

acid solutions [3] and the synthesis of sodium cerium sulfate ($NaCe(SO_4)_2{\cdot}H_2O$) from the leached solution. This process could lead to the way to separate the cerium oxide from PPWs because $NaCe(SO_4)_2{\cdot}H_2O$ is poorly soluble under acidic condition and becomes cerium hydroxide under alkaline condition [4].

In this study, the synthesis of $NaCe(SO_4)_2{\cdot}H_2O$ from CeO_2 in sulfuric acid solutions was experimented at elevated temperatures using a batch-type glass reactor under atmospheric pressure. A number of experiments were conducted to study the effect of Na_2SO_4 addition, sulfuric acid concentration and temperature on the dissolution of CeO_2 and the synthesis of $NaCe(SO_4)_2{\cdot}H_2O$. Because these are important factors on the kinetics of conversion of CeO_2 into $NaCe(SO_4)_2{\cdot}H_2O$ in sulfuric acid solution.

2 Materials and Methods

The cerium oxide (CeO_2) powder (Sigma Aldrich, Ltd.) with the particle size of below 5 μm was used. The experiments of sodium cerium oxide ($NaCe(SO_4)_2{\cdot}H_2O$) synthesis from CeO_2 in sulfuric acid solution were carried out by using a batch glass reactor of 500 mL. CeO_2 powder of 4 mmol was added to 100 mL of sulfuric acid solutions containing Na_2SO_4. The concentration of Na_2SO_4 was ranged from 0.2 to 2.0 mol L^{-1}, and the concentration of sulfuric acid from 8 to 14 M. The solution was heated and kept at the temperatures of 105°C, 115°C, 125°C and 135°C under atmospheric pressure. The solution was stirred by magnetic stirrer at 650 rpm.

To confirm the kinetics of conversion of CeO_2 into $NaCe(SO_4)_2{\cdot}H_2O$, the samples taken at different reaction times were filtered and measured using X-ray diffractometer (PANalytical, X'pert PRO) for mineralogical analysis.

For measuring the weight of CeO_2 residue and synthesized $NaCe(SO_4)_2{\cdot}H_2O$, the precipitate obtained after reaction was filtered from the solution on a 0.5 μm pore size membrane using a pressure filtration unit, and was washed 3 times using ethanol for removal of sulfuric acid. After drying at 45°C for 24 h, the weight (1) of the precipitate consisting of CeO_2 residue and synthesized $NaCe(SO_4)_2{\cdot}H_2O$ was measured by balance. The precipitate was added into 1 M NaOH solution for conversion from $NaCe(SO_4)_2{\cdot}H_2O$ to $Ce(OH)_3$. Then it was added into 1 M H_2SO_4 solution to dissolve $Ce(OH)_3$ and recover CeO_2 residue. The weight (2) of CeO_2 residue was measured by balance after drying at 45°C for 24 h. The difference of (1) and (2) determined the weight of synthesized $NaCe(SO_4)_2{\cdot}H_2O$.

3 Results and Discussion

The conversion of cerium oxide (CeO_2) into sodium cerium sulfate ($NaCe(SO_4)_2{\cdot}H_2O$) in sulfuric acid solutions is supposed to include two chemical reactions as follows.

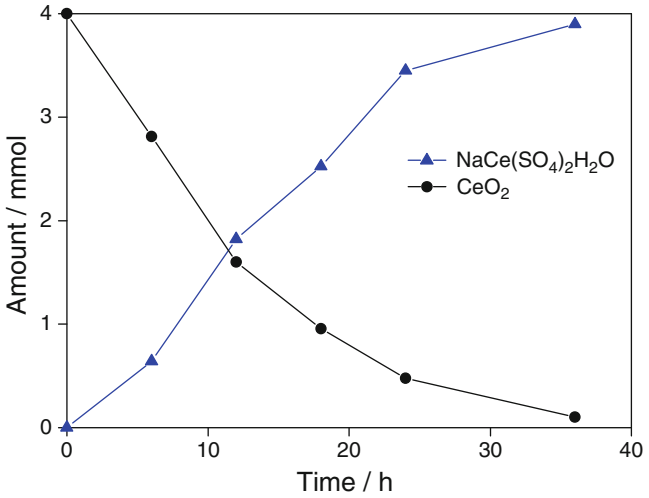

Fig. 1 Amounts of CeO_2 residue and synthesized $NaCe(SO_4)_2{\cdot}H_2O$ at different reaction times in 8 mol dm^{-3} H_2SO_4–0.2 mol dm^{-3} Na_2SO_4 solutions at 125°C

Dissolution of CeO_2 can be ascribed as follow below:

$$CeO_2 + 4H^+ \rightarrow Ce^{4+} + 2H_2O \quad (1)$$

And the dissolution is immediately followed by the synthesis of $NaCe(SO_4)_2{\cdot}H_2O$ as follow below:

$$Ce^{4+} + 2Na_2SO_4 + 3/2H_2O \rightarrow NaCe(SO_4)_2 \cdot H_2O + H^+ + 3Na^+ + 1/4O_2 \quad (2)$$

Figure 1 shows the amounts of CeO_2 and $NaCe(SO_4)_2{\cdot}H_2O$ included in the precipitate at different reaction times. The amount of CeO_2 decreased monotonically with increasing reaction time, while the amount of synthesized $NaCe(SO_4)_2{\cdot}H_2O$ increased. The XRD patterns of the precipitates obtained at different reaction times are shown in Fig. 2. The intensity of the diffraction peaks originated from CeO_2 decreased with an increase in reaction time, while that from $NaCe(SO_4)_2{\cdot}H_2O$ increased. This result is in accord with that shown in Fig. 1. These findings indicate CeO_2 can be converted into $NaCe(SO_4)_2{\cdot}H_2O$ in sulfuric acid solutions containing Na_2SO_4.

The effects of Na_2SO_4 concentration, sulfuric acid concentration and temperature on the synthesis of $NaCe(SO_4)_2{\cdot}H_2O$ from CeO_2 in sulfuric acid solutions were examined, since the variables are important factors related to the kinetics.

$NaCe(SO_4)_2{\cdot}H_2O$ was synthesized from CeO_2 in 8 mol dm^{-3} H_2SO_4 solutions with different Na_2SO_4 concentrations ranged from 0.2 to 2.0 mol dm^{-3}, and the results obtained are shown in Fig. 3. The amount of CeO_2 residue after reaction increases with increasing Na_2SO_4 concentration. This result suggests that the

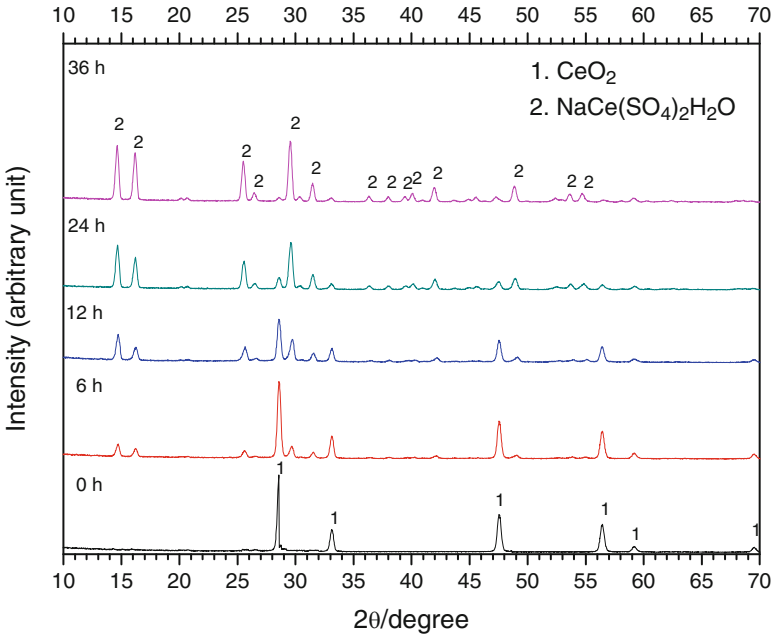

Fig. 2 XRD patterns of the precipitate obtained at different reaction times in 8 mol dm^{-3} H_2SO_4–0.2 mol dm^{-3} Na_2SO_4 solutions at 125°C

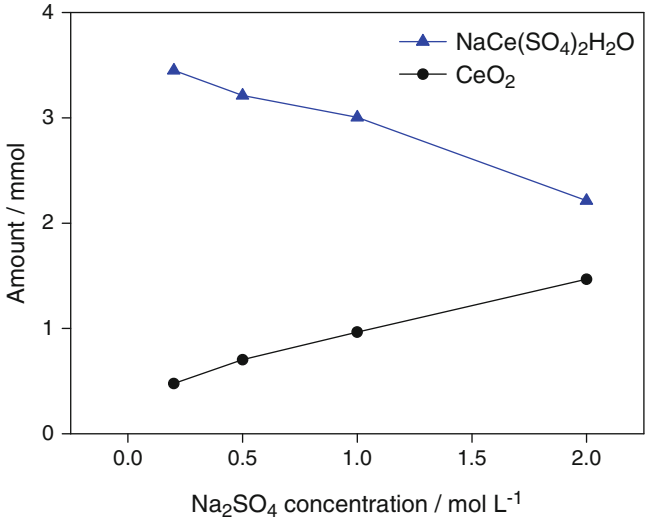

Fig. 3 Effect of Na_2SO_4 concentration on conversion from CeO_2 to $NaCe(SO_4)_2{\cdot}H_2O$ in 8 mol dm^{-3} H_2SO_4 solutions at 125°C for 24 h

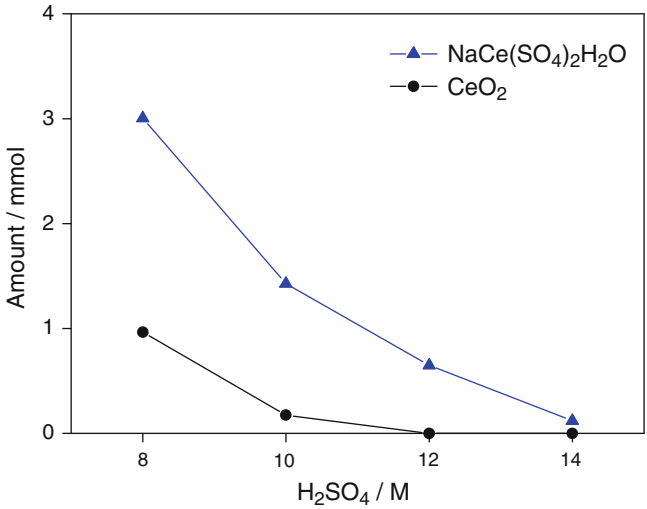

Fig. 4 Effect of sulfuric acid concentration on conversion from CeO_2 to $NaCe(SO_4)_2{\cdot}H_2O$ in sulfuric acid solutions containing 1.0 mol dm^{-3} Na_2SO_4 at 125°C for 24 h

excess of Na_2SO_4 suppresses CeO_2 dissolution and leads to a decrease of $NaCe(SO_4)_2{\cdot}H_2O$ synthesis rate. Figure 4 shows the effect of sulfuric acid concentration on the conversion of CeO_2 into $NaCe(SO_4)_2{\cdot}H_2O$. The increase in sulfuric acid concentration from 8 to 14 mol dm^{-3} increased CeO_2 dissolution rate, but it decreased $NaCe(SO_4)_2{\cdot}H_2O$ synthesis rate. These findings suggest that the solubility of $NaCe(SO_4)_2{\cdot}H_2O$ increased at higher sulfuric acid concentrations. Figure 5 shows the effect of reaction temperature on the conversion of CeO_2 into $NaCe(SO_4)_2{\cdot}H_2O$. Both CeO_2 dissolution and $NaCe(SO_4)_2{\cdot}H_2O$ synthesis rates increased with an increasing reaction temperature. Especially the temperature increase from 125°C to 135°C highly improved $NaCe(SO_4)_2{\cdot}H_2O$ synthesis rate; it is expected that the solubility of $NaCe(SO_4)_2{\cdot}H_2O$ decreased at higher temperatures.

4 Conclusions

The conversion of cerium oxide (CeO_2) into sodium cerium sulfate ($NaCe(SO_4)_2{\cdot}H_2O$) in sulfuric acid solutions has two chemical reactions as follow below:

$$CeO_2 + 4H^+ \rightarrow Ce^{4+} + 2H_2O$$

$$Ce^{4+} + 2Na_2SO_4 + 3/2H_2O \rightarrow NaCe(SO_4)_2 \cdot H_2O + H^+ + 3Na^+ + 1/4O_2$$

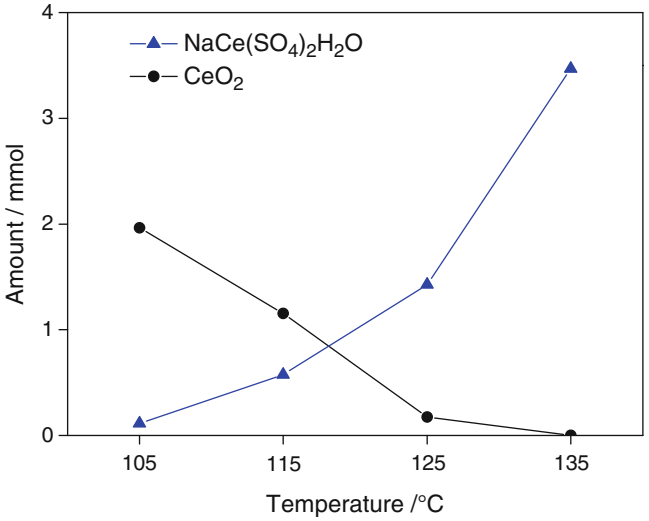

Fig. 5 Effect of temperature on conversion from CeO_2 to $NaCe(SO_4)_2{\cdot}H_2O$ in 10 mol dm^{-3} H_2SO_4–1.0 mol dm^{-3} Na_2SO_4 solutions for 24 h

Na_2SO_4 concentration, sulfuric acid concentration and reaction temperature were the factors to affect the conversion rate. The excess of Na_2SO_4 suppresses CeO_2 dissolution and leads to a decrease of $NaCe(SO_4)_2{\cdot}H_2O$ synthesis rate. The increase in sulfuric acid concentration decreased $NaCe(SO_4)_2{\cdot}H_2O$ synthesis rate. This is attributable to the increase in solubility of $NaCe(SO_4)_2{\cdot}H_2O$ at higher sulfuric acid concentrations. Both CeO_2 dissolution and $NaCe(SO_4)_2{\cdot}H_2O$ synthesis rates increased with an increasing reaction temperature.

Acknowledgement This work was partly supported by an "Energy Science in the Age of Global Warming" of Global Center of Excellence (G-COE) program (J-051) of the Ministry of Education, Culture, Sports, Science and Technology of Japan.

References

1. Sabia R, Stevens HJ, Varner FR (1999) Pitting of a glass-ceramic during polishing wth cerium oxide. Non-Cryst Solids 249:123–130
2. Ong NS, Venkatesh VC (1998) Semi-ductile grinding and polishing of pyrex glass. Mater Process Tech 83:261–266
3. Um N, Miyake M, Hirato T (2010) Dissolution of cerium oxide in sulfuric acid. Zero-Carbon Energy Kyoto 2010, Springer, Tokyo:165–170
4. Lokshin EP, Tareeva OA, Ivleq KG, Kashulina TG (2005) Solubility of double alkali metal (Na, K) rare-earth (La, Ce) sulfates in sulfuric-phosphoric acid solutions at 20°C. Russ J Appl Chem 78:1058–1063

Study on Hydrogen-Jet Development in the Argon Atmosphere

Mohd Radzi Abu Mansor, Shinji Nakao, Katsutaka Nakagami, and Masahiro Shioji

Abstract Hydrogen is one of the promising energy carriers for the future because of its low polluting feature that can be used mainly in internal combustion engine. Since hydrogen combustion in the noble-gas and oxygen atmosphere forms only water, closed-cycle operations for a zero-emission and high-efficiency engine would be realized. In order to find the optimal condition of hydrogen injection in the argon circulated hydrogen engine, characterization of the hydrogen-jet penetration is required to be analyzed. In this study, experiments were made in a constant-volume vessel to investigate the hydrogen-jet developments for different conditions of injection pressure, ambient pressure and nozzle diameter in argon and nitrogen atmospheres. Also, high-speed shadowgraph images were observed at an individual case. Obtained data exhibit that the development of the hydrogen-jet in argon is slower than that in nitrogen due to its high density and faster at a higher injection pressure, at a lower ambient pressure and with a larger nozzle-orifice diameter. Characteristics of hydrogen jets were discussed through those fundamental data, which may help setting design parameters and controlling operational conditions in the argon circulated hydrogen engine.

Keywords Argon • Closed-cycle engine • Constant-volume vessel • Hydrogen-jet • Visualization

M.R.A. Mansor* (✉) • S. Nakao • K. Nakagami • M. Shioji
Graduate School of Energy Science, Kyoto University, Kyoto 606-8501, Japan

*The author M.R.A. Mansor is a PhD student in Graduate School of Energy Science, Kyoto University from Universiti Kebangsaan Malaysia, Bangi, 43600, Malaysia.
e-mail: m.radzi@ax4.ecs.kyoto-u.ac.jp

T. Yao (ed.), *Zero-Carbon Energy Kyoto 2011*, Green Energy and Technology,
DOI 10.1007/978-4-431-54067-0_21,

1 Introduction

The usage of high specific heat ratio argon as a working gas dramatically improves the thermal efficiency of an engine's operation [1, 2]. However, the rare gas argon is difficult to carry in large amount, creating the essential need of recirculation. Hydrogen combustion in a noble-gas and oxygen atmosphere would form only water. Therefore, by simply removing the water element, the reuse of argon would be realized. To date, only a considerable amount of fundamental data for finding the optimal design and operating conditions in argon circulated hydrogen engine can be obtained. This study observes hydrogen-jet development using high-speed shadowgraph images in a constant-volume vessel filled with argon, in order to obtain guideline for hydrogen injection in argon circulated hydrogen engine. The effects of ambient conditions and injection conditions were examined, and its differences in nitrogen atmosphere were also identified.

2 Experimental

2.1 Experimental Setup and Procedure

In this research, experiments were carried out in a constant-volume vessel. The combustion chamber is schematically shown in Figure 1. The chamber is a circular cylinder, 80 mm in diameter, 30 mm in depth, has approximately 150 cc of volume and is fitted with 25 mm thick quartz window for optical access. A solenoid-type gas injector, fitted at the top of the chamber, was used to inject high-pressure hydrogen fuel into the chamber at an injection pressure of up to 15 MPa after filling a predetermined ambient pressure of argon or nitrogen. Table 1 indicates the experimental conditions for the present study. The underlined numbers in the table correspond to the standard conditions.

For the purpose of this study, angle of divergence and penetration length were measured. Angle of divergence of jet ψ refers to the projection line on both sides of the hydrogen-jet diverging from the injector tip when the jet penetrated half way into the vessel. Penetration length x_t were measured horizontally from the end of injector tip to the hydrogen-jet penetration tip.

3 Result and Discussion

3.1 Comparison with Nitrogen Atmosphere

Development of hydrogen-jet in the argon atmosphere was first examined and compared with the data acquired from the experiment in the nitrogen atmosphere, with both charged at standard condition of $p_i = 1.2$ MPa, $T_i = 300$ K. Figure 2 shows

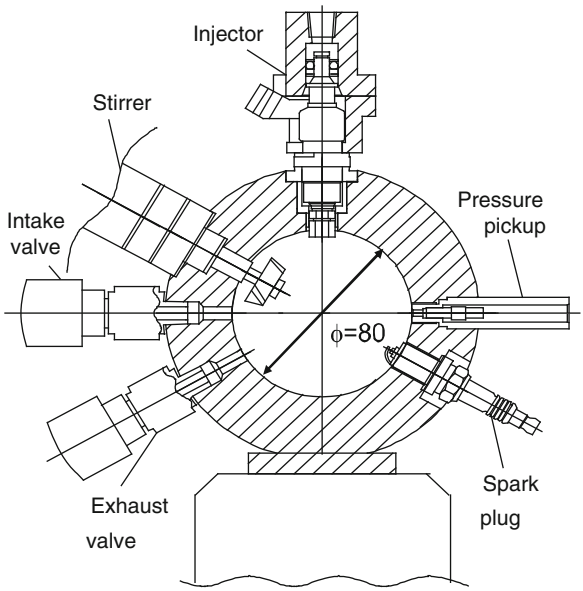

Fig. 1 Cross-section of constant-volume vessel

Table 1 Experimental conditions

Hydrogen jet	
Atmosphere	Argon, Nitrogen
Injection pressure p_j, MPa	4, 8, 14
Ambient pressure p_i, MPa	0.6, 1.2, 1.5
Nozzle-orifice diameter d_N, mm	0.4, 0.56, 0.8

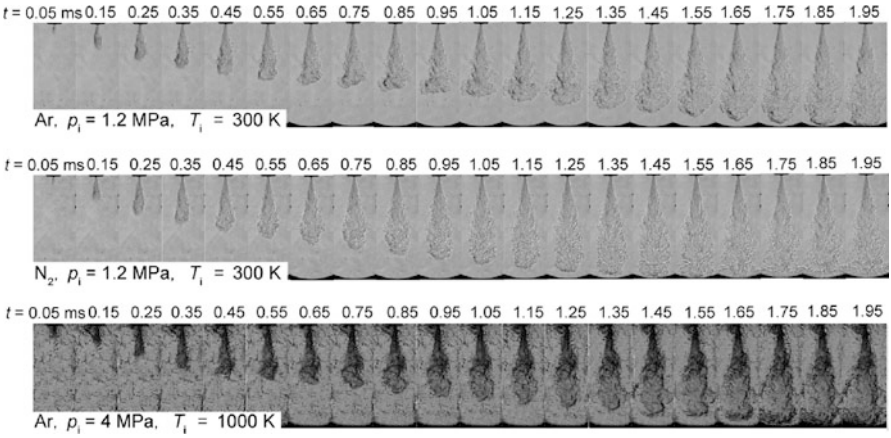

Fig. 2 H_2-Jet developments in Ar and N_2 atmospheres ($p_j = 8$ MPa, $d_N = 0.8$ mm)

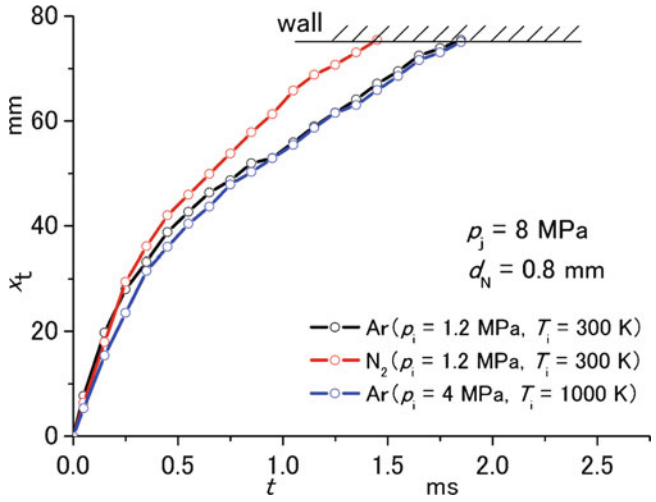

Fig. 3 Penetration length x_t of H_2 Jet in Ar and N_2 atmospheres

the shadowgraph images of hydrogen injected to a pressurized combustion vessel from the injection start to time t. Comparison of the overall images in the upper row and middle row shows that the angle of divergence of hydrogen jet in argon atmosphere is slightly larger. This is because the density of argon is larger than the density of nitrogen, the momentum to the traveling direction is weakened, and the jet flow diffused. To further validate the experiment, stoichiometric hydrogen–oxygen mixture in argon atmosphere combustion to form high temperature high pressure condition ($p_i = 4$ MPa, $T_i = 1{,}000$ K) which equal in density with argon atmosphere at standard condition was performed and the images were shown in the bottom row of Fig. 2.

Figure 3 shows the comparison of the penetration length of hydrogen x_t with time in different atmosphere. The observation result shows the difference between the argon atmosphere and the nitrogen atmosphere start from $x_t = 0.25$ ms with larger expansion recorded from 0.65 ms onward. The hydrogen-jet penetration tip in nitrogen atmosphere hit the bottom wall of constant-volume vessel at $t = 1.45$ ms while penetration tip in the argon atmosphere hit the bottom wall at $t = 1.85$ ms. There is no difference between argon atmosphere in standard condition and high pressure high temperature condition that also hit the bottom wall at $t = 1.85$ ms.

3.2 *Effects of Injection Pressure*

Next, effect of the injection pressure on the hydrogen-jet development was examined. Figure 4 shows the shadowgraph image of hydrogen-jet development injected into the argon atmosphere combustion vessel, with injection pressure

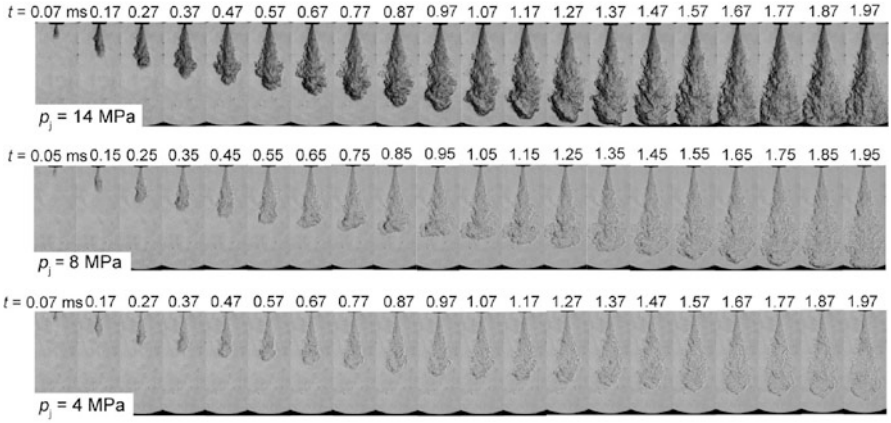

Fig. 4 H_2-Jet developments in Ar atmosphere for different p_j ($T_i = 300$ K, $p_i = 1.2$ MPa, $d_N = 0.8$ mm)

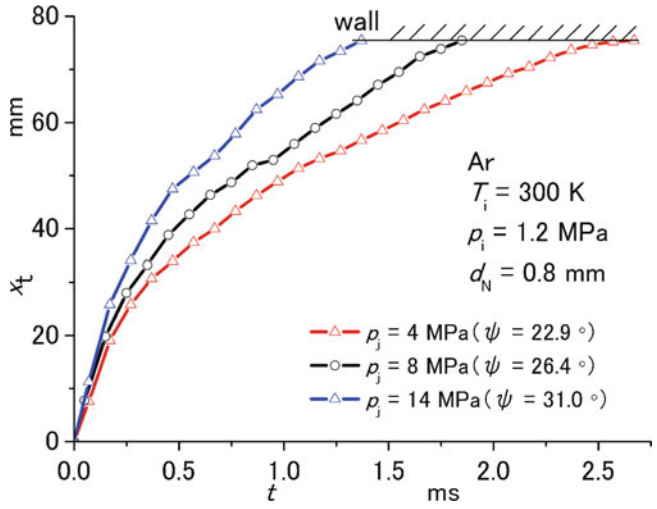

Fig. 5 Penetration length x_t of H_2 Jet for different p_j

of $p_j = 14$, 8, 4 MPa. Angle of divergence of hydrogen jet decrease as p_j decreased and the penetration tip hit the bottom wall at earlier time compared to the low injection pressure. Figure 5 shows the comparison of the penetration length x_t of hydrogen jet for different injection pressure p_j. Higher injection pressure effect the time penetration tip to hit the bottom wall at 1.37, 1.85 and 2.67 ms with $p_j = 14$, 8, and 4 MPa, respectively.

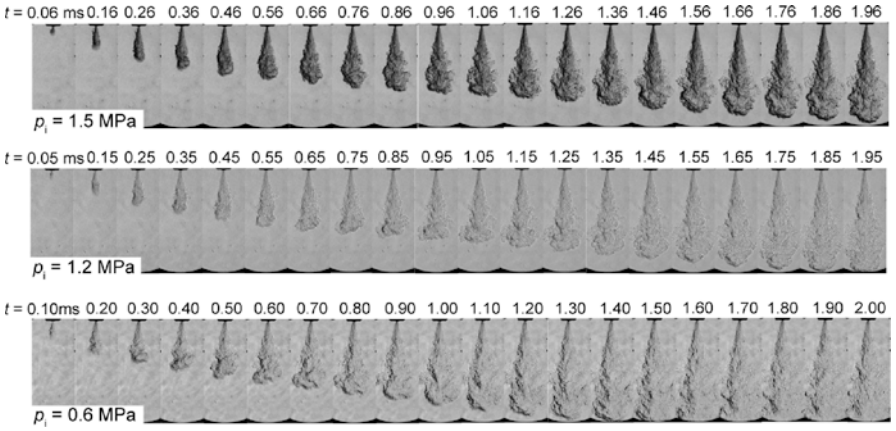

Fig. 6 H_2-Jet developments in Ar atmosphere for different p_i ($T_i = 300$ K, $p_j = 8$ MPa, $d_N = 0.8$ mm)

3.3 *Effects of Ambient Pressure*

Next, effect of ambient pressure on the hydrogen-jet development was examined. Figure 6 shows the shadowgraph image of hydrogen-jet development injected into the argon atmosphere, with ambient pressure of $p_i = 1.5$, 1.2, 0.6 MPa. The result from injection start to time t shows that higher ambient pressure indicate high density which affect the penetration tip to hit the bottom wall at longer time. Figure 7 shows the comparison of the penetration length x_t of hydrogen-jet for different ambient pressure p_i. Higher ambient pressure effect the time penetration tip to hit the bottom wall at 2.11, 1.85 and 1.40 ms with $p_i = 1.5$, 1.2 and 0.6 MPa, respectively. Angle of divergence of jet ψ which were obtained from each image indicating that ψ become smaller as the ambient pressure increased due to the effect of the jet boundary shear.

3.4 *Effects of Nozzle-Orifice Diameter*

Finally, effect of nozzle-orifice diameter on the hydrogen-jet development was examined with standard condition of $p_j = 8$ MPa and $p_i = 1.2$ MPa. Figure 8 shows the shadowgraph image of hydrogen-jet development injected into the argon atmosphere, for different injector nozzle-orifice diameter $d_N = 0.8$, 0.56, 0.4 mm. The result from injection start to time t indicates that larger nozzle-orifice diameter would result in the penetration tip to hit the bottom wall at an earlier time and an increase in the angle of divergence of hydrogen-jet. Figure 9

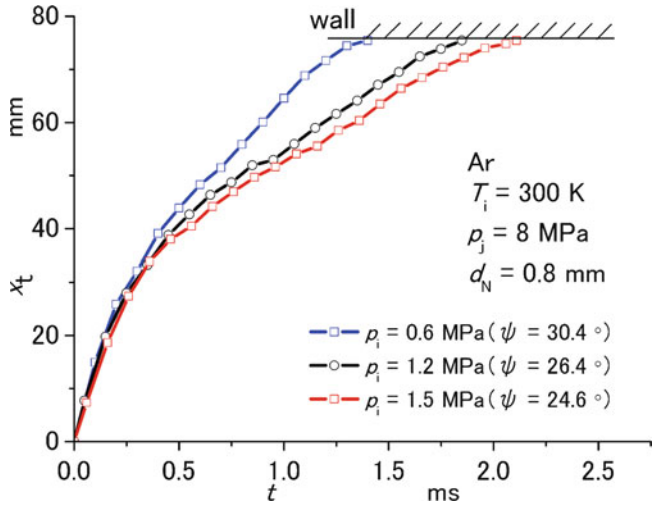

Fig. 7 Penetration length x_t of H_2 Jet for different p_i

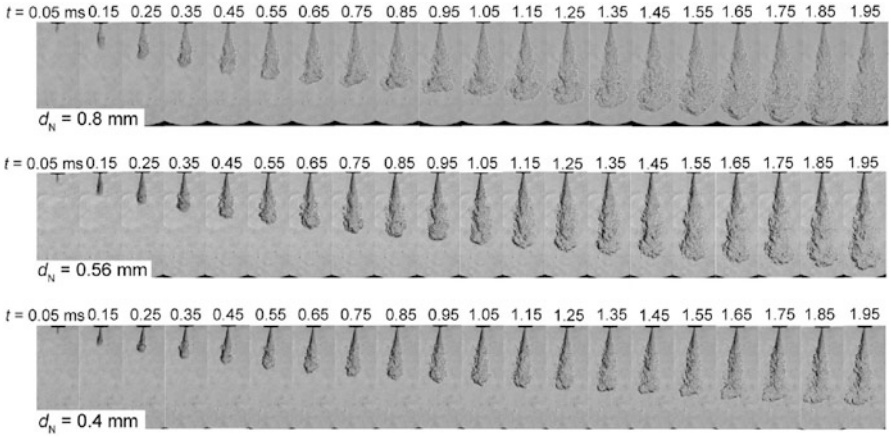

Fig. 8 H_2-Jet developments in Ar atmosphere for different d_N ($T_i = 300$ K, $p_j = 8$ MPa, $p_i = 1.2$ MPa)

shows the comparison of the penetration length x_t of hydrogen-jet for different nozzle-orifice diameter d_N. Larger nozzle-orifice diameter effect the time penetration tip to hit the bottom wall at 1.85, 2.35 and 3.45 ms with $d_N = 0.8$, 0.56 and 0.4 mm, respectively.

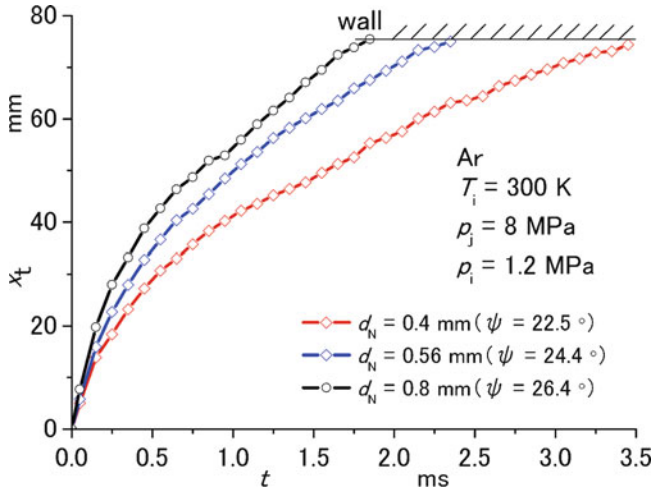

Fig. 9 Penetration length x_t of H_2 Jet for different d_N

4 Conclusions

In order to obtain guideline for hydrogen injection in argon circulated hydrogen engine, observation of hydrogen-jet development using high-speed shadowgraph images in a constant-volume vessel filled with argon has been made. As a result, hydrogen-jet development in argon atmosphere is slower than in nitrogen atmosphere due to higher density of argon. Higher injection pressure and larger nozzle-orifice diameter resulted in a faster hydrogen-jet development and larger angle of divergence. Lower ambient pressure resulted in a faster hydrogen-jet development with larger angle of divergence which is due to the effect of the jet boundary share and viscosity which requires further study of the mechanism.

Acknowledgement The authors were grateful for the support of the Ministry of Education, Culture, Sports, Science and Technology of Japan via "Energy Science in the Age of Global Warming" of Global Center of Excellence (G-COE) program (J-051) and also would like to thank Toyota Motor Corporation for partly supporting the research grant and providing the gas-injection system used in conducting this study.

References

1. Ikegami M, Miwa K, Shioji M (1982) A study of hydrogen fuelled compression ignition engines. Int J Hydrogen Energ 7:341–353
2. Kuroki R, Kato A, Kamiyama E, Sawada D (2010) Study of high efficiency zero-emission argon circulated hydrogen engine. SAE Technical Paper 2010-01-0581

Theoretical Study of Particle Motion Under High Intensity Laser–Plasma Interaction Aiming for High Energy Density Science

Natsumi Iwata, Yasuaki Kishimoto, and Kenji Imadera

Abstract In recent years, high power short pulse lasers in the range of $10^{18–22}$ W/cm^2 have been developed and explored new science and applications. One of them is the fast ignition-based laser fusion, which is expected as one of clean and abundant energy sources. In determining the interaction between such high intensity lasers and plasmas, the ponderomotive force (light pressure) plays an essential role due to the strong non-uniformity of the laser field strength originated from tight focusing of the laser light. The force has been expressed as that proportional to the gradient of the laser field amplitude at the oscillation center of the particle. However, under the tight focusing, not only the gradient, which corresponds to the first-order perturbation to the uniform field, but also the higher order structures, e.g. field curvature to the second order, becomes important in determining the particle orbit. In order to precisely describe the relativistic ponderomotive force including such effects, here, we introduce the noncanonical Lie perturbation theory. We successfully derived the oscillation-center equation of motion up to the second order keeping the Hamiltonian structure rigorously. The resulting equation is found to be same as that of the first order indicating that no additional force appears up to the second order due to the symmetric nature of the field curvature.

Keywords High intensity laser field • Lie perturbation theory • Noncanonical Hamiltonian mechanics • Ponderomotive force

N. Iwata (✉) • Y. Kishimoto • K. Imadera
Graduate School of Energy Science, Kyoto University, Gokasho, Uji, Kyoto 611-0011, Japan
e-mail: iwata@center.iae.kyoto-u.ac.jp

T. Yao (ed.), *Zero-Carbon Energy Kyoto 2011*, Green Energy and Technology,
DOI 10.1007/978-4-431-54067-0_22,

1 Introduction

High-quality and coherent energy plays an important role in energy science as found that laser, a coherent light with low entropy state, is now an essential tool in sus taining not only academic science but also various industrial technologies. Interestingly, even in the case of 1 J light energy, when it is confined in 10 femtoseconds ($= 10^{-14}$ s) in time, the power reaches to 10^{14} W which is larger than the energy that the whole human being is exhausting, i.e., about 10^{13} W. In the past two decades, high power short pulse lasers whose intensities exceed 10^{20} W/cm^2 have been innovatively developed and explored new science referred to as *high energy density science*. They have opened up various applications such as high intensity coherent X-ray and neutron sources, compact particle accelerators, and fast ignition-based laser fusion. Electrons irradiated by such lasers exhibit a nonlinear relativistic behavior, so that the interaction becomes complicated dominated by nonlinear and non-equilibrium processes. Recently, efforts aiming at higher intensities of $10^{23–26}$ W/cm^2 have been made where not only electrons but also ions become relativistic. In this regime, entirely new physical processes, e.g. radiation damping, electron-positron cascade, vacuum breakdown, are expected to dominate the interaction [1, 2]

Since these high intensities can be achieved by reducing the pulse length and/or the spot size to the level of laser wavelength, the *ponderomotive force*, which corresponds to the light pressure resulting from the non-uniformity of the laser field, is of critical importance in determining the interaction. Namely, fundamental physical processes such as propagation of the laser light in various medium, laser wake field generation and particle acceleration are the influence [3]. The ponderomotive force has been generally derived by applying the averaging method to the equation of motion [4–6] and explained as the average force proportional to the gradient of the laser field amplitude at the oscillation center of the particle. This results from the first order perturbation with respect to ε (the ratio of the particle excursion length to the scale length of the gradient of the laser field amplitude). Namely, in this method, the higher-order terms such as second and third derivatives, which correspond to the nonlocal effect of the particle motion, have been neglected. However, they become important under the strong focusing since the laser field amplitude varies inside the excursion length.

Here, we try to extend the theory of the ponderomotive force to include such higher-order nonlocal effects. For this purpose, we introduce the noncanonical Lie perturbation theory [7] which is based on the variational principle in phase space which keeps the Hamiltonian structure rigorously. The theory has been successfully introduced in the gyro-kinetic formalism in describing magnetically confined fusion plasmas [8] and also in the analysis of relativistic beam orbit in free-electron lasers [9, 10]. These studies disclose that the approach is powerful and perspective in determining the long time scale particle motion in complicated field structures. In this paper, we derive the oscillation-center equations of motion up to the second order with respect to ε, although the existing

formula is derived only up to the first order. The precise description for the ponderomotive force can be an important basis in exploring the energy science using the high power lasers.

2 Noncanonical Coordinate Transformation

We consider the motion of a particle with charge q and rest mass m in vacuum irradiated by a high intensity laser represented by normalized vector potential, $\mathbf{a} \equiv q\mathbf{A}/mc^2$. Here, c denotes the speed of light. Then, the relativistic Hamiltonian is given by $h(\mathbf{x};\mathbf{p}_c;\ t) = [m^2c^4 + c^2\ (\mathbf{p}_c – mc\mathbf{a})^2]^{1/2}$, where $\mathbf{p}_c$ is the canonical momentum. Here, in order to investigate the ponderomotive force and the corresponding particle motion in non-uniform laser fields, we perform a noncanonical Lie perturbation analysis based on the Hamiltonian mechanics. In this method, we introduce the extended phase space z_{c}^{μ} and corresponding covariant vector $\gamma_{\mathrm{c}\mu}$ expressed by the canonical variables as $z_{\mathrm{c}}^{\mu} = (t;\ \mathbf{x},\ \boldsymbol{p}c) = (t;\ x,\ y,\ z,\ pcx,\ pcy,\ pcz)$ and $\gamma_{\mathrm{c}\mu} = (-h;\ \mathbf{p}c;\mathbf{0})$, respectively, where the time t is the independent variable. In this paper, we use Latin indices that run from 1 to 6, whereas Greek indices run from 0 to 6. Using this notation, the variational principle from which the equation of motion can be obtained is expressed as $\delta \int \gamma_{\mathrm{c}\mu} dz_{\mathrm{c}}^{\mu} = 0$. We refer to $\widehat{\gamma} \equiv \gamma_{\mu} dz^{\mu}$ as fundamental 1-form.

Here, assuming the laser field in the form

$$\mathbf{a}(x;z;t) = a(x)\sin(\omega t - kz)\widehat{\mathbf{e}}_x, \tag{1}$$

where $\omega \equiv ck$ is the laser frequency and $\widehat{\mathbf{e}}_x$ is the unit vector in the x-direction, we transform the canonical coordinate z_{c}^{μ} to that suitable for the analysis. Since the 1-form, $\gamma_{\mu}\, dz^{\mu}$, is a scalar quantity, the general transformation law from γ_{μ} to the new covariant vector Γ_{μ} under an arbitrary coordinate transformation $z^{\mu} \rightarrow Z^{\mu}$ can be obtained from the relation $\gamma_{\mu}\, dz^{\mu} = \Gamma_{\mu}\, dZ^{\mu}$. As a preparatory transformation for the analysis, we introduce a noncanonical coordinate

$$z^{\mu} = (\eta; x, y, z, px, py, p\eta), \tag{2}$$

where $\eta \equiv \omega t – kz$ is the laser phase, $\mathbf{p} = \mathbf{p}_c – mc\mathbf{a}$ is the mechanical momentum and $p\eta \equiv pz – \gamma mc$, where γ is the relativistic factor. Since p_{η} is the constant of motion in the uniform field, the orbit analysis becomes easier by taking p_{η} as one of the coordinate variables. Then, the corresponding covariant vector is calculated as

$$\gamma_{\mu} = (-K; p_x + mca(x)\sin\eta,\ py,\ p\eta, 0, 0, 0), \tag{3}$$

where $K = -(2kp\eta)^{-1}\left[m^2c^2 + \mathbf{p}_\perp^2 + p_\eta^2\right]$ is the new Hamiltonian. Note that the field a does not explicitly appear in the new Hamiltonian but in the first component of γ_μ, which makes the perturbation analysis prospective.

In the Lie perturbation method, we consider a near-identity transformation of the nth order of ε, $z^\mu \to z'^\mu = \Pi_{m=0}^{n}\exp\left(\varepsilon^m L^{(m)}\right)z^\mu$, under which the corresponding covariant vector is transformed as $\gamma_\mu \to \gamma'_\mu = \Pi_{m=0}^{n}\exp\left(-\varepsilon^m L^{(m)}\right)\gamma_\mu + \partial_\mu S$. Here, S is the gauge function and the operator L is defined by $Lf = g^\mu \partial_\mu f$ for an arbitrary scalar function f and $\left(L\widehat{\xi}\right)_\mu = g^\nu\left(\partial_\nu \xi_\mu - \partial_\mu \xi_\nu\right)$ for an arbitrary 1-form $\widehat{\xi}$, respectively, where g^μ is the Lie generator of the transformation. By carefully choosing the gauge function and the Lie generator, we can lead to the coordinates where the perturbed motion is simplified in each order. Here, we choose the Lie generator that leads to $g^{(n)0} = 0$ and $\overline{g^{(n)j}} = 0$, and also S avoiding secularities [7].

3 Oscillation-Center Equations of Motion in Non-uniform Laser Fields

Here, we introduce a smallness parameter, $\varepsilon \sim l/L$ and $\varepsilon^2 \sim l^2/R$, where l is the transverse excursion length of the particle, L and R are the scaling parameters defined by $L^{-1} \equiv a_x^{-1}\partial_x a_x$and $R^{-1} \equiv a_x^{-1}\partial_x^2 a_x$ corresponding to the field amplitude gradient and curvature, respectively. Note that we evaluate L and R at the oscillation center, $\boldsymbol{X} \equiv \overline{\mathbf{x}}$, where the overbar denotes the average over η-period rapid laser oscillations. By using these parameters, we expand the amplitude of the vector potential around the oscillation center X as

$$a(x) = a(X)\left[1 + \varepsilon\frac{x-X}{L(X)} + \frac{\varepsilon^2}{2}\frac{(x-X)^2}{R(X)}\right] + \partial\left(\varepsilon^3\right). \tag{4}$$

At first, we determine the zeroth order motion with respect to ε. In this order, we regard $a(X)$ as a constant to obtain the unperturbed particle orbit $z^{(0)i}$ in the uniform laser field. Then, the solution of the equation of motion, which can be derived by the variational principle to the zeroth-order 1-form, leads to the figure-eight motion in the x–z plane whose oscillation center drifts in the z-direction [11]. Here, we use the initial condition of $(\mathbf{x}, \mathbf{p}, p_\eta) = (\mathbf{x}_{\perp 0}, 0, 0, 0, p\eta 0)$ and $p_z = p_{z0}$ at $\eta = 0$. Note that $p_{\eta 0} = -mc$ when the initial momentum is zero, i.e., $p_{z0} = 0$. From this analysis, we found that p_η is an invariant for the motion and also that the excursion length is given by $l(X) = -mca(X)/kp_{\eta 0}$.

Next, we determine the higher order motion with respect to ε. For this purpose, we transform the coordinate z^μ to that of the oscillation center, $Z^\mu = (\eta; X, Y, Z, Px, Py, p\eta)$, by using the relation $z^i = Z^i + z^{(0)\,i} - \overline{z}^{(0)\,i}$. The covariant vector in the oscillationcenter coordinate is then obtained as

$$\Gamma_\mu = (-\kappa, P_x + mc(a(x) - a(X))\sin\eta + \varepsilon\alpha, Py, p\eta, 0, 0, 0), \tag{5}$$

where α and the new Hamiltonian κ are given by

$$\kappa = K + [P_x + mc(a(x) - a(X))\sin\,\eta]l\,\sin\,\eta + p_\eta \frac{kl^2}{4}\cos\,2\eta, \tag{6}$$

$$\alpha = \frac{l}{L}\left(\frac{mc}{2}(a(x) - a(X))\cos 2\eta + P_x \cos\eta - p_\eta \frac{kl}{4}\sin 2\eta\right), \tag{7}$$

respectively. Here, the old Hamiltonian K in (6) is written in terms of the new coordinate variables $\mathbf{P}_\perp$, $p\eta$ and η. Note that $a(X)$ is treated as a function of the variable X in this coordinate so that $l = l(X)$ is now a variable depending on the position X. From the zeroth-order 1-form $\widehat{\Gamma}^{(0)}$, we obtain the following equations of motion:

$$\frac{dX}{d\eta} = -\frac{P_x}{kp_\eta} + l\left(1 - \frac{p_{\eta 0}}{p_\eta}\right)\sin\,\eta, \tag{8}$$

$$\frac{dY}{d\eta} = -\frac{Py}{kp_\eta}, \tag{9}$$

$$\frac{dZ}{d\eta} = \frac{1}{2kp_\eta^2}\left[(mc)^2 + (P_x - mca(X)\sin\,\eta)^2 + P_y^2 - p_\eta^2\right] + \frac{kl^2}{4}\cos 2\eta, \tag{10}$$

$$\frac{dP_x}{d\eta} = \varepsilon\frac{l}{L}p\eta\frac{kl}{2}\left[\frac{p_{\eta 0}^2}{p_\eta^2} - \left(1 + \frac{p_{\eta 0}^2}{p_\eta^2}\right)\cos\,2\eta\right] - \varepsilon\frac{l}{L}P_x\left(1 - \frac{p_{\eta 0}}{p_\eta}\right)\sin\,\eta, \tag{11}$$

$$\frac{dP_y}{d\eta} = 0, \tag{12}$$

$$\frac{dp_\eta}{d\eta} = 0. \tag{13}$$

Note that (8)–(13) include the terms up to the first order of e due to the Xderivative of the zeroth-order 1-form in the process of deriving the equations through the variational principle. Using the solution $p_\eta = p_{\eta 0}$, we can reduce the equations of motion in the x-direction to

$$\frac{dX}{d\eta} = \frac{P_x}{mc\varsigma_0 k}, \tag{14}$$

$$\frac{dP_x}{d\eta} = -\varepsilon\frac{l}{L} - mca(X)\left(\frac{1}{2} - \cos 2\eta\right). \tag{15}$$

The first term on the right-hand side of (15) corresponds to the ponderomotive force proportional to the gradient of the field amplitude at the oscillation center, which is consistent with that obtained by the averaging method [6].

Now, we consider the second-order equations of motion. Here, we perform a near-identity Lie transformation from the oscillation-center coordinate Z^μ to a new one, Z'^μ. In the first order, the transformation law for the covariant vector becomes $\Gamma'^{(1)}_\mu = \partial_\mu S^{(1)} - L^{(1)}\Gamma^{(0)}_\mu + \Gamma^{(1)}_\mu$. By taking the Lie generator and the gauge function as those in Sect. 2, the new first-order covariant vector can be expressed as $\Gamma'^{(1)}_\mu = \left(\overline{V^{(0)\mu}\Gamma^{(1)}_\mu}; \mathbf{0}, \mathbf{0}\right)$. Here, $V^{(0)\mu}$ is defined by $V^{(0)0} = 1$ and $V^{(0)i}(Z^\mu) = dZ^{(0)i}/dZ^0$. This leads to $\Gamma'^{(1)}_\mu = 0$, which indicates that the 1-form up to the first order of ε, $\widehat{\Gamma}' = \widehat{\Gamma}^{(0)} + \varepsilon\widehat{\Gamma}'^{(1)}$, is the same as that of the zeroth order.

Therefore, we conclude that the resulting average force up to the second order is the same as that on the right-hand side of (15). This result is relevant because the second-order field structure, i.e. the curvature of the laser field amplitude, has a symmetric nature so that the nonlocal effect is cancelled during single laser period and the second-order ponderomotive force disappears. However, it is noted that the curvature changes the field strength that the particle feels in average during one period. This effect should appear as the increase of the excursion length of the figure-eight motion. This correction will be obtained by the backward Lie transformation in the next higher order analysis.

4 Summary

We presented a new theoretical framework to investigate the ponderomotive force in tightly-focused high intensity laser fields. In order to precisely describe the force considering the higher-order field structure and the corresponding nonlocal effect, we introduced the noncanonical Lie perturbation theory which keeps the Hamiltonian dynamics rigorously. We successfully derived the oscillation-center equations of motion up to the second order with respect to ε. We found that no additional force appears and the formula is essentially the same as that obtained by the averaging method up to this order. This indicates that the second-order nonlocal effect originating from the curvature of the laser field amplitude is exactly canceled in average with respect to the rapid laser period due to the symmetry of the oscillatory particle orbit.

This work shows that the noncanonical Lie perturbation method is perspective in describing complex high intensity laser–plasma interactions. We will extend the present analysis to the third order where the nonlocal effect is expected to appear.

Acknowledgements This work was supported by an "Energy Science in the Age of GlobalWarming" of G-COE program of the Ministry of Education, Culture, Sports, Science and Technology of Japan, and also by a Grant-in-Aid from JSPS (No. 21340171).

References

1. Mourou GA, Tajima T, Bulanov SV (2006) Optics in the relativistic regime. Rev Mod Phys 78:309–371
2. Tajima T (2009) Report on the ELI science. In: Tajima T (ed) Scientific Advisory Committee of Extreme Light Infrastructure, pp 1–18
3. Esarey E, Schroeder CB, Leemans WP (2009) Physics of laser-driven plasma-based electron accelerators. Rev Mod Phys 81:1229–1285
4. Gibbon P (2005) Short pulse laser interactions with matter. Imperial College Press, London, pp 36–44
5. Startsev EA, McKinstrie CJ (1996) Multiple scale derivation of the relativistic ponderomotive force. Phys Rev E 55:7527–7535
6. Quesnel B, Mora P (1998) Theory and simulation of the interaction of ultraintense laser pulses with electrons in vacuum. Phys Rev E 58:3719–3732
7. Cary JR, Littlejohn RG (1983) Noncanonical Hamiltonian mechanics and its application to magnetic field line flow. Ann Phys 151:1–34
8. Brizard AJ, Hahm TS (2007) Foundations of nonlinear gyrokinetic theory. Rev Mod Phys 79:421–468
9. Kishimoto Y, Tokuda S, Sakamoto K (1995) Beam orbit analysis in a wiggler by using a noncanonical perturbation method. Phys Plasmas 2:1316–1325
10. Imadera K, Kishimoto Y (2011) Stability analysis of relativistic electron beams in a wiggler with harmonic gyro-resonance using the noncanonical Lie perturbation method. Plasma Fusion Res 6:1201004
11. Iwata N, Imadera K, Kishimoto Y (2010) Analysis of relativistic particle orbit in a transversely focused high-power laser field by using the noncanonical Lie perturbation method. Plasma Fusion Res 5:028

Simulation of Electron Trajectory in Bulk HTSC Staggered Array Undulator

Ryota Kinjo, Koji Nagahara, Toshiteru Kii, Naoki Kimura, Mahmoud A. Bakr, Yong Woon Choi, Mohamed Omer, Kyohei Yoshida, Keiichi Ishida, Hidekazu Imon, Takuya Komai, Marie Shibata, Kyohei Shimahashi, Heishun Zen, Taro Sonobe, Kai Masuda, Kazunobu Nagasaki, and Hideaki Ohgaki

Abstract To realize short-period high-magnetic-field undulator, we have proposed an undulator using bulk high temperature superconductor in a staggered array structure. To investigate the effect of the longitudinal solenoid field on the electron beam trajectory, the magnetic field near the center of this undulator was modeled and the trajectory of the single electron and the undulator radiation was calculated. As a result, we found that the stronger solenoid field had a good effect on the electron beam confinement. However, we found that the radiation wavelength became longer and the peaks of the spectrum became smaller at stronger solenoid field.

Keywords Bulk high temperature superconductor • Electron trajectory • Undulator • Undulator radiation

1 Introduction

Use of the short-period high-magnetic-field undulator in the middle energy storage rings [1, 2] is the promising way to obtain high-intensity undulator radiation in hard X-ray region. To realize short-period high-magnetic-field undulator, we have proposed an undulator using bulk high temperature superconductor (bulk HTSC) in a staggered array structure [3]. Figure 1 shows the conceptual diagram of the bulk HTSC staggered array undulator (Bulk HTSC SAU). After cooling bulk HTSCs down to the lower temperature than the critical temperature of them, the superconducting currents are induced by the external

R. Kinjo (✉) • K. Nagahara • T. Kii • N. Kimura • M.A. Bakr • Y.W. Choi • M. Omer • K. Yoshida • K. Ishida • H. Imon • T. Komai • M. Shibata • K. Shimahashi • H. Zen • T. Sonobe • K. Masuda • K. Nagasaki • H. Ohgaki
Graduate School of Energy Science, Kyoto University, Kyoto 606-8501, Japan
e-mail: r-kinjo@iae.kyoto-u.ac.jp

T. Yao (ed.), *Zero-Carbon Energy Kyoto 2011*, Green Energy and Technology,
DOI 10.1007/978-4-431-54067-0_23,

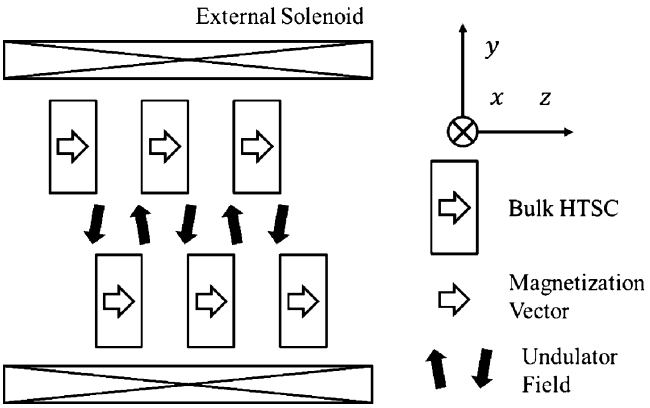

Fig. 1 Conceptual design of Bulk HTSC SAU

solenoid field and the bulk HTSCs are worked as the ten times strong permanent magnets [4]. In Bulk HTSC SAU, these magnets generate the sinusoidal magnetic field in y-direction along the z-axis, i.e. undulator field. The amplitude of the undulator field is depends on the magnetization of the bulk HTSCs, which also depends on the amount of change of the solenoid field. It implies that we can control the undulator field and the solenoid field at the operation independently, if the critical current density is independent from the applied magnetic field to bulk HTSC. This assumption is reasonable in QMG [5]. To choose the value of the solenoid field at the operation time, we have to know the effects of the solenoid field on the electron beam trajectory and on the radiation from the electrons. In this paper, to investigate these effects, we modeled the magnetic field in the center part of this undultor, calculated the trajectory of single electron, and calculated the spectrum of the undulator radiation emitted from 1,000 electrons.

2 Simulation Methods

2.1 Trajectory Calculation

The trajectory of the single electron in three-dimensional space is calculated by using fourth-order Runge–Kutta method. We assumed that the energy of electron was 10 MeV which was generated by radio frequency electron gun in Kyoto University Free Electron Laser facility [6] to obtain the infrared light from this undulator. We neglected the radiation loss of the electron because it should be negligibly-small.

2.2 Magnetic Field Model of the Undulator

In the limit of large undulator periodic number, the Bulk HTSC SAU should only have periodic magnetic fields in the center area. Therefore, the magnetic field model of Bulk HTSC SAU is consisted of the sinusoidal magnetic field in y-direction, B_y, and the constant field in z-direction, B_z. Therefore, we obtain

$$B_x = 0,$$

$$B_y = B_{y0}\cos(k_0 z)\cosh(k_0 y),$$

$$B_z = B_{z0}.$$

where B_{y0} is 1 T, B_{z0} is the same with the solenoid field B_s at the operation, and k_0 is the wavenumber corresponding to the undulator period. We assume that B_{z0} is selected independently from B_{y0}. Note that the our model doesn't satisfy the condition $\nabla \bullet \mathbf{B} = \mathbf{0}$ and $\nabla \times \mathbf{B} = 0$. We neglect the component $B_{y0}\cos(k_0 z)\sinh(k_0 y)$ in B_z because it should be vanished by averaging along the electron trajectories and should not largely affect the radiation spectrum. The solenoid field was changed from 0 to 10 T.

2.3 Undulator Radiation Calculation

We calculate the undulator radiation at the position $(x, y, z) = (0, 0, 10)$. The electric field and the magnetic field generated by the moving electric point charge at the point is calculated from Lienard–Wiechert potential [7] :

$$\mathbf{E}(\mathbf{r},t) = \frac{q}{4\pi\varepsilon_0}\left(\frac{c(\mathbf{n}-\boldsymbol{\beta})(1-\beta^2)R + \mathbf{n}\times\left((\mathbf{n}-\boldsymbol{\beta})\times\dot{\boldsymbol{\beta}}\right)}{cs^3R^2}\right)_{t_r},$$

$$\mathbf{B}(\mathbf{r},t) = \frac{\mathbf{n}\times\mathbf{E}(\mathbf{r},t)}{c}.$$

where q is the charge of the electron, c is the speed of light, ε_0 is the permittivity of vacuum, R is the distance between the electron and the observer, $\mathbf{n}$ is the unit vector from the electron to the observer, $\boldsymbol{\beta}$ is the electron velocity normalized by the speed of light, γ is the Lorentz factor, and s is given by $1 - \mathbf{n} \bullet \boldsymbol{\beta}$. The suffix t_r indicates that the values in the right side of the equation are at the emitted time, while the values in the left side are at the observed time. In sect. 3.2, we calculated the x-component E_x, because the undulator radiation should be polarized in x-direction due to the y-direction undulator field.

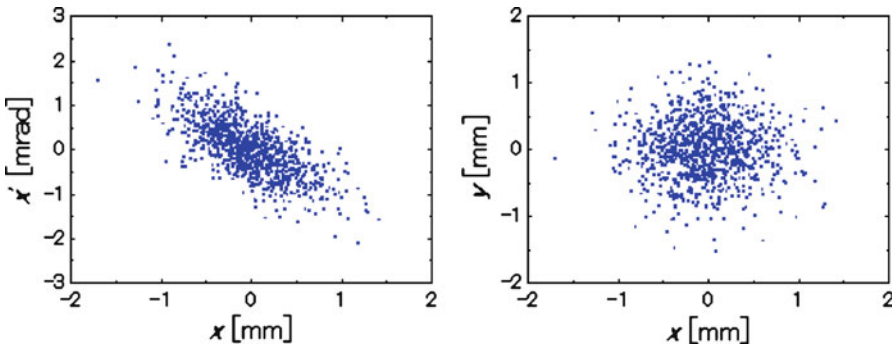

Fig. 2 Electron distribution in phase space (*left*) and real space (*right*) at the entrance of the undulator $(z = 0)$

2.4 Electron Beam Profile

The initial positions (x, y) and angles to z-axis (x', y') of 1,000 electrons were assumed to have Gaussian distribution at $z = 0$. The means of the positions and the angles were zero. The standard deviations are represented by the equations:

$$\sigma_{x(y)} = \sqrt{\epsilon_u \beta_{x(y)}},$$

$$\sigma_{x'(y')} = \sqrt{\epsilon_u \gamma_{x(y)}}.$$

where ϵ_u is the unnormalized emittance, $\beta_{x(y)}$ are Twiss beta parameters, $\gamma_{x(y)}$ are Twss gamma parameters. We applied our accelerators emittance (1.947 mm mrad). We decided to locate the beam waist at the center of the undulator $(\beta_{x(y)} = 1, \gamma_{x(y)} = 2)$. Figure 2 shows the distribution in phase space and real space at the entrance of the undulator. In this calculation, we neglected the interaction between the electrons because of the following reason. At this high electron energy, in the laboratory frame, the electron makes electromagnetic forces only in transverse direction with the angle of $1/\gamma$ and the transverse electrostatic force and the transverse magnetic force balanced.

3 Results and Discussions

3.1 Electron Trajectory

Figure 3 shows the trajectory of electron whose initial condition is $(x, y, z, x', y') = (0, 0, 0, 0.0035, 0.0035)$. The undulation motion is performed in the x-direction. Moreover electron has cyclotron motion along B_s. The stronger B_s

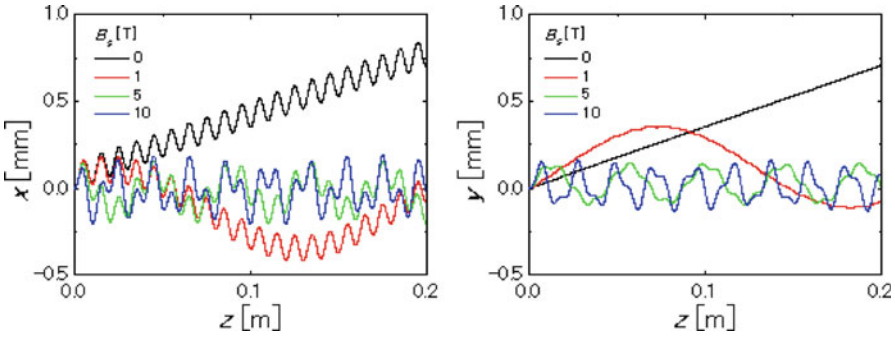

Fig. 3 Electron trajectory at each solenoid field. Electron's initial condition was $(x, y, z, x', y') = (0, 0, 0, 0.0035, 0.0035)$

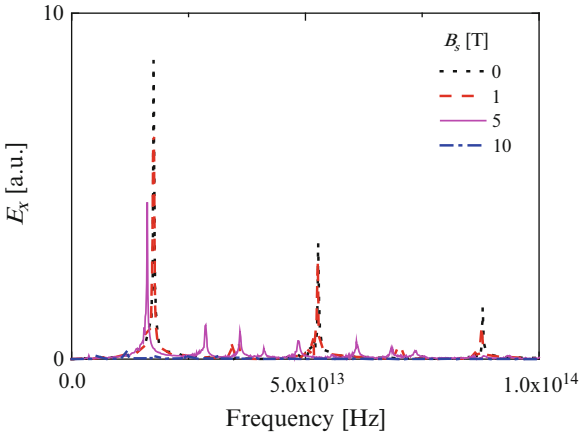

Fig. 4 The spectrum of the radiation from 1,000 electrons

becomes, the smaller the cyclotron radius. This shows that stronger B_s has a better effect on the electron beam confinement. However, we need to consider two unwished effects due to stronger B_s. First, the radiation wavelength can be longer because the electron trajectory is longer. Second, the undulator radiation would diverge because the angle to z-axis is larger (especially in y–z plane). Therefore, we need further discussions on the undulator radiation from the electrons to decide the optimum solenoid field.

3.2 Radiation

Figure 4 shows the spectrum of the undulator radiation emitted from 1,000 electrons through 1 m undulator. The observer position was $(x, y, z) = (0, 0, 10)$. When B_s was zero, the wavelength of the fundamental radiation, the third harmonic,

and the fifth harmonic were 17.0, 5.68, and 3.41 μm respectively. These results agreed with the theoretical equation of undulator radiation λ_u [8]:

$$\lambda_u = \frac{\lambda_0}{2n\gamma}\left(1 + \frac{K^2}{2}\right), (\mathrm{n} = 1, 3, 5, \ldots)$$
$$K \sim 93.34 B_{y0} \lambda_0.$$

where λ_0 is the undulator period and n is the harmonic number.

As B_s got stronger, the spectrum changed as follows. First, E_x of the fundamental radiation and the harmonics were degraded. This was due to the divergence of the radiation because the electron trajectories have the angles with z-axis. Second, the wavelength of the fundamental radiation and the harmonics were shifted to longer wavelength. This was due to the longer trajectory than that at weaker solenoid field. When B_s is 10 T, the spectrum was almost vanished.

4 Conclusions

To investigate the effect of the solenoid field on the trajectory of the electron and the undulator radiation, we calculated the electron trajectory and the spectrum of the undulator radiation with various solenoid fields. As a result, we found that the stronger solenoid field had a good effect on the electron beam confinement. However, we found that the radiation wavelength became longer and the peaks in spectrum became smaller at stronger solenoid field.

Acknowledgments Work supported by the GCOE program, Kyoto University and the Ministry of Education, Science, Sports and Culture of Japan, Grants-in-Aid for Scientific Research B and Grants-in-Aid for JSPS Fellows.

References

1. Clarke JA (2000) Possible insertion devices for the diamond light source. In: Proceedings of European particle accelerator conference 2000, p 2319
2. Boege IG et al (2007) Performance of small gap undulators at the SLS intermediate energy storage ring. In: Proceedings of ninth international conference on synchrotron radiation instrumentation, p 388
3. Kinjo R et al (2008) Bulk high-Tc superconductor staggered array undulator. In: Proceedings of free electron laser conference
4. Tomita M, Murakami M (2003) High-temperature superconductor bulk magnets that can trap magnetic field of over 17 teslas at 29 K. Nature 421:517
5. Morita M, Teshima H, Hirano H (2006) Development of oxide superconductors—high-Tc bulk superconductor, QMG, and its magnetic applications, Nippon Steel Technical Report No. 93
6. Ohgaki H et al (2008) Lasing at 12 μm mid-infrared free electron laser in Kyoto university. Jpn J Appl Phys 47(10):8091
7. Jackson DJ (1998) Classical electrodynamics, 3rd edn. Wiley, New York
8. Kincaid BM (1977) A short-period helical wiggler as an improved source of synchrotron radiation. J Appl Phys 48(7):2684–2691

Part III
Advanced Nuclear Energy Research

(i)
Invited Paper

Current Status of Fukushima Dai'ichi Nuclear Power Plant Accident

Jun Sugimoto

Abstract The nuclear accident occurred at the Fukushima Dai'ichi Nuclear Power Plant on March 11, 2011 was caused by the extremely massive earthquake and gigantic tsunami and resulted in the severe accident that extended over multiple reactors simultaneously. In the present paper the current status of the accident is described in terms of basic information on the plant, sequences and consequences of the accident, and lessons learned so far. Although some details of the accident are still not known well, the sequences, causes and consequences of the accidents are being clarified. The cooling of the reactors has been established toward the complete control of the release of radioactive materials. Compared with the Chernobyl accident, the radiation effects on the general public will probably be not serious due to much smaller amount of radioactive release to the environment. Lessons learned from the accident should be shared all over the world for the higher level of safety of current reactors, and advanced nuclear reactors without the need of evacuation, in principle, should be developed for future.

Keywords Fukushima Dai'ichi • Severe accident • Radioactive materials • Chernobyl

1 Introduction

The nuclear accident that occurred at the Fukushima Dai'ichi Nuclear Power Plant (NPP) of Tokyo Electric Power Co.(TEPCO) on March 11, 2011 was caused by the extremely massive earthquake, Great East Japan Earthquake, and gigantic tsunami rarely seen in the history and resulted in the severe accident that extended over multiple reactors simultaneously. The accident has not yet been completely

J. Sugimoto (✉)
Department of Nuclear Engineering, Kyoto University, Kyoto, Japan
e-mail: sugimoto.jun.8u@kyoto-u.ac.jp

T. Yao (ed.), *Zero-Carbon Energy Kyoto 2011*, Green Energy and Technology,
DOI 10.1007/978-4-431-54067-0_24,

terminated and the details of the accident have not been fully clarified as of August 2011. In the present paper the current status of the accident is described in terms of basic information on the plant, sequences, causes and consequences of the accident, and lessons learned reported at the IAEA Ministerial-level Meeting in June, 2011 [1]. Concerning the future prospects and challenges, short summary is presented mostly by the comparison with Chernobyl accident [2–4].

2 Basic Information

The Fukushima Dai'ichi NPS is located in the towns of Okuma and Futaba, which are in the county of Futaba in Fukushima Prefecture. This NPS consists of six Boiling Water Reactors (BWR) installed, Units 1 through 6, with a total generating capacity of 4,696 MW. Reactor model of Unit 1 is BWR3, that of Units 2 through 4 is BWR4, and that of Units 5 and 6 is BWR5. Containment model of Units 1 through 5 is Mark-1 and that of Unit 6 is Mark-2, respectively. Before the earthquake on March 11, Units 1 through 3 were under operation and Units 4 through 6 were under periodic inspection. Unit 4 was undergoing a major construction for renovations, with all the nuclear fuel in the reactor pressure vessel (RPV) having already been transferred to the spent fuel pool. More details are described in [1].

3 What Happened

The Pacific coast area of eastern Japan was struck by the Tohoku District—off the Pacific Ocean Earthquake, which occurred at 14:46 on March 11, 2011. This earthquake occurred in an area where the Pacific plate sinks beneath the North American plate and the magnitude of the earthquake was 9.0, the largest in Japan's recorded history. Up to now major damage to the reactor facilities which are important for safety functions has not yet to be recognized. All power supplied from total of six external power supply lines connected to the Power Station stopped due to damage to the breakers and the collapse of the power transmission line tower due to the earthquake.

Fukushima Dai'ichi was hit by the first enormous tsunami at 15:27 on March 11, and the next enormous wave around 15:35. The license for the establishment of nuclear reactors at the Fukushima Dai'ichi was based on the assumption that the maximum design basis tsunami height expected was 3.1 m. The assessment in 2002 based on the "Tsunami Assessment Method for Nuclear Power Plants in Japan" proposed by the Japan Society of Civil Engineers indicated a maximum water level of 5.7 m, and TEPCO raised the height of its Unit 6 seawater pump in response to this assessment. However, the height of the tsunami this time was 14–15 m, and the seawater pumps for auxiliary cooling systems were submerged and stopped functioning in all units. Also all the emergency diesel generators and the distribution

boards installed in the basements of the reactor buildings and turbine buildings except for Unit 6 were inundated and stopped functioning. TEPCO's operators followed their manuals for severe accidents and attempted to secure power supplies to recover equipments within the safety systems, such as core cooling and water-injection systems, which had automatically started up. However, ultimately power supplies could not be secured.

Since the core cooling functions using AC power were lost in Units 1 through 3, core cooling systems without the needs of AC power were put into operation. These were operations of isolation condenser in Unit 1, reactor core isolation cooling system (RCIC) in Unit 2, and RCIC and high pressure injection system (HPCI) in Unit 3. These core cooling systems that do not need AC power supplies stopped functioning thereafter, and were switched to alternative injections of freshwater or sea water by fire extinguishing lines, using fire engine pumps. Concerning Units 1 through 3, since the water injection to each reactor core was impossible to continue for several hours, the nuclear fuels were not covered by water but exposed to the steam, leading to a core melt situation. It is believed that part of the melted fuel stayed at the bottom of the RPV. A large amount of hydrogen was generated by chemical reactions mostly between the zirconium fuel cladding and water vapor. In addition, the fuel cladding was damaged and radioactive materials were discharged into the RPV. Further, these hydrogen and radioactive materials were released into the containment vessel. Injected water vaporizes with the heat from the nuclear fuel in the RPV. Accordingly, the pressure rose in the RPVs which had lost their core cooling functions, and the vapor leaked through the safety valves into the containment vessel. The pressure of the containment vessels in Units 1 through 3 thus rose gradually, with PCV wet well vent operations performed several times, in which the gases in the PCVs are released from the vapor area in the suppression chamber into the atmosphere, through the ventilation stack. After the wet well venting of the PCVs, hydrogen explosions occurred in the upper area of the reactor buildings of Units 1 and 3 by the leaked hydrogen from the PCV. As a result of these incidents, a large amount of radioactive materials were released to the environment. After the break of the Unit 3 building, an explosion probably caused by hydrogen occurred in the reactor building of Unit 4 (Fig. 1).

In Unit 4, all core fuels had been transferred to the spent fuel pool for periodic inspection before the earthquake. During this time, in Unit 2 a hydrogen explosion probably occurred and caused damage near the suppression chamber. The urgent task at the site, along with recovery of the power supply and the continuation of water injection to reactor vessels, was water injection to the spent fuel pools. In the spent fuel pool in each unit, the water level continued to drop due to the evaporation of water caused by the heat of the spent fuel in the absence of the pool water cooling by the loss of power supply. Water injection to the spent fuel pool was conducted by the Self-Defense Forces, the Fire and Disaster Management Agency and the National Police Agency, using helicopters and water cannon trucks. Concrete pump trucks were ultimately secured, which led to stable water injection using freshwater from nearby reservoirs after the initial seawater injection. It is noted that the cooling of the reactors has been established in July toward the complete control of the release of radioactive materials hopefully early in 2012.

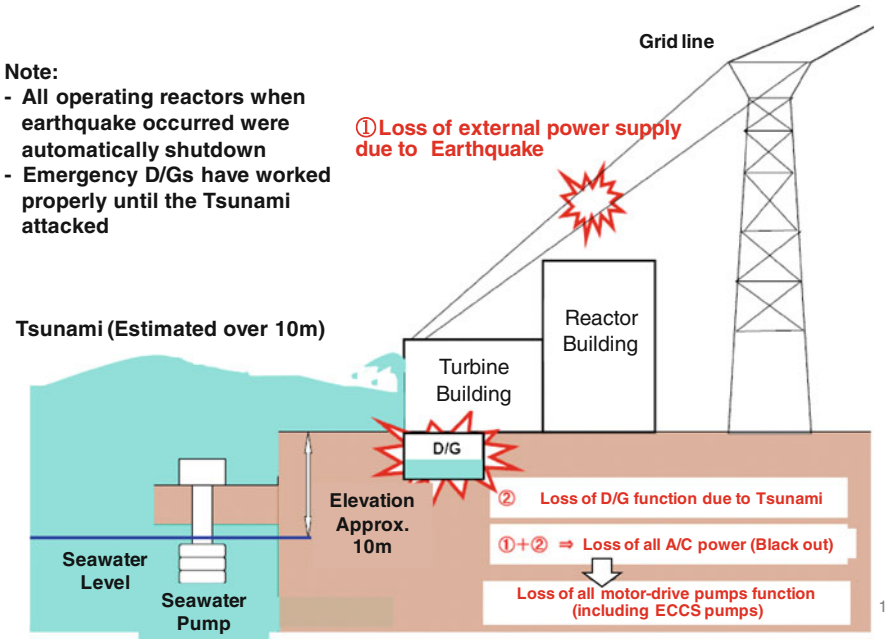

Fig. 1 Main causes of the Fukushima Daiichi accident

4 Consequences of the Accident

Nuclear and Industrial Safety Agency (NISA) and the Nuclear Safety Commission estimated the total amount of radioactive materials released to the environment. NISA estimated the total discharged amount from reactors based on the analytical results with severe accident analysis code by Japan Nuclear Energy Safety Organization and presumed that approximately 1.6×10^{17} Bq of iodine-131 and 1.5×10^{16} Bq of cesium-137 were discharged. The Nuclear Safety Commission estimated the amount of nuclides discharged into the atmosphere (discharged between March 11 and April 5) with the assistance of the Japan Atomic Energy Agency through inverse calculations, based on the data of environmental monitoring and air diffusion calculation; the estimations are 1.5×10^{17} Bq for iodine-131 and 1.2×10^{16} Bq for cesium-137.

Concerning the exposure doses of personnel engaged in radiation work, the total number of workers that had entered the area was 7,800, with an average exposure dose of 7.7 mSv as of May 23. Thirty of these workers had exposure doses above 100 mSv. The internal exposure measurement of the radiation workers has been delayed and the exposure dose, including internal exposure of a certain number of workers, could exceed 250 mSv in the future. On March 24, two workers stepped into accumulated water and their exposure doses have been estimated at less than 2 or 3 Sv. Concerning the radiation exposure to residents in the vicinity, no cases of

harm to health were found in 195,345 (as of May 31) residents who received screening. All 1,080 children who went through thyroid gland exposure evaluation received results lower than the screening level. The estimation and the evaluation of exposure doses of residents in the vicinity are planned to be conducted through the use of the results of environmental monitoring.

Table 1 summarizes the comparison of the consequences between Fukushima Dai'ichi and Chernobyl accidents [2–4]. The amount of fission product released at Chernobyl accident is about several times larger than that of Fukushima Dai'ichi. It should be noted that the radiation effects on workers and the general public in Fukushima Dai'ichi accident will probably be not serious compared with Chernobyl accident due to partial survival of the containment function, early notification and evacuation of the public, and wet condition in the reactor and containment regions in Fukushima accident that enabled higher amount of depositions of radioactive materials in the water left in the containment.

5 Lessons Learned

In the report to IAEA from the Japanese Government, 28 items in five categories are described as lessons learned from the accident so far as follows [1]:

Category 1: Strengthen preventive measures against severe accident
Eight items including strengthen measures against earthquakes and tsunamis, ensure power supplies, robust cooling functions of reactors, PCVs, and spent fuel pools, accident management measures, and response to multi-unit issues.

Category 2: Enhancement of response measures against severe accidents
Seven items including enhancement of measures to prevent hydrogen explosions, containment venting system, radiation exposure management system, training responding to severe accident and instrumentation to identify reactor status.

Category 3: Enhancement of nuclear emergency responses
Seven items including responses to combined emergencies of both large-scale natural disasters and prolonged nuclear accident, reinforcement of environmental monitoring, enhancements of communication at the accident, and clear definition of widespread evacuation areas and radiological protection guidelines.

Category 4: Reinforcement of safety infrastructure
Five items including reinforcement of safety regulatory bodies, establishment and reinforcement of legal structures, criteria and guidelines, human resources for nuclear safety and nuclear emergency preparedness and responses, and effective use of probabilistic safety assessment in risk management.

Category 5: Thoroughly instill a safety culture (one item, same as this title)

The underlying essential lesson will be that a sense of crisis and tension on the possible severe accident was completely lacking, and groundless overconfidence

Table 1 Comparison between Fukushima Daiichi and Chernobyl accidents

	Type of accident	Containment function	Fission product release (10^{15} Bq)	Acute radiation injury of workers	Middle/long term effect on the public	Evacuation
Chernobyl	Reactivity initiated accident due to unstable core design	Totally lost (no containment)	1,760 (I-131) 85 (Cs-137) 3×10^{-2} (Pu-239) Others[a]	134 (28 dead within 3 months)[b,c]	Increased childhood thyroid cancer (over 6,000 cases, 15 dead)[b, c]	Delayed notification to public (1.5–7 d) Totally ~135,000 evacuated
Fukushima	All backout due to earthquake and tsunami	Partially lost (U-2, containment venting for U-1, 3)	~160 (I-131) ~15 (Cs-137) 3×10^{-6} (Pu-239) Others[d]	0 (within 4 months)	Probably and hopefully negligible	Early notification to public Totally ~88,000 evacuated

[a] OECD/NEA 1995
[b] IAEA&WHO 2006
[c] UNSCARE 2011
[d] Japanese Government 2011

against safety covered all nuclear sectors in Japan. We should learn this important lesson with humility, share it among all over the world, and reflect it to future even higher level of safety for current nuclear reactors. Since the long-term relocation completely destroys the local communities, advanced reactors without the need of evacuation, in principle, should be developed for future.

6 Summary

1. Although some details of Fukushima Dai'ichi accidents are still not known well, sequences, causes and consequences of the accidents are being clarified. The cooling of the reactors has been established toward the complete control of the release of radioactive materials.
2. Compared with Chernobyl accident, the radiation effects on both workers at the site and the general public will probably be not serious due to partial survival of the containment function, early notification and evacuation of the general public, and wet condition in the reactor and containment regions in Fukushima Dai'ichi accident.
3. Lessons learned from the accident should be shared all over the world for higher level of safety of current reactors, and advanced reactors without the need of evacuation, in principle, should be developed for future.

References

1. Japanese Government (2011) Report of Japanese Government to the IAEA Ministerial Conference on Nuclear Safety—The Accident at TEPCO's Fukushima Nuclear Power Stations
2. OECD NEA (1995) The Chernobyl reactor accident source term—Development of a consensus view—OECD NEA/CSNI/R(95)24
3. IAEA (2006) Environmental consequences of the Chernobyl accident and their remediation: Twenty years of experience
4. UNSCEAR (2011) The Chernobyl accident —UNSCEAR's assessments of the radiation effects

(ii)

Contributed Papers

The New Era of Geothermal Energy Utilization with Aid of Nuclear Reactor Technology

Takehiko Yokomine, Masato Miura, and Chineo Tawara

Abstract Japan has about 120 active volcanoes. Estimated potential of geothermal power generation is 23,470 MWe from hydrothermal reservoirs to a depth of 3 km. Geothermal energy is expected to be an important role for zero-carbon era. Currently, 21 electric power units at 18 geothermal sites are in operation with a total capacity of 537 MWe, which amounts to about 2.3% of its potential power. The main reason of such a low utilization rate is mainly due to its high cost and impact on ambient surrounding of power plant. We start to develop a new system of geothermal energy conversion. In order to do its first pilot experiment for the proposed system, case studies are carried out by using the two-fluid model which is well developed in the nuclear reactor field. The two types of extraction of hot water, that is, two-phase flow and single-phase liquid flow, have been examined. According to the results of case studies, the required material properties, dimension of test apparatus, experiment conditions, such as inlet pressure and flow rate, have been cleared.

Keywords Downhole coaxial heat exchanger • Geothermal energy • Steam generator • Two-fluid model

1 Introduction

Japan has about 120 active volcanoes, whose estimated potential of geothermal power generation is 20,000 MWe or more from hydrothermal reservoirs. Currently, 20 electric power units at 18 geothermal sites, mainly located in northern Honshu

T. Yokomine (✉) • M. Miura
Department of Nuclear Engineering, Kyoto University, Yoshida, Sakyo, Kyoto 606-8501, Japan
e-mail: yokomine@nucleng.kyoto-u.ac.jp

C. Tawara
Kyushu Power Service Co, Fukuoka, Japan

T. Yao (ed.), *Zero-Carbon Energy Kyoto 2011*, Green Energy and Technology,
DOI 10.1007/978-4-431-54067-0_25,

and Kyushu Islands, are in operation with a total capacity of 537 MWe. This amounts indeed to about 5.3% of the world total capacity of geothermal power plants. Geothermal energy has great advantages compared with other energy systems as follows:

1. Low CO_2 emissions: 28% of solar power and 50% of wind power
2. Increased energy security: geothermal energy is an indigenous supply of energy, providing energy supply and international pricing security
3. Sustainability
4. High availability factors (plant capacity factor) more than 90%
5. Baseload and peaking capability: geothermal power-plants can operate 24 h a day, 365 days a year and are unaffected by climatic factors

Because of above advantages, geothermal power generation should be promoted. As worldwide trend, in fact, utilization of geothermal energy, including both indirect and direct use, is showing favorable growth. In opposition to such a trend, since 1999, geothermal has not been developed further in Japan. In addition, geothermal power, except binary power plant, is not regarded as renewable energy, nor applicable to Renewable Portfolio Standards in Japan. One of the obstacles against geothermal development in Japan is the fact that most of the promising fields are located near or inside national parks or spa resorts. More than 80% of geothermal resource is located in national park. In geothermal development, regulation for the construction of power plant in national park and public acceptance for spa resort residents compel a long lead time. The development has risk due to uncertainty of resource spot, which remains one of the obstacles.

Another obstacle is its high costs, including development and running charge. The most common type of geothermal power generation plants in operation today is flash steam system. Hot water is pumped to the generation equipment at the ground surface. Upon reaching the generation equipment, the pressure is suddenly reduced, allowing some of the hot water to convert or flash into steam. This geothermal steam is then used to power the turbine/generator units to produce electricity. The remaining hot water not flashed into steam, and the water condensed from the steam, is generally pumped back into the reservoir. A part of water is returned to underground through the recharge well. Geothermal fluids (steam or hot water) usually contain gases such as *carbon dioxide, hydrogen sulphide, ammonia, methane,* as well as dissolved chemicals whose concentrations usually increase with temperature. The fluids can react with the total geothermal power generation system, as above mentioned, to cause scaling and corrosion, and may plug injection wells and (e.g., Ca) to form insoluble substances which could precipitate and plug a well hole. Geothermal energy plant requires high cost to remove scale and corrosion and to fix and repair of pipeline and turbine. The waste waters from geothermal plants also have a higher temperature than the environment and therefore become a potential thermal pollutant.

We try to realize geothermal power generation system with closed downhole coaxial heat exchangers as shown in Fig. 1. For this system, working fluid is not geothermal fluid but pure water. The water is highly pressurized before enter the

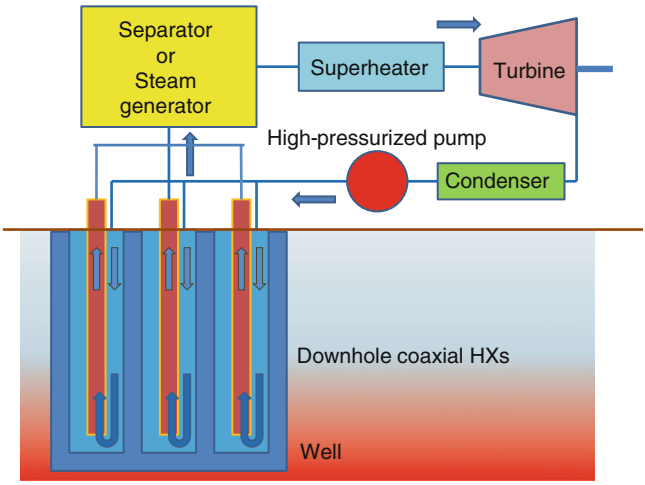

Fig. 1 Geothermal power plant with closed downhole coaxial heat exchangers

downhole and heated up by geothermal energy. The extraction way of hot water has two options; two-phase flow and hot water without boiling. In the case of two-phase flow extraction, the fluid is introduced in the separator. When the single phase liquid water is extracted from the downhole, the fluid is introduced in the steam generator. After that, the fluid is used to power the turbine to produce electricity.

The system has advantages added to the inherent advantages of geothermal energy utilization as follows:

1. Large scale power generation is possible.
2. Scaling and corrosion is free, which can reduce the running cost considerably.
3. Environmental impact is drastically decreased.
4. Aging reduction of power is minimum.
5. The system is installable into existing geothermal power plant, which can greatly reduce both risk and lead time for development.
6. The system can reuse of resting well of existing geothermal power plants.

The concept of downhole coaxial heat exchanger has been investigated firstly by Horne [1]. Horne has been examined the effects of design and operational parameters on the performance of the coaxial type downhole heat exchanger and shown that slightly greater thermal outputs can be obtained in the case that the cold water down the annulus and hot water up through the inner pipe, that is reverse circulation. Morita et al. [2] and Morita and Matsubayashi [3] have been revealed by numerical simulations that very efficient heat extraction can be performed with a highly insulated inner pipe and reverse circulation. They have named the heat exchanger as the “Downhole Coaxial Heat Exchanger”. The initial purpose of their studies was to exploit high temperature and deep geothermal resources such as Hot Wet Rock, Super Hot Rock adjacent to magma and magma with the

downhole coaxial heat exchanger. Morita et al. [4, 5] have performed an experiment to prove the concept at the HGP-A well on the Island of Hawaii. There is, however, no geothermal power plant with downhole coaxial heat exchanger to date.

The system proposed in present study is significantly different from the original system with downhole coaxial heat exchanger on the points that highly pressurized water is introduced and extracted as high-pressurized hot water, still single-phase liquid. We are now planning to carry out the experiment to verify present system. Therefore, present study aims to examine the feasibility of our system by numerical simulation. For simulation, the numerical model developed in the nuclear engineering field is applied.

2 Problem Setting and Numerical Models

As an object of case study, we select the small-scale well; 300 m in depth and 80 mm in diameter, so that the downhole coaxial heat exchanger is totally 600 m in length and 80 mm in outer diameter. The diameter and material property (thermal conductivity) of inner tube is variable.

Two-fluid model is adopted to calculate the fluid flow for both single-phase flow and two-phase flow. In this model, the local, instantaneous conservation equations are averaged in either time or space, or both. The resulting averaged equations for both phases (liquid and gas) yield accurate solutions to a wide variety of practical problems so long as the averaged variables bear some resemblance to the actual situation. Since the averaged macroscopic fields of the two phases are not independent of each other, the averaging process results in phase interaction terms, which couple the transfer of mass, momentum, and energy of each phase across the interfaces. The phase interaction terms can be expressed in terms of the products of the interfacial area concentration and the corresponding driving potentials. The series of model equations, therefore, are complicated. The two-fluid model is widely used in the current nuclear reactor safety analysis codes [6, 7] and performance analysis of nuclear reactor component [8]. So that, the refinement of elemental models is advanced significantly in recent years [9]. Here, only governing conservation equations are shown.

2.1 Mass Conservation

$$\frac{\partial}{\partial t}\left(\alpha_g \rho_g\right) + \frac{\partial}{\partial x_i}\left(\alpha_g \rho_g U_{g,i}\right) = \Gamma \tag{1}$$

$$\frac{\partial}{\partial t}\left(\alpha_l \rho_l\right) + \frac{\partial}{\partial x_i}\left(\alpha_l \rho_l U_{l,i}\right) = -\Gamma \tag{2}$$

α, ρ, and U_i respectively represent volume ratio, density and velocity vector. The subscripts g and l mean variables of gas (vapor) phase and liquid phase, respectively. Γ is the vapor generation rate.

2.2 Momentum Conservation

$$\frac{\partial U_{g,i}}{\partial t} + U_{g,j}\frac{\partial U_{g,i}}{\partial x_i} = -\frac{1}{\rho_g}\frac{\partial P}{\partial x_i} - \frac{M_{g,j}^{\text{int}}}{\alpha_g \rho_g} - \frac{\Gamma^{+}}{\alpha_g \rho_g}\left(U_{g,i} - U_{l,i}\right) + \frac{1}{\alpha_g \rho_g}\frac{\partial \tau_{g,ij}}{\partial x_j} + g_i \tag{3}$$

$$\frac{\partial U_{l,i}}{\partial t} + U_{l,j}\frac{\partial U_{l,i}}{\partial x_i} = -\frac{1}{\rho_l}\frac{\partial P}{\partial x_i} - \frac{M_{l,j}^{\text{int}}}{\alpha_l \rho_l} - \frac{\Gamma^{-}}{\alpha_l \rho_l}\left(U_{g,i} - U_{l,i}\right) + \frac{1}{\alpha_l \rho_l}\frac{\partial \tau_{l,ij}}{\partial x_j} + g_i \tag{4}$$

P and g_i represent pressure and gravity vector. M^{int} and τ_{ij} are interface stress and share stress tensor, respectively.

2.3 Internal Energy Conservation

$$\frac{\partial}{\partial t}\left(\alpha_g \rho_g e_g\right) + \frac{\partial\left(\alpha_g \rho_g e_g U_{g,i}\right)}{\partial x_i} = -P\left[\frac{\partial \alpha_g}{\partial t} + \frac{\partial\left(\alpha_g U_{g,i}\right)}{\partial x_i}\right] + q_g^w + q_g^{\text{int}} + \Gamma h_g^{sat} \tag{5}$$

$$\frac{\partial}{\partial t}\left(\alpha_l \rho_l e_l\right) + \frac{\partial\left(\alpha_l \rho_l e_l U_{l,i}\right)}{\partial x_i} = -P\left[\frac{\partial \alpha_l}{\partial t} + \frac{\partial\left(\alpha_l U_{l,i}\right)}{\partial x_i}\right] + q_l^w + q_l^{\text{int}} - \Gamma h_l^{sat} \tag{6}$$

q^w shows wall heat flux, q^{int} interfacial heat flux and h^{sat} saturated enthalpy.

2.4 Turbulent Energy Conservation

$$\alpha_g \frac{\partial k_g}{\partial t} + \alpha_g U_{g,j}\frac{\partial k_g}{\partial x_i} = \frac{\partial}{\partial x_i}\left(\alpha_g \frac{v_g^t}{\sigma_k}\frac{\partial k_g}{\partial x_i}\right) + \alpha_g\left(\Phi_g - \varepsilon_g\right) \tag{7}$$

$$\alpha_l \frac{\partial k_l}{\partial t} + \alpha_l U_{l,j}\frac{\partial k_l}{\partial x_i} = \frac{\partial}{\partial x_i}\left(\alpha_l \frac{v_l^t}{\sigma_k}\frac{\partial k_l}{\partial x_i}\right) + \alpha_l(\Phi_l - \varepsilon_l) \tag{8}$$

Table 1 Calculation parameters

Inner diameter of inner tube (m)	0.02–0.045
Thermal conductivity of inner tube (W/mK)	0.1–16.3
Flow rate (m^3/s)	5×10^{-4}–5×10^{-3}
Ground temperature (°C)	15
Temperature of bottom of the well (°C)	150–250
Inlet temperature of water (°C)	27

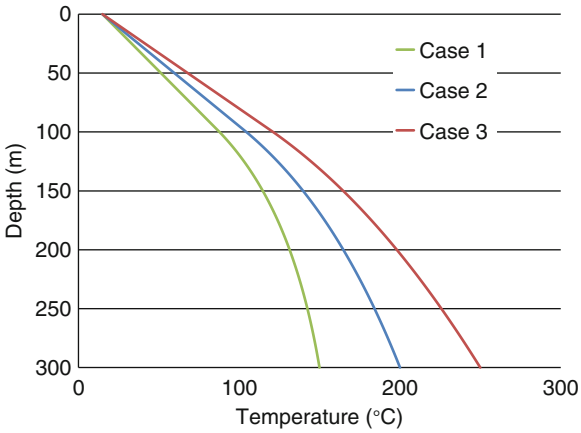

Fig. 2 Assumed temperature profile along the depth of the well

2.5 *Turbulent Energy Dissipation Rate Conservation*

$$\alpha_g \frac{\partial \varepsilon_g}{\partial t} + \alpha_g U_{g,j} \frac{\partial \varepsilon_g}{\partial x_i} = \frac{\partial}{\partial x_i}\left(\alpha_g \frac{v_g^t}{\sigma_\varepsilon} \frac{\partial k_g}{\partial x_i}\right) + \alpha_g \left(C_{\varepsilon 1} \frac{\Phi_g \varepsilon_g}{k_g} - C_{\varepsilon 2} \frac{\varepsilon_g^2}{k_g}\right) \tag{9}$$

$$\alpha_l \frac{\partial \varepsilon_l}{\partial t} + \alpha_l U_{l,j} \frac{\partial \varepsilon_l}{\partial x_i} = \frac{\partial}{\partial x_i}\left(\alpha_l \frac{v_l^t}{\sigma_\varepsilon} \frac{\partial k_l}{\partial x_i}\right) + \alpha_l \left(C_{\varepsilon 1} \frac{\Phi_l \varepsilon_l}{k_l} - C_{\varepsilon 2} \frac{\varepsilon_l^2}{k_l}\right) \tag{10}$$

k and ε represent turbulent energy and its dissipation rate, respectively. Φ means turbulent production term. v^t is eddy viscosity. σ_k, σ_ε, $C_{\varepsilon 1}$ and $C_{\varepsilon 2}$ are model parameters.

Numerical calculations are performed in one-dimension, that is, in flow region, calculation is done in streamwise direction and in the wall region, heat conduction is calculated only in radial direction. Outlet pressure is set to constant, 1 MPa. The other parameter is summarized in Table 1. Three temperature profiles along the depth of well are assumed as Fig. 2. These temperatures are used as the boundary condition of the outer wall surface.

3 Results of Case Studies

Figure 3 shows the effects of temperature profile of underground and thermal conductivity of inner wall on the temperature changes of fluid. In these cases, diameter of inner tube and flow rate are set to the values of 0.03 m and 1×10^{-3} m^3/s, respectively. When the thermal conductivity is 16.3 W/mK, the fluid temperature is considerably decreased when the fluid flows upward in the inner tube independently of the underground temperature profile. In the cases 2 and 3, the boiling is occurred when the fluid flows upward and the temperature is slightly decreased before reaching outlet.

The void fraction profile along the pass for the Case 2 temperature profile is depicted in Fig. 4. If the thermal conductivity of inner tube wall is less than 0.1 W/mK, the void fraction is violently fluctuated near the outlet, which means the water changes the steam at the outlet. On the other hand, when the thermal conductivity is 0.25 W/mK, the fluid condition at the outlet is two-phase flow. In the case more than its value of 0.5 W/mK, the outlet flow is still water without phase change, that is void fraction remains zero. Figure 5 shows the effect of thermal conductivity and diameter of inner tube on the outlet temperature of the fluid for Case 2 temperature profile. When the inner tube is increased in the cases of 1.0 and 16.3 W/mK, the outlet temperature of fluid is decreased. On the other hand, the outlet temperature is independent of inner tube diameter if the thermal conductivity is 0.1 W/mK. Figure 6 draws the thermal output change

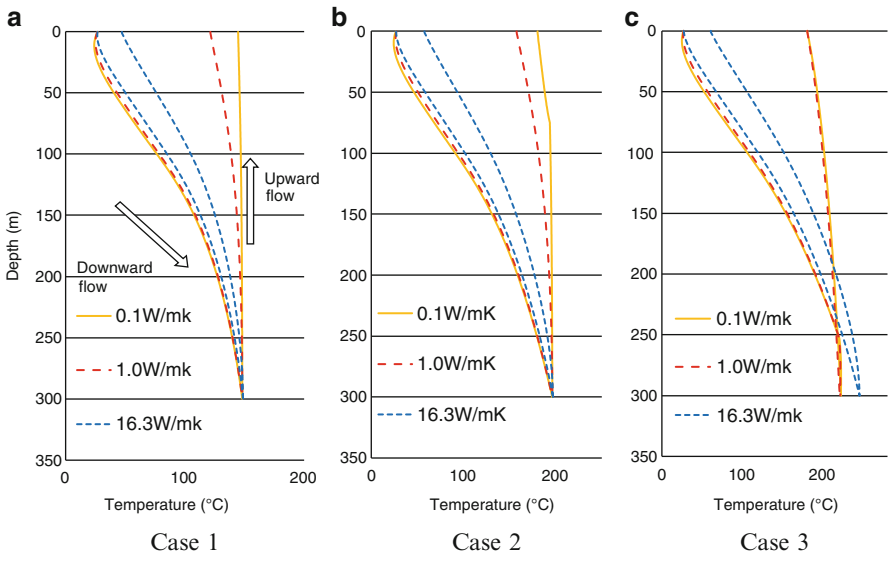

Fig. 3 Change of temperature of fluid

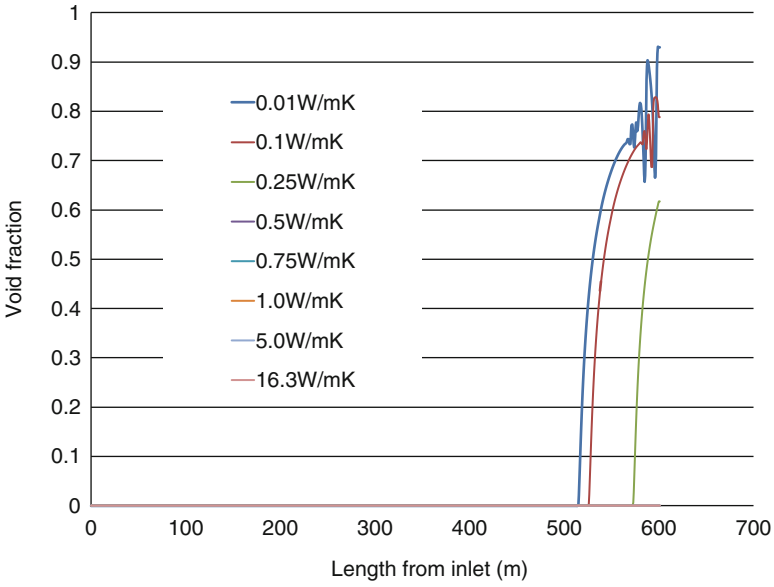

Fig. 4 Void fraction profiles for Case 2 profile

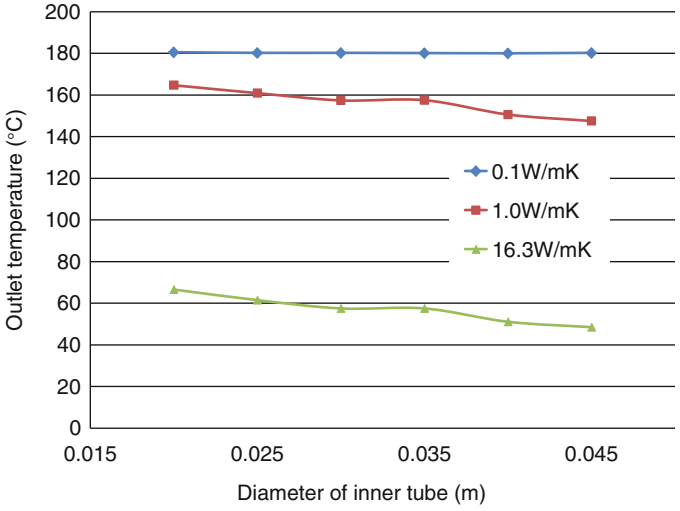

Fig. 5 Effect of thermal conductivity and diameter of inner tube

depending on flow rate. If the flow rate is increased, the thermal output is increased almost linearly. The difference between 0.1 and 1.0 W/mK is small.

Figure 7 shows the dependency of thermal conductivity of the inner tube wall on the inlet pressure which is required to remain the fluid as single-phase liquid water

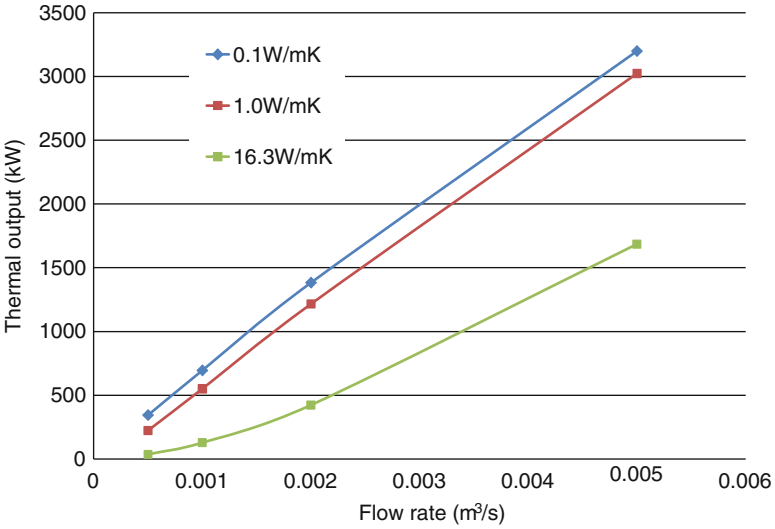

Fig. 6 Dependency of flow rate on thermal output

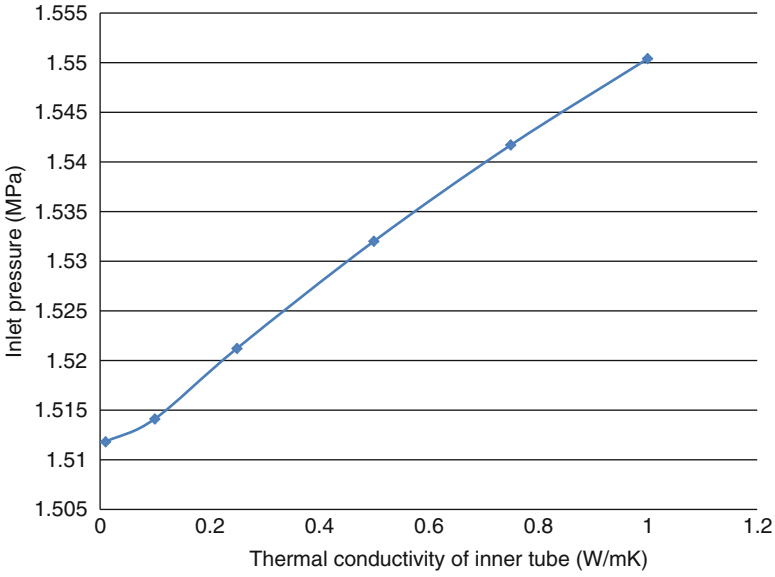

Fig. 7 Dependency of thermal conductivity on required inlet pressure

at the outlet of the downhole coaxial heat exchanger. In order to obtain the value of 1 MPa of outlet pressure, the required inlet pressure is about 1.5 MPa even if the fluid does not occur the phase change. Figure 8 depicts the obtained outlet temperature of water without phase change. The difference between 0.1 and 1.0 W/mK is small.

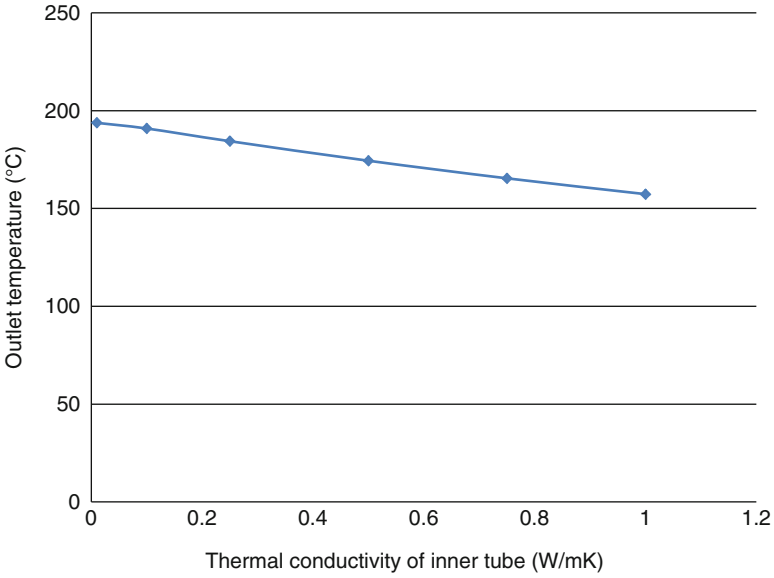

Fig. 8 Obtained outlet temperature without phase-change

According to the above results, the thermal conductivity of the inner wall is less than 1.0 W/mK, the system can be realized as the energy conversion system for the planning experiment.

4 Conclusions

Proposed method of power generation will change the situation of current situation of geothermal energy power generation. According to present result of case study, demonstration test can be started. In order to develop the proposed geothermal power plant, the technology developed for the nuclear reactor, such as numerical simulation code, component devices, such as highly-pressurized water pump and steam generator, and safety analysis in respect of integrity of material is very useful. The technical transfer of nuclear reactor will drastically promote the realization of new geothermal energy plant.

Geothermal energy must play an important role as a resource for reliable supply of energy in Zero-carbon energy scenario.

References

1. Horne RN (1980) Design considerations of a down-hole coaxial geothermal heat exchanger. Geoth Resour Counc Trans 4:569–572
2. Morita K, Matsubayashi O, Kusunoki K (1985) Down-hole coaxial heat exchanger using insulated inner pipe for maximum heat extraction. Geoth Resour Counc Trans 9–1:45–50

3. Morita K, Matsubayashi O (1986) The effect of major design parameters on the performance of a downhole coaxial heat exchanger. J Geoth Res Soc Jpn 8–3:301–322
4. Morita K, Bollmeier WS, Mizogami H (1992) An experiment to prove the concept of the downhole coaxial heat exchanger (DCHE) in Hawaii. Geoth Resour Counc Trans 16:9–16
5. Morita K, Bollmeier WS, Mizogami H (1992) Analysis of the result from the downhole coaxial heat exchanger (DCHE) experiment in Hawaii. Geoth Resour Counc Trans 16:17–23
6. The RELAP5 Code Development Team (TRCDT) (1995) RELAP5/MOD3 code manual, Volume 1 Code structure, system, models, and solution methods. NUREG/CR-5535 (also INEL-95/0174). Idaho National Engineering Laboratory, Idaho Falls, ID
7. Spore JW, Elson JS, Jolly-Woodruff SJ, Knight TD, Lin J-C, Nelson RA, Pasamehmetoglu KO, Steinke RG, Unal C, Mahaffy JH, Murray C (2000) TRAC-M/FORTRAN 90 (version 3.0) theory manual LA-UR-00-910. Los Alamos National Laboratory, Los Alamos, NM
8. Misawa T, Yoshida H, Akimoto H (2008) Development of design technology on thermal-hydraulic performance in tight-lattice rod bundle: IV large paralleled simulation by the advanced two-fluid model code. J Power Energ Syst 2–1:262–270
9. Kataoka I (2010) Development of research on interfacial area transport development of research on interfacial area transport. J Nucl Sci Tech 47–1:1–19

Direct Numerical Simulation of Stably-Stratified Turbulent Channel Flow with CO_2 Supercritical Pressure

Yoshinobu Yamamoto and Tomoaki Kunugi

Abstract Direct Numerical Simulations of stably-stratified turbulent channel flows were carried out to investigate the effects of strongly property change in supercritical pressured fluids on turbulent structures and heat transfer. Fully-developed stably-stratified turbulent channel flows at CO_2 supercritical pressure (7.58 MPa) were targeted. In this condition, Prandtl number changed between 8.8 and 33 and turbulent Richardson number was 14.2. As the results, effects of the property change on the budget of mean energy were remarkably appeared. And flow laminarization was observed due to the buoyancy effect, however, buoyancy effects on turbulent statistics seem to be reduced compared with the same turbulent Richardson condition but low-Pr case.

Keywords Direct numerical simulation • Effects of property change • Supercritical pressured fluid

1 Introduction

It is very important for realizing a high-efficiency heat exchange system such as nuclear and thermal power generations to understand turbulent heat transfer in supercritical pressured fluids. Therefore, many experimental studies [1–6] on heat transfer at supercritical pressured fluids have been conducted and investigated heat transfer coefficients and wall temperature distributions. Recently, with advancements in computational resources and numerical techniques, a Direct Numerical Simulation (DNS) is one of the most useful tools to understand turbulent structures and heat transfer mechanism.

In this study, we investigated relationships between buoyancy effects and property changes on heat transfer under the supercritical pressure condition by means of DNS.

Y. Yamamoto (✉) • T. Kunugi
Department of Nuclear Engineering, Kyoto University, Yoshida, Sakyo, Kyoto 606-8501, Japan
e-mail: zvf05241@nifty.com

T. Yao (ed.), *Zero-Carbon Energy Kyoto 2011*, Green Energy and Technology,
DOI 10.1007/978-4-431-54067-0_26,

2 Objective Flow Fields

Objective flow fields were two-dimensional fully-developed stably-stratified turbulent channel flows at CO_2 supercritical pressure (7.58 MPa). Figure 1 shows the computational domain and coordinate system, where h is the channel half height, g is gravity acceleration, P_{base} (= 7.58 MPa) is the thermodynamic pressure, superscript * denotes instantaneous value, capital letter denotes mean value, x and u^* ($= U + u$) denotes streamwise direction and instantaneous streamwise velocity (= mean velocity + turbulent velocity), y and v^* ($= v$) denotes vertical direction and instantaneous vertical velocity (= turbulent velocity), z and w^* ($= w$) denotes spanwise direction and instantaneous spanwise velocity (= turbulent velocity), θ^* ($= \Theta + \theta$) denotes instantaneous temperature (= mean temperature + turbulent temperature).

Constant temperature conditions were considered as the thermal boundary conditions: top and bottom wall temperatures kept at 32.7° and 31.7°, respectively. In this temperature range, thermal properties of CO_2 were strongly changed and have a sharp peek at 32.2° as shown in Fig. 2.

3 Governing Equations and Numerical Procedures

Governing equations in this study are following the continuity, momentum equations using the low-Mach approximation, and the energy equation.

Continuity equation:

$$\frac{\partial u_i^*}{\partial x_i} = 0, \tag{1}$$

Momentum equations:

$$\frac{\partial u_i^*}{\partial t} + u_j^* \frac{\partial u_i^*}{\partial x_j} = \frac{\rho^* - \langle \rho^* \rangle}{\rho^*}(-g)\delta_{i2} - \frac{1}{\langle \rho^* \rangle}\frac{\partial p'}{\partial x_i} + \frac{1}{\rho^*}\frac{\partial}{\partial x_j}\left(\mu^* \frac{\partial u_i^*}{\partial x_j}\right), \tag{2}$$

Energy equation:

$$\frac{\partial \theta^*}{\partial t} + u_j^* \frac{\partial \theta^*}{\partial x_j} = \frac{1}{\rho^* c_p{}^*}\frac{\partial}{\partial x_j}\left(\lambda^* \frac{\partial \theta^*}{\partial x_j}\right), \tag{3}$$

where t is time, $<\cdot>$ denotes the horizontal averaged value, p is the hydrodynamic pressure, ρ is density, ν is kinetic viscosity, μ is viscosity, C_p is specific heat at constant pressure, λ is thermal conductivity. Einstein summation convention is adapted for an index variable appears twice in a single term. All thermal

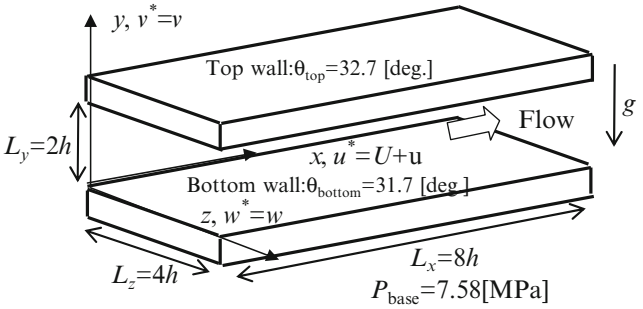

Fig. 1 Computational domain and coordinates system

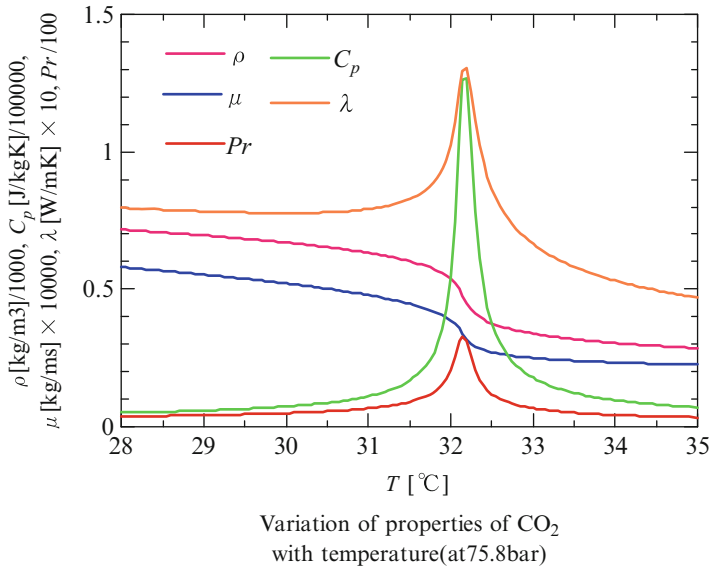

Fig. 2 Thermal properties of CO_2 supercritical pressure (7.58 MPa)

properties were obtained by using PROPATH in the function of temperature (θ*) and thermodynamic pressure (P_{base}).

Numerical procedure is based on a fractional step method; time integration is the Crank-Nicolson scheme for the wall normal viscous term, the Euler implicit scheme for the pressure and buoyancy term, and the third-order Runge–Kutta scheme for others, and a second-order central differencing scheme on staggered grids is adapted for the spatial discretization. As for the boundary condition, no-slip and constant temperature condition were imposed at top and bottom wall, periodic conditions was imposed for streamwise and spanwise directions.

Numerical conditions were shown in Table 1. Time integration was carried out during 30,000 non-dimensional times based on initial friction velocity ($u_{\tau in}$)

Table 1 Numerical condition

	Re_τ	Pr	Ri	Grid number N_x, N_y. N_z	Resolution Δx^+, Δy^+,Δz^+
1	150	8.8–33	0.0	512, 182, 256	2.8, 0.3–2.0, 2.8
2			14.2	576, 182, 288	2.1, 0.3–2.0, 2.1

Re_τ: Reynolds number $= u_{\tau in} h/\nu_0$, Pr: Prandtl number $= \lambda C_p/\lambda$, Ri: Richardson number $= \beta g\ h\Delta\theta/u_{\tau in}{}^2$, β: Coefficient of volume expansion, $\Delta\theta$ ($=\theta_{top}$-θ_{bottom}), N_x, N_y,N_z, Δx^+, Δy^+,Δz^+: grid numbers and grid resolutions normalized by $u_{\tau in}$ and ν_0 for x-, y-,and z-directions

and kinematic viscosity at the bottom wall (ν_0). All quantities in this study were normalized by $u_{\tau in}$ and ν_0, and the temperature difference between top and bottom wall.

4 Results and Discussions

The budget of mean energy equation in CASE1 is expressed as

$$0 = -R\frac{\partial \overline{v\theta}}{\partial y} + \frac{\partial}{\partial y}\left(L\frac{\partial \Theta}{\partial y}\right),\ \rho^* c_p{}^* = \overline{\rho^* c_p{}^*} + \rho c_p\ (= r^* = R + r)\ ,\ \lambda^* = \overline{\lambda^*} + \lambda (= L + \lambda). \tag{4}$$

This equation (4) was consisted of the turbulent heat flux term and the molecular diffusion term. On the other hand, mean energy equation budget on the property change (CASE2) is expressed as

$$0 = -\overline{\left(r\frac{\partial u\theta}{\partial x}\right)} - U\overline{\left(r\frac{\partial \theta}{\partial x}\right)} - \overline{\left(r\frac{\partial w\theta}{\partial z}\right)} - \overline{\left(r\frac{\partial v\theta}{\partial y}\right)} - \overline{\left(r\frac{\partial w\theta}{\partial z}\right)} - \overline{r v}\frac{\partial \Theta}{\partial y} - R\frac{\partial \overline{v\theta}}{\partial y} + \frac{\partial}{\partial y}\overline{\left(\lambda\frac{\partial \theta}{\partial y}\right)} + \frac{\partial}{\partial y}\left(L\frac{\partial \Theta}{\partial y}\right) \tag{5}$$

In (5), correlation terms caused by the property change were appeared in addition to the turbulent heat flux and molecular diffusion term of (4).

Figure 3 shows the budget of mean energy in CASE2. The contribution of the molecular diffusion term (drawn by blue line) was slightly exceeded than one of the turbulent heat flux term (drawn by red line). The correlation terms caused by the property change and temperature convection were significant. Especially, the correlation term between the property change and the spanwise convection (plotted by □) and correlation term between the property change and vertical convection (plotted by Δ) are remarkable.

Effects of vertical and spanwise convection might be resulted by the typical streamwise vortices motion on the wall turbulent coherent structures. On the other hand, correlation terms between the property change and the temperature diffusion (plotted by ×) were insignificant.

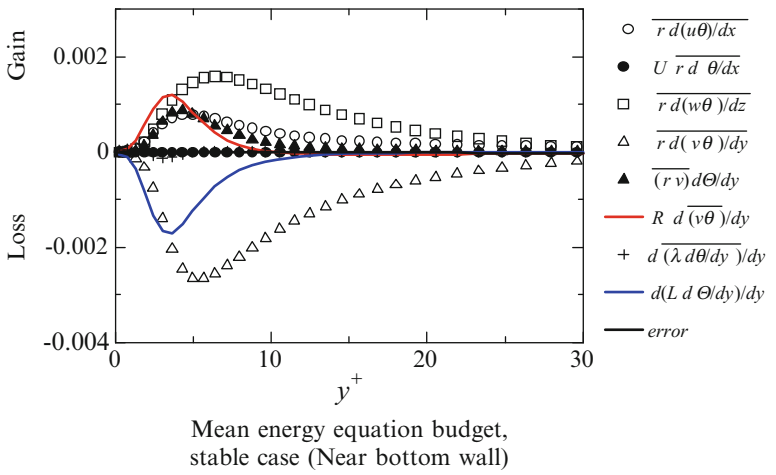

Fig. 3 Budget of mean temperature in CASE2

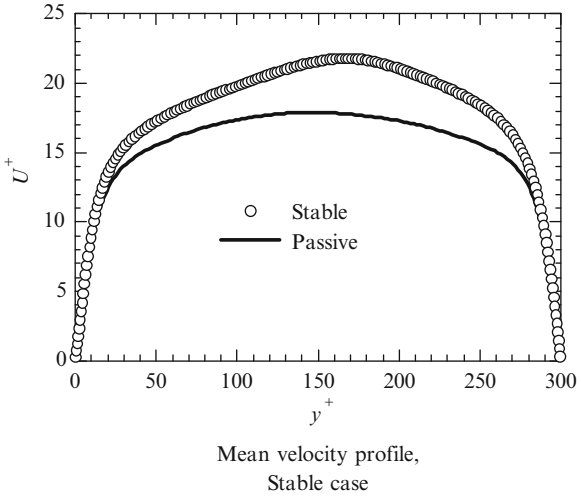

Fig. 4 Mean velocity profiles

Figure 4 shows the mean velocity profile in CASE1 (passive) and CASE2 (stable). Mean velocity profile of CASE2 leans to top wall direction and exceed in mean velocity of CASE1. Turbulent intensity profiles are shown in Fig. 5. Near the bottom wall, the turbulent intensities of CASE2 exceed in those of CASE1. However, near the top wall, turbulent intensities of CASE2 were suppressed compared with those of CASE1. Figure 6 shows the Reynolds shear stress profiles. The tendency of the Reynolds shear stress was similar with the tendency of the turbulent intensity. These indicate that flow laminarization was caused by the stably-stratified effects in this supercritical

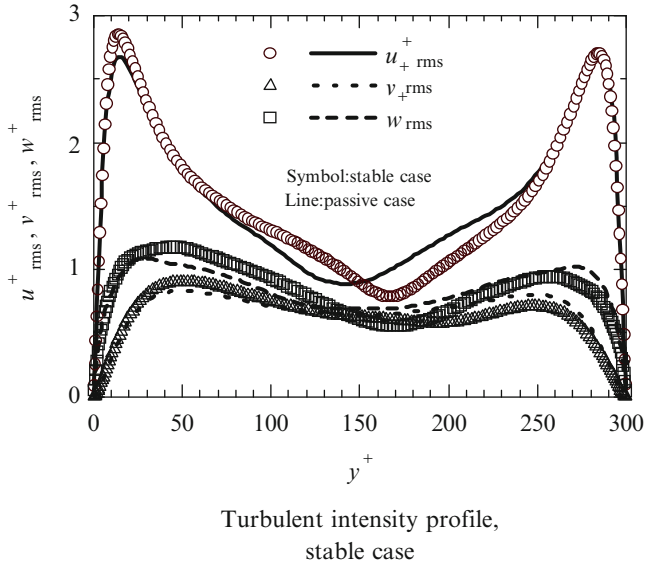

Fig. 5 Turbulent intensity profiles

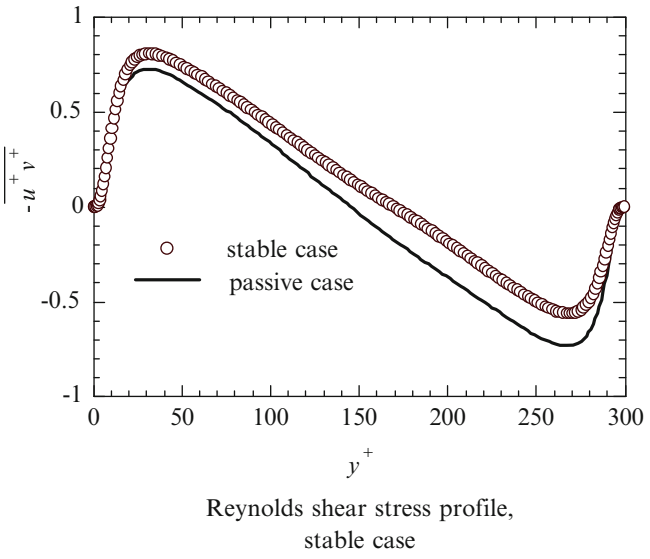

Fig. 6 Reynolds stress profiles

pressure condition. However, buoyancy effects on turbulent statistics seem to be reduced compared with the same turbulent Richardson condition but low-Pr case.

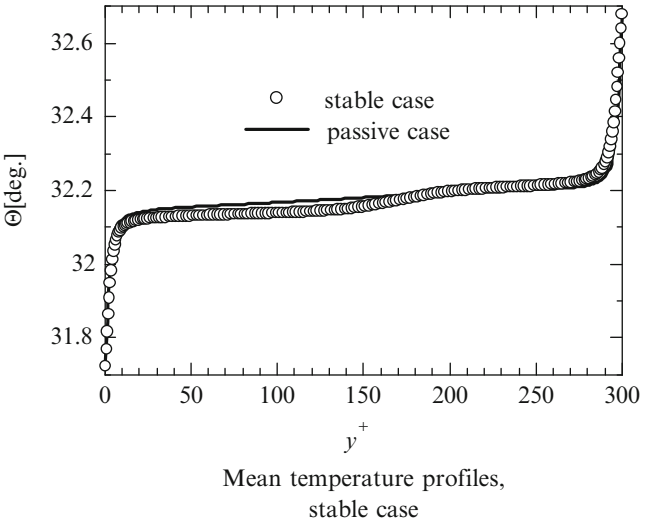

Fig. 7 Mean temperature profiles

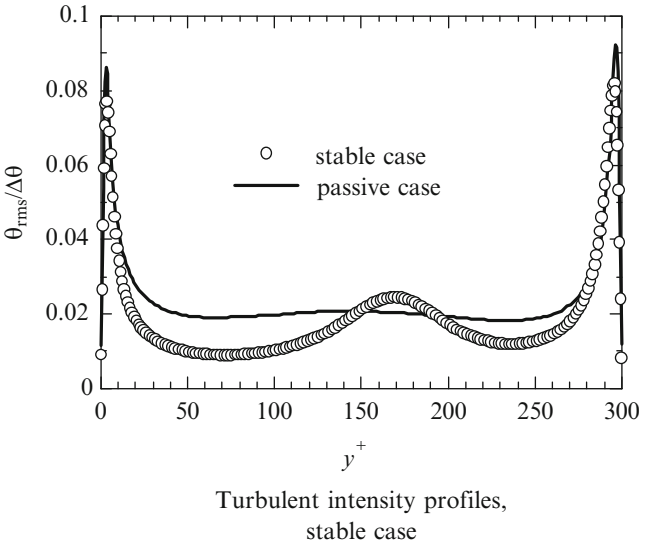

Fig. 8 Temperature intensity profiles

Figure 7 shows mean temperature profiles. The mean temperature profile of CASE2 has the step-bump at $\Theta = 32.2$ in which thermal properties of CO_2 were strongly changed as shown in Fig. 2. Turbulent temperature intensity profiles are shown in Fig. 8. In CASE2, new peak are existed near

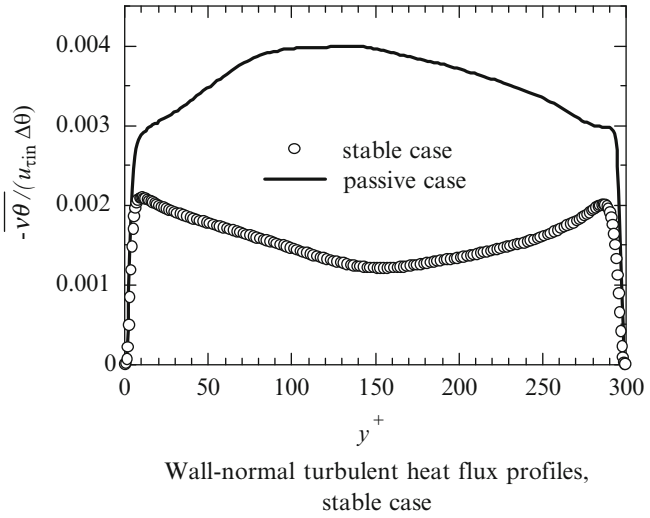

Fig. 9 Wall-normal heat flux profiles

the channel center in which thermal properties of CO_2 were strongly changed. Figure 9 shows wall-normal turbulent heat flux profiles. Turbulent heat flux profile of CASE2 was dramatically suppressed compared with one of CASE1.

Figure 10 shows instantaneous velocity and temperature fields with the end view. Streamwise vortices structures organized the high- and low-speed streaky structures near the bottom- and top-wall, respectively. In side of the bottom wall, streamwise turbulent velocity scales of CASE2, are greater than that of CASE1. In the temperature fields of CASE1, filamentous fluctuations caused by the high-Pr effects were observed. On the other hands, high-wave number fluctuations were suppressed in CASE2. Especially, in the turbulent temperature field of CASE2 temperature fluctuations are restricted. These flow visualization results are consisted with the changes of mean and turbulent statistics profiles between the passive scalar and stably-stratified cases.

5 Conclusions

In this study, Direct Numerical Simulations of fully-developed turbulent channel flows with CO_2 supercritical pressure were conducted. We observed remarkable effects of the property change on the budget of temperature and flow laminarization was also observed due to the buoyancy effect, however, buoyancy effects on turbulent statistics seem to be reduced compared with the same turbulent Richardson condition but low-Pr case.

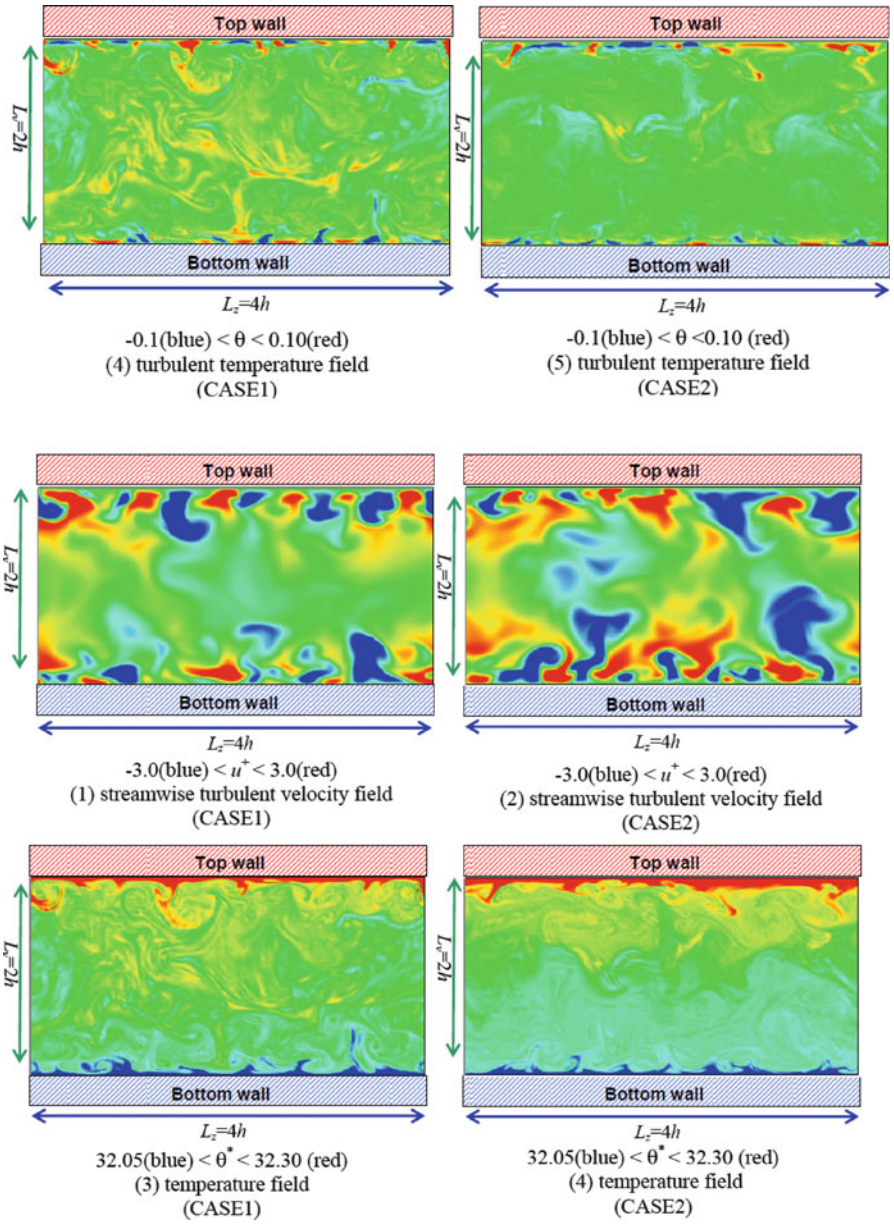

Fig. 10 Flow visualization

Acknowledgement Present DNS were conducted by using the T2K open supercomputer at Information Technology Center, The University of Tokyo. This study was supported by the Global COE program "Energy Science in the Age of Global Warming", MEXT, Japan.

References

1. Shiralkar BS, Griffith P (1970) The effect of swirl, inlet conditions, flow direction, and tube diameter on the heat transfer to fluids at supercritical pressure. J Heat Transfer 92:465
2. Ackerman JW (1970) Pseudoboiling heat transfer to supercritical pressure water in smooth and ribbed tubes. J Heat Transfer 92:490
3. Bourke PJ, Pulling DJ, Gill LE, Denton WH (1970) Forced convective heat transfer to turbulent CO_2 in the supercritical region. Int J Heat Mass Transfer 13:1339
4. Hall WB (1971) Heat transfer near the critical point. Adv Heat Transfer 7:1
5. Yamagata K, Nishikawa K, Hasegawa S, Tsuji T, Yoshida S (1972) Forced convective heat transfer to supercritical water flowing in tubes. Int J Heat Mass Transfer 15:2575
6. Kurganov A, Kaptilnyi AG (1993) Flow structure and turbulent transport of a supercritical pressure fluid in a vertical heated tube under the conditions of mixed convection. Experimental data. Int J Heat Mass Transfer 36:3383

ADS Experiments for the Effectiveness of External Source

Jae-Yong Lim, Cheolho Pyeon, Tsuyoshi Misawa, and Ken Nakajima

Abstract For the confirmation of effectiveness of external neutron source experimentally, Accelerator Driven System (ADS) experiments coupled with FFAG proton accelerator and Kyoto University Critical Assembly as a subcritical system were conducted at February, 2011. By foil activation method with Gold/Indium wires and foils after neutron irradiation at three different external neutron source positions, the variation of neutron multiplication was compared at active core region. The neutron flux increment by 164% and 143% were confirmed when tungsten foils as external source were close to close.

Keywords Accelerator-driven system (ADS) • Fixed field alternating gradient (FFAG) proton accelerator • Foil activation method • Kyoto university critical assembly (KUCA) • Neutron multiplication

1 Introduction

After the tragic accident on Fukushima nuclear power plant at March, 2011, the safety of nuclear plant was re-emphasized worldwide. As a suggested option of a new power plant, an accelerator-driven system has been studied for a few decades which never has the possibility of re-criticality after an unspecified accident and has the capability for TRU transmutation by high-energy neutron injection into a core region [1, 2]. However, numerical analysis or basis experiments by 14 MeV neutrons came from (D,T) accelerator such as Cockcroft type accelerator were performed usually. Since this concept should need high-energy external neutron source without neutron moderator, it seems to be a fast reactor configuration [3, 4].

J.-Y. Lim (✉) • C. Pyeon • T. Misawa • K. Nakajima
Nuclear Engineering Science Division, Research Reactor Institute, Kyoto University, Kumatori, Sennan, Osaka 590-0494, Japan
e-mail: limjy @rri.kyoto-u.ac.jp

T. Yao (ed.), *Zero-Carbon Energy Kyoto 2011*, Green Energy and Technology,
DOI 10.1007/978-4-431-54067-0_27,

In Kyoto University Research Reactor Institute (KURRI), ADS experiments has been conducted from 2004 in order to evaluate the basic characteristics of ADS by coupling between a 14 MeV (D,T) accelerator and a well thermalized core (KUCA A-core) [5–7]. The first high-energy neutron injection was successfully performed on 4th March 2009 using the spallation reactions between protons came from FFAG accelerator and the tungsten target at the KUCA A-core outside. Even though a few pA proton beam intensity was injected into the core, the neutron multiplication was confirmed using the pulse neutron method and Indium foil/wire irradiation method [8]. However, it was not a sufficient intensity to analyze the core characteristics under a subcritical condition experimentally. Therefore, the modification of FFAG accelerator was accomplished for the increase of proton beam current at 2010 and the numerical pre-analyses was fulfilled to figure out the effect of external source position on the core reactivity [9].

In this study, we explained the experiments which conducted at February 2011 in order to verify the effectiveness of external neutrons to subcritical core by changing the position of tungsten foils suggested at previous study.

2 Experiment Setting

2.1 Description of FFAG-KUCA Facilities

For experiments, a coupled system with an FFAG accelerator and a subcritical core was employed which located different buildings—Innovation Research Laboratory (IRL) and KUCA respectively. In order to connect two facilities, a long beam line which has two bending points to fit the different altitudes of them was installed as shown in Fig. 1. Compared with previous experiments, two modifications were applied at the FAG accelerator and the beam line. Firstly, the FFAG complex which consisted of four facilities—(1) ion source, (2) ion-beta, (3) booster and (4) main ring was renewed by substituting from Ion-beta and Booster to a Linac accelerator to supply stable and sustainable protons into Main ring. As a second modification, additional focusing magnets were installed at the end of beam line, the inside of KUCA A-core room to fine adjust protons for the increase of spallation reaction at tungsten target. Finally, 200 pA of proton beam intensity which was 100 times intense than before experiments was obtained approximately after modifications.

As a subcritical system, KUCA A-core was applied which composed of a combination of 23 fuel assemblies and polyethylene moderator/reflector surrounded at core. Each fuel assembly consisted of three sections—a upper and a lower polyethylene reflector and 36 fuel cells which were composed three layers by 1/16″ thickness of a 93% enriched uranium-aluminum (U-Al) alloy, two polyethylene plates with 1/8″ and 1/4″ thickness. Since each assembly had 2″ square geometry horizontally, the dimension of active core region was approximately 28 (W) × 28(D) × 40(H) cm. In contrast with previous core configuration, a slight

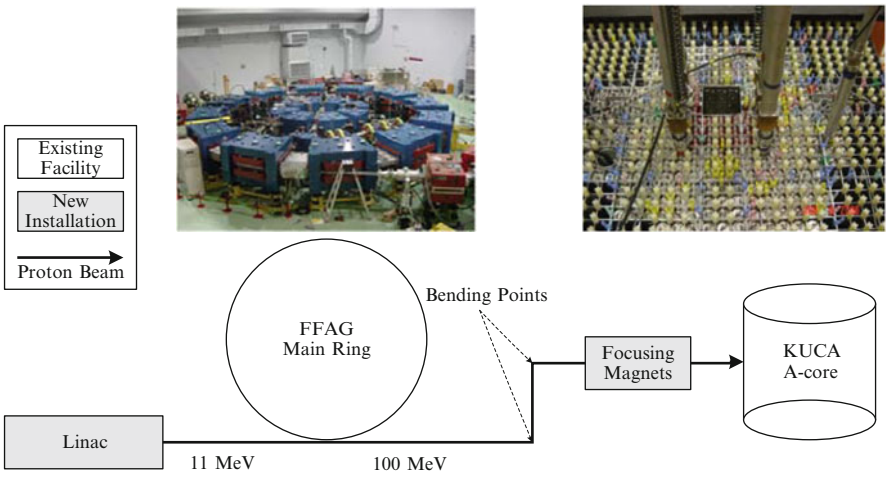

Fig. 1 The configuration of FFAG accelerator and KUCA A-core in the ADS experiments

modification was also adopted at beam duct in accordance with Monte Carlo simulation results. Because a slight higher quantity of neutron reflection could be achieved when the reflector material was substituted from iron to lead, the beam duct consisted of nine void cells with $6'' \times 6''$ cross-section area surrounded by $2''$ thickness lead.

2.2 W Foil Locations and Experimental Conditions

As previous experiment results, it was confirmed that 1 cm thickness of tungsten could be obtained the full-stop of protons with 100 MeV energy and produced a near 60 MeV spallation neutrons [10]. Because of the operation regulation in KURRI, a tungsten target should be installed at the end of proton beam line at least, a tungsten target with 1 cm thickness upper mentioned was divided two parts depend on their functions such as a tungsten target for the installation at a beam line in order to obey the regulation and a tungsten foil for the observation of the core characteristics variation depend on external neutron source position. A set of three tungsten foils which had $5(\phi) \times 0.3(\mathrm{T})$ cm dimension were located at different positions with 17 cm distance gap between each cases inside beam duct as shown in Fig. 2 and Table 1. In these static experiments, the subcritical systems were made by the full insertion of C1, C2 and C3 control rods and by the full withdrawn of S4, S5 and S6 safety rods. By these control rods positions, obtained subcriticalities of WS, WBs and WS′ core were experimentally deduced to be 0.77%, 0.74% and 0.74% Δk/k respectively. In case of WS core, smaller reactivity was shown than that of other cores because a gold wire was set up for the measurement of axial reaction distribution.

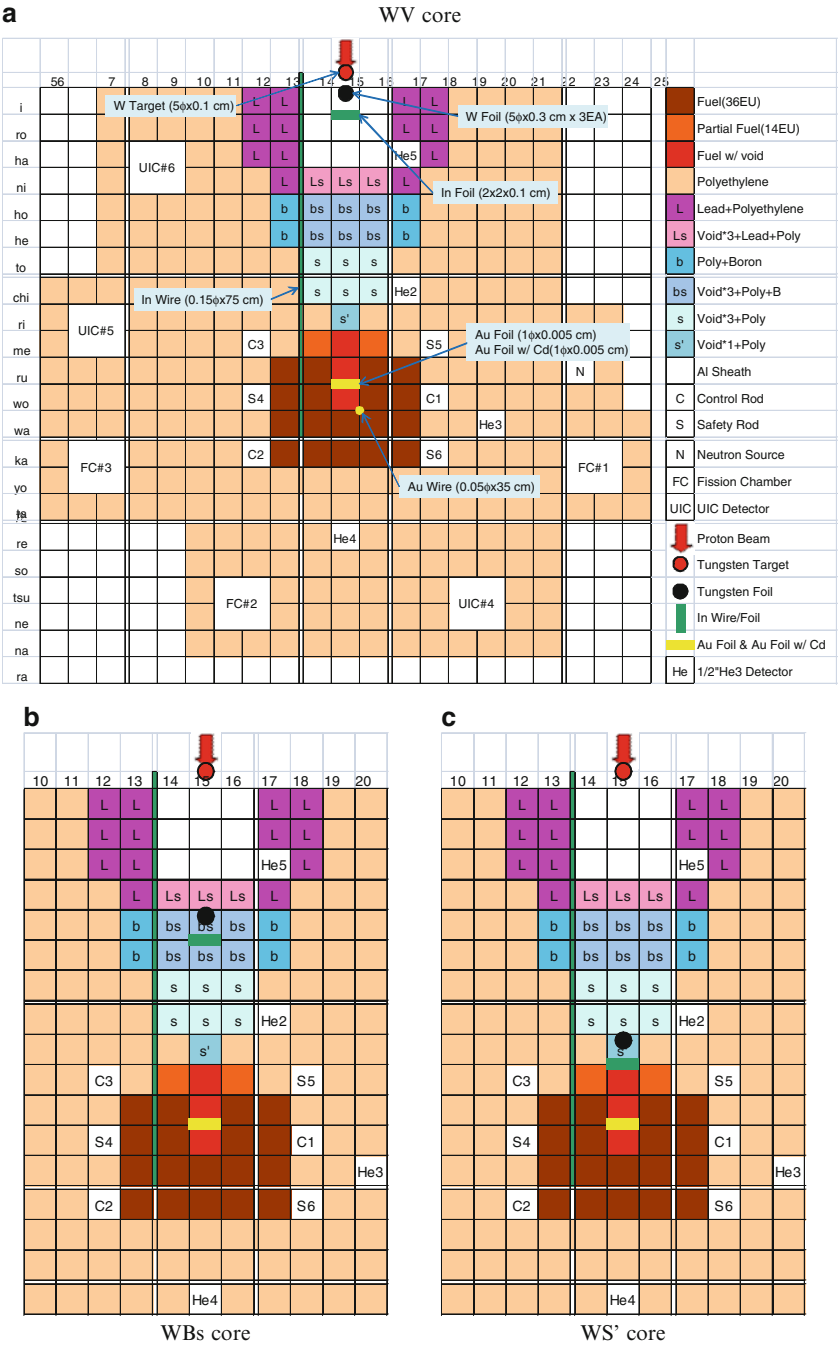

Fig. 2 Three core configurations and the location of installed foils/wires

Table 1 The operation conditions of FFAG and KUCA

	KUCA conditions		FFAG conditions		
Core name	CR & SR position (mm)	Sub-criticality (%△k/k)	Beam intensity (pA)	Repetition rate (Hz)	Width (ns)
WV		0.77	200	20	100
WBs	C1–C3: 0.0 mm	0.74	200		
WS′	S4–S6: 1,200 mm	0.74	150–200		

Experimentally, in order to watch the influence of external neutron source position, various foils and wires were installed at several positions. At first, an indium wire with 0.15 mm diameter and 75 cm length were installed from core surface to core center—from (i, 13–14) to (wa, 13–14) for the ascertainment of radial neutron distribution. To measure the amount of produced spallation neutron, an indium foil with 2 × 2 × 0.1 cm dimension was attached at the behind of tungsten foils secondly. Third foils were a bare gold foil and a gold foil covered by cadmium at core center to calculate relative power changes between each experiment. Finally, an additional indium foil was set up in front of a beam line to normalize the results of foil/wire irradiation experiments, because the operation condition of FFAG accelerator varied during foil irradiation experiments as shown in Table 1.

2.3 Foil Activation Method

The foil activation method is a representative and quiet accurate method for the measurement of neutron flux or distribution because an acquired data—a saturated activity should be proportional to a reaction rate. This saturated activity could be achieved by measuring the total counts of the peak energy of γ-ray emissions using following equation:

$$D_{\infty} = \frac{\lambda T_c C(1+\alpha)}{\varepsilon(1-e^{-\lambda T_i})e^{-\lambda T_w}(1-e^{-\lambda T_c})} \tag{1}$$

where, λ means the decay constant, T_c the measurement counting time, C the counting rate, α an internal conversion coefficient, ε a detection efficiency, T_i the irradiation time, and T_w the waiting time. Especially, for the comparison with relative values of all samples such as a reaction rate distribution by In wire, this (1) could be simplified to (2) when each sample was measured at same detector (Well-type Ge γ-ray detector) during same measurement time (60 sec) after same irradiation period (2 h).

$$D_{\infty}^{R} = \frac{C}{e^{-\lambda T_w}} \tag{2}$$

Table 2 The foil characteristics used in activation method

Foil	Reaction	Threshold (MeV)	Half-life	γ-Ray energy (keV)	Emission rate (%)
In	^{115}In (n, n') ^{115m}In	0.34	4.486 d	336.2	45.8
In	^{115}In (n, γ) ^{116m}In	–	54.29 m	416.9	32.4
				1097.3	55.7
				1293.5	85.0
Au	^{197}Au (n, γ) ^{198}Au	–	2.695 d	411.8	95.5

In this study, following three different reactions by two different materials as shown in Table 2 were used to estimate the reaction rates occurred by thermal and fast neutrons. In case of indium material, a reaction rate originated by fast neutrons could be measured by ^{115}In(n, n′)^{115m}In reaction because of high threshold energy of 0.34 MeV whose cross-section had a peat at 5 MeV. Moreover, a reaction rate dominated by thermal neutrons was also able to measure by ^{115}In(n, γ)^{116m}In reaction using multi-channel analyzer (MCA) which could measure the full width at half maximum (FWHM) of different γ-ray peaks at same time. In case of gold foils and wire, the total count was usually less than that of In foils, because these samples was very thin (wire: 0.05 cm, foil: 0.005 cm) and had light weight. In order to compensate this weak point, a NaI detector with higher efficiency was chosen to reduce the statistical errors of gold foils even though this NaI detector had not worse energy resolution than that of Ge detector.

3 Experiment Results

3.1 Reaction Rate Distribution

A short half-life time of ^{115}In(n, γ)^{116m}In reaction, a irradiated indium wire with 75 cm length was divided by every 2 cm pieces to reduce total measurement time. The reaction rate distributions by three experiment results were shown in Fig. 3 that was normalized by ^{115}In(n, γ)^{116m}In reaction of In foil in front of proton beam line. Since this ^{115}In(n, γ)^{116m}In reaction was contributed to thermal neutrons, thermal neutron peaks caused by polyethylene moderator/reflector were observed at 'SV&14' region—boundary of active core. Any peak was also not found at 'Void', 'Ls', and 'bs' region except leaked thermal neutrons from core at 's' region.

When the same amount of protons was injected this system, the lowest quantity of reaction rate distribution which could be represented to a neutron distribution was revealed at WV core which had the farthest external source. WBs core with a closer external source at 'bs' showed the highest neutron distribution at core. It could be conjectured easily that a closer external source could contribute larger

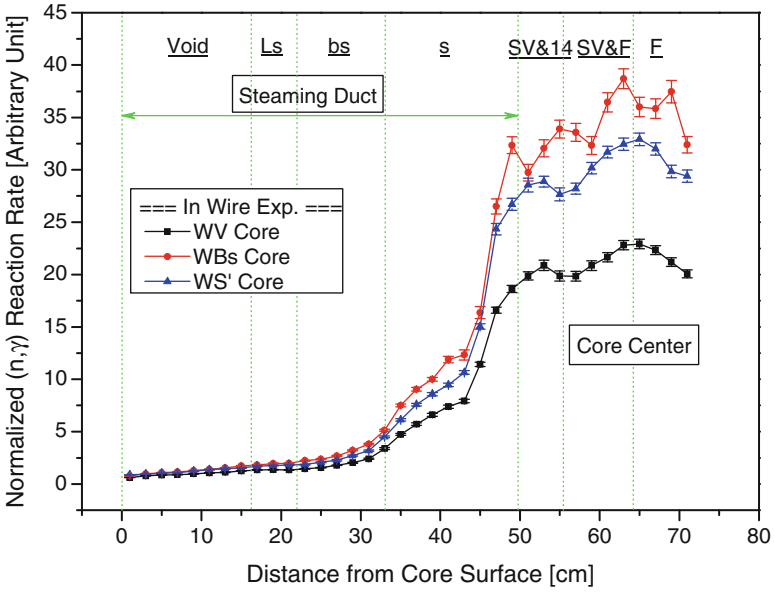

Fig. 3 Horizontal reaction rate distribution by In wire depend on the position of W foils

Table 3 Injected proton amount by MCNPX simulations

Core name	Injected proton into W foils	Standard Deviation	Normalized by WV	Standard Deviation
WV	2.87976E-02	0.0001	100.0	0.0035
WBs	8.33272E-03	0.0002	28.9	0.0069
WS′	3.26183E-04	0.0002	1.1	0.0069

neutron multiplication at core. However, a result contrary to this expectation was exposed at WS′ core which had the closest tungsten foils as a external neutron source. It caused by the proton reduction into tungsten foils because the streaming duct could not transport protons to foils without any loss. After leaving from beam line under the vacuum condition, protons should meet many kinds of structure materials—an aluminum sheet, polyethylene, lead etc. and scatter to many directions even though it could be reflected to steaming duct again by surrounded materials of duct. This presumption was ascertained by Monte Carlo simulation with MCNPX-2.5.0 that reached amounts of protons to tungsten foils for WBs core and BS' core were reduced to 28.9% and only 1.1% in contrasted to that of WV core [11]. In spite of excessive reduction, WS′ core still showed higher reaction rate at core because of the effectiveness of the closest external source.

In order to estimate the axial distribution at core center, a gold wire was installed at (wo-wa, 15–16) position of WV core. Detailed distribution could be obtained by

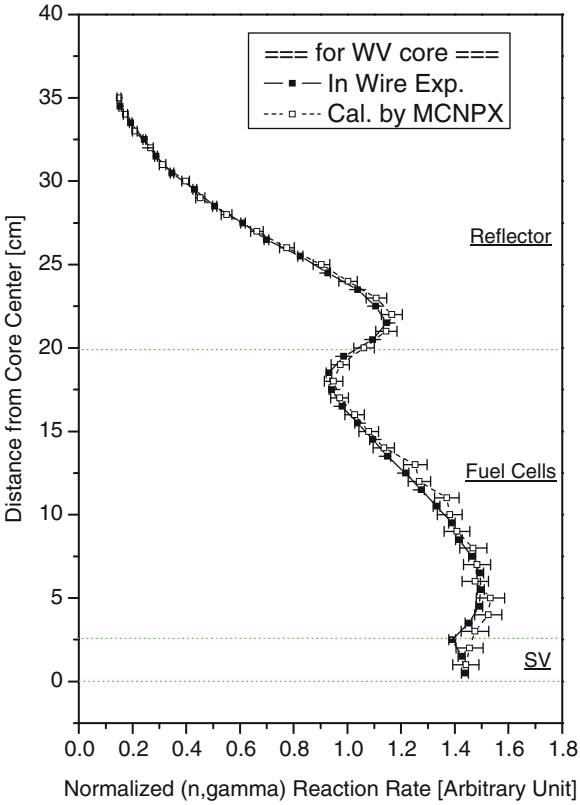

Fig. 4 Comparison of axial reaction rate distribution between experiment and simulation

Au pieces cut with 1 cm length because of higher capture cross-section at thermal neutron energy range. These results were used for two purposes: (1) benchmark for MCNPX simulation and (2) extrapolation distance for the calculation of reactor power using a bare Au foil and a Cd covered Au foil. As shown in Fig. 4, we confirmed that calculation results were agreed with experimental results and the maximum C/E value at core region was less than 2%.

3.2 Neutron Multiplication

As shown in Fig. 5, the calculated neutron spectrum at core center was very similar with that of other cores because three cores were well-thermalized core by a lot of polyethylene moderator. From these results, we could assume that the integrated macroscopic fission cross-sections did not shift depend on different core configuration. Under this assumption, the power comparison between different cores was achieved by the rough estimation because the reactor power was dominant to the total fission reaction at core region and the total reaction rate was also proportional

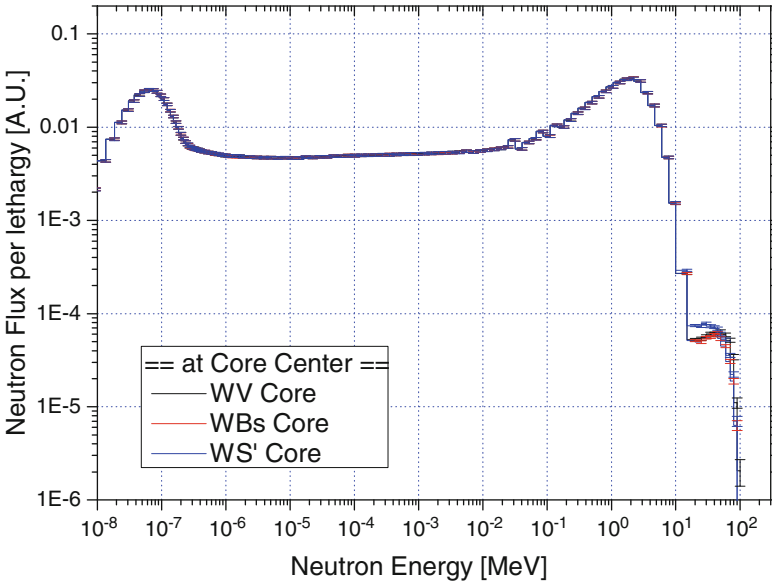

Fig. 5 Neutron spectrum at core center depend on different W foils position

to the summation of activation amount in core region obtained from foil activation method such as following equation:

$$Power \propto \int_{V_{core}} \int_{0}^{thermal} \overline{\Sigma_{f2}} \phi(E) dE dV \propto \sum_{i=core} A_i \tag{3}$$

where, A_i means the saturated activity of ith samples.

From this equation, we obtained the power difference came from the position of external source. When the normalization was accomplished by the summation of saturated activity of WV core, 164% and 143% increment of neutron multiplication was acquired at WBs core and WS′ core respectively.

By using two saturated activity results from a bare Au foil and Cd covered Au foil, the Cd ratio could be obtained which was necessary for the evaluation of real power and thermal neutron flux. For this purpose, two Au foils were attached at axial core center in order to achieve a representative value for the entire core region. However, we found that acquired experimental results, especially for Cd ratio of WS′ core, could not represent the neutron spectrum of entire core because these two foils were located in front of void hole at SV fuel assembly (wo, 15). As shown in Fig. 5, harder spectrum was observed at WS′ core by direct injection of high-energy spallation neutrons from W foils. It made this Cd ratio of WS′ core be larger than an average Cd ratio of whole core and overestimated the quantity of thermal neutron finally. It will be modified by combining numerical analysis.

4 Conclusions

The ADS experiments were conducted using coupled system with FFAG proton accelerator and KUCA in order to estimate the effectiveness of external source position experimentally. Three core configurations with different location of tungsten foils were selected and reaction rates were acquired by various foil activation. Using saturated activity data, we re-confirmed that closer external neutron source was more profitable to increase the neutron multiplication at core; 164% and 143% reaction rate increment were ascertained at WBs core and WS′ core even though only 29% and 1% protons were injected into tungsten foils respectively. For the future work, neutron multiplication M will be evaluated by gold foil activation results and MCNPX simulations.

Acknowledgement This work was partly supported by a "Energy Science in the Age of Global Warming" of Global Center of Excellence (G-COE) program (J-051) of the Ministry of Education, Culture, Sports, Science and Technology (MEXT) of Japan. A part of this study was supported by the Grant-in-Aid for Scientific Research form MEXT from Japan.

References

1. Salvatores M (1999) Accelerator driven systems (ADS), physics principles and specificities. Journal de Physique IV 9(7):17–33
2. Rubbia C et al (1995) Conceptual design of a fast neutron operated high power energy amplifier, CERN/AT/95-44 (ET), European Organization for Nuclear Research (CERN)
3. Millebaud A et al (2007) Prompt multiplication factor measurements in subcritical systems: from MUSE experiment to a demonstration ADS. Prog Nucl Energ 49(2):142–160
4. Kiyavitskaya H (2007) Yalina subcritical facility to investigate neutronics of ADS: Yalina-thermal benchmark, Yalina-booster benchmark. In: IAEA technical meeting. Rome, Italy, 12–16 Nov
5. Pyeon CH et al (2007) Preliminary experiments on accelerator-driven subcritical reactor with pulsed neutron generator in Kyoto university critical assembly. J Nucl Sci Tech 44 (11):1368–1378
6. Pyeon CH et al (2008) Static and kinetic experiments on accelerator-driven system with 14 MeV neutrons in Kyoto university critical assembly. J Nucl Sci Tech 45(11):1171–1182
7. Pyeon CH et al (2009) Reaction rate analyses for an accelerator-driven system with 14 mev neutrons in the Kyoto university critical assembly. J Nucl Sci Tech 460(10):965–972
8. Pyeon CH et al (2009) First injection of spallation neutrons generated by high-energy protons into the Kyoto university critical assembly. J Nucl Sc Tech 46(12):1091–1093
9. Lim JY et al (2011) Nuclear characteristics transition depend on the position of external source on the accelerator-driven system using KUCA and FFAG accelerator. In: Proceedings of the first international symposium on global COE program "Energy science in the age of global warming—toward CO_2 zero-emission energy system", pp 205–213
10. Pyeon CH et al (2010) Reaction rate analysis of nuclear spallation reactions generated by 150, 190, and 235 MeV protons. J Nucl Sci Tech 47(11):1090–1095
11. Pelowitz DB (2005) MCNPX user's manual, version 2.5.0, LA-CP-05-0369, Los Alamos National Laboratory

(iii)
Session Papers

Opportunities and Challenges of Nuclear Power Development in China

Yanping Zhang, Eunju Min, and Suduk Kim

Abstract With real economic growth rate of over 9% per year, China faces a great challenge to meet its increasing energy demand. Nuclear, as a relatively clean energy source has been paid high attention by Chinese government. With China's ambitious target of 86 GW installed nuclear capacity and additional 18 GW under construction by 2020 including inland nuclear power plant, China will become one major country in East Asia along with Korea and Japan (National Development and Reform Commission (2007) Medium- and long-term nuclear power development plan (2005–2020) (in Chinese)). The aim of this paper is to examine the China's nuclear energy program of the past, present in conjunction with the likely future developments of her nuclear energy. Some driving factors including oil supply security, environment pressure and uneven distribution of energy are being discussed. At the same time, questions such as the lack of uranium resource, future disposal of nuclear waste, and reactor safety issues are going to be discussed. As a conclusion, some suggestions and recommendations have been proposed for future nuclear power development in China.

Keywords Chinese nuclear energy • Energy security • Inland nuclear power development • Nuclear safety

1 Introduction

The demand for electricity continues to grow in China with surging economic growth. In eastern areas, supply of electricity hardly satisfied demand in some cities. In 2004, China suffered its worst power shortage since the 1990s, imposing power to be cut or to be limited in 27 out of 31 provinces, municipalities and

Y. Zhang • E. Min • S. Kim (✉)
Graduate School of Energy Studies, Ajou University, YeongtongGu, Suwon 443-749, South Korea
e-mail: suduk@ajou.ac.kr

T. Yao (ed.), *Zero-Carbon Energy Kyoto 2011*, Green Energy and Technology,
DOI 10.1007/978-4-431-54067-0_28,

autonomous regions. Since then, China faces summer power shortage almost every year. In some areas they had to "shut the power down" which hindered economic development and also caused big trouble to local residents.

Nuclear power plants can produce a huge power by consuming relatively small amount of nuclear fuel. For example a 1,000 MW fossil power plant burns about two million tce of coal annually, while a nuclear plant of comparable capacity consumes about 190 tons of natural uranium as fuel. It is argued that nuclear power generation will greatly reduce fossil fuel consumption and alleviate the pressure on the environment caused by coal consumption, because nuclear energy is clean without green-house gas emissions [1].

2 Outlook of China's Energy Market and Opportunities of Nuclear Power

2.1 Energy Outlook of China

In 2010, coal is found to be the biggest part accounting for 68.7% of total primary energy consumption while coal-fired power accounts for over 80% of total power generation in China. Total primary energy demand will grow from 1,929 Mtoe in 2008 to 3,770 Mtoe by 2035

Coal will remain the main energy source, but the share will decrease to 54% (Fig. 1). By 2035, coal-fired power generation will continue to supply most of China's electricity demand accounting for 70%. Nuclear will increase the shares while hydropower will decrease (Fig. 2) [2].

According to IEA World Energy Outlook 2010, total electricity generation of China is expected to grow to 10,000 TWh by 2035 much more than 8,000 TWh estimated by IEEJ [2, 3]. Since many uncertain factors, it is difficult to predict China's power consumption (Fig. 3).

2.2 Opportunities of Nuclear Power in China

China is forecasted to have increasing energy demand, which will be fulfilled mostly by fossil fuels, especially coals. But the heavy reliance on coal brings serious environmental pollution which exposes China into domestic and international pressure. Considering the pressure resulting from coal consumption and the increasing cost of oil and natural gas, nuclear energy is expected to be an inevitable strategic option for China.

Coal-based electricity generation has made China become the world's largest emitter of SO_2 and CO_2 [4]. Subject to international pressure, Chinese government declared her solemn commitment to the reduction of CO_2 emission by 2020.

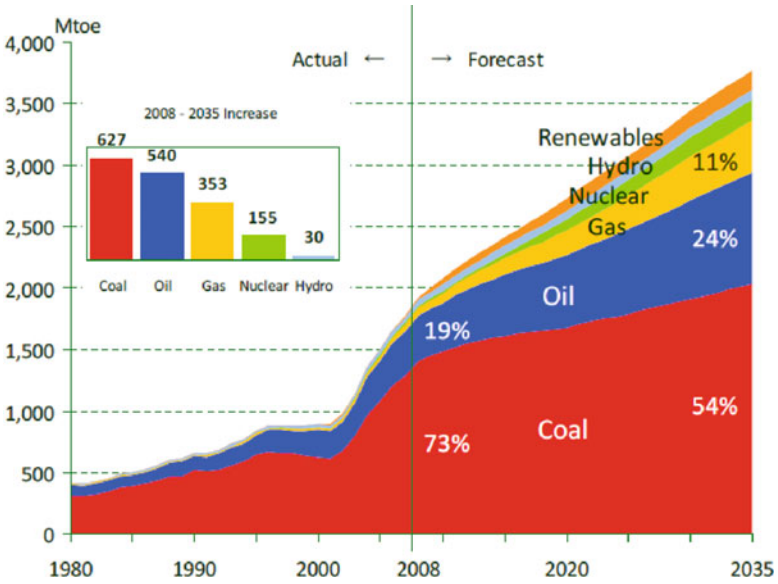

Fig. 1 Primary Energy Demand of China. *Source*: IEEJ, Outlook for BAU Scenario, 2011

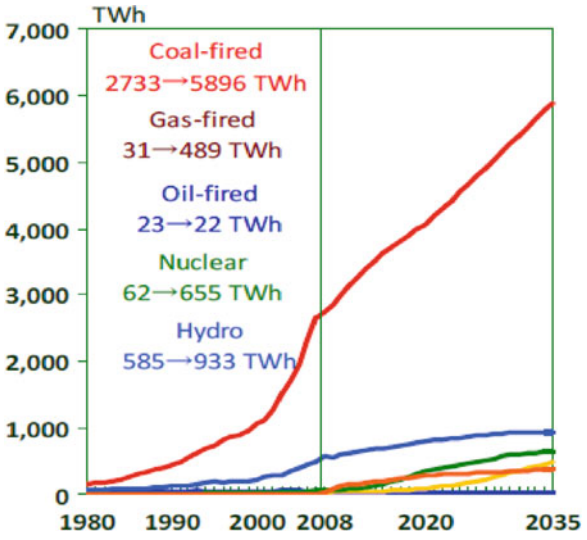

Fig. 2 Electricity Generation Mix of China. *Source*: IEEJ, Outlook for BAU Scenario, 2011

According to the plan, the intensity of carbon dioxide emission is expected to be reduced by 40–50% per GDP than that of 2005 [5].

A large amount of coal must be transported to the eastern coastal regions from west due to the uneven distribution of coal. It not only causes heavy traffic pressure

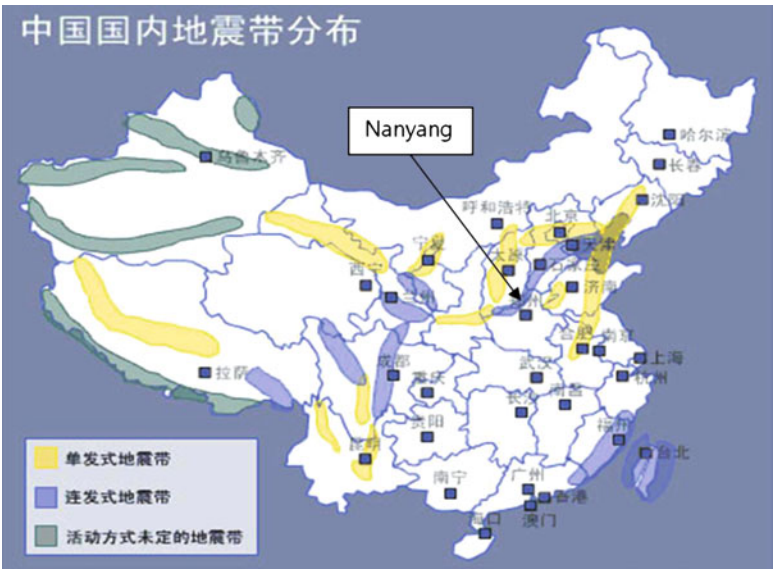

Fig. 3 Earthquake zone of China. *Source*: http://bbs.xmfish.com/read-htm-tid-4125436-page-1.html

but also increases the coal prices. China's coal import started growing since 2002 because the cost of importing coal became competitive with domestic production.

With the rising energy demand, China became a net oil importer in 1993 and a net coal importer in 2007. Currently, almost half of China's oil is imported from Middle East. According to the IEA's World Energy Outlook 2010, China will import 79% of the oil for consumption by 2030, accounting for a larger increment in oil demand than any other country [3]. Considering the future oil supply security, however, nuclear and renewable energy are being paid much attention.

3 The Challenges of Nuclear Power Development

3.1 Overview of Global Nuclear Development

According to the statistical data of World Nuclear Association (WNA), there are 440 units of operable nuclear reactors all over the world distributed in 30 countries with combined capacity of 376,511 MWe. The total generated electricity is 2,630 billion KWh, accounting for 13.8% of total electricity generation. However, electricity generation from nuclear power takes a small share of 1.8% in total electricity production of China [6].

Table 1 includes only those future reactors in the world envisaged in specific plans and proposals and expected to be operating by 2030. It can be seen that USA

Table 1 World nuclear power reactors ranking (Aug 1st 2011) (Unit : MWe net)

	Operable		Operable + under construction		Operable + under construction + planned		Operable + under construction + planned + proposed	
1	USA	101,421	USA	102,639	USA	109,839	**China**	**222,971**
2	France	63,130	France	64,850	**China**	**99,971**	USA	148,439
3	Japan	44,642	Japan	47,398	France	66,570	Russia	76,044
4	Russia	23,084	**China**	**39,981**	Japan	61,170	India	72,985
5	Germany	20,339	Russia	32,044	Russia	48,044	Japan	67,930
6	South Korea	18,785	South Korea	24,585	South Korea	32,985	France	67,670
7	Ukraine	13,168	Germany	20,339	India	23,985	Ukraine	37,868
8	Canada	12,679	Canada	14,179	Germany	20,339	South Korea	32,985
9	**China**	**11,271**	Ukraine	13,168	Canada	17,479	UK	29,425
10	UK	10,745	UK	10,745	UK	17,425	Canada	21,279
Total	World	371,584	World	432,918	World	605,013	World	993,318

Source: WNA, Nuclear Power in China, Aug 1st 2011

Fig. 4 Nanyang Nuclear Power Plant. *Source*: www.heneng.net

ranks first for operable capacity, but in a long term China will hold the biggest total capacity(including under construction, planned and proposed reactors), which is much higher than any other countries.

3.2 Nuclear Development of China

Since China put its first nuclear power plant (named Qinshan) into commercial operation in 1992, there has 14 nuclear reactors in operation with the capacity of 11,271 MWe and the electricity generation has reached 71 billion TWh until August 1st of 2011. Most of the nuclear reactors are located in coastal areas and generally use seawater for cooling a direct once-through cycle and they have been playing an important role for coastal economic development [7].

China has started its strong expansion of inland nuclear power plant with half of the planned nuclear power plants will be located in inland. For example Nanyang nuclear power plant in Henan province (Fig. 4). But the issue to be concerned is some of the plants are nearby earthquake zone, which could be a serious threat for nuclear safety not only to China herself, but also to the neighboring countries considering the seasonal wind direction of this region as is indicated by Sakurai [8].

3.3 Challenges in the Development of Nuclear Power in China

According to a WNA report, around 5.469 million tU of uranium resource is available in the world in 2007, only less than 1% of which is distributed in China. Currently, China's nuclear power plant needs a relatively small amount of the uranium resources. In the long term, however, the uranium demand is increasing and the import will be the only choice.

Although nuclear is considered as emission-free energy, it still produces hazardous waste. Nuclear waste can be divided into high-level waste (HLW) and low-level waste (LLW). Now, China has a small scale of nuclear generation, so that only a small quantity of nuclear waste has to be handled. With China's ambitious nuclear plan, the nuclear disposal waste will become a very important issue.

Due to the proliferation risk, nuclear energy development in China is strictly supervised by Chinese government [1]. Chinese government has issued some laws and regulations such as "nuclear power plant site selection safety regulation" (HAF101) [9], "nuclear power plant emergency management regulation" (HAF002) [10] etc. All the regulations and standards are adopted from international regulations by International Atomic Energy Agency (IAEA) [11, 12]. As was discussed earlier, an additional concern is the strong expansion of inland nuclear power plant with almost half of the planning nuclear power plants will be located in inland. Some of the plants are nearby earthquake zone, which could be a serious threat for nuclear safety.

4 Suggestions and Recommendations

In this paper, potential opportunities together with the challenges in the development of nuclear in China have been discussed in view of long term energy in China. As a conclusion, issues indentified in this process such as the sustainable uranium supply, acceleration of the development nuclear waste treatment technology, enhancement of the nuclear safety, the issuance of "Atomic Energy Law", and strengthening the cooperation among China, Korea and Japan are discussed for future suggestions and recommendation.

In the past 20 years, due to the small scale of nuclear generation, the utilization of uranium demand is relatively small. With its ambitious target the demand of uranium resource mainly depends on imported uranium resource. Therefore, ensuring the sustained supplying of uranium resource will be very important for China.

Nuclear waste increases as the number of operating nuclear power units grows, the nuclear waste will be a big worrying issue. Therefore, it is crucial for China to exploit the cleaner technology not only for the safety of the environment but also for people's health.

It is necessary for China to be concerned with the safety, especially considering some of planned reactors are around earthquake zone. National Nuclear Safety Administration (NNSA) as the nuclear safety regulator should establish the standards of site selection, seismic level and upgrade the emergency procedures.

The problem of Chinese management system relating to nuclear is that there are too many departments having different opinions to the legislations which are not easily reconciled. China began to start the first draft of the "Atomic Energy Act" in 1984 but the official "Atomic Energy Act" have still not yet be issued [13]. The "Atomic Energy Law" is important for safety supervision and management, radiation protection, non-proliferation and physical protection, etc.

Currently, the total operable capacity of China, Korea and Japan accounts for 20% of the total of the world, additional reactors under construction and planned will account for almost 32%.

Considering such a high ratio of nuclear capacity expected in three north eastern Asian countries, the more strengthened cooperation among these countries is very important, especially in the aspect of nuclear safety. Once a nuclear accident happens in any of the three countries, it will surely affect other Asian countries. The three countries should set an institutional framework to enhance the cooperation for the safety of nuclear power development and EURATOM (European Atomic Energy Community) could be a good example to refer to.

References

1. Zhou S, Zhang XL (2010) Nuclear energy development in China: a study of opportunities and challenges. Energy 35:4282–4288
2. IEEJ (2011) Outlook for BAU Scenario, http://eneken.ieej.or.jp/data/3791.pdf
3. IEA (2010) World Energy Outlook, http://www.iea.org/weo/docs/weo2010/WEO2010_ES_English.pdf
4. Xu YC (2008) Nuclear energy in China: contested regimes. Energy 33:1197–1205
5. Coruche L, Kilburn M (2010) Nuclear energy in China and Hong Kong, Civic exchange, http://www.civic-exchange.org/wp/wp-content/uploads/2010/11/Nuclear_energy_in_China_and_Hong_Kong_en.pdf
6. World Nuclear Association (WNA), http://www.world-nuclear.org
7. Nuclear Threat Initiative (NTI), http://www.nti.org
8. Sakurai T (2010) Modeling study on long-range transboundary air pollutions in Northeast Asia. In: 13th international conference on harmonization within atmospheric dispersion modelling for regulatory purposes, Paris, France, 1–4 June 2010
9. National Nuclear Safety Administration (1991) Nuclear power plant site selection safety regulation (HAF101) (in Chinese)
10. State Council of the People's Republic of China (1993) 8.4, Nuclear Power Site Selection Safety Regulation (HAF002) (in Chinese)
11. Wang ZC (2007) Nuclear challenges and china's choices, China Security: 52–65
12. Zhou Y, Rengico C (2010) Is China ready for its nuclear expansion? Energ Pol 39(2011):777–781
13. Jin W. The current situation and issues of China Atomic Energy Law Legislation (In Chinese)

Measurement of Spatial Distributions of Fusion Reactions in an Inertial Electrostatic Confinement Fusion Device Driven by a Ring-Shaped Magnetron Ion Source

Taiju Kajiwara, Kai Masuda, John Kipritidis, Yu Yamagaki, and Kazunobu Nagasaki

Abstract In an inertial electrostatic confinement (IEC) fusion device, the so-called 'beam–beam' reactions are preferable as their fusion rate shows I^2-dependence. In previous experiments with a newly developed-IEC device driven by a ring-shaped ion source at low pressure (several mPa D2), we observed I^2-dependence of neutron production rate for the first time in the world. It is necessary to clarify what brought this I^2-dependence. Measurement of spatial distribution of proton production by DD fusion reactions should be an effective means of determining the contribution of beam–beam reactions. With this new low pressure IEC, however, the detector should be nearer the IEC center in order to detect ample proton count rate, limiting X-ray flux on the detector by the collimator. Additionally, spatial resolution is required to be higher than the previous system to distinguish the central gridded cathode space from the cathode surface. We have designed a new measurement system. The spatial resolution was expected to be high enough. New setup has been ready, and experiments in the new IEC will be done very soon.

Keywords Fusion • Inertial electrostatic confinement • Proton detection

T. Kajiwara (✉) • Y. Yamagaki
Graduate School of Energy Science, Kyoto University, Kyoto 611-0011, Japan
e-mail: k-taiju@iae.kyoto-u.ac.jp

K. Masuda • K. Nagasaki
Institute of Advanced Energy, Kyoto University, Kyoto 611-0011, Japan

J. Kipritidis
Applied and Plasma Physics, School of Physics, The University of Sydney, Sydney, Australia

T. Yao (ed.), *Zero-Carbon Energy Kyoto 2011*, Green Energy and Technology,
DOI 10.1007/978-4-431-54067-0_29,

1 Introduction

An inertial electrostatic confinement (IEC) fusion device consists of a central high transparent cathode grid (with voltage V_{grid} 10–100 kV and current I_{grid} 10–100 mA) and an outer grounded anode aiming to converge ion beams of a 0.1–5 Pa D2 (or D_2-^{3}He) glow discharge into the central cathode space [1]. IEC can be a transportable neutron source which is expected to be useful for advanced researches such as accelerator-driven subcritical reactors. In order to improve the IEC efficiency, or ratio of fusion rate to input power, we shall enhance most preferable fusion reactions between energetic ions (the so-called "beam–beam" reactions) and clarify its physics. Because its fusion rate is expected to be proportional to the square of I_{grid} in contrast with linear dependence of another reactions, reactions between an ion and a gas molecule, or reactions between an ion anda molecule embedded in a central cathode grid. We obtained neutron yield that were proportional to 1.7th power of I_{grid} and some experimental results which indicated the beam–beam reactions for the first time in the world with an IEC driven by a ring-shaped magnetron ion source (RS-MIS) [2]. This device produces ring shaped plasma in the vicinity of itself, and ions in the plasma are converged into the central cathode cylindrically, unlike linearly convergence by conventional pencil-shape ion source. It can produce ions in low pressure (several mPa), and then ions' lifetime are extended by reduction of charge exchange. Therefore, ion density at the center of IEC in which beam–beam reaction were expected to occur should have been much higher than the previous one. RS-MIS consists of a central spherical cathode grid, which is 150 mm in diameter, a ring-shaped magnetron ion source, 364 mm in diameter, and spherical grounded anode grid, 445 mm in diameter, in a cylindrical vacuum chamber as shown in Fig. 1. These fusion reactions should have distinct spatial distribution, at the center of a gridded cathode, throughout the volume of gas, and at the cathode surface, respectively. It should therefore be possible to determine the relative contribution of them by measuring the spatial distribution of fusion reactions.

A proton measurement system made up of a movable detector and a collimator with a tomographic analysis method (Maximum Likelihood Expectation Maximization method; ML-EM method [3, 4]) has been used for estimation of the distribution on a glow discharge driven IEC [5–7], and it was found to be useful to distinguish contributions of D-D and D-^{3}He reactions with respect to the observed proton energy. For the new low pressure and low current device, however, the movable range of the proton measurement system was limited, and the detector was too far from the IEC to obtain an ample count rate.

2 Design of New Proton Measurement System

An improved proton collimation system for measurement of spatial distribution of fusion reactions in the low pressure driven IEC device has to meet two requirements. First, the proton detector should be closer to the IEC than the one

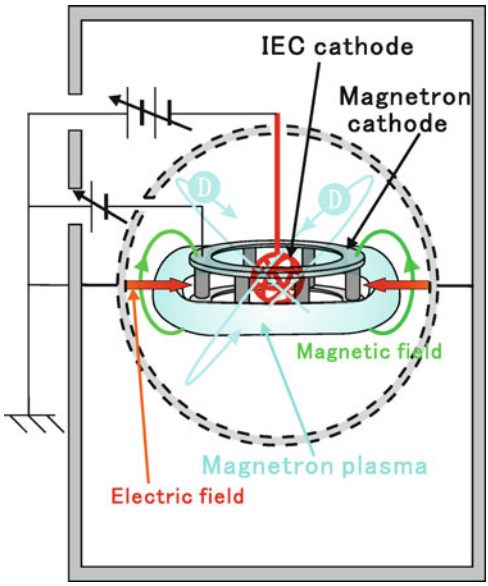

Fig. 1 The low pressure driven IEC by the ring-shaped magnetron ion source

of the previous system. In the new low pressure device, I_{grid} is only up to 1 mA at 5 mPa and $V_{grid} = 60$ kV, and its fusion rate, or proton yield, is about 1/30 of that of the glow driven IEC at $V_{grid} = 60$ kV and $I_{grid} = 30$ mA. We should move the detector closer to the IEC to obtain realistic proton count rate more than 10counts/s at least. We should also move the collimator closer to the IEC to keep the pileup X-ray noise level low enough to distinguish from proton signals. Second, the detector should be able to look at areas outside of the cathode, in order to make spatial resolution better by distinguishing the beam–beam reaction occurring at the center from the beam-grid occurring on the cathode.

Based on these requirements, we designed a new proton measurement system shown in Fig. 2. It consists of a proton detector and a collimator mounted on the IEC vacuum chamber through a flexible bellow. The detector is a kind of Schottky barrier diode of Si and Au foil. Its sensitive area is 600 mm^2 large and 150 μm thick. It is arranged on a SUS304 flange via SUS304 rods. A Peltier device is attached to the detector in order to reduce the thermal noise by cooling. The collimator is 1 mm thick Pb plate which has a 20 mm bore in diameter. It is arranged in the vicinity of the anode, and is supported by a 200 mm long SUS304 cylinder. The flange on which the detector is mounted and the cylinder with the collimator are connected each other by a nipple flange and a conical reducer made of SUS304. The bellow is 200 mm long and was made of stainless steel. Upper side of the bellow is fixed by two hinges, and it is the center of rotation of the measurement system, the detector and the collimator. A stepping motor is arranged next to one of flanges of the bellow, and it rotates the measurement system. Two rectangular magnets are mounted around the collimator. They bend electrons' trajectories and reduce the noise from X-ray which is emitted by the electrons hitting the detector.

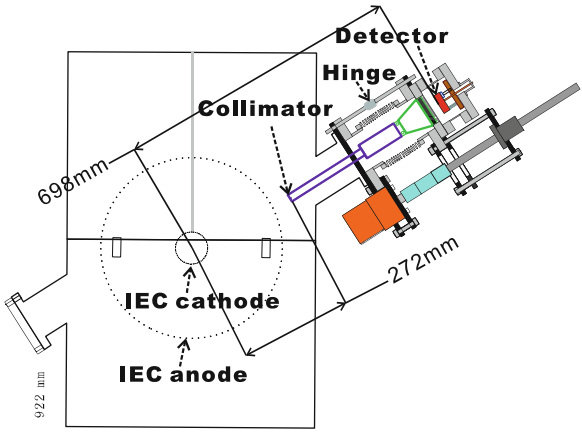

Fig. 2 The new designed proton measurement system for the low pressure driven IEC

The distance between the detector and the center of device is 698 mm. This is 618 mm shorter than the previous system. Bore diameter of the new collimator is 20 mm, and the distance between the collimator and the center is 272 mm. This is 300 mm shorter than the previous one.

2.1 Performance Evaluation of the New System

2.1.1 X-Ray Pileup Noise and Proton Count Rate

We numerically evaluated appropriate experimental parameters to maintain the X-ray noise level and proton count rate at that time for the new system with following assumptions. (1) source volumes of protons (V_P) and X-ray (V_X) are a sphere of 8 mm in diameter at the center of the IEC and a spherical shell of 680 mm in diameter which corresponded to the surface of the anode, respectively. (2) protons and X-rays cannot go through the duct wall and collimator plate. (3) their reflection on the apparatus wall is negligible. (4) X-ray noise level and proton count rate are proportional to I_{grid} and solid angles of the detector as seen from their source regions. The averages of solid angles for the sources of protons and X-rays of the new system ($\Omega_{P,\ New}$ and $\Omega_{X,\ New}$) and of the previous one ($\Omega_{P,\ Pre}$ and $\Omega_{X,\ Pre}$) are shown in Table 1. Referring to an experimental result of the previous system for a glow driven IEC with 60 kV, 30 mA and 50#/s of proton count rate, the maximum current of the low pressure IEC to maintain the same X-ray noise level as the reference can be evaluated like (1) at 60 kV.

$$30\text{mA} \times \frac{\Omega_{X,New}}{\Omega_{X,Pre}} \sim 4\text{mA}. \tag{1}$$

Table 1 Solid angles of the detector from the assumed proton and X-ray source regions of the new or previous proton measurement system

	Previous	New
Proton $\Omega_p \equiv \frac{1}{v_p}\int_{vp} \omega dV$ [sr]	$\Omega_{\mathrm{P,\ New}} = 1.18 \times 10^{-5}$	$\Omega_{\mathrm{P,\ Pre}} = 7.20 \times 10^{-5}$
X-ray $\Omega_x \equiv \frac{1}{v_x}\int_{vx} \omega dV$ [sr]	$\Omega_{\mathrm{X,\ New}} = 7.73 \times 10^{-7}$	$\Omega_{\mathrm{X,\ Pre}} = 5.38 \times 10^{-6}$

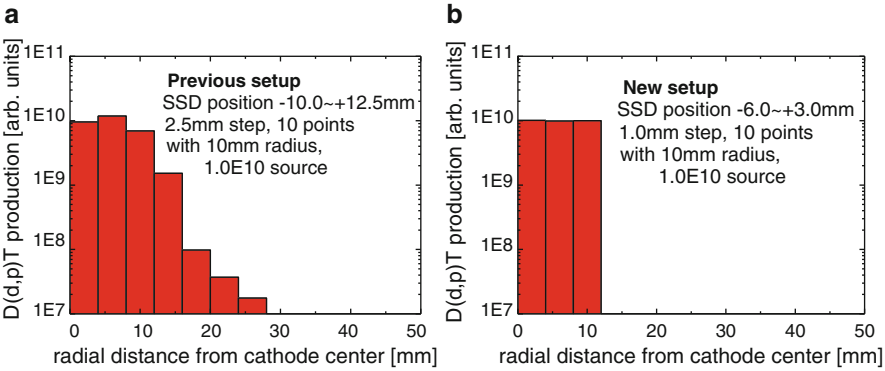

Fig. 3 Simulation results of reconstructed proton birth place by ML-EM method

This current is expected to be high enough for the low pressure driven IEC to measure the obvious beam–beam reaction. Similarly, for the same noise level, in other words, at the parameters of 4 mA and 60 kV, proton count rate can be expressed like following.

$$50\#\ /\mathrm{s} \times \frac{\Omega_{\mathrm{X,New}}}{\Omega_{\mathrm{X,Pre}}} \times \frac{\Omega_{\mathrm{P,New}}}{\Omega_{\mathrm{P,Pre}}} \sim 44\#\ /\mathrm{s}. \tag{2}$$

This count rate is big enough to obtain significant proton counts during realistic experimental time.

2.1.2 Spatial Resolution

Visible area for the detector in the anode is almost twice larger than the previous one. We evaluated spatial resolutions of the new measurement system and the previous system. We assumed a uniform spherical proton source, which is 10 mm in radius at the center of the IEC. We calculated the number of detectable protons using solid angles of the detector as seen from the source region, and then we reconstructed the spatial distributions of the proton source for each setup via the ML-EM algorithm as shown in Fig. 3. The calculated volume was divided into

4 mm thick spherical shells. The detector was moved from the lower limit to the upper limit of its vertical position for each case. Figure 3a, which was the result of the previous measurement system, showed spreading distribution of fusion reactions, although the given source was uniform. On the other hand, Fig. 3b, the result of the new measurement system, shows central uniform fusion reactions obviously corresponding to the given source. For other region source, the cathode surface or volumetric area around the cathode, the new system showed much lower dispersion compared with the previous system.

3 Conclusions

We have designed a new proton measurement system for the low pressure IEC driven by RS-MIS and evaluated its performance numerically. Pileup X-ray noise was estimated to be acceptable level up to 4 mA of IEC cathode current at 60 kV, and proton count rate would be high enough to obtain significant signal counts in a realistic experimental period at the same parameter. Spatial resolution is high enough to measure the central 20 mm diameter proton source, at least. That system has been already installed on the low pressure IEC, and proton measurement experiments with D_2 gas will be done.

Acknowledgement This work is performed with the support and under the auspices of the NIFS Collaboration Research program (NIFS09KCHH026), and is also supported by Grants-in-Aid for Scientific Research in Japan (Grant No. 22686011).

References

1. Hirsch RL (1967) Inertial-electrostatic confinement of ionized fusion gases. J Appl Phys 38:11
2. Masuda K et al (2010) Cathode grid current dependence of D (d, n) 3He reaction rates in an inertial electrostatic confinement device driven by a ring-shaped magnetron ion source. Plasma Phys Contr Fusion 52
3. Moon TK (1996) IEEE Signal Process Mag, pp 47
4. Zen H et al (2005) Quantitative evaluation of transverse phase space tomography. In: Proceedings of the 27th international free electron laser conference, Stanford University, CA, USA, August 21–26, pp.592–595, APS
5. Masuda K et al (2006) Spatial distribution of D-D/D-^{3}He advanced fuels fusion reactions in an inertial electrostatic confinement device. Fusion Energy, 21st IAEA conference
6. Fujimoto T et al (2007) Intensity distribution of D-3He fusion reaction rate in an IEC device. IEEE 2007
7. Masuda K et al (2009) Diagnostic system development for D-D and D-3He reaction distributions in an inertial-electrostatic confinement device by collimated proton measurements. Fusion Sci Tech 56:528

Nonlinear Collision Effect on α Particle Confinement in Toroidal Plasmas

Yoshitada Masaoka and Sadayoshi Murakami

Abstract We study the α-particle confinement including the collisions with various plasma species such as electron, deuterium, tritium, and high-energy α-particle. GNET code (Global NEoclassical Transport) is improved to take into account the nonlinear collision effect in a heliotron fusion reactor based on the LHD configurations. We analyze the real and velocity space distributions and the energy and particle loss rate changing the background plasma parameters, and verify the effects of collision with high-energy particles on the α-particle confinement.

Keyword LHD • Nonlinear collision • Nuclear fusion • Plasma heating • α-Particle confinement

1 Introduction

In a helical system, the confinement magnetic field is generated mainly by the helical coil current. This system has several advantages, such as the prolonged confinement of a steady state and no plasma disruption caused by plasma current. However, high-energy particle trajectories are complicated in a three dimensional magnetic confinement. It is necessary to study the high-energy particle orbits and behaviors in the helical system. Especially, high-energy α particles generated by nuclear fusion reaction heat plasma and keep the temperature high. If they are lost, the heating power is reduced and the first wall would be damaged locally. Thus, it is necessary for these particles to confine until the thermalization.

Since the relative velocity between high-energy α-particle sometimes become very small, although the amount of high-energy α-particle is less than the amount of

Y. Masaoka (✉) • S. Murakami
Department of Nuclear Engineering, Kyoto University, Yoshida-Honmachi, Sakyo-ku, Kyoto 606-8501, Japan
e-mail: masaoka@p-grp.nucleng.kyoto-u.ac.jp; murakami@nucleng.kyoto-u.ac.jp

T. Yao (ed.), *Zero-Carbon Energy Kyoto 2011*, Green Energy and Technology,
DOI 10.1007/978-4-431-54067-0_30,

thermal other ions, the nonlinear collisions between α-particles would have some effect on velocity scattering. Although the amount of high-energy α particles are much less than thermal ions, it is considered that the nonlinear collision by each fast α particle has usually larger effect than that by other background ions [1]. This nonlinear collision effect may lead to deteriorate the α particle confinement, because of increasing a pitch angle scattering. Thus the analysis including the both complicated orbit and nonlinear collision effects are necessary to make clear the α-particle confinement in heliotrons.

2 Simulation Model

In this study, we assumed a heriotron type fusion reactor extending the LHD magnetic configuration [2]. This reactor is based on the NeoClassical transport optimized (NC) configuration which is the inward shifted magnetic configuration optimized the neoclassical transport based on $R_{ax} = 3.53$ m in LHD [3]. R_{ax} is the magnetic axis position in the major radius. This reactor configuration has the plasma volume of 1,000 m^3 and the magnetic strength of 5 T at the plasma center.

In order to analyze a stationary distribution of α particles including the nonlinear collision effects, we solve the drift kinetic equation for α particles in five dimension phase space using the GNET (Global NEoclassical Transport) code [4]. This code uses a Monte Carlo technique to calculate the distribution function following test particles. The drift kinetic equation is described as follows;

$$\frac{\partial f}{\partial t} + (\mathbf{v}_{\parallel} + \mathbf{v}_D) \cdot \nabla f + \dot{\mathbf{v}} \cdot \nabla_V f = C(f) + L(f) + S_\alpha \tag{1}$$

where f is the distribution function of α particles, $\mathbf{v}_{\parallel}$ and $\mathbf{v}_D$ are the velocity parallel to magnetic line and the drift velocity respectively. L is the loss term form the last closed flux surface and S_α is the source term of the α particles generated by fusion reaction. The source term S_α is evaluated by using fusion reaction rate.

C is the Coulomb collision operator including the linear collision effects C^{linear} and the nonlinear collision effect $C^{nonlinear}$. C^{linear} includes the operator of the pitch angle scattering and the energy scattering with background ions and electrons. These operators have been evaluated by Boozer and Kuo-Petravic [5] and are described as follows;

$$\lambda_n = \lambda_{n-1}(1 - \nu_d \tau) \pm \left[\left(1 - \lambda_{n-1}^2\right)\nu_d \tau\right]^{1/2} \tag{2}$$

$$E_n = E_{n-1} - (2\nu\tau)\left[E_{n-1}\left(\frac{3}{2} + \frac{E_{n-1}}{\nu}\frac{dv}{dE_{n-1}}\right)\right] \pm 2\left\{E_T E_{n-1}(\nu\tau)\right\}^{1/2} \tag{3}$$

where $\lambda = v_{\parallel}/v$. v and $v_{\parallel}$ are the particle velocity and the velocity parallel to magnetic line. v_d is the deflection collision frequency. τ is length of a time step. n and $n-1$ are numbers of time step, and the symbol $\pm$ means the sign is to be chosen randomly. E_n, E_T are the energy at time step n and thermal energy respectively. The subscript k, l are the components of Einstein convention.

We can write the nonlinear collision operator $C^{nonlinear}$ with Rosenbluth potentials [6] as

$$C^{nonlinear} = \Lambda_c \left\{ f(\mathbf{v}) \frac{\partial^2 \phi(\mathbf{v})}{\partial v_k^2} + \frac{\partial \phi(\mathbf{v})}{\partial v_k} \frac{\partial f(\mathbf{v})}{\partial v_k} \right\} - \Lambda_c \left\{ \frac{\partial^3 \psi(\mathbf{v})}{\partial v_k^2 \partial v_l} \frac{\partial f(\mathbf{v})}{\partial v_l} + \frac{\partial^2 \psi(\mathbf{v})}{\partial v_k \partial v_l} \frac{\partial^2 f(\mathbf{v})}{\partial v_k \partial v_l} \right\}, \tag{4}$$

where $\Lambda_c = ln\Lambda (e_\alpha e_b / m_\alpha \varepsilon_0)^2$. Λ is the Coulomb logarithm. e_α and e_b are charges of test α-particles and of background ions and electrons, especially. m_α is the mass of test α-particles and ε_0 is permittivity of free space. ϕ and ψ are Rosenbluth potentials and written as

$$\phi(\mathbf{v}) = \frac{1}{2\pi} \frac{1}{v} \int\int \left(1 + \frac{\mathbf{v} \cdot \mathbf{v}'}{v^2} \right) f_b(\mathbf{v}') dv'_{\parallel} dv'_{\perp}, \tag{5}$$

$$\psi(\mathbf{v}) = \frac{1}{4\pi} v \int\int \left(1 - \frac{\mathbf{v} \cdot \mathbf{v}'}{v^2} \right) f_b(\mathbf{v}') dv'_{\parallel} dv'_{\perp}, \tag{6}$$

where the subscript b means background α particle. The superscript $'$ means background ions and electrons. In order to estimate of the velocity changes by nonlinear collision, we rewrite $C^{nonlinear}$ using $v_{\parallel}$ and $v_{\perp}$ as follows;

$$\begin{aligned} C^{nonlinear} &= \Lambda_a \left\{ f(\mathbf{v}) \left(\frac{\partial^2 \phi(\mathbf{v})}{\partial v_{\parallel}^2} + 2 \frac{\partial^2 \phi(\mathbf{v})}{\partial v_{\perp}^2} \right) + \left(\frac{\partial \phi(\mathbf{v})}{\partial v_{\parallel}} \frac{\partial f(\mathbf{v})}{\partial v_{\parallel}} + 2 \frac{\partial \phi(\mathbf{v})}{\partial v_{\perp}} \frac{\partial f(\mathbf{v})}{\partial v_{\perp}} \right) \right. \\ &\quad \left. - \left(\frac{\partial^2 \psi(\mathbf{v})}{\partial v_{\parallel} \partial v_{\perp}} \frac{\partial^2 f(\mathbf{v})}{\partial v_{\parallel} \partial v_{\perp}} + 2 \frac{\partial \psi(\mathbf{v})}{\partial v_{\perp}} \frac{\partial^2 f(\mathbf{v})}{\partial v_{\perp}^2 \partial} \right) \right\} \\ &= \Lambda_a \left\{ \frac{\partial^2 \phi(\mathbf{v})}{\partial v_{\parallel}^2} + \frac{\partial \phi(\mathbf{v})}{\partial v_{\parallel}} \frac{\partial}{\partial v_{\parallel}} - \frac{\partial^2 \psi(\mathbf{v})}{\partial v_{\parallel} \partial v_{\perp}} \frac{\partial^2}{\partial v_{\parallel} \partial v_{\perp}} \right\} f(\mathbf{v}) \\ &\quad + 2\Lambda_c \left\{ \frac{\partial^2 \phi(\mathbf{v})}{\partial v_{\perp}^2} + \frac{\partial \psi(\mathbf{v})}{\partial v_{\perp}} \frac{\partial}{\partial v_{\perp}} - \frac{\partial^2 \psi(\mathbf{v})}{\partial v_{\perp}^2} \frac{\partial^2}{\partial v_{\perp}^2} \right\} f(\mathbf{v}), \end{aligned} \tag{7}$$

where third order derivation is ignored. $v_{\parallel}$ and $v_{\perp}$ are the velocities parallel and perpendicular to magnetic filed lines. This nonlinear operator consists of the

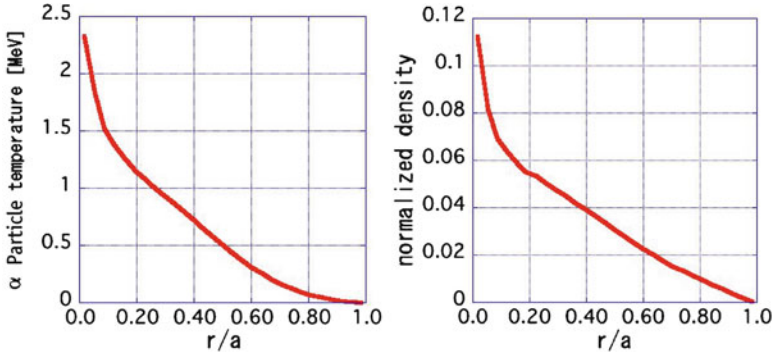

Fig. 1 The background α particle temperature and density profiles. The density profile is a distribution function

parallel and perpendicular components as $C^{nonlinear} = C_{\parallel}^{nonlinear} + C_{\perp}^{nonlinear}$. These operators are described as follows;

$$C_{\parallel}^{nonlinear} = \Lambda_c \left\{ \frac{\partial^2 \phi(\mathbf{v})}{\partial v_{\parallel}^2} + \frac{\partial \phi(\mathbf{v})}{\partial v_{\parallel}} \frac{\partial}{\partial v_{\parallel}} \right\} f(\mathbf{v}) \tag{8}$$

$$C_{\perp}^{nonlinear} = 2\Lambda \left\{ \frac{\partial^2 \phi(\mathbf{v})}{\partial v_{\perp}^2} + \frac{\partial \psi(\mathbf{v})}{\partial v_{\perp}} \frac{\partial}{\partial v_{\perp}} - \frac{\partial^2 \psi(\mathbf{v})}{\partial v_{\perp}^2} \frac{\partial^2}{\partial v_{\perp}^2} \right\} f(\mathbf{v}) \tag{9}$$

In this paper, we assumed that the background plasma consists of electrons, deuterium, tritium, and α particles. Electron temperature T_e and density n_e profiles are taken to be

$$T_e(\rho)[\mathrm{keV}] = 9.5(1 - \rho^2) + 0.5, \tag{10}$$

$$n_e(\rho)[10^{20}\mathrm{m}^{-3}] = 1.9(1 - \rho^8) + 0.1, \tag{11}$$

where ρ is normalized minor radius. The α particles temperature T_α and density n_α profiles are taken as Fig. 1. These profiles T_α and n_α are obtained by simulation assumed that the background plasma consists of electrons and deuterium. The deuterium and tritium temperatures T_D, T_T are the same as T_e. Their density n_D and n_T are assumed to be the change neutrality of plasma; $n_D = n_T \propto n_e$. In addition T_α are assumed the Maxwellian energy distribution for the α-particle in order to validate the nonlinear collision operator comparing with the linear operator as a first step.

3 Simulation Results

We run the GNET code with a varying the background plasma parameter until the test α particles are thermalized. We estimate α particle confinement with four cases of the background plasma conditions : Case 1: electrons and deuterium (1.0), Case 2: electrons, deuterium (0.5), and tritium (0.5), Case 3: electrons, deuterium (0.45), tritium (0.45), and α particles (using linear collision operator) (0.1), Case 4: deuterium (0.45), tritium (0.45), α particles (using nonlinear collision operator) (0.1), where the number of parentheses are the ratio of ion charge density.

Figure 2 shows the overall-average velocity-space distribution of α particles for each cases. $v_{\parallel}$ is the velocity parallel to magnetic field lines and $v_{\perp}$ is the velocity perpendicular to magnetic field lines. The volume of $v_{\parallel}$ and $v_{\perp}$ are normalized by the velocity with 1 MeV. Contours take logarithm of the velocity space distribution. Tritium and α particles are heavier than deuterium. The pitch angle scattering effect depends on the background plasma mass and this effect becomes stronger. The fraction of high-energy α-particles with the velocity $v_{\parallel}<0$ increases as the background plasma spices increase. The results of case 3 and 4 in Fig. 2 show very similar velocity-space distributions. This indicates the validity of our nonlinear collision operator.

Figure 3 shows the time evolution of the energy and particle loss fraction of α particle for each case. The change of loss fraction for each shows clear difference. The energy loss fraction increases from 5% to 6% and the particle loss fraction increases from 11.6% to 14.5%. We can see that the loss fraction depends on the background plasma mass density. Thus, we must take into account plasma component when the mass density of the background plasma varies largely.

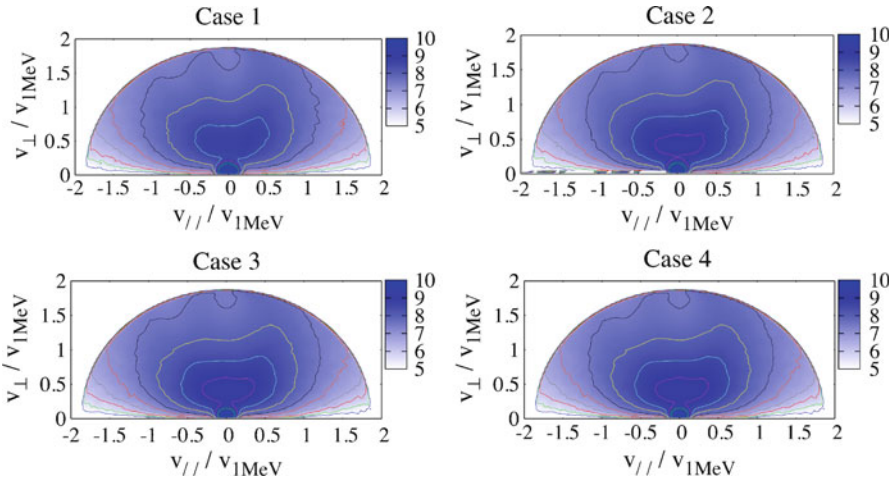

Fig. 2 Contours taking logarithm of the overall-average velocity-space distribution $\ln(f_{\alpha})$

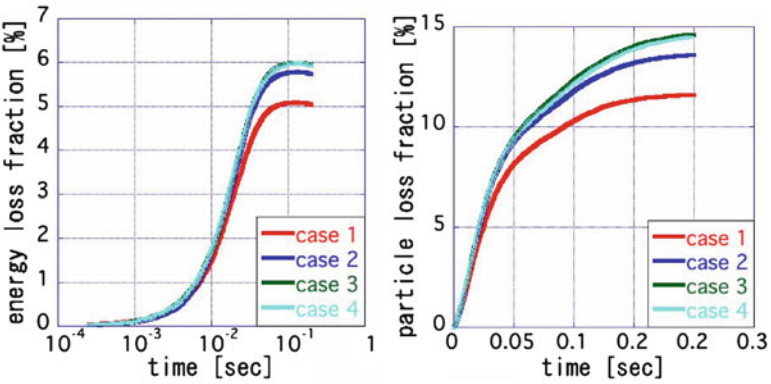

Fig. 3 The energy and particle loss fraction of α particle calculated until thermarization

The results of case 3 and 4 show that the energy loss fractions are 6% and 5.98% and the particle loss fraction are 14.6% and 14.5%, respectively. This also indicate the validity of our nonlinear collision operator.

4 Conclusion

We have investigated α particle confinement in a helical type fusion reactor with varying the background plasma parameter and the collision operator, keeping the charge neutrality. We found that increasing mass density of background plasma lead to degradation of the confinement efficiency of the α particle because of increasing the pitch angle effect. For each collision operator (the case 3 and case 4), the α particle confinement are almost same. This indicate the validity of our nonlinear collision operator.

Acknowledgments The authors were grateful for the support of the Ministry of Education, Culture, Sports, Science and Technology of Japan via "Energy Science in the Age of Global Warming" of Global Center of Excellence (G-COE) program (J-051).

References

1. Okano K, Umeda N, Kamada Y et al (2001) Non-linear increment of beam stopping cross-section by circulating fast ions. In: Proceedings of the 28th EPS conference control. Fusion Plasma Phys, pp 809–812
2. Iiyoshi A et al (1999) Overview of the large helical device project. Nucl Fusion 39:1245
3. Murakami S et al (2002) Neoclassical transport optimization of LHD. Nucl Fusion 42:L19
4. Murakami S et al (2006) A global simulation of ICRF heating in the LHD. Nucl Fusion 46:S425
5. Boozer A, Kuo-Petravic G et al (1981) Monte Carlo evaluation of transport coefficients. Phys Fluids 24(5):851
6. Rosenbluth N et al (1957) Fokker-Planck equation for an inverse-square force. Phys Rev 107:1

High-Temperature Ultrasonic Doppler Velocimetry for Lead-Lithium Flows

Yoshitaka Ueki, Tomoaki Kunugi, Masaru Hirabayashi, Keiichi Nagai, Junichi Saito, Kuniaki Ara, Neil B. Morley, and Takehiko Yokomine

Abstract Nuclear fusion reactors are a promising candidate of the future power source. Magnetic confinement fusion (MCF) blankets adopt high-temperature liquid metals (LM) such as the lead-lithium eutectic alloy (PbLi), as a coolant/tritium breeder. Developments of the LM-MCF blankets require comprehensive understanding of the high-temperature LM flows under the influence of the plasma-confining magnetic field. A high-temperature ultrasonic Doppler velocimetry (HT-UDV) has been developed as a flow diagnostic technique to acquire local velocity profiles of the opaque, high-temperature LM flow. This paper describes HT-UDV technique that has been successfully applied to measure velocity profiles of PbLi flows. The impact of tracer particles is investigated to determine requirements for HT-UDV measurement of PbLi flows. The HT-UDV system is tested on a PbLi flow driven by a rotating-disk in an inert atmosphere. We find that a sufficient amount of particles contained in the molten PbLi are required to successfully measure PbLi velocity profiles by HT-UDV. An X-ray diffraction analysis is performed to identify those particles in PbLi, and indicates that those particles were made of the lead mono-oxide (PbO). Since the specific densities of PbLi and PbO are close to each other, the PbO particles are expected to be well-dispersed in the bulk of molten PbLi. We conclude that the excellent dispersion of PbO particles enables the HT-UDV to obtain reliable velocity profiles for operation times of around 12 h.

Y. Ueki (✉) • T. Kunugi • T. Yokomine
Department of Nuclear Engineering, Kyoto University, Yoshida Honmachi, Sakyo, Kyoto 606-8501, Japan
e-mail: yoshi@nucleng.kyoto-u.ac.jp

M. Hirabayashi • K. Nagai • J. Saito • K. Ara
Advanced Nuclear System Research & Development Directorate, Japan Atomic Energy Agency, O-arai, Ibaraki, Japan

N.B. Morley
Mechanical and Aerospace Engineering, University of California, Los Angeles, CA, USA

T. Yao (ed.), *Zero-Carbon Energy Kyoto 2011*, Green Energy and Technology,
DOI 10.1007/978-4-431-54067-0_31,

Keywords High-temperature • Lead-lithium • Ultrasonic Doppler velocimetry

1 Introduction

The heat and mass transfer in a liquid metal flow under the influence of a plasma-confining magnetic field is significantly affected by magneto-hydrodynamic (MHD) effects arising from the interaction between the applied field and electrical currents induced inside the moving liquid metal (such as lead-lithium eutectic alloy: PbLi). However, the understanding of MHD flows in fusion-relevant conditions is limited since the MHD flow regimes are determined by multiple effects such as a strong magnetic field, buoyancy forces, interfacial phenomena related to the liquid metal wettability, and the complex flow passage geometry [1]. A technique to measure local velocity inside these opaque liquid metal flows is necessary to study such effects. Therefore, we have been developing high-temperature, ultrasonic Doppler velocimetry (HT-UDV) as a PbLi flow diagnostic.

UDV is based on pulsed ultrasonic echography together with the detection of the instantaneous Doppler shift frequency [2, 3]. The travelling time between the emission and reception of a pulsed ultrasound provides spatial information, and the Doppler shift frequency provides the velocity. UDV has the following advantages: (1) acquisition of spatial-temporal velocity information along the beam line of ultrasound, (2) a non-intrusive method, and (3) applicability to opaque fluids, such as liquid metals.

UDV requires the following prerequisites: (1) ultrasonic transmission at the interface of the UDV probe material and the target fluid, (2) acoustic properties of the target fluid, and (3) ultrasonic reflecting particles (in other words: tracer particles). If it comes to that UDV is applied to a flow field measurement of a high-temperature liquid metal, UDV requires high-temperature UDV probes or waveguide sensors [4, 5], in order to overcome its high-temperature operation. In this study, we employ high-temperature UDV probes since they are more compact than waveguide sensors, and therefore can fit in a narrow gap between electromagnets to measure PbLi flows in a magnetic field.

In the past, UDV has been applied to various liquid metals, such as mercury (Hg) [2, 3], gallium (Ga) [6, 7], and gallium-indium-tin eutectic ally (GaInSn) by using the normal transducer [8], and sodium (Na) [4], lead-bismuth (PbBi), and bronze (CuSn) by using the acoustic waveguide [5]. Nevertheless, UDV has not been applied to PbLi flows. As a prerequisite, the authors have measured PbLi acoustic properties, the results of which indicate that the acoustic coupling between PbLi and the wetting material of the HT-UDV titanium (Ti) tipped probe is good enough for the HT-UDV measurement [9].

The UDV technique requires the presence of ultrasound reflecting particles inside a target fluid. Artificial or natural particles, gas bubbles, or fluctuations in density can work for this purpose [10]. The UDV signal quality depends on parameters such as the concentration and size of the particles, as well as the

ultrasonic reflection characteristics of the particles. Usually the liquid metals contain some natural impurities such as oxide particles etc. It is favorable to utilize these natural impurities suspended in the liquid metals to work as tracer particles instead of seeding any artificial tracer particles in the liquid metals. Since mercury contains a higher concentration of natural oxides, introducing small bubbles are necessary to reflect emitted ultrasound [3]. According to the past references [6, 7], it is important, but not easy, to choose suitable tracer particles for each liquid metal.

A goal of this study is to determine suitable tracer particles for the HT-UDV measurement of PbLi flows. We applied the HT-UDV to a PbLi flow driven by a rotating-disk in an inert atmosphere glovebox in order to determine if the natural particles contained in PbLi work as tracer particles.

2 Velocity Profile Measurement of PbLi Flows

2.1 Experiment Setup

The HT-UDV measurement was performed in an argon-filled glovebox, where the oxygen and the moisture were controlled to stay under 1 ppm in concentration. PbLi ingots (from Atlantic Metals & Alloys, Inc.) were melted in a melt pot inside the glovebox. After removing PbLi oxides, the molten PbLi was transferred to a test cylinder, shown in Fig. 1. The test cylinder and the disk were made of an austenitic stainless steel. The test cylinder was 90 mm in diameter, and 120 mm in height, and heated by an electric heater underneath it. The PbLi temperature was controlled to stay at around 320°C, in order to mitigate the PbLi corrosion effect. The physical properties of the molten PbLi at 320°C are shown in Table 1. The PbLi flow was driven by the rotating disk which was spinning in the vicinity of the cylinder bottom. The disk-rotating frequency was about 500 rpm, either in clockwise and counter-clockwise directions.

In this study, we employed a HT-UDV probe (JAEA-type transducer). The HT-UDV probe was loosely inserted into the probe port of the test cylinder. The HT-UDV probe was connected to a UDV system (UVP Monitor model X-1, by Met-Flow SA). A set of the UDV measurement parameters is shown in Table 2.

2.2 Measurement Results

Mean velocity profiles were determined by averaging 1,024 single profiles, and shown in Fig. 2. The horizontal axis shows the distance from the cylinder surface, and the vertical axis shows the mean velocity profiles. In this study, we found that the measured velocity profiles were continuous. When the molten PbLi does not contain any suitable type or sufficient amount of tracer particles, we cannot acquire

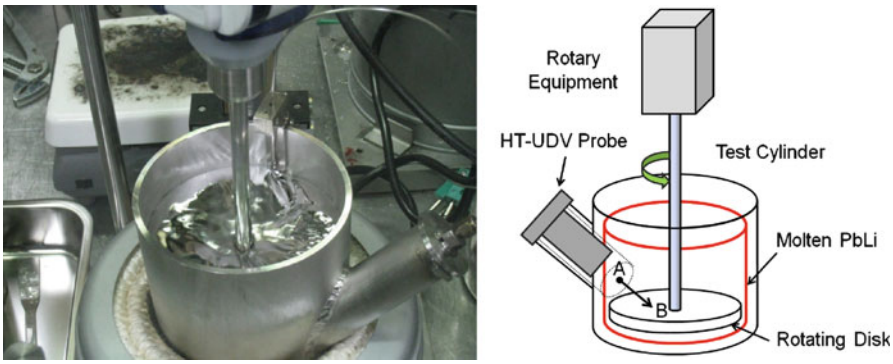

Fig. 1 Photograph and schematic view of the HT-UDV measurement of the PbLi flows

Table 1 Physical properties of molten PbLi at 320°C [9, 11]

Melting point	235°C
Density	9.45×10^3 kg/m^3
Kinetic viscosity	2.10×10^{-7} m^2/s
Sound velocity	1.78×10^3 m/s

Table 2 Set of system parameters adjusted in this experiment

Ultrasonic frequency	4 MHz
Ultrasonic emission voltage	160 V
Number of emitted cycles: n	4
Doppler angle	45°
Plus repetition rate	7,812 Hz
Maximum depth	114 mm
Spatial resolution in the longitudinal direction	1.78 mm
Temporal resolution (single profile)	37.2 ms
Number of profiles for averaging	1,024

any velocity profiles due to the insufficient signal reception of the probe. Based on this, we infer that the HT-UDV technique was successfully applied to the molten PbLi flows, and that the amount of the tracer particles, which were naturally contained in the molten PbLi, was sufficient for the HT-UDV measurement.

3 Chemical Analyses of PbLi

The PbLi eutectic alloy was fabricated by the Atlantic Metals & Alloys, Inc. in the USA. The chemical composition of the PbLi alloy was examined by an inductively coupled plasma–mass spectrometry (ICP-MS). The chemical composition was 84.2 at %Pb and 15.8 at %Li, and at almost the Pb-Li eutectic point (84.3 at %Pb and 15.7 at %Li, revised by Okamoto [12]). The percentage of

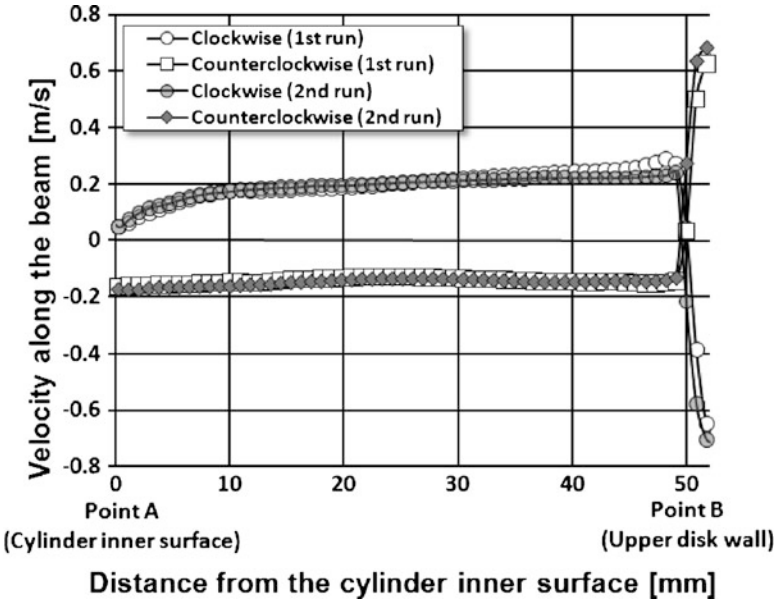

Fig. 2 Average velocity profile along the ultrasonic beam

impurities, such as Cu, Zn, Fe, Ag, Bi and Si in the alloy, was less than the detection limit of an inductively coupled plasma–Auger electron spectrometry (ICP-AES).

3.1 Tracer Particles for PbLi Flows

An X-ray diffraction (XRD) analyses shows that the bulk of the solidified PbLi contains some amount of a lead monoxide (PbO), despite the presence of many Li atoms in the molten PbLi. The specific density of PbO at room temperature is around 9.53, and is close to the 9.45 of PbLi (at 320°C). Because of this, we infer that PbO exists uniformly in the bulk, and small quantities of PbO exist on the liquid surface due to the difference in the specific density. Since the melting point of PbO is around 886°C, the PbO particles are expected to be still in solid state at around 320°C, and dispersed in the molten PbLi. Based on our results, we conclude that the PbO particles, which are naturally contained in molten PbLi, are dispersed in the molten PbLi to work as HT-UDV tracer particles.

A recent study [13] on the tritium release from thermal-neutron irradiated PbLi showed that tritium was mainly released as molecule (HT) form, and about 10% of tritium was released as water (HTO). The formation of HTO would be induced by the reaction of residual oxygen impurity, which also indicates not a small amount of oxygen exist in the PbLi.

4 Conclusion

This study has demonstrated that the HT-UDV has been successfully applied to measure the velocity profiles of molten PbLi flows. We have showed that the PbO particles, which are naturally contained in the molten PbLi, have capability to work as the HT-UDV tracer particles in the time range of approximately 12 h.

However under the influence of a strong magnetic field, the induced electric currents can close through the probe and the attached conducting port structure. This additional circuit may cause significant disturbances of the MHD flow field around the probe, which should be clarified in the future.

Acknowledgments The authors were grateful for the support of the Ministry of Education, Culture, Sports, Science and Technology of Japan via "Energy Science in the Age of Global Warming" of Global Center of Excellence (G-COE) program (J-051). The authors are grateful for the great financial support of the Japan MEXT and the US DOE via the Japan-US Joint Research Project, Tritium, Irradiation and Thermofluid for America and Nippon (TITAN).

References

1. Smolentsev S, Moreau R, Buhler L, Mistrangelo C (2010) MHD thermofluid issue of liquid metal blankets: Phenomena and advances. Fusion Eng Des 85:1196–1205
2. Takeda Y (1991) Development of an ultrasound velocity profile monitor. Nucl Eng Des 126:277–284
3. Takeda Y, Kikura H (2002) Flow mapping of the mercury flow. Exp Fluid 32:161–169
4. Eckert S, Gerbeth G (2002) Velocity measurements in liquid sodium by means of ultrasonic Doppler velocimetry. Exp Fluid 32:542–546
5. Eckert S, Gerbeth G, Melnikov V-I (2003) Velocity measurements at high temperatures by ultrasound Doppler velocimetry using an acoustic wave guide. Exp Fluid 35:381–388
6. Brito D, Nataf H-C, Cardin P, Aubert J, Masson J-P (2001) Ultrasonic Doppler velocimetry in liquid gallium. Exp Fluid 35:653–663
7. Tasaka Y, Takeda Y, Yanagisawa T (2008) Ultrasonic visualization of thermal convective motion in a liquid gallium layer. Flow Meas Instrum 15:145–153
8. Cramer A, Zhang C, Eckert S (2004) "Local flow structures in liquid metals measured by ultrasonic Doppler velocimetry". Flow Meas Instrum 15:145–153
9. Ueki Y, Hirabayashi M, Kunugi T, Yokomine T, Ara K (2009) Acoustic properties of Pb-17Li alloy for ultrasonic Doppler velocimetry. Fusion Sci Tech 56:846–850
10. Eckert S, Cramer A, Gerbeth G (2007) Velocity measurement techniques for liquid metal flows. In: Molokov S et al (eds) Magnetohydrodynamics—historical evolution and trends. Springer, Heidelberg, pp 275–294
11. Mas De Les Valls E, Sadano LA, Batet L, Ricapito I, Aiello A, Gastaldi O, Gabriel F (2008) Lead-lithium eutectic material database for nuclear fusion technology. J Nucl Mater 376:353–357
12. Okamoto H (1993) Li-Pb (lithium-lead). J Phase Equil 14:770
13. Kobayashi M, Hamada A, Matsuoka K, Suzuki M, Osuo J, Edao Y, Fukada S, Yamanishi T, Oya Y, Okuno K (2011) Kinetics of tritium release from thermal neutron-irradiated $Li_{0.17}Pb_{0.83}$. ICFRM-15. Charleston, South Carolina, USA

Numerical Investigation of Subcooled Pool Boiling Bubble Behavior

Yasuo Ose and Tomoaki Kunugi

Abstract In this paper, three dimensional numerical simulations based on the MARS (Multi-interface Advection and Reconstruction Solver) with the developed bubble growth/condensation model consisted of the improved phase-change model and the introduction of the relaxation time based on a quasi-thermal equilibrium state have been conducted for a subcooled pool boiling phenomenon especially regarding to a bubble departing behavior from the heated surface. The results of the numerical simulations were compared with the visualization experimental data, and then the effect of the degree of subcooling on the bubble departing behavior including their shape changes from the heated surface were numerically investigated. As the results, the numerical results of bubble departing behavior from the heated surface showed in good agreement with the experimental observations quantitatively.

Keywords Boiling bubble growth/condensation model • Bubble aspect ratio • Bubble behavior • Numerical simulation • Subcooled pool boiling

1 Introduction

Boiling phenomena is a key to remove the heat from the fuel rods in nuclear reactors such as BWR (Boiling Water Reactor), because the boiling heat transfer has enormous heat transfer coefficient compared to the convection of single-phase flows. It will also play a significant role of the thermal management in nuclear reactors. Therefore, in order to clarify the mechanism of boiling phenomena, it has been studied extensively over the decades.

Y. Ose (✉) • T. Kunugi
Department of Nuclear Engineering, Kyoto University, Yoshida, Sakyo, Kyoto 606-8501, Japan
e-mail: ose@nucleng.kyoto-u.ac.jp

T. Yao (ed.), *Zero-Carbon Energy Kyoto 2011*, Green Energy and Technology,
DOI 10.1007/978-4-431-54067-0_32,

This study focuses on the subcooled pool boiling. Since the subcooled boiling is occurred under a condition below the saturation temperature, it is the most complex phenomenon compared to the saturated boiling, because it includes not only the convective heat transfer but also the rapid evaporation and condensation processes. Although the subcooled boiling is very important phenomenon mentioned above, the essential mechanism has not yet been experimentally clarified until today, because the bubble nucleation and growth processes are too fast to observe even by using the current high speed camera. On the other hand, the numerical simulation is more promising as an alternative approach to understand these processes.

In this study, in order to clarify the heat transfer characteristics of the subcooled pool boiling and to discuss on its mechanism, a boiling bubble growth/condensation model for the numerical simulation on the subcooled pool boiling phenomena has been developed [1]. In this paper, unsteady three dimensional numerical simulations based on the MARS (Multi-interface Advection and Reconstruction Solver) [2] with the developed bubble growth/condensation model were performed for the bubble departing process from the heated surface. The results of the numerical simulations were compared with the experimental observations, and then the effect of the degree of subcooling on the bubble departing behavior including their shape changes from the heated surface were investigated.

2 Numerical Simulation

2.1 Computational Domain

In order to simulate the bubble departing behaviors observed by a visualization experiments in the subcooled pool boiling, three dimensional numerical simulations based on the MARS with the developed boiling bubble growth/condensation model were conducted for the bubble departing behaviors from the heated surface in the subcooled pool boiling. Here, the detail of this model is described in the reference [1]. The visualization of the subcooled nucleate pool-boiling experiment under atmospheric pressure was conducted by using the ultra-high-speed video camera mounted on a long-focus microscope system [3]. Figure 1 shows the computational domain in this numerical simulation. The computational domain size was 2.7 mm × 2.0 mm × 2.7 mm. The grid size was 20−100 μm in x- and z-directions, respectively, and was 20 μm in y-direction. The number of computational grids was 103 × 83 × 103, and time increment in the computation was set to 1 μs. The periodic boundary conditions were imposed at the x- and z-directions respectively. The non-slip wall velocity boundary conditions were applied to all walls, and the upper boundary condition in y-direction was set to a constant hydraulic pressure condition. The computational conditions were basically the same as the experiments. The initial pressure was set to an atmospheric pressure and the degrees of subcooling in the water pool

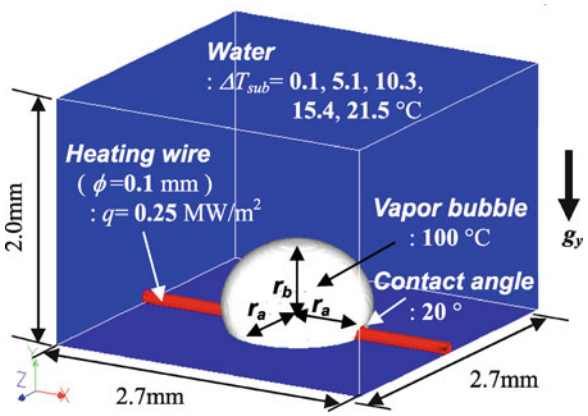

Fig. 1 Computational domain

Table 1 Table of initial bubble radius

ΔT_{sub} (°C)	r_a (mm)	r_b (mm)	ΔT_{sub} (°C)	r_a (mm)	r_b (mm)
0.1	0.70	0.51	15.4	0.49	0.38
5.1	0.62	0.47	21.5	0.44	0.35
10.3	0.56	0.48			

were set to 0.1°C, 5.1°C, 10.3°C, 15.4°C and 21.5°C as the same as the experimental conditions. The heating platinum wire of 0.1 mm in diameter used in the experiment was located at the bottom of computational domain, and the volumetric heat source at the center of the wire was set to 0.2 W which was corresponding to the heat flux on the heated surface in the experiment: 0.25 MW/m^2. The initial temperature of heating wire was set to 110°C which was estimated by using a waiting time obtained from both the experimental results and the analytical solution of unsteady heat conduction. In order to evaluate the heart transfer characteristics of the heated surface, the solid heat conduction from the center of the heating wire to its surface was numerically considered. In order to consider the wettability on the heated wire surface, the contact angle between the wire surface and the liquid was set to 20°.

Since it is focused on the bubble departing behavior from the heated wire surface in this study, the initial bubble shape was assumed at the maximum bubble size in a horizontal direction obtained from the experimental data. The initial bubble diameter was thus set to as shown in Table 1, and an initial bubble was put as a hemispherical shape at the center of the heated surface as shown in Fig. 1. The initial bubble temperature was also set to the saturated temperature corresponding to an atmospheric pressure. Although the velocity and temperature fields around the growing bubble was existed in the experiments, these initial fields in this numerical simulation was assumed to be both stationary and homogenous temperature fields with the degree of subcooling, because the experimental data corresponding to these fields could not be obtained.

3 Results and Discussions

Figures 2a, b show the time variation of bubble departing behavior observed in the experiments (upper) and the numerical simulation (lower) at $\Delta T_{sub} = 10.3°C$ and 21.5°C, respectively. The results of numerical simulation show the bubble shapes as an iso-surface corresponding to the volume of fluid fraction of 0.5, the temperature contours and the velocity vectors. At $\Delta T_{sub} = 10.3°C$ (Fig. 2a), the numerical results retrieve the experimental one that the bubble becomes from the flattened shape in the superheated layer to the vertically-elongated one in the saturated or subcooled liquid layer before the bubble departure from the heated wire surface. At $\Delta T_{sub} = 21.5°C$ (Fig. 2b), the bubble shape becomes more vertically-elongated with increase of the degree of subcooling. From the results of numerical simulation at $\Delta T_{sub} = 21.5°C$, it is found that a large upward velocity like a jet from the bottom of bubble to the top appears when the bubble becomes the vertically-elongated shape. Figure 3 shows the comparison of bubble shapes just before the bubble departure from the heated wire surface, and also shows the comparison between experimental and numerical results at various degrees of subcooling. As a result, the bubble shapes predicted by the numerical simulations are reasonably in good agreement with those shapes obtained by the experiments.

In order to validate the time variation of bubble shape changes obtained from the numerical results, Fig. 4 shows a quantitative comparison of the time variation of the bubble aspect ratio between the experimental data and the numerical simulation results at various degrees of subcooling. The open symbols depict the data corresponding to from a beginning of the bubble growth to just before the bubble departure. The solid symbols depict the data corresponding to after the bubble departure in the subcooled pool boiling. The solid line denotes the numerical results corresponding to from the beginning of the bubble growth to just before the bubble departure. As the result, the trends of the time variations of the bubble aspect ratio obtained from the numerical results are shown to be similar to the experimental data: with increase of the degree of subcooling, (1) the bubble becomes more vertically-elongated shape, (2) the time interval from the bubble nucleation to its departure from the heated surface is decreasing.

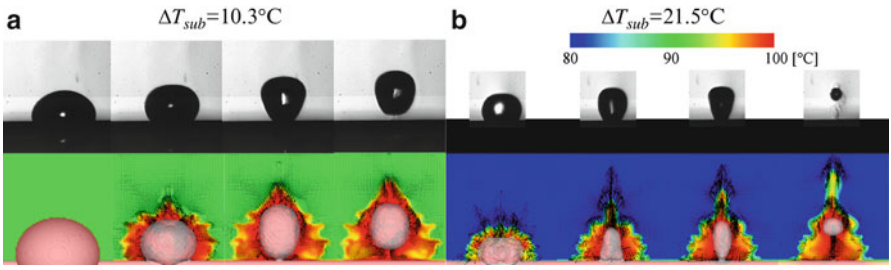

Fig. 2 The comparison of time variation of bubble departing behavior between experimental and numerical results at (**a**) ΔT_{sub}=10.3°C, (**b**) ΔT_{sub}=21.5°C (*Upper*: Experimental Results, *Lower*: Numerical Results)

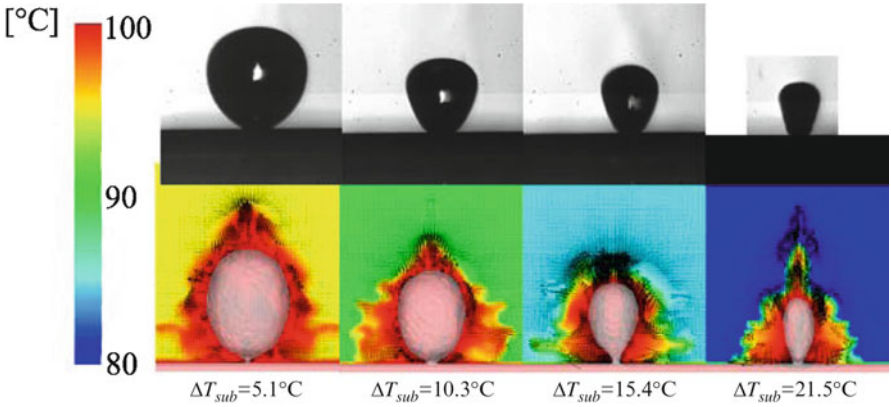

Fig. 3 The comparison of bubble shapes just before bubble departing from heated surface between experimental and numerical results at various degrees of subcooling (*Upper*: Experimental Results, *Lower*: Numerical Results)

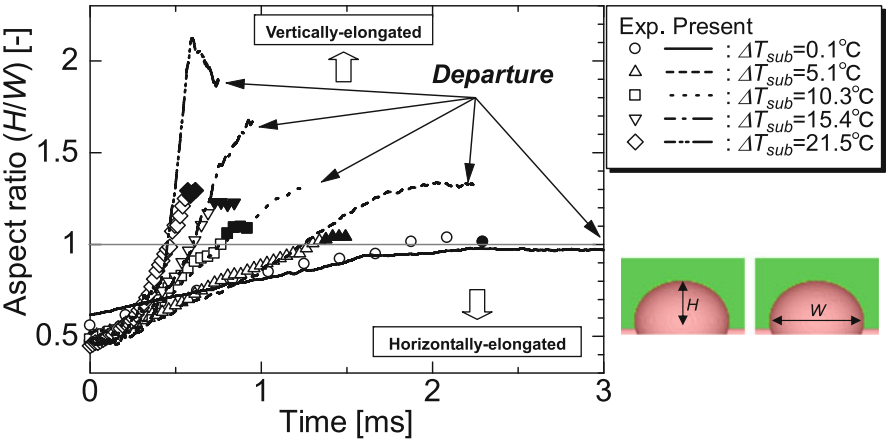

Fig. 4 The comparison of time variation of bubble aspect ratio between experimental data and numerical results

However, it can be seen that the numerical results are over predicted the time interval which from the bubble nucleation to its departure from the heated surface compared with the experimental data. This reason might be considered that the initial condition of numerical simulations could not be completely consistent with the experimental conditions such as the property of heated wire surface and the temperature and velocity fields around the growing bubble. Consequently, while the initial conditions both velocity and temperature fields are very important factor in order to achieve high accuracy prediction, it would

say that the present numerical simulation based on the MARS with the developed boiling bubble growth/condensation model can predict the bubble departure from the heated surface in subcooled pool boiling behaviors as experimentally observed.

4 Conclusions

The numerical simulations based on the MARS with the developed boiling bubble growth/condensation model considering the relaxation time based on the quasi-thermal equilibrium hypothesis were conducted for the bubble departing behavior from the heated wire surface in subcooled pool boiling. The results of numerical simulations were compared with the experimental results, especially for the bubble shapes. As the results, the numerical results for the bubble departing behavior showed in good agreement with the experimental results as follows:

1. The time interval from the bubble nucleation to its departing from the heated surface decreases with increase of the degree of subcooling.
2. The aspect ratio of the bubble shape increases with increase of the degree of subcooling, i.e., the bubble shape becomes more vertically-elongated before the bubble departure from the heated surface.

As mentioned above, it is concluded that the present boiling bubble growth/condensation model can retrieve the bubble departing behavior from the heated surface in subcooled pool boiling.

Acknowledgement This work was partly supported by a "Energy Science in the Age of Global Warming" of Global Center of Excellence (G-COE) program (J-051) of the Ministry of Education, Culture, Sports, Science and Technology of Japan.

References

1. Ose Y, Kunugi T (2010) Numerical simulation of subcooled boiling Springer. In: Yao T (ed) Zero-carbon energy Kyoto 2009. Heidelberg, pp. 354–359
2. Kunugi T (2001) MARS for multiphase calculation. Comput Fluid Dynam J 9:563–571
3. Ose Y, Kawara Z, Kunugi T (2009) Numerical simulation of subcooled boiling compared with experimental data and analytical equations. In: Proceedings of the 13th international topical meeting on nuclear reactor thermal hydraulics: N13P1202 (CD-ROM)

Gas–Liquid Two-Phase Turbulent Flow in Square Duct

Haomin Sun and Tomoaki Kunugi

Abstract As for the turbulent two-phase flow in the non-circular duct, the flow could show an anisotropic turbulence feature in liquid phase because of the existence of a transverse circulatory flow named a second-kind of secondary flow. In this study, a bubbly upward turbulent flow in a large square duct has been conducted. As the preliminary measurement, an axial mean velocity of liquid single-phase flow was measured by a Pitot tube at a cross-sectional average velocity of 0.4 m/s. Its isotach was distorted towards the corner of the duct. In addition, the local void fraction distribution was measured by the optical probe system. The result showed a tendency to have a peak at the corner of the duct.

Keywords Anisotropic turbulence • Bubbly flow • Optical probe • Secondary flow • Void fraction

1 Introduction

Gas–liquid two-phase turbulent flow appears in many industrial energy plants and systems, such as light water nuclear reactor, boiler, condenser, mixing devices and so on. Therefore, many researches have been carried out the experimental studies on the turbulent flow characteristics in the circular pipe flow. The detailed measurements of gas–liquid two-phase flow in the circular pipe were conducted by Serizawa et al. [1], indicating that the void fraction distribution changes from a wall peak to a center peak as the gas flow rate increasing at a constant liquid flow rate. Serizawa et al. [2] also measured local liquid velocity and turbulence intensity distribution in the bubbly upward flow. In those cases, an isotropic turbulence for

H. Sun (✉) • T. Kunugi
Department of Nuclear Engineering, Kyoto University, Yoshida-Honmachi, Sakyoku, Kyoto 606-8501, Japan
e-mail: decrease-co2@nucleng.kyoto-u.ac.jp; kunugi@nucleng.kyoto-u.ac.jp

T. Yao (ed.), *Zero-Carbon Energy Kyoto 2011*, Green Energy and Technology,
DOI 10.1007/978-4-431-54067-0_33,

liquid phase has been expected because of the circular pipe. On the other hand, it is well-known that the turbulence single-phase flow in a non-circular duct shows an anisotropic turbulence feature such as a second kind of secondary flow: This secondary flow is caused by the anisotropic distribution of turbulence shear stresses in the cross-section of the duct.

The secondary flow in single-phase flow has been measured in detail firstly by Hoagland [3] using a hot-wire anemometer. Although the secondary flow velocity is on the order of 1% of the maximum axial flow velocity, it affects the axial flow strongly, even distorting its isotach distribution. In order to study the mechanism of the secondary flow in the non-circular ducts, Brundrett and Baines [4] investigated the production of axial vorticity and found it was associated with the region near the bisector and the relative proximity of the fluid element to the walls of the duct. Hereafter Gessner and Jones [5] enriched the knowledge of the secondary flow in the non-circular ducts by examining the Reynolds number effect, local wall shear stress and Reynolds equation along the secondary flow streamline.

Even though many studies regarding the single-phase turbulent flow in the non-circular duct have been carried out, few works were focused on the two-phase turbulent flow in the non-circular duct. In order to grasp the anisotropic turbulence effect on the air–liquid two-phase flow, a bubbly upward turbulent flow in the square duct was constructed. In this paper, the preliminary measurement was reported.

2 Experimental Apparatus

A schematic diagram of the experimental loop is shown in Fig. 1. The cross-section and the length of the square duct are 136 mm $\times$ 136 mm and about 2.8 m respectively. Filtered tap-water was stored to the tank and introduced from the bottom of the square duct from four inlets located at each sidewall to the square duct by the pump (Grundfos Co. CRN90-1) for guaranteeing a symmetric flow supply of liquid. In the bubbly flow, air was supplied by the air compressor (Hokuetsu Industries Co. SAS37SD) and injected from the location lower than the water inlets. In order to inject bubbles homogeneously, bubbles were produced by 7 $\times$ 7 sintered-metal rod bundle located at the bottom region of square duct. After the bubbly flow flowed through the square duct, air was separated from the bubbly flow in the gas–water separator located at the top of the square duct.

Four pressure taps were set in the distance of 0.03, 0.93, 1.48 and 2.16 m from the top of the sintered-metal rod to measure the differential pressure between two pressure taps by a differential pressure transmitter (Yokogawa Co. EJA110). In addition, as for the transverse measurement the probe support was set to the x–y stage which was fixed on the gas–water separator. The Pitot tube and the optical probe were fixed to the probe support and could move in a whole quarter area of the testing cross-section in the distance of 2.32 m from the top of the sintered-metal rod.

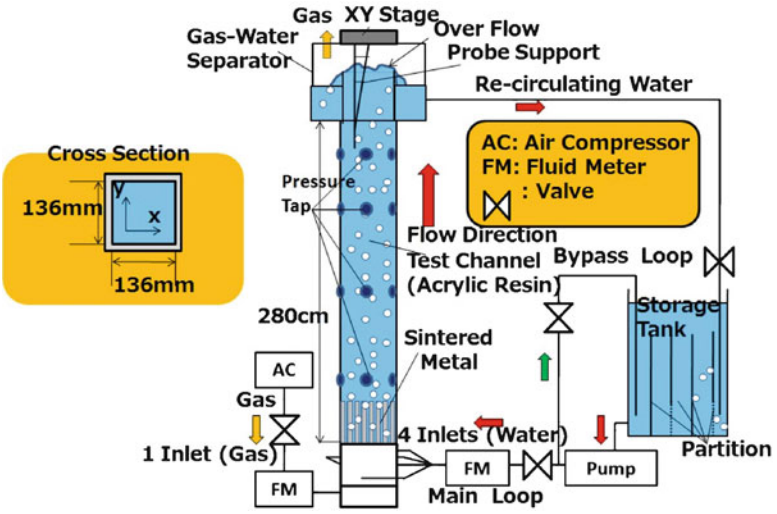

Fig. 1 Schematic diagram of experimental loop

3 Local Axial Mean Velocity Distribution Measurement

3.1 Experiment

For liquid single-phase upward flow, the axial mean velocity distribution in the testing cross-section was measured by the Pitot tube at the cross-sectional average velocity of 0.4 m/s. The differential pressure of the Pitot tube was measured by using a manometer with the working fluid of kerosene, which can measure a low pressure difference due to its density similar to that of water. The velocity measurement was conducted in one-eighth of the testing cross-section because of the symmetry of flow. The measuring points were the intersection points of the lines aligned in parallel with and in the distance of 3, 5, 8, 12, 17, 23, 30, 38, 47, 57, 68 mm from each wall respectively, as shown in Fig. 2.

3.2 Result and Discussion

The distribution of average axial velocity was shown in Fig. 3. The highest velocity and the lowest one were in the center and the corner of the square duct respectively. Similar to the result of Brundrett and Baines [4] and Gessner and Jones [5] for the single-phase gas flow in non-circular duct, the isotach distribution of the axial mean velocity was distorted. It might be attributed to the liquid transport by the secondary flow toward the corner.

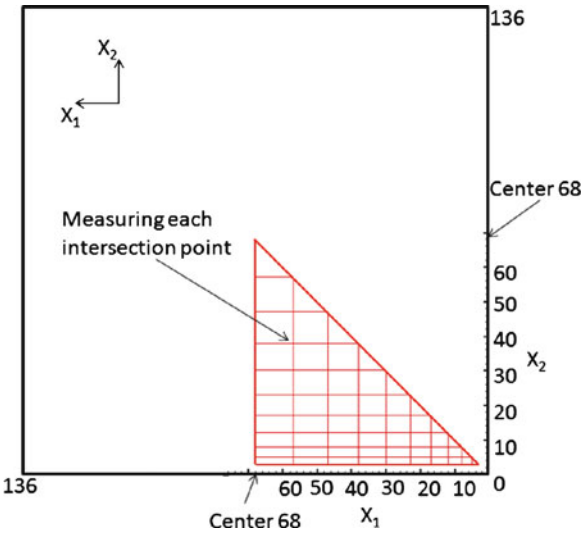

Fig. 2 Measuring points

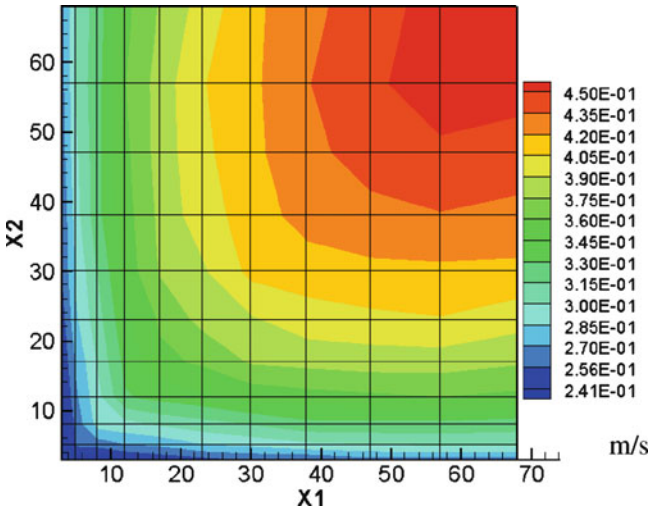

Fig. 3 Axial mean velocity distribution

4 Local Void Fraction Distribution Measurement

4.1 Experiment

For bubbly upward flow in the square duct, the local void fraction distribution α in the testing cross-section was measured by using the optical probe (RBI Co.) at the combination of air volumetric flux; $J_g = 0.018$, 0.036, 0.072 m/s and water

volumetric flux; $J_l = 0.2, 0.4, 0.8$ m/s. The measuring points were the same to those of the axial mean velocity measurement. The bubble diameter was around 3 mm. Through detecting the light reflection from the tip of the optical probe, the phase of surrounding fluid could be determined. High reflection indicates the air phase and low for the water phase. The light signal was converted to the digital signal by an A/D converter (YOKOGAWA Co., WE7275). Three times measurements at every point were carried out with the sampling rate of 10 kHz and the sampling time of 100 s. The output indicating the air phase was set to between 5.5 and 6.5 V and the water phase between −0.5 and 0.5 V respectively. When the signal was surpassed to 1.5 V in the rising bubble edge, the probe was thought to pass through the top surface of the bubble. On the other hand, when the signal falls down to 4.5 V in the falling bubble edge, the probe was thought to pass the bottom surface of the bubble. The local void fraction was determined by a time ratio between the air phase and the total phase.

4.2 Result and Discussion

The distributions of local void fraction for each condition were shown in Fig. 4.

Through comparing the cross-sectional void fractions obtained from the optical probe with the volumetric void fraction from the measurement of differential pressure near the testing cross-section, measuring error for almost all flow conditions was determined to be within ±10%. Because the inhomogeneity of bubble distribution at the inlet was found, especially for the case of low water volumetric flux, it is only discussed on the conditions of $J_l = 0.4$ and 0.8 m/s. For these flow conditions, the void fraction was becoming larger as approaching to the wall and had a peak at the corner region. The distribution of the void fraction in the first measuring line near the wall was shown in Fig. 5. It shows that the void fraction tends to be larger at the corner region and the center of the wall.

Two reasons to explain these results are proposed as follows: (1) Saffman force [6] due to the liquid velocity gradient near the wall push bubbles to the wall. (2) The secondary flow transport bubbles to the wall, especially to the corner region and the center of the wall.

5 Conclusion Remarks

The following conclusions were drawn:

1. For single-phase water flow in the square duct, the isotach distribution of the axial mean velocity was distorted near the corner region due to the secondary flow.

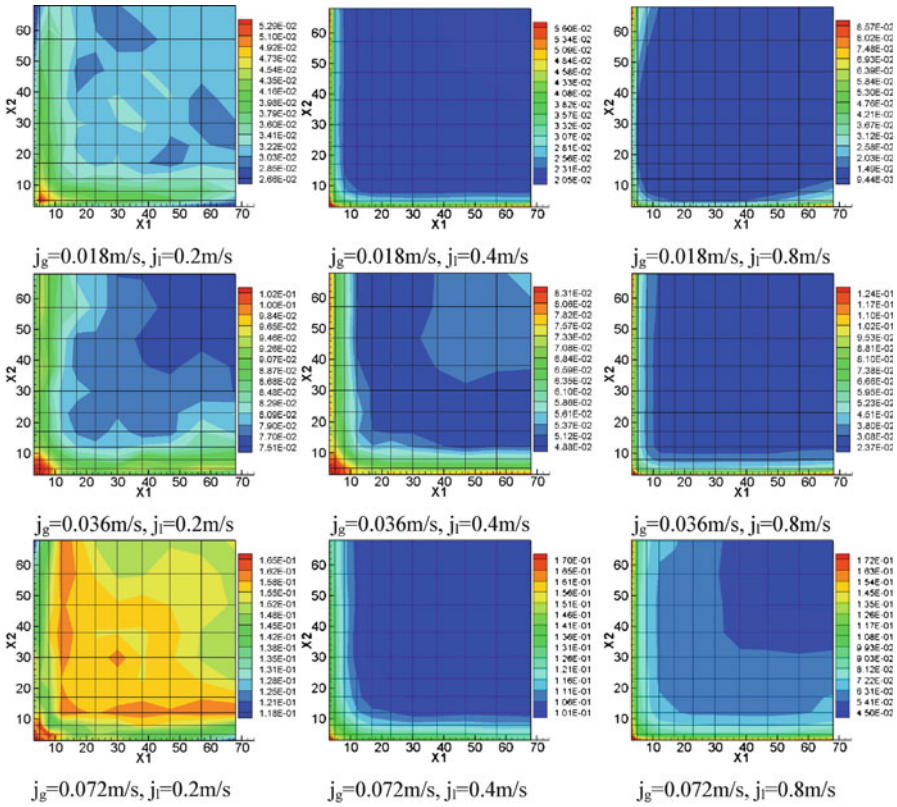

Fig. 4 The distribution of local void fraction at each flow condition

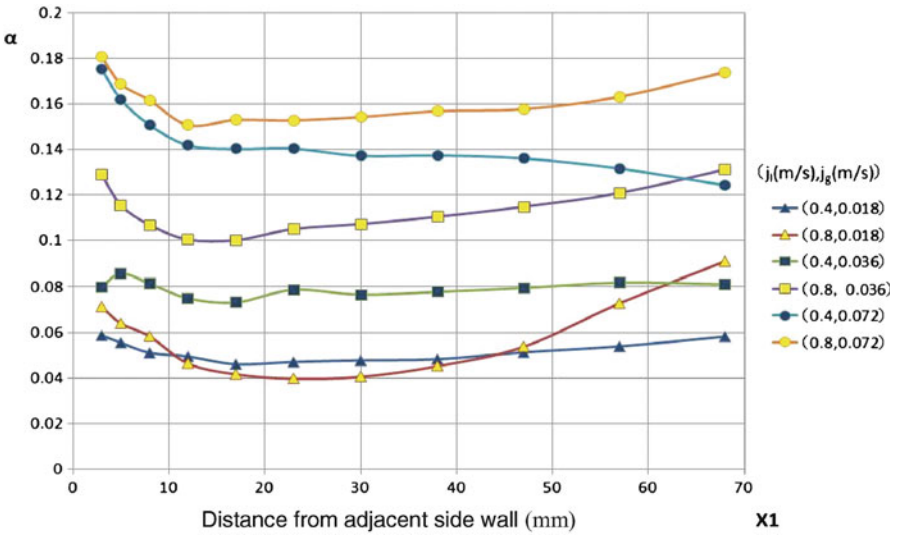

Fig. 5 The distribution of local void fraction in the first line near the wall

2. For bubbly flow in the square duct, the void fraction showed large value near the walls compared to the center region and had a peak at corner region. Either the Saffman force or the secondary flow could transport bubbles to those areas.

In the future work, the detail measurement about the void fraction, the bubble velocity for gas phase, the average velocities and the Reynolds stresses for liquid phase will be done after making assure the symmetry of both air and water phases.

Acknowledgement This work was partly supported by "Energy Science in the Age of Global Warming" of Global Center of Excellence (G-COE) program (J-051) of the Ministry of Education, Culture, Sports, Science and Technology of Japan.

References

1. Serizawa A, Kataoka I, Michiyoshi I (1975) Turbulence structure of air–water bubbly flow—2. Local properties. Int J Multiphas Flow 2:235–246
2. Serizawa A, Kataoka I (1990) Turbulence suppression in bubbly two-phase flow. Nucl Eng Des 122:1–16
3. Hoagland LL (1960) Fully developed turbulent flow in straight rectangular ducts—secondary flow, its cause and effect on the primary flow. Ph.D. thesis, Department of Mechanical Engineering, Massachusetts Institute of Technology
4. Brundrett E, Baines WD (1964) The production and diffusion of vorticity in duct flow. J Fluid Mech 19:375
5. Gessner FB, Jones JB (1965) On some aspects of fully-developed turbulent flow in rectangular channels. J Fluid Mech 23(4):689–713
6. Saffman PG (1965) The lift on a small sphere in a slow shear flow. J Fluid Mech 22:385–400

Development of Microbubble Generation Method

Li-Fang Jiao, Tomoaki Kunugi, Feng-Chen Li, and Zensaku Kawara

Abstract In microbubble drag-reducing technology, the energy consumption in microbubble generation is often too large to achieve a high efficient energy conversion. The purpose of this research is to improve the efficiency of the microbubble generation method in practical applications. In this paper, microbubbles are generated by a special designed nozzle, whose principle is a converging flow. In water, it is possible to generate bubbles, whose diameter ranges from 1.5 to 4 mm, by using this nozzle. If a very little amount of Cetyltrimethylammonium Chloride (CTAC) surfactant is added to the water at T = 20°C, the average diameter of bubbles of 46.7–48.6 μm can be generated because of the reduction of the surface tension of the bubbles. It was found that the amount of air injected showed weak influence on the generated bubble size. It was also found that the counter-ion sodium salicylate (NaSal) could assist to enlarge the bubble and reduced the bubble dispersion due to the change of fluid property. After adding NaSal to the CTAC solution, the average bubble diameter generated was enlarged to 122 μm, however, this bubble size is still effective to reduce the turbulence drag in practical application.

Keywords Low surface tension • Microbubble generation • Small size • Surfactant

L.-F. Jiao • T. Kunugi (✉) • Z. Kawara
Graduate School of Engineering, Kyoto University, Yoshida Honmachi, Sakyo, Kyoto 606-8501, Japan
e-mail: kunugi@nucleng.kyoto-u.ac.jp

F.-C. Li
School of Energy Science and Engineering, Harbin Institute of Technology, Harbin 150001, China

T. Yao (ed.), *Zero-Carbon Energy Kyoto 2011*, Green Energy and Technology,
DOI 10.1007/978-4-431-54067-0_34,

1 Introduction

Microbubble drag-reducing technology (MBDR) [1], which is to reduce the turbulence drag by injecting microbubbles (MB) into the turbulent boundary layer, has a great potential in naval applications because of no environmental impact and low cost. It is generally believed that the drag reduction can be optimized by injecting a little amount of MB, whose size should be in between the thicknesses of viscous and turbulent boundary layers [2–5]. However, it is still a challenge to control the bubble size and the injecting location in practical applications.

The effective bubble size reducing the drag varies with the flow conditions, but it mainly ranges from 10 to 500 μm [6, 7]. In general, there are three ways to generate MB. The most common way is that a compression of air dissolves into liquid and the MB are generated by a specially designed nozzle, i.e., the cavitations and a high shear flow occurred at the nozzle exit enhance the nucleation of small bubbles (they might be potentially nano-bubbles). The second way is to use a power ultrasound to induce the cavitations locally at points of extreme rarefaction in the standing ultrasonic waves. Both ways usually need high power densities and consume a lot of energy for either the compression or ultrasonic treatment. The third way is to use an air stream supplied under low pressure and breaks up the air stream to many small bubbles whether it is a mechanical vibration, a converging flow or a fluidic oscillation. The third way is widely used because of low energy consumption, but it is difficult to reduce the bubble size up to micron scales. That is the reason why the reduction in drag is often not observed in large scale experiments of MBDR applications [8].

On the other hand, a surfactant can highly reduce the surface tension of air–water interface. In this paper, in order to improve the third way of MB generation the usage of surfactant has been developed.

2 Experimental System

2.1 Working Fluids

Considering of the synergy effect of MBDR and viscoelastic drag-reducing (VEDR) on the turbulent drag reduction, we choose a cationic surfactant—cetyltrimethylammonium chloride (CTAC), which is often used in VEDR technology—to reduce the surface tension.

In pure surfactant solutions, the surfactant molecular have the tendency to assemble together to generate the micelle structures above critical micellation concentration. These micelle structures easily spread to rod-like structures, and even further interlace the network structures while certain counter-ions are present [9] as schematically shown in Fig. 1. The existence of such micelle structures is thought to be the main reason of the fluid viscoelasticity. Moreover, a sodium salicylate (NaSal) is often used as the counter-ions in CTAC solutions in VEDR

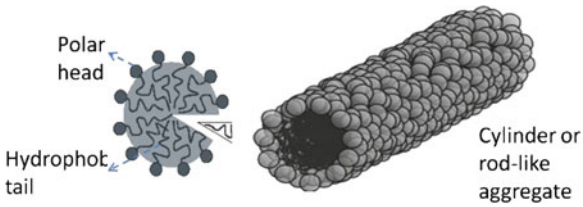

Fig. 1 A schematic view of the development process of micelle structures in surfactant solution

Table 1 Working fluid information

Name	Produce company	Molecular weight	Chemical formula
CTAC	Nakalai	320.00	$[CH_3(CH_2)_{15}N\ (CH_3)_3]Cl$
NaSal		160.10	$C_7H_5O_3Na$

technology. In this study, we observed the changes of bubble size in pure 100 ppm CTAC solution and also 100 ppm/100 ppm CTAC/NaSal solution at 20°C. The detail information of CTAC and NaSal are shown in Table 1.

2.2 Microbubble Generation and Observation Systems

A special designed nozzle was used to make two high-speed converging flows and generate microbubbles as shown in Fig. 2. The surfactant solution was supplied into the nozzle and made a high-speed converging flow, and simultaneously generated both a large flow disturbance and a low pressure region. Finally, the air dissolved into the flow and broke up into small bubbles, and eventually the bubbly flow was formed at the outlet of the nozzle.

In the experiments, both aqueous solution and air were set in a closed acrylic tank (500 mm × 500 mm × 100 mm) and then mixed together by using the nozzle as shown in Fig. 3. The major experimental variables were the bubble size and void fraction. Bubble size was recorded by a high-speed video camera as shown in Fig. 4. This camera was operated at 100 fps and with the spatial resolution of 512 × 512 pixels. Since the bubble was very small, the bubble shape was nearly a sphere. Therefore, we calculated the bubble size as a sphere obtained from the photographs taken by the high-speed camera. Void fraction was also calculated by dividing the amount of bubble volume by the solution volume at the static condition.

2.3 Experimental Results

2.3.1 Reference Case: Bubble Generation in Water

Firstly, bubble size was measured in pure water at T = 20°C. In water cases, the diameters of the generated bubbles were in the range from1.5 to 4 mm, so they are too large to show the high drag reduction in MBDR technology.

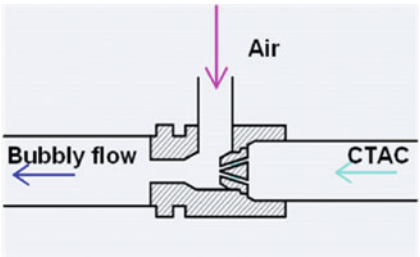

Fig. 2 Flow-converging nozzle

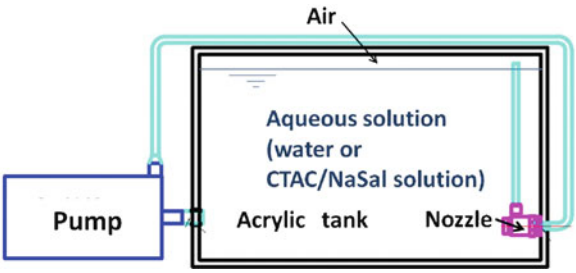

Fig. 3 Schematic of MB generating system

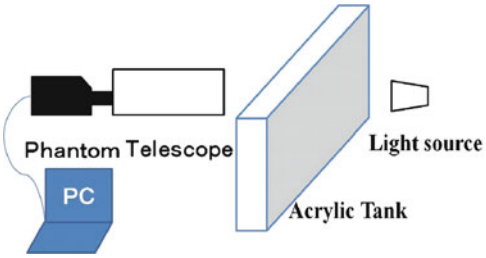

Fig. 4 Schematic visualization system

2.3.2 Microbubble Generation in 100 ppm CTAC Solution

In the pure CTAC solution, the generated bubble size was highly reduced. After rotating the pump, a milk like solution immediately flowed out from the nozzle to the tank. After few seconds, the solution containing the air bubbles in the tank was almost completely mixed. Since the bubble density (bubble number per volume of the solution) was very large in the tank, it was possible to observe the bubbles near the wall by the high-speed camera. Assuming the bubble size distribution is two-dimensional, three locations to measure the bubble were chosen: the distances from the left down corner of tank in height and length were

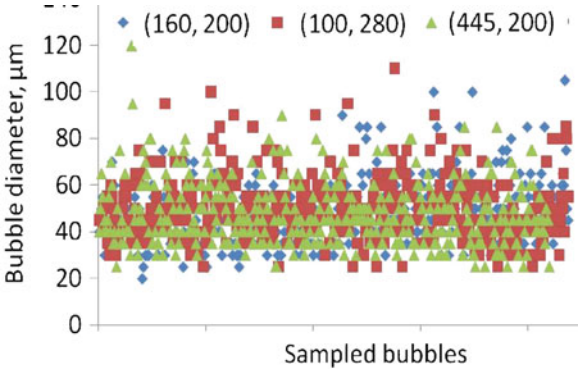

Fig. 5 Bubble size at different locations at void Fraction $\alpha = 5\%$ in 100 ppm CTAC solution

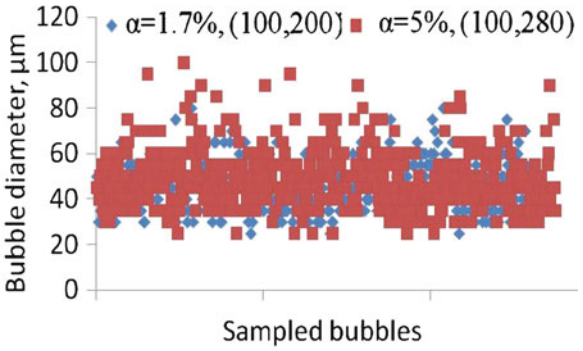

Fig. 6 Bubble size distribution at different void fractions in 100 ppm CTAC solution

(160, 200 mm), (100, 280 mm) and (445, 200 mm), respectively. From Fig. 5, it is observed that the average bubble diameters are 47.8, 48.6 and 47.8 μm at (160, 200 mm), (100, 280 mm) and (445, 200 mm), respectively. The differences of bubble size at the different locations are small, thus it is considered that the size of the generated bubbles is homogeneous in the tank. In other words, the nozzle generated bubble size is almost uniform. Since the monomers of surfactant tend to absorb at the interface of bubbles and solution, a resist film may exist on the surface of bubbles and thus the coalescence of bubbles would be very difficult. As the result, the generated bubbles are difficult to coalescence with each other in surfactant solutions.

The bubble size distributions at the various void fractions were also observed as shown in Fig. 6. According to Fig. 6, the average diameters of bubbles were 46.7 and 48.6 μm at 1.7% and 5% void fraction, respectively. This means the air breaking-up ability of this nozzle is nearly the same for all conditions of the present study. Since 5% void fraction is large enough for MBDR in practical applications, the further increase of the void fraction has not been done here.

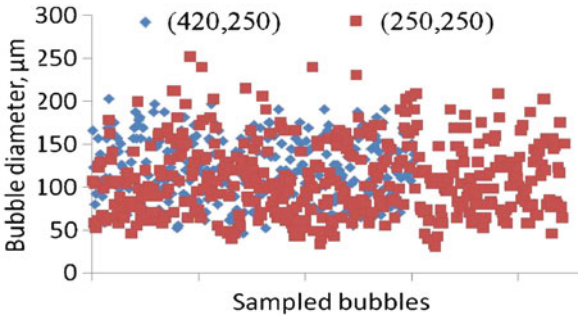

Fig. 7 Average bubble diameter at different location

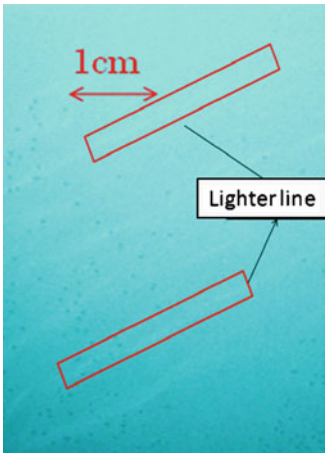

Fig. 8 Light line photo

2.3.3 Microbubble Generation in 100 ppm/100 ppm CTAC/NaSal Solution

After adding NaSal to the CTAC solution, the solution showed the high visocelasticity, which is possible to further reduce the fractional drag through injecting together with MB to turbulent boundary layer [10]. In 100 ppm/100 ppm CTAC/NaSal solution, the bubble size was enlarged to 122 and 109 μm at (420, 250 mm) and (250, 250 mm), respectively as shown in Fig. 7. From the figure, it was also found that the bubble size was smaller at the center of the tank than at the area near the wall. In addition, the bubbles tent to assemble together following the flow streams as shown in Fig. 8, in which the lighter lines mean many bubbles located in that areas. This fact indicates that the bubbles might be captured by surrounding fluid and flow together in the viscoelastic fluid. This was different from the pure CTAC cases, in which bubbles tent to diffuse quickly under the both buoyancy force and flow turbulence around them. This phenomenon may be explained by the following two reasons: (a) the turbulence in the flow is highly

suppressed due to the viscoelasticity; (b) the existence of micelle structures can absorb the bubbles strongly and reduce the effect of buoyancy force. This part will be further observed in future.

3 Conclusion and Remarks

Adding very little CTAC to water, it is easy to break air streams up microbubbles whose average diameter was smaller than 50 μm under the action of proper disturbance. In CTAC solutions, the bubbles diffused quickly after their injection and became homogenous within a few seconds. On the other hand, after adding NaSal in CTAC solution, the bubble average diameter was enlarged from 50 to around 120 μm. Moreover, the bubbles tend to move together with the surrounding flow. In current situations, both CTAC and CTAC/NaSal cases can generate the effective drag-reducing size bubbles by using the present designed nozzle. This improvement of the MB generating method would be very meaningful in MBDR's practical applications.

Acknowledgment The authors were grateful for the support of the Ministry of Education, Culture, Sports, Science and Technology of Japan via "Energy Science in the Age of Global Warming" of Global Center of Excellence (G-COE) program (J-051).

References

1. McCormick ME, Bhattacharyya R (1973) Drag reduction of a submersible hull by electrolysis. J Nav Eng 85:11–16
2. Pal S, Merkle CL, Deusch S (1988) Bubble characteristics at trajectories in a microbubble boundary layer. Phys Fluid 31:742–751
3. Madavan NK, Merkle CL, Deutsch S (1985) Numerical investigations into the mechanisms of microbubble drag reduction. ASME J Fluid Eng 107:370–377
4. Oishi Y, Murai Y, Tasaka Y, Yasushi T (2009) Frictional drag reduction by wavy advection of deformable bubbles. J Phys 147, 012020: 1–14
5. Madavan NK, Deutsch S, Merkle CL (1984) Drag reduction on turbulent skin friction by microbubbles. Phys Fluid 27:356–361
6. Huang J, Murai Y et al (2008) Shallow DOF-based particle tracking velocimetry applied to horizontal bubble wall turbulence. Flow Meas Instrum 19:93–105
7. Shen XC, Ceccio SL, Perlin M (2006) Influence of bubble size on micro-bubble drag reduction. Exp Fluid 41:415–424
8. Aoki K, Hishida K, Kodama Y (2006) Measurements of near wall turbulent structure in a microbubble flow using a highly magnifying telecentric PIV/PTV system. In: 13th international symposium applications of laser techniques to fluid mechanics Lisbon, Portugal, 26–29 June 2006:1333
9. Claussen TM, Vinson PK, Minter JR, Davis HT, Talmon Y, Miller WG (1992) Viscoelastic micellar solutions: microscopy and rheology. J Phys Chem 96:474–484
10. Fontaine AA, Deutsch S, Brungart TA et al (1999) Drag reduction by coupled systems: microbubble injection with homogeneous polymer and surfactant solutions. Exp Fluid 26:397–403

Gyro-Kinetic Simulation of Ion Temperature Gradient Driven Drift Wave Instability in the Presence of a Magnetic Island

Paul P. Hilscher, Kenji Imadera, Jiquan Li, and Yasuaki Kishimoto

Abstract The ion temperature gradient (ITG) mode instability in the presence of a meso-scale magnetic island using a gyro-kinetic simulation code is investigated. The difference between a model with full gyro-kinetic effects and one reduced to first order—is emphasized.

We find that a magnetic island causes radial and poloidal modes to couple with each other, thus play a stabilizing role by allowing energy transfer to stable modes. For larger island sizes, new rational surfaces appear, which again may excite destabilization. In contrast to gyro-O(1) and gyro-fluid simulations, full gyro-kinetic simulation have a larger mode spectra due to short-wavelength effects, which limits energy transfer and thus stabilization is relaxed.

Keywords Fusion plasma • Gyro-kinetics • Magnetic islands • Turbulence

1 Introduction

Tokamaks are very promising to supply mankind's future energy demand. But, present day Tokamaks fail to achieve a positive energy balance mainly because plasma confinement is lost due to various instabilities in the plasma, ranging from the MHD scale down to micro-turbulences gyro-radius scale of particles. Single-scale micro-turbulences are now mainly well explored, where an adiabatic response of the opposite charged species is assumed for scale separation, e.g. Lee et al. [1] or Jenko et al. [2].

But taking also multi-scale interaction into account is crucial, as it may strongly alter simulation results. For example, during a Tokamak discharge, MHD

P.P. Hilscher (✉) • K. Imadera • J. Li • Y. Kishimoto
Department of Fundamental Energy Science, Graduate School of Energy Science, Kyoto University, Gokasho, Uji, Kyoto 611-0011, Japan
e-mail: paul@center.iae.kyoto-u.ac.jp

T. Yao (ed.), *Zero-Carbon Energy Kyoto 2011*, Green Energy and Technology,
DOI 10.1007/978-4-431-54067-0_35,

instabilities take place, which result in a magnetic island. The saturated magnetic island can span several ion gyro-radii as discovered by Isayama et al. [3]. In the same time, a temperature gradient develops and the plasma becomes unstable to drift-wave instabilities, like the ITG mode. The ITG mode happens on a much faster time scale and thus the magnetic island can be assumed to be stationary during the time, the ITG instability develops.

In the next sections, we investigate the effects of magnetic islands on ITG instability growth, in dependence of the island's width. ITG turbulence on a magnetic island was first studied by Wang et al. [4], who discovered using a gyro-fluid simulation code, that for an island size $w < 10$, the island has a stabilizing role due to mode–mode coupling effects. Above this threshold, the destabilizing effect due to the appearance of additional rational surfaces dominates. Here, we investigate Wang's setup using a gyro-kinetic model, where kinetic effects are retained.

2 Calculation Model

2.1 Geometry

We reduce the Tokamak geometry to a sheared slab geometry, where near the rational surface $x = 0$, the magnetic field can be written as $\mathbf{B} = (0, \hat{s}x, 1)$. Thus the parallel gradient $k_\parallel$ takes the form $k_\parallel = (0, \hat{s}x, 1) \cdot \left(k_x, k_y, k_z\right) \approx \hat{s}xk_y$, where $\hat{s}$ is the magnetic shear and $k_z = 0$ is taken for a single rational surface. This allows us to reduce the gyro-kinetic equation system by one spatial dimension $(x,y,z) \rightarrow (x,y)$.

2.2 Gyro-Kinetic Equation System

For the numerical investigation of micro-turbulence, we employ a self-developed gyro-kinetic code, see Hilscher et al. [5]. We use a *local approximation*, where the temperature and density is assumed to be constant, but with finite temperature and density gradients along the x-direction $\eta_i = L_n/L_T$, with L_T, the temperature length scale and L_n, the density length scale. Also, we assume the electrons to be adiabatic. The domain is assumed to be periodic along x and y. The normalized gyro-kinetic equations are a coupled integro-differential equation system of the *Vlasov equation* in the linear regime -

$$\frac{\partial F_1}{\partial t} = \left(1 + \eta_i \left[\frac{v_\parallel^2}{2} - \mu - \frac{3}{2}\right]\right) \frac{\partial \langle\phi\rangle}{\partial y} F_0 + v_\parallel \hat{s}x \left(\frac{\partial F_1}{\partial y} + \frac{\partial \langle\phi\rangle}{\partial y} F_0\right),$$

where $v_\parallel$ is the parallel velocity, μ the magnetic moment, ϕ the electric potential and the Maxwellian $F_0 = \frac{1}{\sqrt{2\pi}} e^{-v_\parallel^2/2-\mu}$ of the ion distribution, while $F_1(x, y, v_\parallel, \mu)$ is

its deviation, and the brackets $\langle A \rangle$ denotes the gyro-average calculated by $\langle A \rangle = \mathrm{J}_0(\sqrt{2\mu k_\perp^2})A$ [1]—and the *Poisson equation*

$$\int_{\mu=0}^{\infty} \int_{v=-\infty}^{\infty} F_1 dv_\parallel d\mu = \left[1 - \Gamma_0(k_\perp^2)\right]\phi + \phi,$$

where $\Gamma_0(k_\perp^2) = \mathrm{I}_0(k_\perp^2)e^{-k_\perp^2}$ [2], $k_\perp^2 = k_x^2 + k_y^2$, and the last term is due to the adiabatic response term of the electrons.

2.3 Reduction to First Order Gyro-Kinetic Effects

In order to further reduce the numerical cost of the simulations, a common approach is to neglect perturbations of F_1 in the μ direction and including gyro-kinetic effects only to first order in $k_\perp^2$. Using this approximation, the Vlasov and Poisson equation can then be directly integrated over μ, thus reducing the velocity dimensionality from $(v_\parallel, \mu) \rightarrow (v_\parallel)$. The Vlasov equation then takes the form

$$\frac{\partial F_1}{\partial t} = \left(1 + \frac{\eta_i}{2}\left[v_\parallel^2 - k_\perp^2 - 1\right]\right)\frac{\partial \langle\phi\rangle}{\partial y}F_0 + v_\parallel \hat{s}x\left(\frac{\partial F_1}{\partial y} + \frac{\partial \langle\phi\rangle}{\partial y}F_0\right).$$

Here, gyro-averaging is performed by multiplying the exponential function $\langle A \rangle = A\, e^{-k_\perp^2}$, and $F_0 = \frac{1}{\sqrt{2\pi}}e^{-v_\parallel^2/2}, F_1(x, y, v_\parallel)$.

We refer to this approximation as gyro-O(1). This approximation is often used, as it greatly reduces computational cost due to reduced dimensionality, while still keeping the most important gyro-kinetic effects, see e.g. Nakata et al. [6].

2.4 Gyro-Kinetic Equation with Magnetic Island

The magnetic island structure can be embedded into the gyro-kinetic equation system, by starting from an electro-magnetic system, e.g. see Jenko et al. [2] and dropping all time-dependent terms for the magnetic vector potential $A_{1\parallel}$. This is valid, as the evolution of the magnetic island is in general much slower than the micro-turbulence timescale. The linear Vlasov equation with a stationary $A_{1\parallel}$ is then

$$\frac{\partial F_1^{'}}{\partial t} = \frac{\partial F_1}{\partial t} + v_\parallel\left[\langle A_{1\parallel}\rangle, F_1\right] - v_\parallel\left[\langle A_{1\parallel}\rangle, \phi\right]F_0.$$

[1] J_0 is the zeroth-order Bessel function of first kind.

[2] I_0 is the modified Bessel function of zeroth order and first kind.

The latter terms appear due to the magnetic island. The Poisson equation remains unmodified.

The structure of the magnetic island is usually computed by an MHD code, see e.g. Janvier [7]. But in order to simplify analysis, we assume an analytic approximation from Connor et al. [8], with

$$A_{1\parallel} = -\frac{w^2 \hat{s}}{16} cos(\zeta x) cos(k_T \left[y - \frac{L_y}{2} \right]) \quad .$$

For the subsequent simulations, we choose ζ=0.1, $k_T = 0.2$, $\hat{s} = 0.4$ and w is the assumed magnetic island width.

3 Results

For a first insight, we investigate the analytic solution of the linear dispersion relation in the constant-θ approximation.[3] As shown in Fig. 1, the *gyro case* exhibits a so called short-wavelength mode (sw-mode) in the $k_y \gg 1$ region, which neither exists in the gyro-O(1) case nor in the fluid limit.

The ϕ-potential of an ITG simulation with $\eta_i = 4.2$ and an island of width $w = 20$ is shown in Fig. 2. A magnetic island results in a mode–mode coupling, see Fig. 3, which may transfer energy to stable modes and thus reduce instability growth. However, this may be counterbalanced, as shown by Wang et al. [4], by appearance of additional rational surfaces when $w > 0$.[4]

Further, we analyze the system's instability growth in dependence of the magnetic island width w. The results are shown in Fig. 4. Inclusion of a magnetic island has an overall damping effect. For an island width of $w \sim 14$, the instability due to additional rational surfaces increases, but in contrast to Wang's case, further increasing the island size does not result in further destabilization, but further stabilization for gyro-O(1)—probably due to its highly dissipative nature in $k_y \gg 1$; for the gyro case, growthrates saturates as energy transfer is limited due to the sw-mode.

4 Summary and Outlook

We investigated the ITG turbulence under the influence of a magnetic island using a gyro-kinetic code. We compared gyro-kinetic and first-order gyro-kinetic simulations. We showed that the inclusion of a magnetic island does in general

[3] The magnetic field $\mathbf{B} = (0, \theta, 1)$ and the x-y plane has a constant angle θ.

[4] From the rational surface equation $k_\parallel = 0 = \hat{s} x k_y - \left(\nabla \times A_{1\parallel}\right) \cdot \mathbf{k}$.

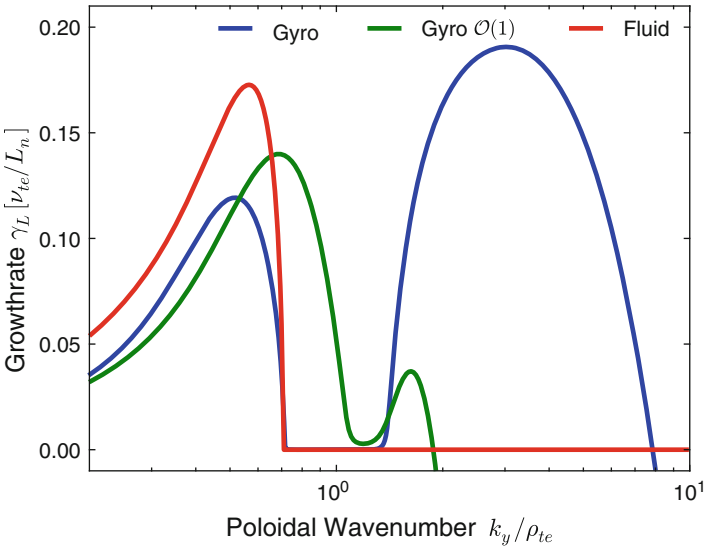

Fig. 1 Solution of dispersion relation in the constant-θ approximation, with $\theta = 0.1$; $k_x = 0$ and $\eta_i = 6$. Shown is the solution in full gyro-kinetics, gyro-O(1), and in fluid approximation $w \gg k_\parallel v_{te}$. If full gyro-kinetic effects are kept, growth in the high-k region due to short wavelength effects can be observed

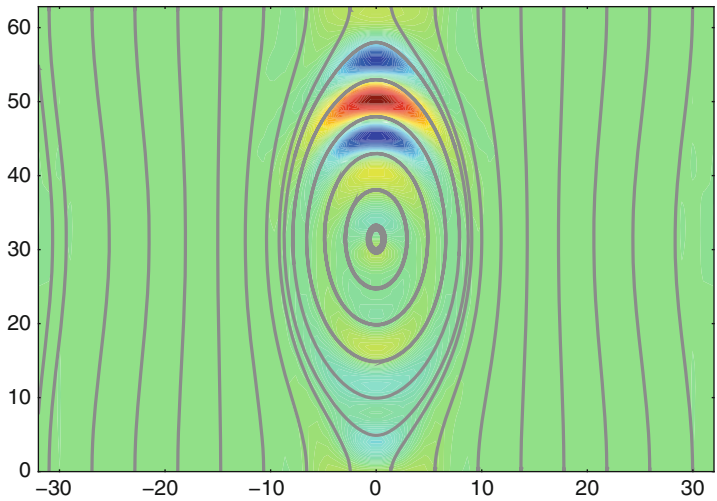

Fig. 2 Contour plot of ϕ potential for an island width $w = 20$ and $\eta_i = 4.2$ and gyro-O(1) model. Due to the magnetic island, new rational surfaces may appear which in turn may excited turbulence along rational surfaces

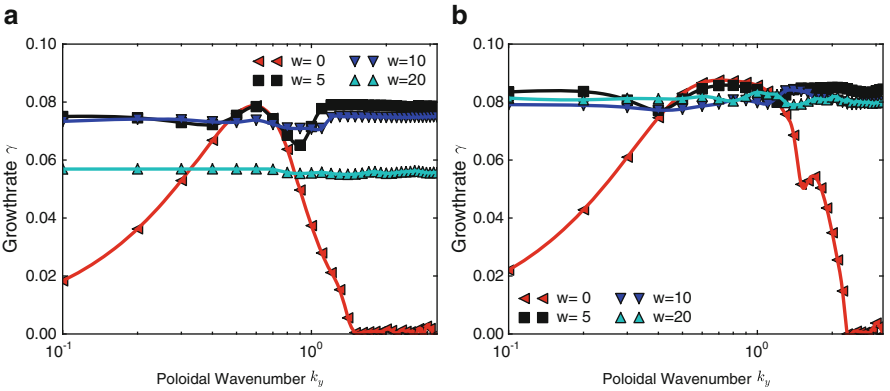

Fig. 3 Growth rates for poloidal modes for magnetic island widths of $w = 0$, 5, 10, 20. Mode–mode coupling results in equal growth of all poloidal modes and dissipates energy by stable modes: (**a**) gyro-O(1); (**b**) gyro

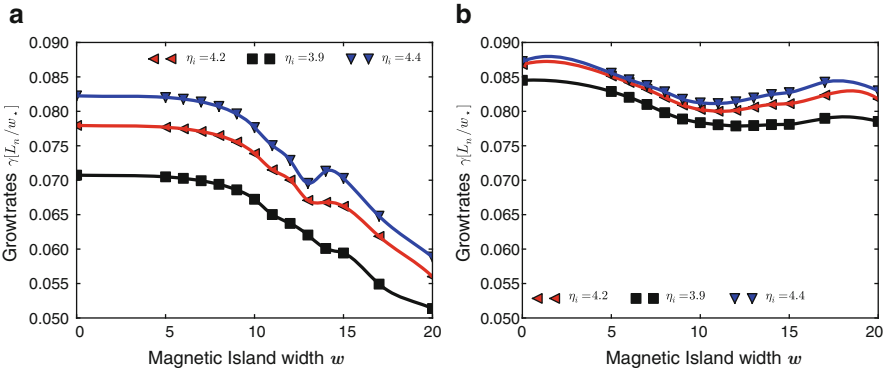

Fig. 4 Growth rates of electric field energy for different island widths w and $\eta_i = 3.9$, 4.2, 4.4. Instability growth is reduced by mode–mode coupling. For $w \sim 14$, the appearance of additional rational surfaces for large island widths may increase again turbulence: (**a**) gyro-O(1); (**b**) gyro-kinetic

stabilize the ITG turbulence due to mode–mode coupling. The short-wavelength effects have a profound influence on stability, due to unstable modes in $k_y \gg 1$, in contrast to fluid and gyro-O(1), which were stable and dissipated energy.

In subsequent work, we will investigate the sw-modes in presence of kinetic electrons.

Acknowledgments The author (P.H.) is grateful for the support of the Ministry of Education, Culture, Sports, Science and Technology of Japan via "Energy Science in the Age of Global Warming" of Global Center of Excellence (G-COE) program (J-051).

References

1. Lee GS, Diamond PH (1986) Theory of ion-temperature-gradient-driven turbulence in tokamaks. Phys Fluid 29(10):3291–3313
2. Dorland W, Jenko F, Kotschenreuther M, Rogers BN (2000) Electron temperature gradient turbulence. Phys Rev Lett 85(26):5579–5582
3. Isayama A, Kamada Y, Ozeki T, Isei N (1999) Measurement of magnetic island width in long-pulse, high-β_N discharges in JT-60U. Plasma Phys Contr Fusion 41(1):35
4. Wang ZX, Li JQ, Kishimoto Y, Dong JQ (2009) Magnetic-island-induced ion temperature gradient mode. Phys Plasma 16(6):060703
5. Hilscher PP, Imadera K, Li J, Kishimoto Y (2010) Towards gyrokinetic simulations of multi-scale micro-turbulence in tokamaks. In: Yao T (ed) Zero-carbon energy Kyoto 2010. Springer, Tokyo, pp 239–244
6. Nakata M, Watanabe TH, Sugama H, Horton W (2011) Effects of parallel dynamics on vortex structures in electron temperature gradient driven turbulence. Phys Plasma 18(1):012303
7. Janvier M (2011) Study of the nonlinear dynamics of double tearing modes to understand explisive magnetic reconnection in fuion and astrophysical plasmas. PhD Thesis, 16
8. Connor JW, Waelbroeck FL, Wilson HR (2001) The role of polarization current in magnetic island evolution. Phys Plasma 8:2835–2848

Thermodynamic Stability of Nd(III) Complex in Ternary Mixtures of Molten Alkali Chlorides

Kazuhito Fukasawa, Akihiro Uehara, Takayuki Nagai, Toshiyuki Fujii, and Hajimu Yamana

Abstract Thermodynamic stability of Nd(III) complex in molten ternary mixtures of alkali chlorides was estimated by employing electrochemical techniques, and its dependence on the melt compositions was investigated. The Gibbs energy change of Nd(III) complex was proportional to the polarizing power of solvent alkali cations. The dependence was similar to that for binary mixtures of alkali chlorides. The result suggests that the thermodynamic stability of $NdCl_6^{3-}$ in the mixtures of alkali chlorides can be explained by averaged radius of alkali cations.

Keywords Neodymium • Polarizing power of solvent cations • Symmetry of octahedral coordination structure • Ternary molten salt • Thermodynamic stability

1 Introduction

Suitable management of spent nuclear fuels is necessary to use nuclear energy toward future low carbon society. Pyrochemical reprocessing using molten salts as reaction media is a candidate process for separation of lanthanide (Ln) and actinide (An) elements from the spent fuels [1–4]. Uranium and plutonium are recovered as fuel materials, and minor actinides (Np, Am, and Cm) separated would be diminished through transmutation processes to decrease their long-life radiotoxicities. Neodymium (Nd) is a major fission product in the spent fuels and a strong neutron absorber that should be separated from fuel elements. It is essential to understand

K. Fukasawa (✉)
Graduate School of Engineering, Kyoto University, Kyoto, Japan
e-mail: k.fukasawa@aw2.ecs.kyoto-u.ac.jp

A. Uehara • T. Fujii • H. Yamana
Research Reactor Institute, Kyoto University, Kumatori, Sennan, Osaka, Japan

T. Nagai
Nuclear Fuel Cycle Engineering Lab, Japan Atomic Energy Agency, Tokai, Naka, Ibaraki, Japan

T. Yao (ed.), *Zero-Carbon Energy Kyoto 2011*, Green Energy and Technology,
DOI 10.1007/978-4-431-54067-0_36,

the redox potential of Nd as well as reaction mechanism at an electrode controlled by the composition of molten salts in order to attain high selectivity of ND in the reprocessing process.

The electrochemical behavior of Nd ions has been reported for binary mixtures of alkali chlorides [5–9], LiCl–ACl_2 (A = Ca, Sr, and Ba) [7, 8] and NaCl-$CaCl_2$ [9], where Nd^{3+} is reduced to metal by two steps via divalent as follows:

$$Nd^{3+} + e^- \rightleftarrows Nd^{2+} \quad (1)$$

$$Nd^{2+} + 2e^- \rightleftarrows Nd^0(\text{metal}) \quad (2)$$

Thermodynamic properties of Nd in ternary mixtures, on the other hand, have not been investigated. Some ternary mixtures possess lower melting point, e.g., 619 K for LiCl–NaCl–KCl (55:9:36 mol%) and 538 K for LiCl–KCl–CsCl (58:13:29 mol%) eutectics [10], compared with that of a typical binary system, LiCl–KCl eutectic melt (59:41 mol%) at 628 K. This feature may be suitable for the reprocessing at moderate operation temperature. In this context, we investigated the electrochemical behavior of Nd in ternary mixtures of molten alkali chlorides.

2 Experimental

All experiments were carried out under an Ar atmosphere (O_2 and $H_2O < 1$ ppm). Anhydrous chlorides (99.99% purity) were purchased from Aldrich-APL LLC and used without further purification. 0.3–0.6 mol% $NdCl_3$ was dissolved in various ternary mixtures of alkali chlorides, where equimolar NaCl–KCl or KCl–CsCl mixture (31:69 mol%) was added into LiCl melt. Experimental temperature was controlled in the range from 623 to 923 ± 3 K.

An electrochemical measurement system Hz-5000 (Hokuto Denko Co.) was used for cyclic voltammetry (CV) and the differential pulse voltammetry (DPV). The sweep rate of CV for extracting peak potentials was 100 mV s^{-1}. The pulse height, period, and width of DPV were 50 mV, 100 and 10 ms, respectively. A tungsten wire (99.95%, Nilaco Co.) of 1 mm diameter, a pyrographite rod (99.99%, Tokai Carbon Co., Ltd.) of 3 mm diameter, and a Ag/Ag^+ electrode were used for the working, counter, and reference electrodes, respectively. In each measurement, the potential of chlorine gas evolution (Cl_2/Cl^-) on the pyrographite electrode [11] was determined to calibrate the Ag/Ag^+ electrode.

3 Result and Discussion

3.1 Determination of Gibbs Energy Change of Nd(III) Formation

Figure 1a shows typical cyclic voltammograms of Nd in molten LiCl–KCl–CsCl mixtures at 923 K. The cathodic wave i_{C1} associated with an anodic wave i_{A1} is attributable to the soluble–soluble Nd^{3+}/Nd^{2+} couple. The cathodic peak i_{C2} with a sharp anodic peak i_{A2} corresponds to the Nd^{2+}/Nd^{0} soluble–insoluble system. Decrease of current densities was due to the concentration of Nd^{3+}. All peaks were clearly observed for pure LiCl system, while the overlap of i_{C1} and i_{C2} in voltammograms was enhanced by adding MCl (M = K, Cs) into LiCl and it could not be resolved. In order to obtain sharp wave i_{C1}, DPV was performed. The result in LiCl–KCl–CsCl mixtures at 923 K is shown in Fig. 1b, in which the first peak was clearly obtained until LiCl mole fraction, χ_{LiCl}, is more than 0.7. The convolution analysis [12] was also applied for cyclic voltammograms.

The disproportionation reaction of Nd takes place in molten chlorides [5, 9, 13],

$$3Nd^{2+} \rightleftarrows 2Nd^{3+} + Nd^{0}(\text{metal}) \tag{3}$$

Its interference in the following analyses is considered to be insignificant [6].

The standard redox potential of the Nd^{3+}/Nd^{2+} couple, $E^{\circ}{}_{3/2}$, was determined by DPV [12] and by the convolution analysis of CV [12] in the case of $0.58 \leq \chi_{LiCl} \leq 0.7$. Detail analytical procedure of DPV is explained in our previous paper [6]. The values of density of the melt and diffusion coefficient of Nd^{3+}, $D_{Nd(III)}$, in the melt are required for the convolution analysis. The former was reported for LiCl–KCl–CsCl eutectic in the temperature from 573 to 723 K [14]. The data was extrapolated for our experimental temperatures. The density for LiCl–NaCl–KCl (50:25:25 mol%) was evaluated by averaging those of equimolar LiCl–NaCl and LiCl–KCl at 920 K [15]. For other mixtures, the value was estimated by a linear interpolation between the values of pure LiCl and the above melt. The value of $D_{Nd(III)}$ for LiCl–KCl eutectic melt [16] was substituted for all systems. It would change depending on the melt composition [17], which would cause uncertainty of ± 10 mV on the $E^{\circ}{}_{3/2}$ value. The activity of both trivalent and divalent ions was set to be unity in the present analyses.

The standard redox potential of the Nd^{2+}/Nd^{0} couple, $E^{\circ}{}_{2/0}$, was evaluated from CV [18]. The standard redox potential of the Nd^{3+}/Nd^{0} couple, $E^{\circ}{}_{3/0}$, was calculated from $E^{\circ}{}_{3/2}$ and $E^{\circ}{}_{2/0}$ by employing the following equation,

$$E^{\circ}_{3/0} = \frac{E^{\circ}_{3/2} + 2E^{\circ}_{2/0}}{3} \tag{4}$$

The standard Gibbs energy change of Nd(III) formation, $\Delta G^{\circ}{}_{3/0}$, was derived as

$$\Delta G^{\circ}_{3/0} = nFE^{\circ}_{3/0} \tag{5}$$

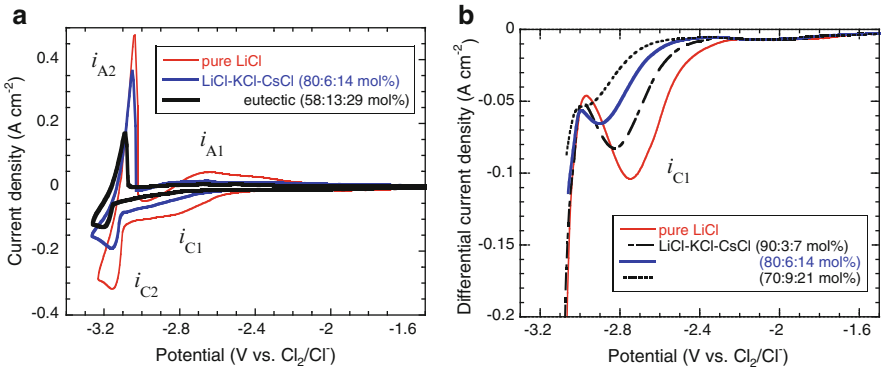

Fig. 1 (**a**) Cyclic voltammograms and (**b**) differential pulse voltammograms of Nd for molten LiCl–KCl–CsCl mixtures at 923 K

3.2 *Dependence of $\Delta G^\circ_{3/0}$ on the Melt Compositions*

The obtained $\Delta G^\circ_{3/0}$ values for LiCl–KCl–CsCl and LiCl–NaCl–KCl systems are shown in Fig. 2 with those for binary alkali chloride mixtures [6]. The value decreases with χ_{LiCl}, which means that Nd(III) complex was stabilized by the increase of averaged radius of solvent alkali cations (Li < Na < K < Cs). It is reported that the thermodynamic stability of Nd(III) complex showed linear correlation with the polarizing power of solvent cations, P, which is defined as

$$P = \Sigma \chi \frac{z}{r^2} \tag{6}$$

where χ, z, and r are the mole fraction, the valence, and the ionic radii of solvent alkali cations. As shown in Fig. 2b, our present results are on the similar slope vs. P. The correlation between the thermodynamic stability and the symmetry of the octahedral coordination structure of Nd(III) complex, $NdCl_6^{3-}$, has been pointed out for binary mixtures of alkali chlorides [6]. The interaction between the complex and ions in outer coordination spheres would be more complicated in ternary mixtures than that in binary mixtures because of the increase of ion species. The present results suggest that the interaction of alkali cations to the structure as well as the thermodynamic stability of the complex may be averaged.

3.3 *Temperature Dependence of $\Delta G^\circ_{3/0}$ for LiCl–KCl–CsCl Eutectic*

CVs of Nd for the LiCl–KCl–CsCl eutectic melt were carried out at different temperatures from 673 to 923 K, from which $\Delta G^\circ_{3/0}$ values were evaluated as

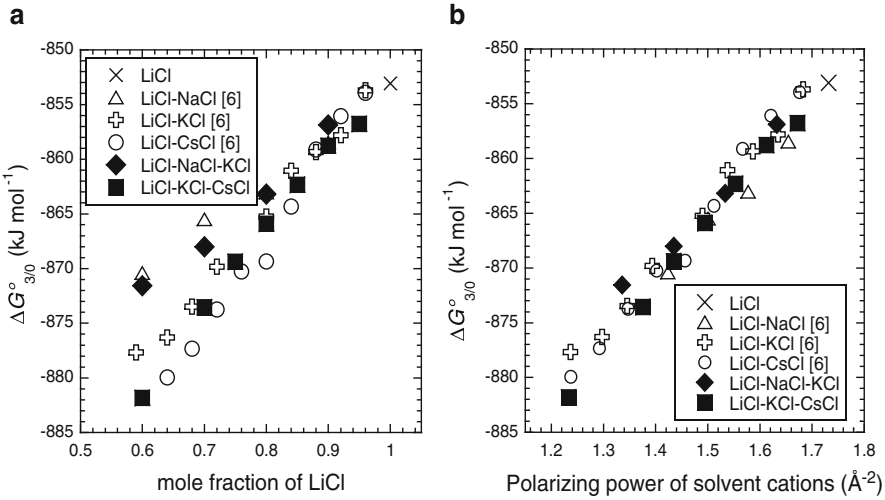

Fig. 2 Dependences of $\Delta G^{\circ}_{3/0}$ on (**a**) mole fraction of LiCl and (**b**) the polarizing power of solvent cations for binary and ternary systems at 923 K

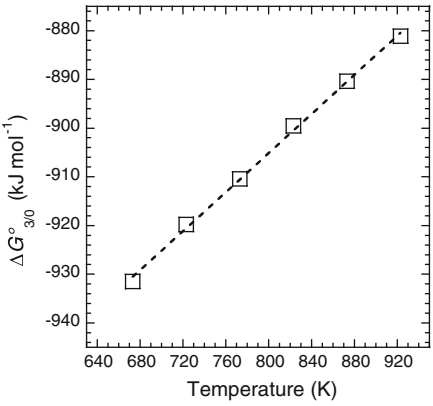

Fig. 3 Temperature dependences of $\Delta G^{\circ}_{3/0}$ for LiCl–KCl–CsCl eutectic melt

shown in Fig. 3. Enthalpy and entropy terms, ΔH and ΔS, can be derived from the temperature dependence of $\Delta G^{\circ}_{3/0}$ as

$$\Delta G = \Delta H - \mathrm{T}\Delta S \tag{7}$$

The result is shown in Table 1. These values were comparable to the reported ones for the LiCl–KCl eutectic melt: $\Delta H = -1061.2$ kJ and $\Delta S = -0.222$ kJ K^{-1} [9].

The lower limit of experimental temperature was 673 K, even higher than the melting point of this system. At lower temperature than 673 K, the melt was

Table 1 Evaluated values of enthalpy and entropy change of Nd(III) formation for LiCl–KCl–CsCl eutectic melt

Terms	Values
ΔH	−1,065 (kJ/mol)
ΔS	−0.201 (kJ/(mol K))

separated into two phases in transparent (upside) and in denser green (downside), which means that most of Nd^{3+} ions were concentrated at the bottom of the melt. The concentration of Nd^{3+} in the transparent phase was analyzed by absorption spectrophotometry to be about 0.02 M, i.e., 85% of Nd^{3+} ions initially added were settled at the bottom. Adequate electrochemical measurements, hence, could not be performed.

4 Conclusion

Thermodynamic stability of Nd(III) complex in ternary mixtures of molten alkali chlorides was proportional to the polarizing power of solvent alkali cations. The slope was similar to that for binary mixtures of alkali chlorides. The result suggests that the interaction of surrounding alkali cations to the complex can be averaged to determine the octahedral symmetry of the complex, $NdCl_6^{3-}$. It was confirmed that the operating temperature of electrorefining process can be decreased to 673 K by using ternary molten salt media, 100 K lower than that assumed for general pyroprocess. The lower temperature limit of 673 K is even higher than the melting point of the melt at 538 K due to unexpected phase separation.

Acknowledgement Part of this work was financially supported by an "Energy Science in the Age of Global Warming" of Global Center of Excellence (G-COE) program (J-051) of the Ministry of Education, Culture, Sports, Science and Technology of Japan.

References

1. Chang YI (1989) Nucl Technol 88:129
2. Koyama T, Iizuka M, Shoji Y, Fujita R, Tanaka H, Kobayashi T, Tokiwai M (1997) J Nucl Sci Tech 34:384
3. Iizuka M, Uozumi K, Inoue T, Iwai T, Shirai O, Arai Y (2007) J Nucl Mater 299:32
4. Roy JJ, Grantham LF, Grimmett DL, Fusselman SP, Kruger CL, Storvick TS, Inoue T, Sakamura Y, Takahashi N (1996) J Electrochem Soc 143(8):2487
5. Yamana H, Park BG, Shirai O, Fujii T, Uehara A, Moriyama H (2006) J Alloy Compd 408–412:66
6. Fukasawa K, Uehara A, Nagai T, Fujii T, Yamana H (2011) J Alloy Compd 509(16):5112

7. Fukasawa K, Uehara A, Nagai T, Fujii T, Yamana H (2009) Zero-Carbon Energy Kyoto 2009 - Proceedings of the first international symposium of Global COE program, Springer, New York, p 330
8. Fukasawa K, Uehara A, Nagai T, Fujii T, Yamana H (2011) J Nucl Mater 414:265
9. Castrillejo Y, Bermejo MR, Barrado E, Martinez AM, Arocas PD (2003) J Electroanal Chem 545:141
10. Cook LP, McMurdie HF (1989) Phase diagram for ceramists. The American Ceramic Society, Inc., Ohio
11. Murakami T, Nohira T, Ogata YH, Ito Y (2005) Electrochem Solid State Lett 8(1):E1–E3
12. Bard AJ, Faulkner LR (2001) Electrochemical Methods -Fundamentals and Applications, 2nd Edition, Wiley, New York
13. Hayashi H, Akabori M, Ogawa T, Minato K, Naturforsch Z (2004) 59a:705
14. Ito H, Hasegawa Y (2001) J Chem Eng Data 46:1203
15. Janz GJ, Tomkins RPT, Allen CB, Downey JR Jr, Gardner GL, Krebs U, Singer SK (1975) J Phys Chem Ref Data 4(4):871
16. Matsumiya M, Matsumoto S, Matsuura H (2005) Electrochemistry 73(8):570
17. Kuznetsov SA, Gaune-Escard M (2005) In: Proceedings of the 7th international symposium on molten salts chemistry and technology MS7, Toulouse, France, Aug 29–Sep 2, p 855
18. Berzins T, Delahay P (1953) J Am Chem Soc 75:555

Modeling of Two-Dimensional Transport in Tokamak Plasmas

Haruki Seto and Atsushi Fukuyama

Abstract For integrated modeling of core and peripheral plasmas and analysis of transient transport phenomena where poloidal dependence of quantity is important, describing transport phenomena in the entire tokamak plasma as two-dimensional problems is desirable and becoming feasible owing to recent remarkable progress in computational resources. The set of two-dimensional transport equations with poloidal angle dependence is formulated from Braginskii's equations and the neoclassical theory in order to develop an integrated two-dimensional transport simulation code.

Keywords Integrated modeling • Neoclassical transport • Two-dimensional transport

1 Introduction

For practical use of magnetic fusion energy, it is indispensable to understand key transport processes in fusion plasmas and to predict time evolution of the spatial profiles of particle density, plasma flow and temperature for each particle species. In most of conventional transport simulations in tokamaks, transport in a core region has been described as a one-dimensional problem by the use of flux-surface-averaging, while transport in a peripheral region as a two-dimensional problem with simplified transport models and plasma flow, for example SOLDOR [1] and B2.5 [2]. Recent remarkable progress in computational technology, however, has made more rigorous two-dimensional simulation of tokamak plasmas feasible. In such a simulation, the neoclassical viscosity [3] driven by the inhomogeneity of the magnetic field intensity is essential for consistent analysis including

H. Seto (✉) • A. Fukuyama
Kyoto University, Kyoto, Japan
e-mail: seto@p-grp.nucleng.kyoto-u.ac.jp; fukuyama@nucleng.kyoto-u.ac.jp

T. Yao (ed.), *Zero-Carbon Energy Kyoto 2011*, Green Energy and Technology,
DOI 10.1007/978-4-431-54067-0_37,

both core and peripheral transport in toroidal fusion device. In the present study, the set of transport equations including the neoclassical viscosity is formulated from Braginskii's equations [4] in order to develop an integrated two-dimensional transport simulation code.

Short descriptions of coordinate systems, assumptions, and Braginskii's equations as a start point of deriving transport equations are given in Sect. 2. In Sect. 3, three dimensional transport equations are derived from Braginskii's equations including the neoclassical viscosity. Finally a short summary is given in Sect. 4.

2 Preliminaries

2.1 Coordinate Systems

Two coordinate systems are employed for axisymmetric tokamak plasmas. The former is a magnetic flux coordinate system (MFCS) $(\xi_1, \xi_2, \xi_3) = (\rho, \chi, \zeta)$, where $\rho \in [0, 1]$ is a flux label function, $\chi \in [0, 2\,\pi)$ is an angle variable in the poloidal direction, and $\zeta \in [0, 2\,\pi)$ is an angle variable in the toroidal direction. Its covariant metric tensor is expressed as g_{ij}, its contravariant metric tensor g^{ij}, and its jacobian $\sqrt{g}$. MFCS is suitable for describing equilibrium configuration of plasmas, since it is constructed based on the profile of equilibrium magnetic field. The latter is the local orthogonal coordinate system (LOCS) $(\xi_1^{\mathrm{L}}, \xi_2^{\mathrm{L}}, \xi_3^{\mathrm{L}}) = (r, \wedge, \|)$, where r indicates the radial direction and its unit basis vector is defined as $\mathbf{e}_r \equiv \nabla\rho/|\nabla\rho|$, $\|$ indicates the parallel direction to the magnetic field $\mathbf{B}$ and its basis vector is $\mathbf{e}_\| \equiv \mathbf{B}/B$, and $\wedge$ indicates the direction perpendicular to both $\mathbf{e}_r$ and $\mathbf{e}_\|$ and its unit basis vector is $\mathbf{e}_\wedge \equiv \mathbf{e}_\| \times \mathbf{e}_\rho$. LOCS is employed to describe Braginskii's equations, since it describes the behavior of magnetized plasmas in a simplified form.

For compatibility with the neoclassical transport theory, three components of vector quantities are taken as $(\xi_1^{\mathrm{N}}, \xi_2^{\mathrm{N}}, \xi_3^{\mathrm{N}}) = (\rho, \|, \zeta)$ which indicates the radial direction, the field line direction, and toroidal direction respectively, $(\mathbf{e}^{\xi_1^{\mathrm{N}}}, \mathbf{e}^{\xi_2^{\mathrm{N}}}, \mathbf{e}^{\xi_3^{\mathrm{N}}}) = (\nabla\rho, \mathbf{e}_\|, \nabla\zeta)$. In the present study, these three components are named the neoclassical theory oriented components (NOCs).

2.2 Assumptions

In the present study, the following four assumptions have been made to derive the transport equations. The first is that the plasma has toroidal axisymmetry, which means that all physical quantities are independent of the toroidal angle variables. The second is that the quantities related to MHD equilibrium depend only on the flux label 'ρ'; the poloidal flux function ψ, the toroidal flux function ψ_t, the toroidal

current function I, the electrostatic potential ϕ, the total plasma pressure p, and the rotational transform ι. This assumption makes it possible to reduce the magnetic equilibrium problem to two-dimensional. The third is that phenomena with the Alfvén time scale are much faster than the relaxation process such as diffusion of magnetic field and transport phenomena, which implies that the MHD equilibrium is attained much faster than the relaxation processes. Finally, the fourth is that the time derivatives of basis vectors are small enough to be ignored for simplicity when we take the time derivative of vector quantities.

2.3 Braginskii's Equations

Braginskii's equations [4] describe the time evolutions of particle densities n_a, velocities $\mathbf{u}_a$, and pressures p_a of species a in weakly collisional two-fluid plasmas ($\tau_a|\Omega_a| \gg 1$), where τ_a is the collision time and Ω_a is the cyclotron frequency. Braginskii's equations consist of equations of continuity, equations of motion, and equations of energy for electron and ions respectively. The equation of continuity can be written as

$$\frac{\partial n_a}{\partial t} = \nabla \cdot (n_a \mathbf{u}_a) + S_a \tag{1}$$

where n_a is the density of particle, $\mathbf{u}_a$ is the flow velocity, and S_a is the source of particle. The equation of motion is expressed as

$$\frac{\partial}{\partial t}(m_a n_a \mathbf{u}_a) + \nabla \cdot (m_a n_a \mathbf{u}_a \mathbf{u}_a) = -\nabla p_a - \nabla \cdot \vec{\pi}_a + e_a n_a (\mathbf{E} + \mathbf{u}_a \times \mathbf{B}) + \mathbf{R}_a + m_a S_a \mathbf{u}_a \tag{2}$$

where m_a is the mass of particle, p_a is the isotropic component of pressure, $\vec{\pi}_a$ is the anisotropic component of pressure, e_a is the charge of particle, $\mathbf{E}$ is the electric field, and $\mathbf{R}_a$ is the momentum exchange term. The equation of energy transport is given by

$$\frac{\partial}{\partial t}\left(\frac{3}{2} p_a\right) + \nabla \cdot \left(\mathbf{q}_a + \frac{5}{2} p_a \mathbf{u}_a\right) = -\vec{\pi}_a \cdot \nabla \cdot \mathbf{u}_a + \mathbf{u}_a \cdot \nabla p_a + Q_a + S_{p_a} \tag{3}$$

where $\mathbf{q}_a$ is the heat flux, Q_a is the energy exchange term, $S_{p_a} \equiv S_{E_a} - \frac{1}{2} m_a u_a^2 S_a$, and S_{E_a} is the source of energy. In the strongly magnetized limit ($\tau_a|\Omega_a| \to \infty$), the momentum exchange term $\mathbf{R}_a$, the heat flux $\mathbf{q}_a$, and the energy exchange term Q_a can be written as follows respectively,

$$\mathbf{R}_a = \pm\left\{-\frac{m_e n_e}{\tau_e}\left(0.51\,\mathbf{u}_\parallel + \mathbf{u}_\perp\right) - 0.71 n_e \nabla_\parallel T_e + \frac{3}{2}\frac{n_e}{\tau_e \Omega_e}\nabla_\wedge T_e\right\} \tag{4}$$

$$\mathbf{q}_a = \mathbf{q}_{T_a} + \mathbf{q}_{u_a} \tag{5}$$

$$\mathbf{q}_{T_a} = -n_a \chi_{a\parallel}\nabla_\parallel T_a - n_a \chi_{a\wedge}\nabla_\wedge T_a - n_a \chi_{a\perp}\nabla_\perp T_a \tag{6}$$

$$\mathbf{q}_{u_e} = 0.71 n_e T_e\,\mathbf{u}_\parallel - \frac{3}{2}\frac{n_e T_e}{\tau_e \Omega_e}\,\mathbf{u}_\wedge, \qquad \mathbf{q}_{u_i} = \mathbf{0} \tag{7}$$

$$Q_e = -\,\mathbf{R}_e \cdot \mathbf{u} - Q_i, \qquad Q_i = \frac{3 n_e m_e}{m_i \tau_e}(T_e - T_i)$$

$$\nabla_\parallel \equiv \mathbf{e}_\parallel\,\mathbf{e}_\parallel \cdot \nabla, \qquad \nabla_\wedge \equiv \mathbf{e}_\parallel \times \nabla \tag{8}$$

where $\mathbf{u} \equiv \mathbf{u}_e - \mathbf{u}_i$ is the relative flow velocity, $\chi_{a\perp}$, $\chi_{a\wedge}$, and $\chi_{a\parallel}$ are the thermal diffusivity in the perpendicular direction, the diamagnetic direction, and the parallel direction respectively. The upper sign of double sign indicates equation for electron and the lower for ion. In the next section, the transport equations with poloidal angle dependence are derived from these equations.

3 Derivation of Transport Equations

The transport equations consist of the equation for particle density, momentum, and energy for both electron and ion in MFCS. The equation for particle density is expressed in the same form as (1)

$$\frac{\partial n_a}{\partial t} + \nabla \cdot (n_a\,\mathbf{u}_a) = S_a \tag{9}$$

The equation for momentum is derived from (2), though the different coordinate system is used. The neoclassical viscosity tensor [3] which is driven by the inhomogeneous magnetic field intensity is expressed as

$$\vec{\pi}_a \equiv 3\left(\mu_{a1}^{\mathrm{neo}}\hat{u}_{a\chi} + \mu_{a2}^{\mathrm{neo}}\frac{2\hat{q}_{a\chi}}{5p_a}\right)\nabla_\parallel B\left(\frac{1}{3}\overleftrightarrow{I} - \mathbf{e}_\parallel\,\mathbf{e}_\parallel\right)$$

where μ_{a1}^{neo} and μ_{a2}^{neo} are the neoclassical viscosity coefficients, $\hat{u}_{a\chi} \equiv \mathbf{u}_a \cdot \nabla\chi/\mathbf{B}\cdot\nabla\chi$ and $\hat{q}_{a\chi} \equiv \mathbf{q}_a \cdot \nabla\chi/\mathbf{B}\cdot\nabla\chi$. In the small gyro-radius limit, $\rho_a/L \ll 1$, μ_{a1}^{neo} is reduced to the Braginskii's parallel viscosity η_a^{Bra} and μ_{a2}^{neo} vanishes. Since the neoclassical viscosity tensor is composed of the unit tensor $\overleftrightarrow{I}$ and the dyadic $\mathbf{e}_\parallel\mathbf{e}_\parallel$, the divergence of the neoclassical viscosity tensor $\nabla \cdot \vec{\pi}_a$ can be written as

$$\nabla \cdot \vec{\pi}_a = N_a^{\mathrm{neo}} \nabla_{\|} \ln B + \frac{1}{3} \nabla N_a^{\mathrm{neo}} - \nabla_{\|} N_a^{\mathrm{neo}} - N_a^{\mathrm{neo}} \kappa \tag{10}$$

$$N_a^{\mathrm{neo}} \equiv 3\eta_a^{\mathrm{Bra}} \mathcal{T}^{2i} u_a^{\xi_i^{\mathrm{N}}} \frac{\partial \ln B}{\partial \chi} \tag{11}$$

where, $\mathcal{T}^{ij} \equiv \mathbf{e}_{\xi_i} \cdot \mathbf{e}^{\xi_j^{\mathrm{N}}}$ is the transformation matrix from MFCS to NOCs, and $\kappa \equiv \mathbf{e}_{\|} \times \nabla \mathbf{e}_{\|} = -\mathbf{e}_{\|} \times (\nabla \times \mathbf{e}_{\|})$ is the curvature vector of the magnetic field.

Substituting (10) into (2) and taking dot product of (2) and $\mathbf{e}^{\xi_i^{\mathrm{N}}}$, we obtain equations for momentum in each direction of NOCs. The force balance in the radial and the toroidal directions is assumed in the transport time scale. First, taking the dot product of (2) and $\nabla \rho$, we obtain force balance equation in the radial direction

$$\begin{aligned} 0 = &- F_a^{\mathrm{kin},1} - \sum_{i=1}^{3} g^{1i} \frac{\partial p_a}{\partial \xi_i} - \sum_{i=1}^{3} \frac{1}{3} g^{1i} \frac{\partial N_a^{\mathrm{neo}}}{\partial \xi_i} + N_a^{\mathrm{neo}} \kappa^{\rho} - g^{11} e_a n_a \frac{\partial \phi}{\partial \rho} \\ &+ \sum_{i=1}^{3} C_a^{\mathrm{Lor},i} n_a u_a^{\xi_i^{\mathrm{N}}} \mp \frac{3}{2} \frac{\mu^2{}_2 I}{\Omega_a \tau_a \psi'} n_e \frac{\partial T_e}{\partial \chi} + m_a S_a u_a^{\rho} \end{aligned} \tag{12}$$

where $\mu^i{}_p \equiv \nabla \xi_i \cdot \mathbf{e}_{\xi_p^{\mathrm{L}}}$ is the transformation matrix from the LOCS to MFCS. In (12), $F_a^{\mathrm{kin},i}$ is the contravariant component of kinetic force vector in MFCS and expressed by

$$F_a^{\mathrm{kin},i} \equiv \sum_{j,k,l,m=1}^{3} \left[\frac{1}{\sqrt{g}} \frac{\partial}{\partial \xi_j} \left(\sqrt{g} \mathrm{T}^{jikl} m_a n_a u_a^{\xi_k^{\mathrm{N}}} u_a^{\xi_l^{\mathrm{N}}} \right) + \left\{ {i \atop jk} \right\} \mathrm{T}^{jklm} m_a n_a u_a^{\xi_l^{\mathrm{N}}} u_a^{\xi_m^{\mathrm{N}}} \right] \tag{13}$$

and $C_a^{\mathrm{Lor},i}$ is the coefficient of the Lorentz force term expressed by

$$C_a^{\mathrm{Lor},1} = 0, \quad C_a^{\mathrm{Lor},2} = \frac{e_a B I}{\psi'}, \quad C_a^{\mathrm{Lor},3} = -\frac{e_a B^2 R^2}{\psi'} \tag{14}$$

where $\mathrm{T}^{ijkl} \equiv \mathrm{T}^{ik} \mathrm{T}^{jl}$, $\left\{ {i \atop jk} \right\}$ is the Christoffel symbol of the second kind, R is the major radius, and the prime '′' indicates the ρ derivative. Second, taking dot products of (2) and $\boldsymbol{\varepsilon}\|$, we obtain the equation for momentum in the parallel direction

$$\begin{aligned} \frac{\partial}{\partial t} \left(m_a n_a u_{a\|} \right) = &- \sum_{i=1}^{3} C_a^{\mathrm{kin},i} F_a^{\mathrm{kin},i} - \mu^2{}_2 \frac{\partial p_a}{\partial \chi} - \mu^2{}_2 N_a^{\mathrm{neo}} \frac{\partial \ln B}{\partial \chi} + \frac{2}{3} \mu^2{}_2 \frac{\partial N_a^{\mathrm{neo}}}{\partial \chi} \\ &+ \mu^2{}_2 e_a n_a \frac{\partial \phi}{\partial \chi} \mp \frac{m_e n_e}{\tau_e} \left(u_{e\|} - u_{i\|} \right) \mp 0.71 \mu^2{}_2 n_e \frac{\partial T_e}{\partial \chi} + m_a S_a u_{a\|} \end{aligned} \tag{15}$$

where $C_a^{\mathrm{kin},i}$ is the coefficient of kinetic stress force in each direction defined as

$$C_a^{\mathrm{kin},1} = \frac{\psi' g_{21}}{\sqrt{g}B}, \quad C_a^{\mathrm{kin},2} = \frac{\psi' g_{22}}{\sqrt{g}B}, \quad C_a^{\mathrm{kin},3} = \frac{I}{B} \tag{16}$$

Finally taking the dot product of (2) and $\nabla\zeta$, we obtain the equation for momentum in the toroidal direction

$$\begin{aligned} 0 = &- F_a^{\mathrm{kin},3} - \mu^3{}_2\mu^2{}_2 N_a^{\mathrm{neo}} \frac{\partial \ln B}{\partial \chi} + \mu^3{}_2\mu^2{}_2 \frac{\partial N_a^{\mathrm{neo}}}{\partial \chi} + N_a^{\mathrm{neo}} \kappa^\zeta + \frac{e_a \psi'}{R^2} n_a u_a^\rho \\ &\mp \frac{m_e n_e}{\tau_e} \left\{ \left(u_e^\zeta - u_i^\zeta \right) - 0.49 \left(u_{e\|} - u_{i\|} \right) \right\} \\ &\mp \left[0.71 \mu^3{}_2\mu^2{}_2 n_e \frac{\partial T_e}{\partial \chi} + \sum_{i=1}^{3} \frac{3}{2} \frac{\psi' g^{33} g^{1i}}{\Omega_e \tau_e} n_e \frac{\partial T_e}{\partial \xi_i} \right] + m_a S_a u_a^\zeta \end{aligned} \tag{17}$$

The equation for energy is obtained by transforming (3) into the advection–diffusion form

$$\frac{3}{2} \frac{\partial p_a}{\partial t} = -\nabla \cdot \left(p_a \, \mathbf{u}_{p_a} - n_a \vec{\chi}_a \cdot \nabla T_a \right) + Q_{p_a} \tag{18}$$

where $\mathbf{u}_{p_a} \equiv \frac{5}{2}\mathbf{u}_a + p_a^{-1}\mathbf{q}_{u_a}$ is the energy flow velocity, $Q_{p_a} \equiv \frac{3}{2} T_a S_a + \mathbf{u}_a \cdot \nabla p_a - \vec{\pi}_a \cdot \nabla \cdot \mathbf{u}_a + Q_a$ the energy source, and $\vec{\chi}_a$ the diffusion tensor in MFCS given by

$$\chi_a^{ij} = \chi_{a\perp} \mu^i{}_1 \mu^j{}_1 + \chi_{a\perp} \mu^i{}_2 \mu^j{}_2 + \chi_{a\|} \mu^i{}_3 \mu^j{}_3 + \chi_{a\wedge} \left(\mu^i{}_2 \mu^j{}_1 - \mu^i{}_1 \mu^j{}_2 \right) \tag{19}$$

4 Conclusion

Equations required for two-dimensional transport modeling for tokamak plasmas have been derived for integrated analysis of both core and peripheral region. Transport equations (9), (12), (15), (17), and (18) describes the time evolution of density, parallel flow and temperature in MFCS and reduced to two-dimensional with toroidal axisymmetry. These equations include the neoclassical viscosity force more consistently than the previous formulations [1, 2] and will make it possible to evaluate the poloidal dependence of the heating efficiency in the core region and more consistently describe the interaction between the core and the peripheral plasma.

Acknowledgments This work is supported by Grant-in-Aid for Science Research (S) (20226017) from JSPS and partly by G-COE program (J-051) from MEXT.

References

1. Simizu K et al (2003) Simulation of divertor detachment characteristics in JT-60 with superconducting coils. J Nucl Mater 313–316:1277–1281
2. Rozhansky VA et al (2001) Simulation of tokamak edge plasma including self-consistent electric fields. Nucl Fusion 41:387–401
3. Hirshman SP, Sigmar DJ (1981) Neoclassical transport of impurities in tokamak plasmas. Nucl Fusion 21(9):1079
4. Braginskii SI (1965) Transport processes in a plasma. In: Leontovich MA (ed) Reviews of plasma physics, vol 1. Consultants Bureau, New York, p 205

Current Status of the Non-destructive Assay for ^{235}U and ^{239}Pu Toward More Secure Nuclear Power

Mohamed Omer, Mahmoud A. Bakr, Ryota Kinjo, Yong Woon Choi, Kyohei Yoshida, Naoki Kimura, Keiichi Ishida, Takuya Komai, Kyohei Shimahashi, Hidekazu Imon, Marie Shibata, Taro Sonobe, Heishun Zen, Toshitada Hori, Toshiteru Kii, Kai Masuda, Hideaki Ohgaki, Ryoichi Hajima, and Takehito Hayakawa

Abstract Nuclear energy still represents one important option for energy sources that do not emit CO_2 even after the Fukushima accident. Right now, it constitutes about 16–17% of the world's total power supply, and is expected to increase and spread significantly by the coming three decades. Special nuclear materials (SNM), mainly ^{235}U and ^{239}Pu, used as fuels for nuclear power plants are required to be fully controlled and accounted by the IAEA. Non-destructive assay (NDA) for screening SNM is an important for countering terrorism as well as accountability purposes, because it is difficult to detect hidden SNM. NDA methods are mainly classified into two categories in terms of radiation detection; neutron-spectrometry methods and gamma-spectroscopy methods. This paper is devoted to discuss the current status of the NDA different techniques and assess usage of nuclear resonance fluorescence (NRF) technique in combination with quasi-monochromatic gamma-rays generated by laser Compton backscattering as a promising one.

Keywords Laser compton scattering • Non-destructive assay • Nuclear energy • Nuclear resonance fluorescence • Special nuclear materials

M. Omer (✉) • M.A. Bakr • R. Kinjo • Y.W. Choi • K. Yoshida • N. Kimura • K. Ishida • T. Komai • K. Shimahashi • H. Imon • M. Shibata • T. Sonobe • H. Zen • T. Hori • T. Kii • K. Masuda • H. Ohgaki
Institute of Advanced Energy, Kyoto University, Gokasho, Uji, Kyoto 611-0011, Japan
e-mail: omer_sci@iae.kyoto-u.ac.jp

R. Hajima • T. Hayakawa
Japan Atomic Energy Agency, Tokai, Ibaraki, Japan

T. Yao (ed.), *Zero-Carbon Energy Kyoto 2011*, Green Energy and Technology,
DOI 10.1007/978-4-431-54067-0_38,

1 Introduction

Nuclear power is growing up and is expected to constitute 30% (more than 500 nuclear power plant) of the world power supply by the coming three decades. More than 30 counties are now using nuclear power [1]. This implies much security consideration especially to counter terrorism threats through the transportation and accounting the storage of spent nuclear fuels. Special nuclear materials (SNMs) such as uranium-235 and plutonium-239 are the cornerstones in nuclear energy whether they are working (fuel rods) or spent (waste fuel) materials. These materials are required to be fully controlled and assessed by the international atomic energy agency (IAEA). Screening of SNMs by means of non-destructive assay (NDA) techniques was identified by many researchers, however; more works are required for improving detection of SNMs. The most important technical issues limiting NDA are interrogation source and detection system. According to interrogation source, NDAs are classified into two categories, fission based and fluorescence based methods. On the other hand, according to radiation detection system NDAs are classified to neutron and gamma spectrometry. In the current paper, several NDA techniques are discussed in the light of their interrogation sources, mechanisms, and limitations as well as possibility combinations between/among them for hybrid NDA methods.

2 NDA Methods

In this section, most common fission based NDAs are reviewed. Furthermore, fluorescence based NDAs, basically NRF and XRF, are discussed.

2.1 Fission Based NDAs

2.1.1 Delayed Neutrons Analysis (DNA)

Delayed neutrons analysis (DNA) technique is one of the fission based NDA methodologies. It is relatively old one, since it was the basis of shufflers, instruments that assay nuclear materials non-destructively by irradiating them to ^{252}Cf neutron source and detecting their fissile contents. Shufflers were firstly conceived in 1969 [2]. The mechanism of DNA is as follows, after a neutron induced fission occurs, two nuclides are produced with a small number of prompt neutrons. Seconds to minutes later, neutrons are emitted by the fission products. These neutrons are called delayed neutrons while their emitters are called precursors. About 1.6% of the fission neutrons from ^{235}U are delayed, but only about 0.6% of ^{239}Pu's fission neutrons are delayed [2]. SNM is quantified by

Table 1 Delayed neutron parameters for ^{235}U and ^{239}Pu [2]

Group #	$T_{1/2}$ (s)		n_{DN} (neutron per fission)	
	^{235}U	^{239}Pu	^{235}U	^{239}Pu
1	55.72	54.28	5.20×10^{-4}	2.10×10^{-4}
2	22.72	23.04	3.46×10^{-3}	1.82×10^{-3}
3	6.22	5.60	3.10×10^{-3}	1.29×10^{-3}
4	2.30	2.13	6.24×10^{-3}	1.99×10^{-3}
5	0.61	0.62	1.82×10^{-3}	5.20×10^{-4}
6	0.23	0.28	6.60×10^{-4}	2.70×10^{-4}

measuring the content of corresponding precursors. Precursors are divided to six groups according to their time decay. Total population P(t) of precursors depends on time *t* decay and number of delayed neutrons in each group as shown in equation (1) [2].

$$P(t) = \sum_{j=1}^{6} n_{DN} e^{-t/T_{1/2}} \tag{1}$$

where n_{DN} is the average number of delayed neutrons and $T_{1/2}$ is the half life time. Table 1 shows the delayed neutron parameters for ^{235}U and ^{239}Pu. Therefore, the signature of an SNM is the properties of its precursors.

2.1.2 Differential Die-Away (DDA)

In DDA technique the object under inspection is irradiated to burst of neutrons generated by deuteron–tritium (DT) neutron source, which is likely producing 14 MeV neutrons. The key issue of DDA is the difference of neutrons' kinetics in fissile material and in non-fissile ones. If the interrogated object does not have a fissile material, the neutrons coming from the generator are thermalized (die-away) or decayed through the shielding and no fast neutrons are detected up to the next pulse. But if a fissile material exists, it is induced by thermalized neutrons and fast neutrons are detected few microseconds later. The thermal neutron population inside of the medium will rise quickly, on a sub-microsecond time-scale, due to the thermalization of the fast neutrons. Then as the thermal neutrons are either absorbed or escape, the population will decrease exponentially as shown in Fig. 1. The time constant for thermal neutron decay is determined by the physical size and the absorption cross-section of the medium, and is typically a few orders of magnitude slower than the fast neutrons, with a decay time on the order of hundreds of microseconds [3, 4].

2.1.3 Delayed Gammas (DG)

DG is an NDA technique in which the object to be tested is interrogated by neutron or bremsstrahlung (photo fission) source. The fission produces two elements. These fragments are going to be the starting point of a decay chain. In this chain, unstable

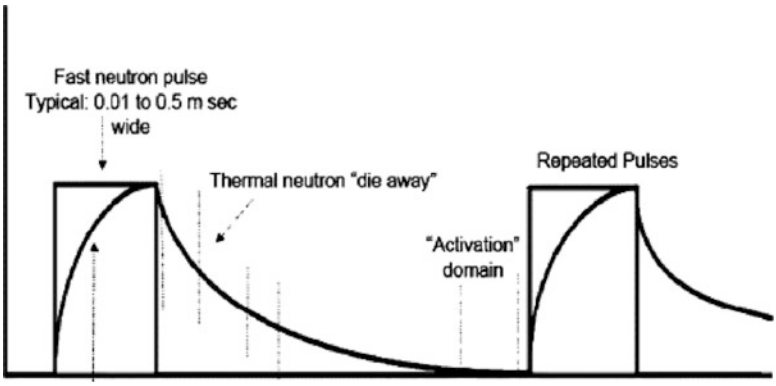

Fig. 1 Time line of neutron die-away measurement [5]

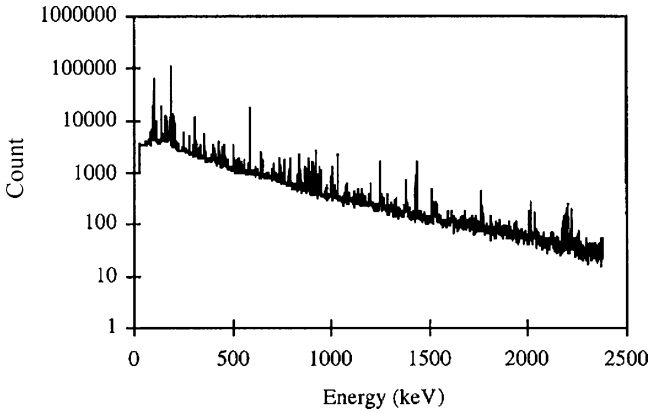

Fig. 2 Delayed gamma spectrum of an irradiated uranium-235 sample enriched to 93% [6]

daughters of these two initial fragments will then appear. Fission products are in excess of neutron and will disintegrate by neutron emission or beta emission. Very often, this disintegration can be spotted together with gamma emission. Still, the probability of fragment production is connected to three parameters: nucleus target, particle type and its energy. The delayed gamma spectra are rich and complex (Fig. 2). This complexity can be notably seen during the first few minutes following the end of the irradiation period [6]. DG depends on the fact that the distribution of fission fragments produced when these isotopes fission is unique.

2.1.4 Neutron Multiplicity Analysis (NMA)

NMA is an interrogation NDA technique that is mainly based on the distribution of number of neutrons emitted by an SNM during fission. The number of neutrons emitted in spontaneous fission can vary from zero to six or more. The process is

random, or statistical, in nature, and the distribution of the number of emitted neutrons is called the neutron multiplicity distribution [7].

Neutron multiplicity counting is one way to get a third quantity. The average number of neutrons emitted by a spontaneous fission in plutonium is approximately two, and the average number emitted by an induced fission in plutonium is approximately three. Multiplicity counting can be used to determine the neutron multiplication because the number of neutrons emitted in a burst following a spontaneous fission increases with increasing multiplication. The three measured quantities used for multiplicity counting are called the singles, doubles, and triples counting rates. The singles and doubles rates are the same as the totals and coincidence rates in conventional coincidence counting. The triples rate is new and measures a higher level of correlation in the neutron pulse stream. For analysis, the singles doubles, and triples rates are expressed as functions of the ^{240}Pu spontaneous fission rate, the neutron multiplication, and the (α, n) yield. These three equations are then solved for the three unknowns; finally, the plutonium mass is determined from the ^{240}Pu mass and the isotopic composition [7]. The total mass of plutonium can be determined by the following two equations [7]:

$$^{240}\mathrm{Pu}_{\mathrm{eff}} = 2.52\,^{238}\mathrm{Pu} + {}^{240}\mathrm{Pu} + 1.68\,^{242}\mathrm{Pu}\ldots \tag{2}$$

$$^{\mathrm{Total}}\mathrm{Pu} = {}^{240}\mathrm{Pu}_{eff}/(2.52f_{238} + f_{240} + 1.68f_{242})\ldots \tag{3}$$

where f_{238}, f_{240}, and f_{242} are the fractions of the plutonium isotopes present in the sample. ^{238}Pu, ^{240}Pu and ^{242}Pu represent the isotopic composition of plutonium which can be obtained by another means such as gamma ray spectroscopy or mass spectrometry.

2.2 *Fluorescence Based NDAs*

2.2.1 X-Ray Fluorescence (XRF)

XRF is a fluorescence based NDA technique. The signature of XRF for U and Pu is shown in Table 2. The interrogation source is the gamma rays of the spent fuel. However, high-Z elements, such as uranium and plutonium, have large photoelectric cross sections for absorption of the spent fuel gamma rays. As a result the gamma-ray flux in the spent fuel will generate fluorescent X rays from uranium and plutonium. This leads to a substantial generation rate of uranium and plutonium K X rays in the 95–117 keV energy range. This technique quantifies the relative mass of uranium to plutonium in very thin exterior layer of a fuel rod.

Table 2 XRF properties of U and Pu [8]

Uranium	Energy (keV)	Plutonium	Energy (keV)
U-$K_{\alpha1}$	98.43	Pu-$K_{\alpha1}$	103.73
U-$K_{\alpha2}$	94.67	Pu-$K_{\alpha2}$	99.53
U-$K_{\beta1}$	111.30	Pu-$K_{\beta1}$	117.23
U-$K_{\beta3}$	110.42	Pu-$K_{\beta3}$	116.24
U-$K_{\beta2}$	114.4	Pu-$K_{\beta2}$	120.54

Relative excitation probabilities for creating Pu and/or K rays through photo and electron interactions can lead to quantify the relative mass [3, 8].

For example, photons with energies greater than the K absorption edge of Pu 121.8 keV the Pu Xray production rate will be enhanced compared to U because of the higher photoelectric cross section for Pu. With photon energies greater than 122 keV the ratio of photoelectric absorption cross sections is close to (ZPu/ZU) = (94/92) = 1.09. From the K edge of U at 115.6 to 121.8 keV only U K-rays will be generated. The uncertainty of XRF is measured to be less than 5% [8].

2.2.2 Nuclear Resonance Fluorescence (NRF)

NRF is an active interrogation fluorescence based technique. NRF is a phenomenon in which a high-energy photon excites a nucleus to a higher level that subsequently decays rapidly (in picoseconds) to a lower lying level by emitting a gamma ray of energy equal to the energy difference between the resonance level and lower-lying level. This process is analogous to atomic fluorescence where photons excite an atomic-bound electron to a higher energy level. The resonant energies in NRF are in the 1–10 MeV range. As a result, the attenuation pathlengths for NRF photons are much longer than x-ray photons and thermal neutrons used in other assay techniques, allowing the technique to work through many inches of lead or steel or several feet of hydrogenous material [9]. Since it is not based on fission interrogation, NRF may be able to determine elemental SNMs independently.

A strong gamma-ray beam is required for NRF method. However a conventional gamma-ray source or bremsstrahlung cannot provide a high signal-to-noise ratio, because it has a high energy spread which does not correspond to NRF levels and becomes background noise. Recently, proposed high intensity laser Compton backscattering (LCS) gamma ray source for NDA (Fig. 3) represents substantial development for nuclear material management [10–12]. This LCS gamma source has many merits over other interrogation sources. It is quasi-monochromatic, high intensity and tunability. Therefore, it is excellent for SNM screening by using NRF measurements in coupling with LCS gamma source. Interrogation signature of ^{235}U and ^{239}Pu are shown in Table 3. These signatures can investigate the isotopic composition of the inspected material, however, the flux of gamma ray source is not sufficient to realize rapid identification.

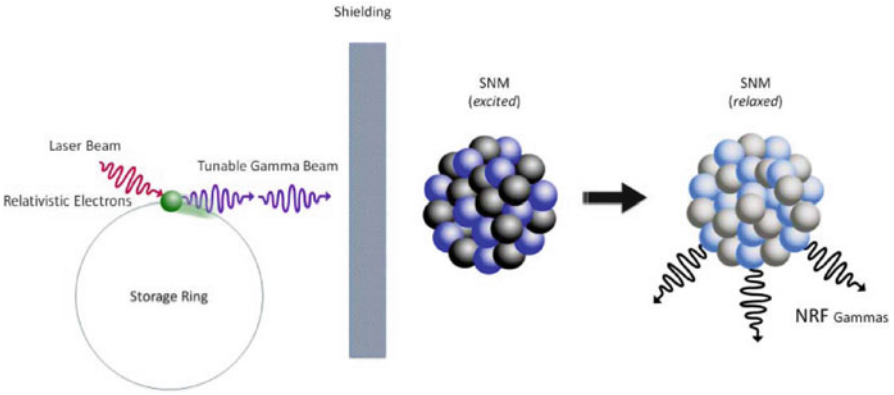

Fig. 3 NRF interrogation system with LCS

Table 3 NRF properties of U and Pu [9]

SNM	NRF excitation energies (keV)			
^{235}U	1656.23	1733.60	1862.31	2006.19
^{239}Pu	2040.25	2143.56	2423.48	2471.07

3 Discussion

Based on the signature, interrogation source and detection system, all NDA methods have some drawbacks that limit fast, individual and independent inspection of SNM. Fission base techniques provide fast recognition of the SNM existence inside a cargo; however, they cannot provide a reliable level of accuracy concerning SNM composition. Fluorescence based NDAs can be represented as an intrinsic interrogation method because none of SNM is transformed, however; the low flux of interrogation source lead to slow inspection procedures.

Interrogation source, whether neutron or gamma ray sources, need much improvement to facilitate NDA. For DNA, high intensity neutron source is needed, typically 10^{12}–10^{13} n/s. In general high flux neutron causes large amount of background radiation as well as makes the shielding of the inspection system difficult. Another limitation exist for both DNA and DDA, that is they rely on thermal neutrons having very small energies makes the system sometimes blind toward very thick and absorbing shielding. Similar effect appears dealing with DG and XRF, since the interrogation signatures have very low gamma ray energies, however; recently Campbell et al. reported high energy delayed gamma interrogation method [13]. Providing convenient electronics and timing facilities, NMA is good candidate for accurate determination of SNM's mass. A drawback, that it needs an auxiliary tool for isotopic identification. This can be provided by NRF, which can identify isotopes even with thick shielding [9, 10]. Currently, however, the LCS gamma source can only generate low flux gamma rays.

Table 4 Properties of NDA methods

NDA	Signature	Merits	Demerits
DNA	Delayed neutrons of fission precursors	Unique signature	High background and weak penetration
DDA	Thermal neutrons	Fast recognition of SNM	Weak penetration
DG	Gamma photons from fission products	Unique signature	Weak penetration
NMA	Distribution of fission neutrons	Well identified relative masses	High cost for coincidence measurements
XRF	Characteristic atomic levels	Elemental identification	Weak penetration
NRF	Characteristic nuclear levels	Isotopic identification	Slow inspection

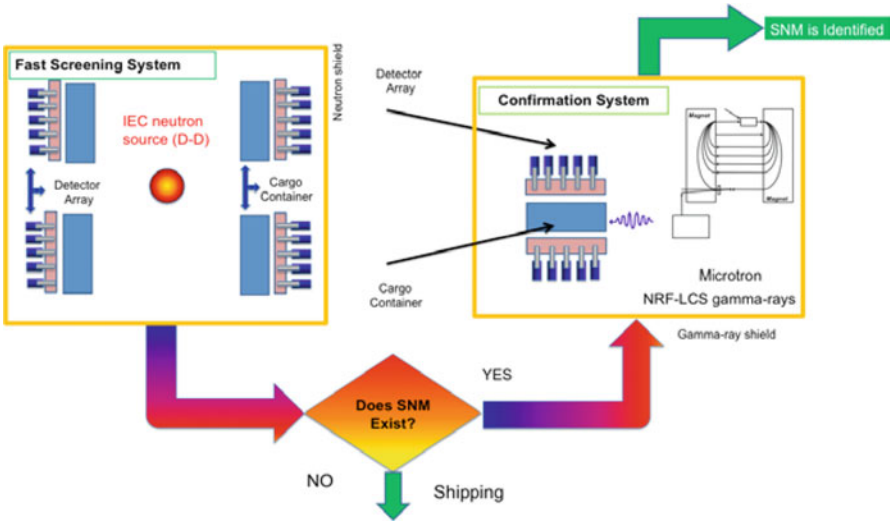

Fig. 4 SNM detection system with neutron/gamma concept

This method is the most recent technique among all NDAs [3], so we expect that much work can increase the intensity of LCS gamma source or to provide some molding tools to enable NRF to interrogate SNM independently. However, the LCS gamma source can only generate low flux gamma rays. Merits and demerits of different NDA methods are summarized in Table 4. Therefore we propose the SNM inspection system with neutron/gamma-ray hybrid concept (Fig. 4) [14].

The neutron from the inertial electrostatic confinement fusion source can be used for a fast pre-screening process because of the high fission material sensitivity of neutron method. The quasi-monochromatic gamma-ray beam from the laser Compton Backscattering source can be used for post-screening process for precise inspection. Nuclear resonance fluorescence method should be employed for the isotope identification because of its high selectivity and high penetration for the shielding.

4 Conclusions

We reviewed different techniques of NDA for hidden SNMs. Much research is still needed to construct a realistic inspection system. Logical combinations between two different NDAs appear in the picture. For good interrogation of SNM, hybrid DDA and NRF is suggested. DDA can be used as a very fast technique to act as a switch, i.e. to just recognize the existence of SNM. One benefit is that the fast neutrons being thermalized through the shielding can easily interrogate SNM. On the other hand, NRF can recognize the isotope composition of the SNM. This system is proposed and being tested by our group.

Acknowledgment The authors would like to thank Dr. M. Seya, JAEA, for his valuable discussions through the course of this work. The authors also would like to thank G-COE program (Energy Science in the Age of Global Worming) Kyoto University for financial support. This work is supported by Special Coordination Funds for Promoting Science and Technology in Japan (Grant No. 066).

References

1. News Staff (2011) Nuclear Power's Global Fallout, Science Magazine 331:1502–1503
2. Rinard PM (2001) Application guide to shufflers, Los Alamos National Laboratory report LA-13819-MS
3. Tobin SJ et al (2008) Determination of Pu in spent fuel with NDA—why an integrated approach? In: Institute of nuclear material management 49th annual conference, LA-UR-08-03763
4. Jordan KA et al (2008) Nucl Instrum Methods Phys Res A 589:436–444
5. Yee RM et al (2009) Thermal Neutron Die-Away Studies in a 14 MeV Neutron-Based Active Interrogation System, IEEE Trans Nucl Sci 56(3)
6. Gmar M, Capdevila JM (1999) Use of delayed gamma spectra for detection of actinides (U,Pu) by photofission, Nucl Instrum Methods Phys Res A 422:841–845
7. Ensslin N et al (1998) Application guide to neutron multiplicity counting, Los Alamos National Laboratory report LA-13422-M
8. Rudy C et al (2005) Determination of Pu in spent fuel assemblies by X-ray fluorescence, Institute of Nuclear Material Management annual conference, LA-UR-05-4283
9. Bertozzi W et al (2008) Nuclear resonance fluorescence excitations near 2 MeV in 235U and 239Pu, Phys Rev C 78:041601(R)
10. Hayakawa T et al (2010) Nondestructive assay of plutonium and minor actinide in spent fuel using nuclear resonance fluorescence with laser Compton scattering γ-rays, Nucl Instrum Methods Phys Res A 621:695–700
11. Hajima R et al (2008) Proposal of Nondestructive Radionuclide Assay Using a High-Flux Gamma-Ray Source and Nuclear Resonance Fluorescence, J Nucl Sci Tech 45(5):441–451
12. Kikuzawa N et al (2009) Nondestructive Detection of Heavily Shielded Materials by Using Nuclear Resonance Fluorescence with a Laser-Compton Scattering γ-ray Source, APEX 2:036502
13. Campbell LW et al (2011) High-Energy Delayed Gamma Spectroscopy for Spent Nuclear Fuel Assay, IEEE Trans Nucl Sci 58(1)
14. Ohgaki H et al (2010) IEEE international conference on technologies for homeland security (HST). Waltham, MA, USA, pp 525–529

The Strain Rate Effect on High-Temperature Tensile Properties of High-Cr Oxide Dispersion Strengthened Steels

Hwanil Je and Akihiko Kimura

Abstract The development of heat resistant structural materials is essential to sustain zero-emission energy for reducing greenhouse gas emission such as carbon dioxide gas by elevating operation temperature of nuclear and fossil power plants. Oxide dispersion strengthened (ODS) steels have received considerable attention because they show superior performances at high temperatures. In this research, the effect of strain rate on the deformation behavior was investigated at high-temperatures to apply it to advanced fossil and nuclear power plants. The materials used were three kinds of 15Cr-4Al-2W-ODS steels of which the other chemical compositions were slightly changed by the addition of small amount of alloying element. Steady strain rate tests (SSRT) were performed at a strain rate ranging from 1×10^{-3} to 1×10^{-6} s^{-1} in a vacuum of 2.3×10^{-3} Pa at a temperature of 773 K. The test temperature was controlled within in an error of ± 3 K. The fractured surface was observed by scanning electron microscope (SEM), and the reduction in area of the specimens was measured to investigate the effects of strain rate on the deformation and fracture mode. Tensile yield stress is remarkably dependent on the strain rate, showing a large increase with increasing strain rate, while tensile elongation is not remarkably influenced by strain rate. According to the precise observations of fractured surface, there was no strain rate effect on the fracture mode, and only ductile fracture was observed for all the specimens tested in the study. This trend was independent of material.

Keywords Fracture behavior • High-temperature deformation mode • Steady strain rate test • Strain rate effects

H. Je (✉)
Graduate School of Energy Science, Kyoto University, Gokasho, Uji, Kyoto 611-0011, Japan
e-mail: hi-je@iae.kyoto-u.ac.jp

A. Kimura
Institute of Advanced Energy, Kyoto University, Gokasho, Uji, Kyoto 611-0011, Japan

T. Yao (ed.), *Zero-Carbon Energy Kyoto 2011*, Green Energy and Technology,
DOI 10.1007/978-4-431-54067-0_39,

1 Introduction

Since the Industrial Revolution in the seventeenth century, CO_2 concentration in the atmosphere has been increased as a result of human activities, such as the burning of oil, coal and gases, as well as deforestation. Recently, global atmospheric concentration of CO_2 was about 35% higher than that before the Industrial Revolution. Nuclear power is considered to be contributing to environmental benefits with reducing CO_2 emission.

One of the critical issues towards high burn-up operation of nuclear power plant has been considered to be development of fuel clad material that can overcome the requirement of materials performance, such as low susceptibility to stress corrosion cracking (SCC) and high temperature performance. Oxide dispersion strengthened (ODS) steels have been developed for the application to fuel cladding material [1–6]. Since high-strength ODS steels are considered to be susceptible to SCC, evaluation of SCC behavior of ODS steels is important for practical application to the life-extension and the safety operation of nuclear power plants. Strain rate dependence of the fracture mode is a characteristic trend of SCC of metallic materials. Before investigating the SCC behavior in corrosion environment, such as supercritical pressurized water, strain rate dependence in a vacuum should be investigated as basal information of material behavior.

In this study, the effect of strain rate on the deformation behavior was investigated at high-temperatures in order to get fundamental data for research on the susceptibility to SCC of ODS steels and to apply it to advanced fossil and nuclear power plants.

2 Experimental

The materials used were three kinds of 15Cr-4Al-2W-ODSsteels of which the other chemical compositions were slightly changed by the addition of small amount of alloying elements. The chemical compositions were shown in Table 1. The details of the fabrication process of the ODS steels are given in the previous papers [1–3]. All of the ODS steels were finally heat treated at 1323 K for 1 h, then air-cooled. The tensile specimens with a gauge length of 5 mm, a width of 1.2 mm and a thickness of 0.45 mm were cut out from the extruded bars in the longitudinal directions. To prevent the effect of surface defect on the deformation process during the tensile test, the surface of specimens was mechanically polished using 0.25 μm alumina abrasive particles.

Table 1 Chemical compositions of ODS steels (SOC-9, SOC-14 and SOC-16) (wt%)

Material	C	Cr	W	Al	Ti	Y	O	N	Ar	Hf	Zr	Y_2O_3
SOC-9	0.03	15.42	1.85	3.8	0.1	0.28	0.16	0.004	0.0068	–	–	0.36
SOC-14	0.052	14.85	1.84	3.73	0.09	0.27	0.17	0.009	0.0061	–	0.63	0.34
SOC-16	0.043	14.54	1.93	3.01	0.13	0.28	0.17	0.006	0.0064	0.62	–	0.36

Steady strain rate tests (SSRT) were performed at a strain rate ranging from 1×10^{-3} to 1×10^{-6} s^{-1} in a vacuum of 2.3×10^{-3} Pa at a temperature of 773 K. The test temperature was controlled within in an error of ± 3 K.

The fractured surface was observed by scanning electron microscope (SEM), and the reduction in area of the tested specimens was measured to investigate the effects of strain rate on the fracture mode in inactive environment.

3 Results

3.1 Tensile Properties

Figures 1a–c show the stress-strain curves of ODS steels at 773 K in a vacuum with the different strain rate ranging from 1×10^{-3} to 1×10^{-6} s^{-1}, as a function of materials which are SOC-9, SOC-14 and SOC-16, indicating the lower the strain rate, the lower the ultimate tensile strength for all the materials used in this research at the test conditions. However, the tensile strength of all the materials is very similar at each strain rate and no strain rate dependence is observed for the steels, although the tensile elongation is different among the materials more or less at each strain rate. The yield strength of the ODS steels decreased with decreasing strain rate, as shown in Fig. 1d.

In the previous works on tensile tests at 973 K, the tensile strength of Al-added ODS steels (SOC-9) was increased by the addition of Zr (SOC-14) or Hf (SOC-16). However, in this study the tensile strength of these materials is almost same at test temperature of 773 K. At 973 K, the deformation mechanism of ferritic steels has been considered to be grain boundary sliding which accelerates creep deformation at a lower applied stress than yield stress. SOC-14 and -16 ODS steels showed a higher creep strength than SOC-9 ODS steel, which is due to the suppression of the grain boundary sliding by the precipitation of Zr or Hf carbides and oxides at grain boundaries but not strengthening.

3.2 Fracture Mode

The susceptibility of SCC can be evaluated by the observation of fracture mode change from ductile to brittle grain boundary and/or cleavage fracture and measuring reduction in area. Reduction in area after SSRT of ODS steels in a vacuum was shown in Fig. 2a. Relatively constant value from 65% to 80% was obtained without regarding to material.

Figure 2b is representative fracture surface and specimen side surface of SOC-14 which was deformed at strain rates of 1×10^{-3} and 1×10^{-6} s^{-1}. The dimple size of the fracture surface which tested at the strain rate of 1×10^{-3} s^{-1} is smaller than

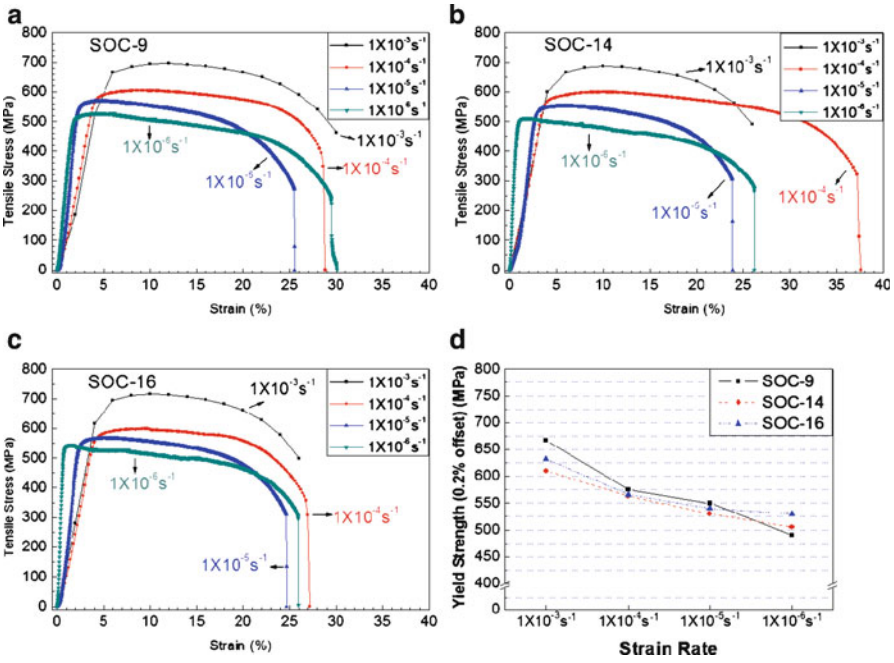

Fig. 1 Tensile test results of steady strain rate test for ODS steels at 773 K in a vacuum at different strain rates ranging from 1×10^{-3} to 1×10^{-6} s^{-1}: (**a**) SOC-9, (**b**) SOC-14, (**c**) SOC-16, and (**d**) yield stress of ODS steels as a function of strain rate

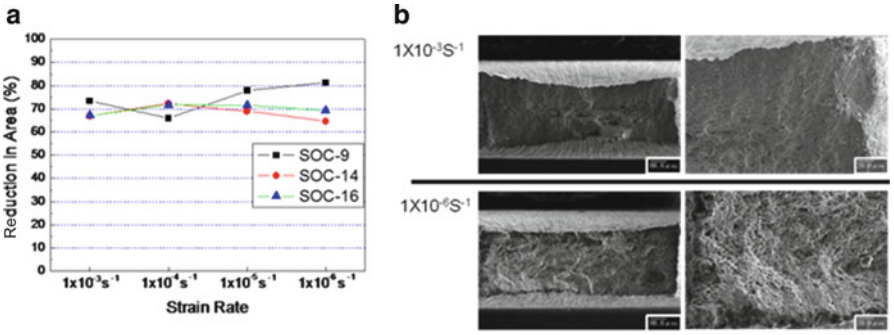

Fig. 2 Analysis of fracture mode: (**a**) Reduction in area after tensile test of the specimens, (**b**) SEM images of SOC-14 after tests at the strain rate of 1×10^{-3} and 1×10^{-6} s^{-1}

that of the fracture surface which tested at the strain rate of 1×10^{-6} s^{-1}. However, according to the result of reduction in area and the observation of fractured surface, all the specimens tested in this study exhibit ductile fracture mode, indicating high reduction in area and many dimples on the fracture surface.

4 Discussion

There is a simple relationship between the plastic strain and the dislocation density. It is based on the fact that when a dislocation moves, two atoms on sites adjacent across the plane of motion are displaced relative to each other by the Burgers vector b. With this relationship, therefore, it is well known that the strain rate ($\dot{\varepsilon}$) can be expressed by

$$\dot{\varepsilon} = \rho_m b \bar{v} \tag{1}$$

where b is Burgers vector, ρ_m is density of mobile dislocations, and $\bar{U}$ is average velocity of dislocation.

By repeating the experiment for different times and stress levels the velocity can be determined as a function of stress as shown in Fig. 3. In the range of velocity between 10^{-7} and 10^{-3} cm s^{-1}, the logarithm of the velocity varies linearly with the logarithm of the applied stress, thus

$$v \propto \left(\frac{\tau}{\tau_0}\right)^m \tag{2}$$

where ν is the velocity of dislocations, τ is the applied shear stress resolved in the slip plane, τ_0 is the shear stress for $\upsilon = 1$ cm s^{-1}, m is a constant [7]. The value of $m \approx 31$ was revealed by means of plotting from the results of SSRT for ODS steels. The dislocation velocity of ODS steels at tested conditions was very sensitive to the applied shear stress, compare to the other materials. This implies that the deformation mechanism of the ODS steels could be interpreted in terms of thermally activated dislocation motion and/or possibly grain boundary sliding, namely "dislocation mechanism".

5 Summary

In this study, the strain rate effects on high-temperature tensile properties of high-Cr ODS steels were investigated as a basal information of SCC research for ODS steels. The susceptibility of SCC is generally evaluated by SSRT at different strain rates. Before the tests in corrosive environment, the test was carried out in a vacuum to investigate strain rate effects without any corrosive environment. And the main results obtained are the following:

1. The result of SSRT in a vacuum at 773 K with the different ODS steels (SOC-9, SOC-14, SOC-16) shows that the lower the strain rate, the lower the tensile strength. However, no material dependence was shown with the tested specimens.

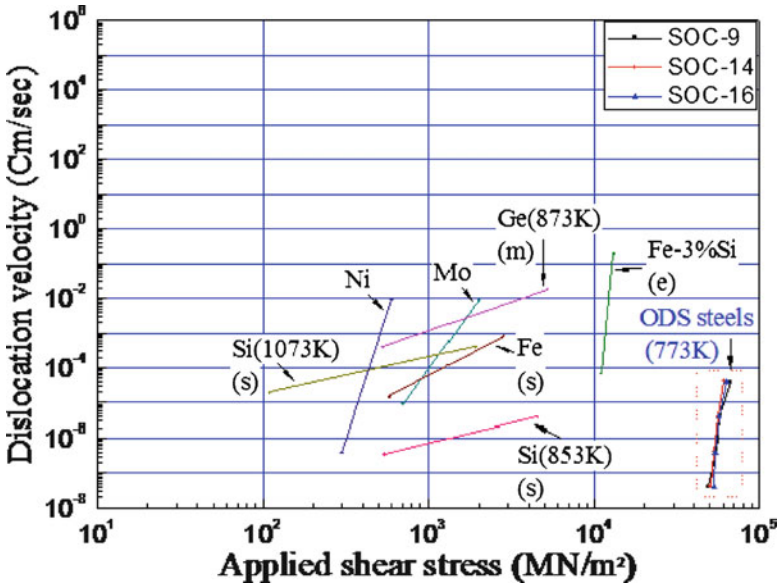

Fig. 3 The dependence of dislocation velocity on applied shear stress with various kinds of materials and ODS steels

2. Tensile yield stress is remarkably dependent on the strain rate, showing a large increase with increasing strain rate, while tensile elongation is not remarkably influenced by strain rate.
3. Reduction in area after SSRT in a vacuum at 773 K was relatively constant, regardless of strain rate.
4. According to the precise observations of fractured surface, there was no strain rate effect on the fracture mode, and only ductile fracture was observed for all the specimens tested in the study. This trend was independent of material.
5. The *m* value in (2) for the ODS steels was 31 that is very large, implying that the deformation mechanism is related with thermally-activated dislocation motion and/or possibly grain boundary sliding.

Acknowledgement The authors were grateful for the support of the Ministry of Education, Culture, Sports, Science and Technology of Japan via "Energy Science in the Age of Global Warming" of Global Center of Excellence (G-COE) program (J-051).

References

1. Kimura A, Cho HS, Lee JS, Kasada R, Ukai S, Fujiwara M (2004) R&D of oxide dispersion strengthened steels for high burn-up fuel claddings. Proceedings of ICAPP'04. Paper 4009:2070–2076

2. Takaya S, Furukawa T, Inoue M, Fujisawa T, Okuda T, Abe F, Ohnuki S, Kimura A (2008) Corrosion resistance of Al-alloying high Cr-ODS steels in stagnant lead-bismuth. J Nucl Mater 83:1471–1476
3. Iwata NY, Kasada R, Kimura A, Okuda T, Inoue M, Abe F, Ukai S, Fujisawa T (2009) Characterization of mechanically-alloyed powders for high-Cr oxide dispersion strengthened ferritic steel. ISIJ Int 49(12):914–919
4. Takaya S, Furukawa T, Aoto K, Müller G, Weisenburger A, Heinzel A, Inoue M, Okuda T, Abe F, Ohnuki S, Fujisawa T, Kimura A (2009) Corrosion behavior of Al-alloying high Cr-ODS steels in lead-bismuth eutectic. J Nucl Mater 386–388:507–510
5. Chen J, Pouchon MA, Kimura A, Jung P, Hoffelner W (2009) Irradiation creep and microstructural changes in an advanced ODS ferritic steel during helium implantation under stress. J Nucl Mater 386–388:143–146
6. Oh S, Lee JS, Jang C, Kimura A (2009) Irradiation hardening and embrittlement in high-Cr oxide dispersion strengthened steels. J Nucl Mater 386–388:503–506
7. Hull D, Bacon DJ (2001) Introduction to dislocations, 4th edn., pp 49–59

Development of Composite Material with Directional Property for High Thermal Conductivity for Divertor

Sunghun Kim, Hanki Yoon, Kazuyuki Noborio, and Satoshi Konishi

Abstract The divertor is one of the high heat flux (HHF) components of fusion reactor which has to withstand a high surface heat flux. Tungsten has high thermal conductivity and expected to transfer heat, substrate of the diverter structure that carries coolant in it has lower thermal conductivity. The high temperature divertor will be needed for DEMO to efficiently use heat. In order to satisfy the requirements, multi-layer structure would be a possible option for HHF components. This concept will have a difficulty due to the different thermal conductivity and thermal stress because of high temperature gradient. To solve the above problem, C_f/SiC composite is first studied as a model material. Carbon fiber that has high thermal conductivity placed perpendicular to the flow of the coolant in C_f/SiC composite is expected to improve the directional thermal conductivity. C_f/SiC composite was evaluated in terms of mechanical properties and micro structures as structural materials. Thermal conductivity of C_f/SiC composite will be evaluated as the next research.

Keywords C-SiC • Divertor • Heat flux • Thermal conductivity • Thermal stress

S. Kim (✉)
Graduate School of Energy Science, Kyoto University, Gokasho, Uji, Kyoto 611-0011, Japan
e-mail: sunghun_kim@iae.kyoto-u.ac.jp

H. Yoon
Department of Mechanical Engineering, Dong-Eui University, Busan, South Korea

K. Noborio • S. Konishi
Institute of Advanced Science, Kyoto University, Gokasho, Uji, Kyoto 611-0011, Japan

T. Yao (ed.), *Zero-Carbon Energy Kyoto 2011*, Green Energy and Technology,
DOI 10.1007/978-4-431-54067-0_40,

1 Introduction

One of the most challenging components of the ITER machine is the "divertor" which has to absorb extremely high heat-fluxes and to keep the plasma impurity at a reasonable low level. It is located at the bottom of the plasma chamber [1].

The development of suitable technologies for the manufacturing of high heat-flux components was one of the major efforts of the ITER and DEMO projects.

In this study, C_f/SiC composite is studied as a model material that has previously been fabricated. Specially, carbon fiber that has high thermal conductivity placed perpendicular to the flow of the coolant in C_f/SiC composite is expected to improve the directional thermal conductivity as shown in Fig. 1 [2, 3]. Monolithic SiC or C_f/SiC composite was made by hot-pressing method, and then monolithic SiC or C_f/SiC composite was evaluated in terms of mechanical properties and microstructures. Thermal conductivity of C_f/SiC composite will be evaluated as the next research.

2 Experimental Procedure

The main powder used SiC which has the average particle size of 50 nm. Also, Al_2O_3:Y_2O_3:SiO_2 composition as sintering additives were Al_2O_3 + Y_2O_3 = 10 wt % (Al_2O_3:Y_2O_3 = 6:4) and SiO_2 = 3 wt% and carbon fiber used reinforcement. Table 1 shows the basic quality of the powders used in experiment. Carbon fibers (M60JB, Toray Industries Inc., Japan) with an average diameter of 4–5 μm were used as the reinforcement to obtain C_f/SiC composite. In order to obtain monolithic SiC, nano-SiC powder with the sintering additives was ball-milled in acetone using SiC balls for 12 h at 160 rpm rotation speed by planetary mill equipment to obtain the slurry. After drying during 24 h, the mixed powders were screened through a 100-mesh sieve and sintered for 1 h at 1800°C under the 20 MPa pressure as shown in Fig. 2. In order to C_f/SiC, the mixed slurry impregnated inside unidirectional carbon fiber of 20 mm, dried and sintered as same conditions. The fiber volume

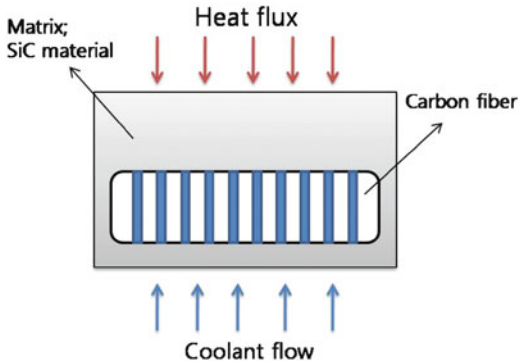

Fig. 1 Divertor component concept placed perpendicular to the flow of the coolant in C_f/SiC composite

Table 1 The properties of materials used in experiment

	Particle size (μm)	Density (g/cm^3)	Purity (%)
SiC	0.05	3.20	99.1
Al_2O_3	1	3.98	99.9
Y_2O_3	2–3	6.00	99.9
SiO_2	0.8	2.20	99.9
C fiber		1.97	

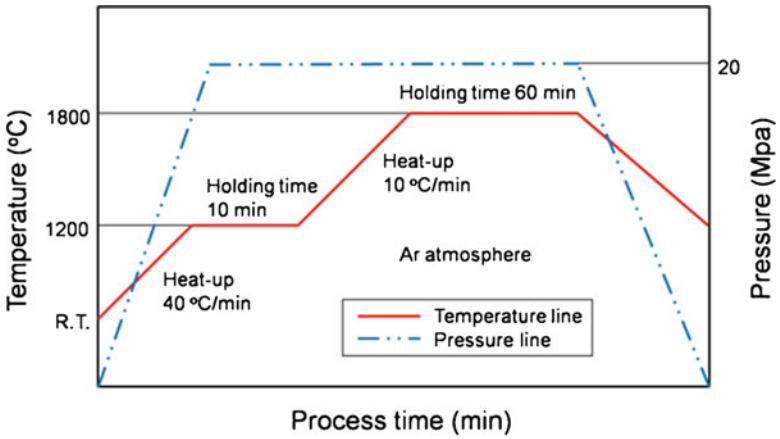

Fig. 2 The fabrication process by hot-pressing

fraction is about 1% in C_f/SiC composite. The samples were cut and ground into 4.4 mm × 2.2 mm × 40 mm specimens for 4-point-bending test in R&B Unitech-T testing machine, operated at a crosshead speed of 0.5 mm/min and a span of 32 mm.

The density of each sample was measured by the Archimedes method. The fracture surfaces were observed by scanning electron microscopy.

3 Results and Discussion

Table 2 shows the average of density on Monolithic SiC and C_f/SiC composite by Archimedes method. The relative densities of all sintering body appeared excellent sintering property nearby theoretical density. Especially, monolithic SiC and C_f/SiC composite have about 95% and 98% respectively. So they come out the densification in process. Therefore they expect good bending strength from these results.

Figure 3 shows the XRD pattern of monolithic and composite by X'Pert PRO MPD machine of the PANalytical. They appeared the same pattern at (35.75),

Table 2 The average of density by Archimedes method

	Theoretical density (g/cm^3)	Measured density (g/cm^3)	Relative density (%)
Molithic SiC	3.254643	3.20306	98.41511
C_f/SiC composite	3.242437	3.07522	94.84287

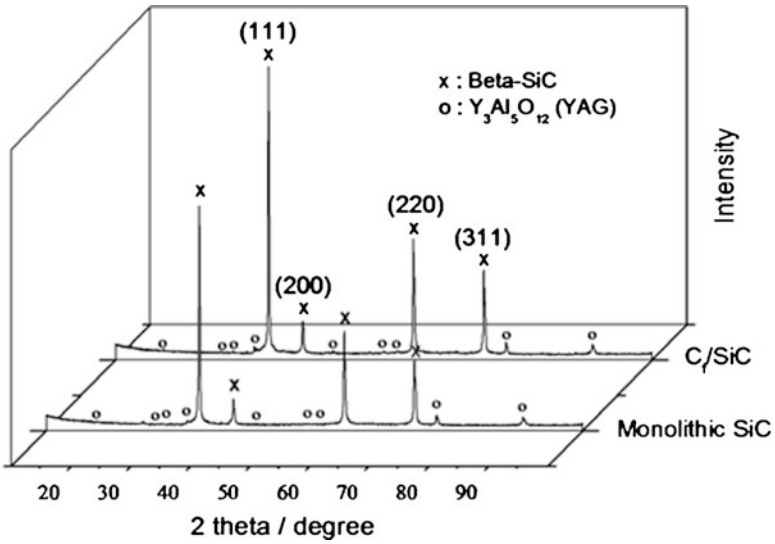

Fig. 3 XRD pattern of monolithic SiC and C_f/SiC composite

(41.39), (60.04), (72.05), (75.39) and (89.96) of two theta as original pattern of β-SiC in this result of XRD analysis [4]. And they exists the β-SiC with crystal structure of cubic. In this result, the sintered monolithic SiC and C_f/SiC composite seldom have the impurity except for silicon, carbon and silicon carbide. But, there are small amount of oxide remnants including aluminum and yttrium (mostly $Y_3A_{l5}O_{12}$: Yttrium Aluminum Garnet (YAG)).

Figure 4 shows the flexural strength by four point bending test on monolithic SiC and C_f/SiC composite and the test result of each data shows the average of five times. In this figure, bending strength of monolithic SiC and C_f/SiC composite were 361 and 521 MPa, respectively. The C_f/SiC composite was show superiority bending strength than monolithic SiC as difference of 160 MPa. The C_f/SiC composite was improves bending strength because of interfacial bonding force between matrix and fiber on surface of fiber at loading point.

Figures 5 and 6 show the microstructure of fracture surface on monolithic SiC and C_f/SiC composite by Quanta 200 FEG machine of the FEI. In the case of monolithic SiC, the particle of round shape was transform square shape and particle was grows over 200 nm in Fig. 4. The C_f/SiC composite came out similar trend with monolithic but growth of particle was come out over 500 nm, also the C_f/SiC

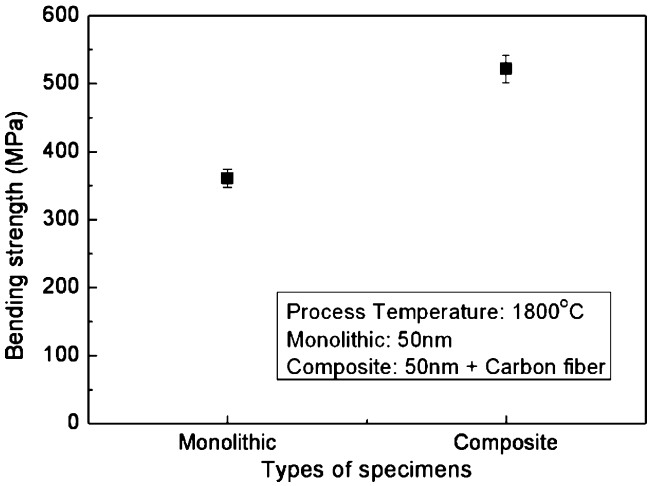

Fig. 4 Bending strength of monolithic SiC and C_f/SiC composite

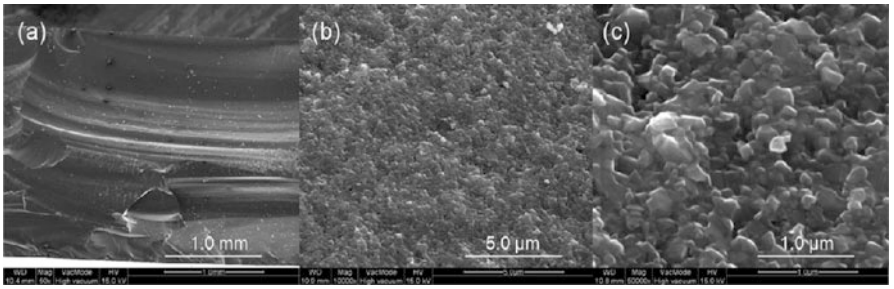

Fig. 5 Fracture surface of monolithic SiC

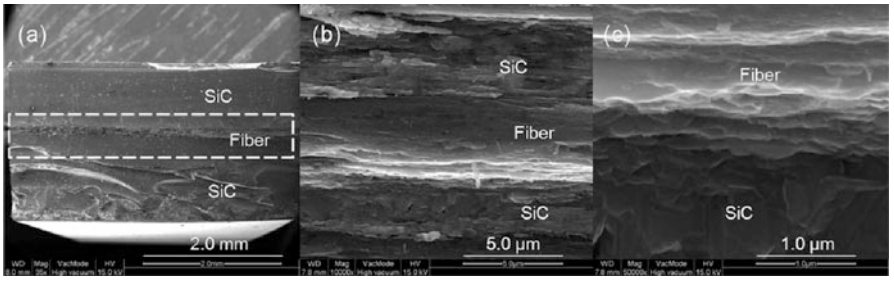

Fig. 6 Fracture surface of C_f/SiC composite

composite was has bonding well because matrix and fiber have good interfacial bonding force in Fig. 5. In these figures, all sintering body of monolithic SiC and C_f/SiC composite became densification like trend of density without many open pores. Therefore, the reason of increasing bending strength on the C_f/SiC composite is due to the interfacial bonding force.

4 Conclusions

The C_f/SiC composite was evaluated in terms of the improvement of strength compared to monolithic SiC in this study.

The monolithic SiC or C_f/SiC composite was made by hot-pressing. Excellent densification was obtained. The β-SiC with crystal structure of cubic same as pattern of the reference. The sufficient strength for structural materials was obtained. The C_f/SiC composite has been improved the strength than monolithic SiC as the result of four point bending test indicated. Bonding between matrix and fiber was supposed to have excellent interfacial bonding force. Improved sinterability of the matrix in composite was seen as the presence of YAG [5]. High bending stress (or heat stress) occur due to high temperature gradient to generate high heat load in the coolant structural material of divertor. So, coolant structural material must withstand this heat stress for structural safety of divertor. In this study, I think that it is suitable for coolant structural material because bending strength of C_f/SiC composite has been improved the strength compared with monolithic SiC. Also, Thermal conductivity of C_f/SiC composite will be evaluated as the next research.

Acknowledgement This work was partly supported by an "Energy Science in the Age of Global Warming" of Global Center of Excellence (G-COE) program (J-051) of the Ministry of Education, Culture, Sports, Science and Technology of Japan.

References

1. Merola M, Danner W, Pick M (2005) EU R&D on divertor components. Fusion Eng Des 75–79:325–331
2. Wang M, Qinjun NP (2009) Thermal conductivity enhancement of carbon fiber composite. Appl Therm Eng 29:418–421
3. Merola M, Matera R (1994) Survey of coolant option of monolithic CFC divertor. Fusion Eng Des 24:257–273
4. Thibault NW (1944) Am Mineral 29
5. Yano T, Yoshida K (1998) Proceedings of the 3rd Korea-Japan seminar on advanced reactor, pp 133–139

Author Index

T. Yao (ed.), *Zero-Carbon Energy Kyoto 2011*, Green Energy and Technology,
DOI 10.1007/978-4-431-54067-0,

Keyword Index